Failure mechanisms in sensitive volcanic soils in the Tauranga Region, New Zealand

A thesis submitted in partial fulfilment

of the requirements for the degree

of

Master of Science (Earth Sciences)

at

The University of Waikato

by

Philippa Mills

2016

THE UNIVERSITY OF
WAIKATO
Te Whare Wānanga o Waikato

ABSTRACT

Sensitive soils derived from weathered pyroclastic materials have contributed to major landslides in the Bay of Plenty. Sensitive soils have a high ratio of peak to remoulded undrained strength. While it is known that (a) sensitive soils flow once failed, causing long runout distances, and (b) these failures often occur following heavy rainfall, the mechanisms that lead to failure are less understood. The aim of this thesis is to determine static and cyclic failure mechanisms of sensitive soils sampled from the failure scarps of two recent landslides in the Tauranga Region. Revelations about how these soils fail will allow slope stability models to more accurately capture geomechanical behaviour.

Recent publications on sensitive soils derived from glacial till materials have indicated that these soils are brittle materials displaying undrained strain softening behaviour, where deviator stress drops significantly following peak stress. Failure is governed by rate dependant, excess pore pressure gradients accumulating during undrained, consolidated triaxial compression (Gylland *et al.* 2013c; 2014; Thakur *et al.* 2014). These publications provided a methodological backbone for this thesis. Field methods included geomorphological and stratigraphic site characterisation, and sampling of extra sensitive soil suspected of contributing to failure. Laboratory methods included geotechnical tests (Atterberg Limits, moisture content, bulk and particle density, particle size distribution, and static and cyclic undrained, consolidated triaxial tests). Static triaxial testing was undertaken at a high compression rate of 0.5mm/min to model rapid undrained during slope failure. Different combinations of average and cyclic shear stresses allowed replication of Anderson's (2015) cyclic contour plot. Shear zone microstructure of failed triaxial samples was analysed using thin section and micro-CT techniques.

Two coastal cliff landslide sites were characterised and sampled: (1) a significant landslide at Bramley Drive, Omokoroa, which initially occurred in 1979, with reactivations in 2011 and 2012, and (2) a landslide on the south side of Matua Peninsula, which occurred in 2012. The bowl-shaped landslide crater at Bramley Drive and long runout component of sensitive material are likely due to failure within an over-thickened sequence pyroclastic material (Pahoia Tephras), which initially accumulated in a paleovalley. At Matua, the failure surface was long, slightly rotational, and comprised a sequence of variable sandy lenses and silty clays. Landslide debris comprised remoulded sensitive material underlying intact overlying blocks, indicating failure of a sensitive soil layer at depth. Material sampled at Omokoroa (OM1) was an extra sensitive ($S_t = 15 \pm 3$) silty CLAY, 19 m from top of profile within Pahoia Tephras. Material at Matua (M1) was an extra sensitive ($S_t = 10 \pm 1$) silty CLAY, 16 m from the top, within the Matua Subgroup. Clay mineralogy of these soils is known to be various morphologies of hydrated halloysite.

Samples from both sites have dominant clay fractions (OM1: clay: 62.6%, silt: 37.3%, sand: 0.1%, M1: clay: 40.1%, silt: 22.3 %, sand: 37.6%). High porosity (OM1: 70% M1:66%), void ratio (OM1: 2.3 M1: 1.8), and moisture content (OM1: 72%, M1: 64%), together with low wet and dry bulk densities (wet b.d: OM1:1320 kgm^{-3}, M1: 1690 kgm^{-3}, dry b.d: OM1: 760 kgm^{-3}, M1: 980 kgm^{-3}), are in keeping with previously published values of halloysite-rich clays derived from pyroclastic material. Atterberg Limits are high for both materials (Liquid limit: OM1: 66 M1: 52, Plastic limit: OM1: 41, M1: 37, Plasticity index: OM1: 25 M1: 15, Liquidity index: OM1: 2.9 M1: 1.8). M1 and OM1 both plot below the A-line in the range of high compressibility silts (MH). M1 and OM1 both have low activity, reflecting the hydrated halloysite composition (OM1: 0.4, M1: 0.4).

Static undrained, consolidated triaxial tests show that failure occurs at less than or near to 5% strain for all tests, indicating brittle failure. Two main types of failure mechanisms were recognised from triaxial results. Post failure, type A was characterised by significant strain softening, contractive, left trending p'q' stress paths, and a rise in global pore pressure after failure. Type B response post-peak deviator stress showed minor to no strain softening, dilative, right trending p'q' paths, and a drop in global pore water pressure. In general, test rate, confining pressure and material affect the type of failure: higher compression rates and confining pressures correlate with type A failure, whereas the opposite is true for type B failure. Failure modes observed in failed triaxial samples were either wedge or shear, with the exception of M1a (tested at 75 kPa confining pressure) which failed by barrel deformation. Strain softening increased with effective confining pressure (R^2= 0.58). Average effective cohesion and friction remain essentially consistent between peak and residual states (OM1: c'f = 26, c'r = 24, φ'f = 31, φ'r=26, M1: c'f = 17, c'r = 17 φ'f = 32, φ'r = 29).

Thin sections captured shear zones tested at 240 kPa and 340 kPa (OM1), and 150 kPa and 255 kPa (M1) confining stress. Riedel shears (R and R') and P shears were observed in all thin sections. Evidence for progressive failure, most notably changes in the abundance and spacing of shears along the same shear zone, was found in both materials. Clay mineral realignment was observed in shear zones. Micro-CT results showed clay matrix material to be denser in shear zones, implying localised contraction of microstructure.

I infer that type A failure mechanism is comparable to sensitive soils that Gylland *et al.* (2013c; 2014) studied. During compression, pore pressure does not have time to dissipate, leading to excess pore pressure gradients, which initiate brittle failure where a release of potential energy results in R shear fractures and R' fractures which become linked by P shears. Microstructural collapse within these fractures induces further excess pore pressure, liquefying material in shear zones, and resulting in a loss of material resistance as evidenced by the strain softening behaviour observed. Realigned material in shear zones provides a pathway for excess pore pressure to dissipate, finally registering as a rise in pore pressure in the post-peak region. Integrity of cohesive bonds and asperity interaction is preserved during shearing, resulting in little to reduction of c' and φ'. For type B failure, lower confining pressures and/or test rates mean that pore pressure has ample time to dissipate during compression, so that when the critical state line in p'q' diagrams is reached, grains interlock, causing pore pressures to drop (dilation).

Boulanger & Idriss (2007) conclude that for sensitive materials, it is difficult to assess the strain or ground displacement that will reduce the clay from peak to residual strength during cyclic loading. In this study, I utilised a new geotechnical tool, a cyclic contour plot (Anderson, 2015), that predicts the cycles to failure, and the average shear strain and cyclic shear strain at failure, for combinations of applied average and cyclic shear stresses. Seven samples were tested at different combinations of average and cyclic shear stresses. Tests with high average and low cyclic shear stress applications resulted in progressive, positive strain accumulation. Tests with no average but high cyclic shear stresses resulted in progressive accumulation of strain in both positive and negative directions. In comparison to Drammen Clay (Anderson, 2015), in general, for the same application of average and cyclic shear stress, failure occurs after a lesser number of cycles, but both average and cyclic strain accumulation is lower. Although limited microstructural evidence was analysed, observations tests show similar mechanisms as described above are responsible for failure under cyclic stresses; post-failure strain softening occurs, and excess pore pressure increases. One

micro-CT sample of an entire failed sample tested at high (60 kPa) cyclic shear stress and zero average shear stress shows intense contraction in the shear zone.

It is likely that following heavy rainfall events, excess pore pressure gradients develop in sensitive material at Bramley Drive and Matua, resulting in localised fracture development. Collapse of the disturbed sensitive soil in developing shear zones releases additional pore water, enhancing pore water pressure gradients and leading to progressive fracture. Ultimately, breakdown of the sensitive material results in liquefaction along a macroscopic failure surface and rafting away overlying material.

ACKNOWLEDGEMENTS

First and foremost I would like to thank my chief supervisor Dr Vicki Moon for firstly her unwavering support from when I first approached her about an MSc thesis topic, right to the very end of thesis writing.

Thank you to Callaghan Innovation for providing funding for this project through the student grant scheme. Thank you to Peter Maxwell for assisting the funding application process. This funding has allowed me to dedicate all the hours I want to on this thesis, while not worrying about financial constraints of day to day living as a student.

Thank you to MBIE for the funding for the trip to Bremen, Germany, to carry out geotechnical testing under the INTERCOAST project IC28, and participate in the Annual INTERCOAST workshop.

Thank you to the University of Waikato for the Masters Research Scholarship.

Thank you to the team at Coffey Geotechnics, notably Kori Lentfer, who initiated and supported the Callaghan Innovation student grant application process. Thank you also to Dave Sullivan, Sally Hargraves, Chris Armstrong, and the Tauranga and Auckland teams at Coffey for supporting the thesis, offering me a graduate position, and answering technical questions. Thank you also for the opportunity to present the research findings at the Young Geotechnical Professional Conference in Queenstown, 2016.

Thank you to Dr Willem De Lange, Prof. Chris Battershill, Te Puea Dempsey and Sydney Wright from the University of Waikato, and Max Kluger, Tobias Mörz, Stefan Krieter and Katrin Huhn from the University of Bremen, Germany, for organising the four week excursion at the University of Bremen. The amount of knowledge that I managed to fit into my brain over these four weeks still baffles me. A special thanks to Max Kluger and Ja Nett Brandt for welcoming me into their homes for the duration of the stay, and showing me the delights of Bremen. Thank you to Alfred the triaxial machine that produced such brilliant results and cooperated throughout the triaxial testing procedure. Participation in the INTERCOAST workshop and getting to know PhD students and other researchers was a very inspiring experience. After four weeks of German culture saturation, some things stuck in my routine upon returning to NZ, namely German recycling habits, and also cycling around the city.

A huge thank you to my partner James, for being the rock to lean on through good times and bad, especially during those tough final months. Thank you also for helping me with field work and geotechnical discussion.

I would like to acknowledge my mother and father for their moral and also financial support throughout this thesis. The perseverance and dedication I have poured into this work are learned from behaviours you both taught me from a young age.

Thank you to field work helpers including James McCardy, Jonno Rau, Dean Sandwell, Royce Sitiaga, Jo Zeke, Ben Stewart, and Chris Morcom, for epic days spinning yarns and getting covered in mud at the bottom of landslides. Thanks to lab work helpers including Renat Radiosinsky, Kirsty Vincent, Adrian Pittari, and Annette Rogers.

Last but definitely not least, a huge thankyou to my friends, especially those that have gone through earth sciences with me since the start of 2011. Gneiss work, great schist guys! Thanks also to the holy flying spaghetti monster.

TABLE OF CONTENTS

LIST OF FIGURES

LIST OF TABLES

CHAPTER 1

INTRODUCTION

1.1 Background and motivation

Regions where sensitive soils are present in the soil regolith are particularly prone to unpredictable, substantial landslides, which can be catastrophic if located near infrastructure and people. Soil sensitivity is defined by the ratio of peak to remoulded strength, at the same moisture content (NZGS, 2005). Values of < 2 are insensitive, 4 – 8 are considered sensitive, 8 – 16 are "extra-sensitive", and > 16 are referred to as "quick clays" (NZGS, 2005).

Recent and historic landslide events in the Tauranga Region have been attributed to sensitivity in weathered pyroclastic soils, yet the fundamental failure behaviour of these soils is not well understood. Several notable landslide events that are attributed to sensitive soils in the Tauranga Region include (1) the Ruahihi Canal failure in 1981 (Hatrick, 1982), (2) a significant coastal cliff collapse at Bramley Drive in 1979 (Gulliver & Houghton 1980), and (3) numerous landslides in the Tauranga City margins following heavy rainfall in 2005. Landslides which have occurred on residents properties have left the property owner in the difficult position of either having to pay for expensive geotechnical works, or sell the property at a highly depreciated value.

Research on sensitive soil failure is largely focussed on regions in Canada and Scandinavia, where failures have resulted in significant damage to infrastructure, as well as loss of land (Geertsema & Torrance, 2005; Locat *et al.* 2011). An example of the catastrophic nature of these landslides is exemplified by the St Jean Vianney (Quebec, Canada) landslide of 1971, which resulted in 31 fatalities, destroyed 40 houses, a highway bridge, local roads, and a power transformer (Tavenas *et al.* 1971). Sensitivity in soils in Scandinavia and Canada is related to the deposition and isostatic rebound of marine terraces comprised of fine grained glacial till, concurrent with retreating glaciers 7 – 12,000 years ago (Torrance, 2014). Other locations where sensitive soils have been identified include North America, Japan, Indonesia and New Zealand (Wesley, 1977; Egashira & Ohtsubo, 1982; Jacquet, 1990; Mitchell & Soga, 2013).

In New Zealand, sensitive soils are derived from rhyolitic and andesitic tephra (Jacquet, 1990). The prevalence of andesitic and rhyolitic volcanism in the central North Island over the last 2 million years has resulted in extensive deposition of loose pyroclastic material (Leonard *et al.* 2010). Sensitive soils have been studied in Taranaki and Huntly by Jacquet (1990), and in Tauranga (Smalley *et al.* 1980; Wesley, 2007; Keam, 2008; Wyatt, 2009; Arthurs, 2010; Cunningham, 2012, Moon *et al.* 2015). Tauranga City and harbour margins in particular are predisposed to landslide failure due to (a) the steep sided nature of the coastal cliffs, and (b) the weak and/or sensitive nature of materials that comprise the cliffs.

Studies on failure mechanisms in the Tauranga Region where sensitivity is suspected to be involved are limited to several specific case studies (Oliver, 1997; Burns & Cowbourne, 2003). The fundamental failure mechanisms of these materials at a microstructural level have not yet been studied. Landslides have generally occurred following heavy rainfall, suggesting pore water pressure development is linked to failure (Moon *et al.* 2013; 2015).

Of importance is that commonly employed slope stability software analyses that use finite element modelling techniques are not accurately capturing failure properties of sensitive soils (Gylland *et al.* 2014). Gylland *et al.* (2014) suggests that failure properties of the soil must first be studied, so that results can be incorporated when modelling failure.

Recently published literature regarding static failure mechanisms in sensitive soils in the northern hemisphere provide a methodological backbone for static failure mechanisms for this thesis (Thakur, 2007; Gylland *et al.* 2012; Gylland *et al.* 2013c; Gylland *et al.* 2014; Thakur *et al.* 2014).

Recent unexpected major earthquake events in Christchurch have highlighted the importance of studying cyclic failure mechanisms, even in areas where there has been little historic seismic activity, such as Tauranga. Cyclic failure properties of sensitive material have not been studied before in New Zealand. In this study I attempt the first known replication of the cyclic contour plot, which is a new geotechnical tool developed by Anderson (2015). The main benefit of the cyclic contour plot is that a large amount of information about the failure properties of a soil, at different combinations of average shear stresses (e.g. a heavy rainfall event or building a house) and cyclic shear stresses (e.g. pile driving, earthquakes) can be observed on one diagram.

1.2 Aims

The overarching aim of this thesis is to identify laboratory static and cyclic failure mechanisms of two sensitive soils that are believed to have contributed to landslide failures in the Tauranga region. Objectives to achieve this goal are:

1. Investigate, characterise and sample two landslide sites in Tauranga, where sensitive soils are believed to contribute to failure;
2. Replication of methods employed by Gylland *et al.* (2013c), to elucidate static failure mechanisms, which include:
    A) undrained, consolidated triaxial tests at higher compression rates than recommended by the British Standard 1377 (1990) Part 8: Shear strength tests (effective stress) and;
    B) microstructural analysis of shear zones of failed triaxial samples using thin section and micro-CT techniques;
3. Replication of methods developed by Anderson (2015) to develop contour plots for cyclic failure conditions:
    A) perform undrained, consolidated cyclic triaxial tests on sensitive material at different combinations of average shear stress and cyclic shear stress, in order to:
    B) plot normalised average and cyclic shear stress results on a cyclic contour plot, to derive failure properties;
4. Compare failure mechanisms of sensitive soils in Tauranga to sensitive soil failure mechanisms in the northern hemisphere;
5. Relate laboratory failure mechanisms to geomorphological characteristics in an attempt to characterise landslide failure mechanisms at the two sites initially characterised.

1.3 Research benefits

Research benefits include:

(a) Improved accuracy and precision of soil strength parameters, which are crucial for geotechnical design of structures such as retaining walls and foundations.

(b) A basis for studies concerning modelling slope stability in sensitive material, and landslide susceptibility mapping in the Tauranga Region. Hazard maps will allow the council to plan and zone future developments more efficiently, leading to reductions in landslide hazard;

(c) Exposure of a new geotechnical tool (the cyclic contour plot) which has the potential for wide application within the geotechnical industry.

1.4 Thesis layout

Chapter 2 presents a literature review of the definition and evolution of sensitivity in volcanic ash soils and glacial till soils from the Northern Hemisphere, current theories on field and laboratory failure mechanisms in sensitive soils derived from glacial till, a review of cyclic failure in sensitive materials, and finally a brief review of Tauranga geology and clay mineralogy. Chapter 3 presents field and laboratory methods used.

Results are presented in Chapters, 4, 5, 6 and 7. Chapter 4 outlines justification for site selection, and geomorphic and stratigraphic properties of each site chosen. Chapter 5 presents geomechanical properties of samples collected from each site, including static triaxial test results and failed specimen characterisation. Chapter 6 outlines the microstructural properties of shear zones in failed triaxial samples from evidence obtained from thin sections and micro-CT analysis. Cyclic triaxial test results and contour plot development is presented in Chapter 7.

Chapter 8 discusses the observations presented in results chapters in light of relevant literature. Laboratory static and cyclic failure mechanisms are discussed, and related back to each site in an attempt to determine failure mechanisms of recent landslides at each site. Finally, Chapter 9 summarises research findings and provides recommendations for future research topics.

CHAPTER 2

LITERATURE REVIEW

2.1 Chapter framework

Section 2.2 presents a synopsis of definition, origin, and properties of sensitive soils in local and international contexts. Landslides related to sensitivity in Tauranga are also outlined in Section 2.2. Section 2.3 presents geological formations in the Tauranga Region of relevance to this thesis. Section 2.4 summarises the development of progressive failure theory in north hemisphere sensitive soils, and how fracture mechanics principles have been recently applied to progressive failure theory. Section 2.5 outlines the current theories on static failure mechanisms in laboratory tests on northern hemispheric sensitive soils. Finally, section 2.6 briefly summarises literature regarding cyclic failure and the cyclic contour plot concept.

2.2 Sensitive soils

2.2.1 Definition of sensitivity

Sensitivity (St), the ratio of undisturbed, undrained peak shear strength to remoulded, undrained shear strength, defines the loss of soil strength upon remoulding (Selby, 1993; Lefebvre, 1996). The greater the sensitivity, the more prone a soil is to remoulding and flowing once the peak strength has been surpassed. **Table 2.1** presents the definition of sensitivity given by NZGS (2005).

2.2.2 Global distribution of sensitive soils

Sensitivity in Northern Hemispheric regions including Eastern Canada and Scandinavia is related to the distribution of uplifted marine terraces comprised of fine grained glacial till (Rankka *et al.* 2004). Marine quick clay has also been found in Japan (Egashira & Ohtsubo, 1982) and Alaska (Updike & Carpenter, 1986). Other regions where sensitive soils are found include areas where significant amounts of andesitic and rhyolitic volcanic ash has been deposited, such as New Zealand (Jacquet, 1990), Indonesia (Wesley, 1977), Hawaii (Wieczorek, 1982) and Japan (Sasaki, 1974).

Table 2.1. Sensitive soil classification according to NZGS, (2005).

Shear strength ratio (undisturbed/ remoulded)	Descriptive term
1	Insensitive
1-2	Low sensitivity
2-4	Medium sensitivity
4-8	Sensitive
8-16	Extra-sensitive
>16	Quick

2.2.3 Sensitive soils derived from glacial outwash plains

Sensitivity in Eastern Canada and Scandinavia has evolved over the last 11,000 years, following the termination of the last ice-age. Glacial retreat resulted in deposition of shallow marine terraces comprised of illite rich clay to silt sized glacial till at the glacial toe. Concomitant with glacial retreat, these terraces isostatically rebound, resulting in subaerial exposure. Subaerial weathering has since resulted in river channels cutting through these landscapes, which contribute to sensitive soil failure (Torrance, 2014). Torrance (2014) outlined the successive geological development of high undisturbed strength, and low remoulded strength in northern hemisphere sensitive soils. A summary of Torrance's (2014) findings is presented below.

2.2.3.1 Development of high undisturbed strength

Firstly, the slow settling rate of illite-rich glacial till through the water column at the glacier toe allowed flocculation of particles into a "cardhouse" structure, with edge to edge and edge to face particle contacts (**Figure 2.1**) (Rankka *et al.*, 2004 after Goldschmidt, 1926).

Sodium ions from seawater electrostatically bonded with negatively charged clay minerals to uphold the cardhouse structure, even after uplift of terraces. High void ratios and low permeabilities allows large amounts of water to be retained by the soil, preventing further consolidation, and inducing fluidisation upon remoulding (Torrance, 2014).

2.2.3.2 Development of low remoulded strength

Subaerial exposure of illite-rich marine terraces to fresh water sources contributes to development of low remoulded strength (Rankka *et al.* 2004). The electric double layer is created due to the negatively charged surface of a clay

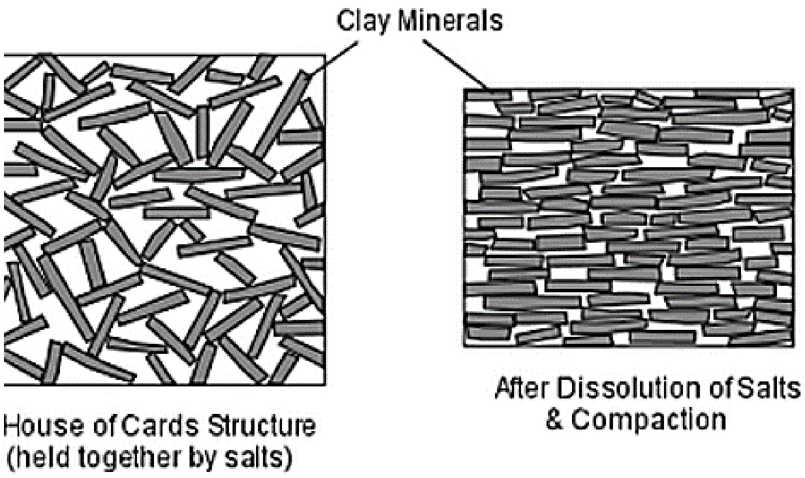

Figure 2.1. Salt precipitates in the pore spaces, allowing a cardhouse structure. Upon leaching, salts dissolve and this structure is lost and cannot develop again. Figure source: http://www.tulane.edu

mineral electrostatically bonding with the positively charged cations in pore water (Mojid, 2014). Firstly, Na^+ is leached from the electric double layer around clay minerals by fresh water (**Figure 2.2**). Na^+ concentration is reduced by either (1) percolation of fresh water from rainfall or snowmelt or (2) artesian water pressures forcing groundwater into sensitive soil deposits from below or adjacent regions, or (3) diffusion of salts towards areas of lower concentration (Rankka *et al.* 2004). Leaching of positive charges results in an overall negative charge between soil particles, so upon disturbance clay minerals essentially repel each other. When combined with high moisture contents, the effect is a very rapid loss of strength and consequent flowing of material (Torrance, 2014).

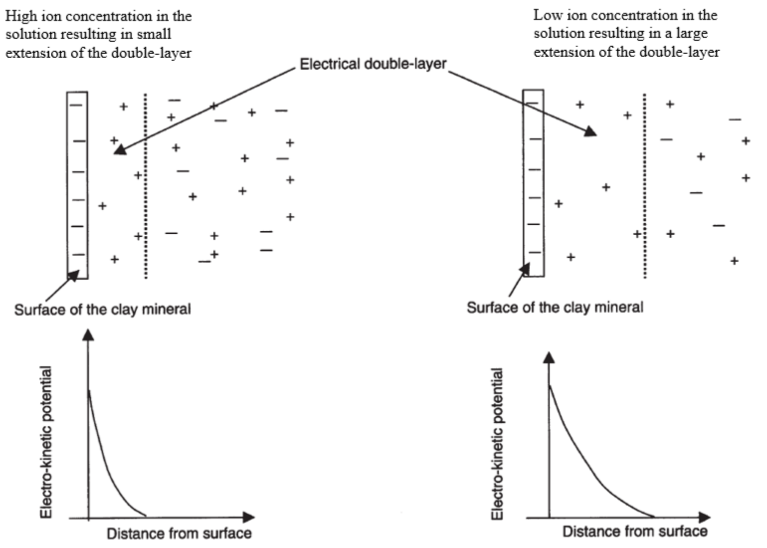

Figure 2.2. The ion concentration of the water determines the extent of the diffuse double layer. Monovalent ions such as K^+ and Na^+ increase the extent of the double layer, whereas Mg_2^+ and Ca_2^+ decrease the extent of the double layer (Rankka *et al.* 2004).

2.2.4 Sensitive soils derived from volcanic ash

2.2.4.1 Global occurrence

Sensitive soils derived from volcanic ash have been located in Indonesia (Wesley, 1973 & 1977), Japan (Sasaki, 1974), Hawaii (Wieczorek, 1982) and New Zealand (Smalley, 1980; Jacquet, 1990, Keam, 2008; Wyatt, 2009; Arthurs, 2010; Cunningham, 2012; Moon *et al.* 2015). From geotechnical testing and mineralogical analysis of some volcanic ash clays from Java, Indonesia, Wesley (1973 & 1977) illustrated that halloysite clay minerals correlated with sensitivity rather than allophane clay minerals. In Japan, Sasaki also noted the prevalence of halloysite in volcanic derived quick clays in the Kitami Clay (Sasaki, 1974).

2.2.4.2 Sensitive soils in NZ

Sensitive soils in New Zealand are residual soils, derived from weathering of andesitic and rhyolitic pyroclastic material (Wesley, 2009). Sensitive soils have been located in pyroclastic air fall deposits, pyroclastic flow deposits, and the colluvial, fluvial, and reworking products of these (Moon *et al.* 2013). Volcanic parent material contains glass, pumice, crystal fragments, and clay minerals (Parfitt, 1990; Arthurs, 2010).

In 1990, Jacquet studied sensitive soils from the Taranaki and Waikato Regions. Sensitivities between 5 and 55 were recorded near saturation. Sensitivity was attributed to high undisturbed strength created by electrostatic and physical bonds. Physical bonds included imogolite fibres linking allophane particles which did not reform following remoulding. Jacquet (1990) attributed microstructural characteristics to be more important than mineralogy, due to destruction of imogolite fibres between clay minerals. Jacquet (1990) states that high observed peak strength values are due to oxidising conditions, allowing formation of cementing iron oxide bonds, and hence drying out of the soil.

Moon *et al.* (2015) outlines a plausible theory for the development of sensitivity in the Tauranga Region. Fine grained material from the Taupo and Coromandel Volcanic Zones was deposited in a loose arrangement either primarily by air settling or secondarily in low energy fluvial, lacustrine or estuarine environments. Significant loading has not occurred since deposition, therefore the open structure has likely been preserved. Moon *et al.* (2015) suggested that small pore space, high moisture content and little atmospheric exposure guarantees the local environment to stay wet, with little water movement (Moon *et al.* 2015). Silica leached from volcanic glasses in overlying tephras, along with weathering of mafic minerals, may promote formation of platy halloysite morphologies over allophane. Initially, cations leached into the system from overlying volcanic material promote, cohesion. Eventually, this cation supply diminishes, and the pore water has a low cation concentration i.e. a weaker electrostatic bonding. The lowered concentration of cations in the pore water results in a loss of true cohesion between clay particles (Moon *et al.* 2015). The soil structure is left open and has little strength from a combination of true cohesion, apparent cohesion due to water films in the pores, and minor frictional strength across grain contacts (Moon *et al.* 2015).

2.2.5 Landslides related to sensitivity in the Tauranga Region

Several cases of sensitive soils in the Tauranga Region have resulted in catastrophic failure, namely the Ruahihi Canal Failure in 1981 (**Figure 2.3**d), the slump at Bramley Drive, Omokoroa in 1979 (**Figure 2.3**c), and the landslides in Otumoetai in 2005 (**Figure 2.3**a & b). These failures occurred following periods of heavy rainfall, and all three resulted in significant infrastructural damage. The fluidity of debris, consistent across each failure, which induces long run-out distances, has been linked to sensitive soils (Gulliver & Houghton, 1980; Keam, 2008; Wesley, 2007; Wyatt, 2009; Arthurs, 2010; Cunningham, 2012).

Sensitive material at Ruahihi comprised rhyolitic Waimakariri Ignimbrite (Burns & Cowbourne, 2003). Elevated groundwater and piping erosion was encouraged because a fill layer covering the Waimakariri Ignimbrite was preventing drainage of the underlying Waihou Ignimbrite. Porous halloysite microstructures were attributed to be the cause of sensitivities as high as 60 (Prebble, 1986).

In 2005, high rainfall triggered many landslides around Tauranga, including one major site at Landscape Road in Otumoetai. Wesley (2007) accredited long runout distances of these landslides to water accumulation in sensitive Pahoia Tephra units. The loss of land area due to landsliding can be seen in **Figure 2.3a & b**.

A highly sensitive (S_t = 140) flowslide occurred in August, 1979 at Omokoroa Peninsula (**Figure 2.3c**) (Smalley *et al.* 1980). Clay mineralogy was found to be 80% hydrated halloysite with minor amounts of quartz and crystobalite, however, determination of Atterberg limits resulted in the conclusion that the soil was actually a silt. Moisture contents were greater than respective liquid limits, allowing material to flow once peak strength was reached (Smalley *et al.* 1980). Smalley *et al.* (1980) also offered a tentative conclusion that brittle deformation was causational in sensitive soil failure. Keam (2008) found that the failure mechanism was excess pore water from natural and anthropogenic sources causing loss of strength of sensitive soil.

The failure was reactivated on the 11th May 2011. A prolonged period of heavy rainfall prior to sliding was accredited to inducing failure. The Tonkin and Taylor report suggests that additional loss in soil strength was due to weathering of exposed sensitive layers (Tonkin and Taylor, 2011).

Moon *et al.* (2013) inferred from CPTu testing that the soil profile at Bramley Drive has a large, singular aquifer with high water pressures in poorly drained materials. The small size of halloysitic clay particles and structure of these particles, result in a soil with tightly confined, small pore spaces. Therefore, soils can accommodate high amounts of water which cannot move easily (Moon *et al.* 2013).

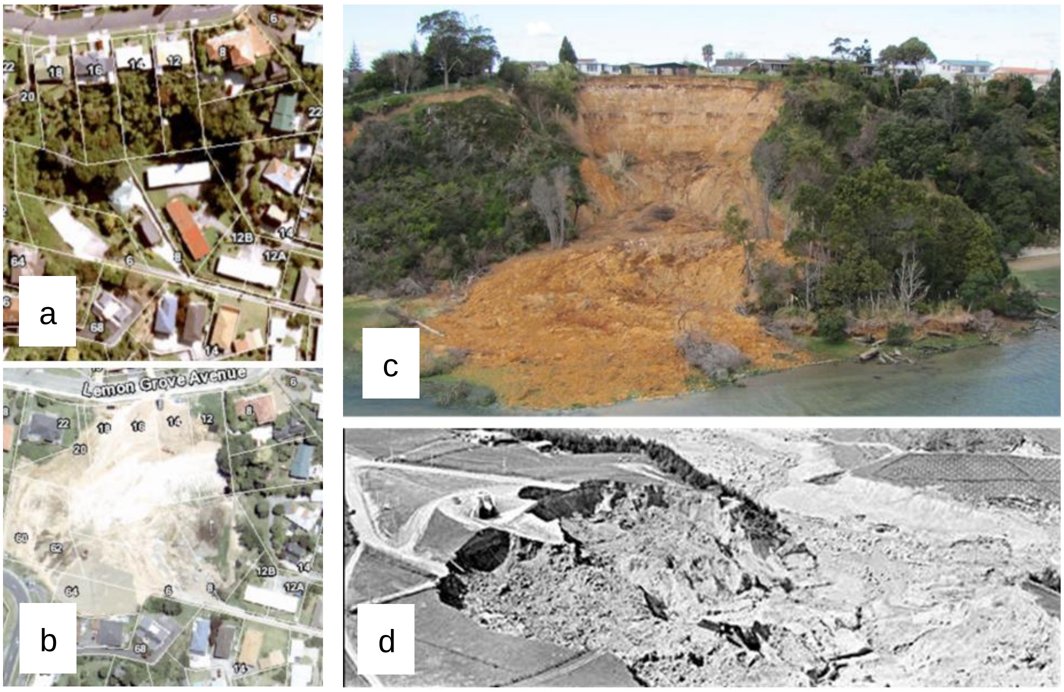

Figure 2.3. Figures a and b show an aerial view of the land affected by landslides which happened on Landscape Road, Otumoetai in 2005 following a period of heavy rainfall (Tauranga City Council Mapi Viewer). Figure 2.4 c is the slump at Bramley Drive taken in September 2012. The initial landslide occurred in 1979, and was subsequently reactivated in 2011 (Photo: Peter Clark, Western Bay of Plenty Regional Council). Figure 2.4d is an aerial view of the Ruahihi slip in September 1981. (Photo: David de la Hyde).

Kluger *et al.* (2015) further investigated the Bramley Drive failure by comparing the stratigraphy, mineralogy, soil shear strength and clay morphology down a 24 m borehole drilled behind the landslide scarp (**Figure 2.4**). They found that the morphology of halloysite has a strong influence on sensitivity, with high sphere-low tube morphologies correlating with high sensitivity, and low sphere-high tube morphologies correlating with lower sensitivity. The diameter of the halloysite spheres increases with sensitivity, however a dependence on tube length was not observed. A highly sensitive silt layer with dominantly halloysite spheres was found at 23 m depth (left **Figure 2.4**). The overall sensitivity was also plotted against peak and remoulded strength (**Figure 2.4**). In contrast to andesitic sensitive materials in Taranaki (Jacquet, 1990), sensitivity correlates more strongly with the remoulded strength rather than the peak strength (Kluger *et al.*, 2015).

2.2.5.1 Suspected failure mechanisms

Moon *et al.* (2015) concluded that the relationship of failures to pore water pressure thus far are as follows: (1) water rapidly infiltrates through permeable layers at the top of the profile, (2) lower permeability of deeper profiles inhibits water from draining further, therefore water tables and saturation are consistently high. Therefore, pore water pressure is induced with little addition of water, triggering failure (Moon *et al.* 2013).

2.2.6 Clay mineralogy of Tauranga sensitive material

Until recently, it was thought that allophane was primarily responsible for soil sensitivity. Historically, allophane, a short range order aluminosilicate clay mineral, was suspected to initially form as a primary weathering product of volcanic glass, and gradually weather over time to produce halloysite, a 1:1 phyllosilicate clay with a ratio of 1 tetrahedral to 1 octahedral sheet (Selby, 1993). However, a recent alternative and now widely accepted hypothesis is that halloysite forms in response to certain environmental conditions, rather than gradually as a weathering product of allophane over time (Chruchman & Lowe, 2012). Primarily, prevailing conditions for halloysite formation are a silica-rich environment, and a wet, slow-draining soil profile (Churchman & Lowe, 2012). Thus, climate, depth of burial, parent material composition, tephra thickness, drainage, vegetation and human impact can influence halloysite formation (Chruchman & Lowe, 2012). At the Bramley Drive landslide, recent SEM (scanning electron microscopy) analysis of borehole material shows that halloysite morphology influences sensitivity (**Figure 2.4**).

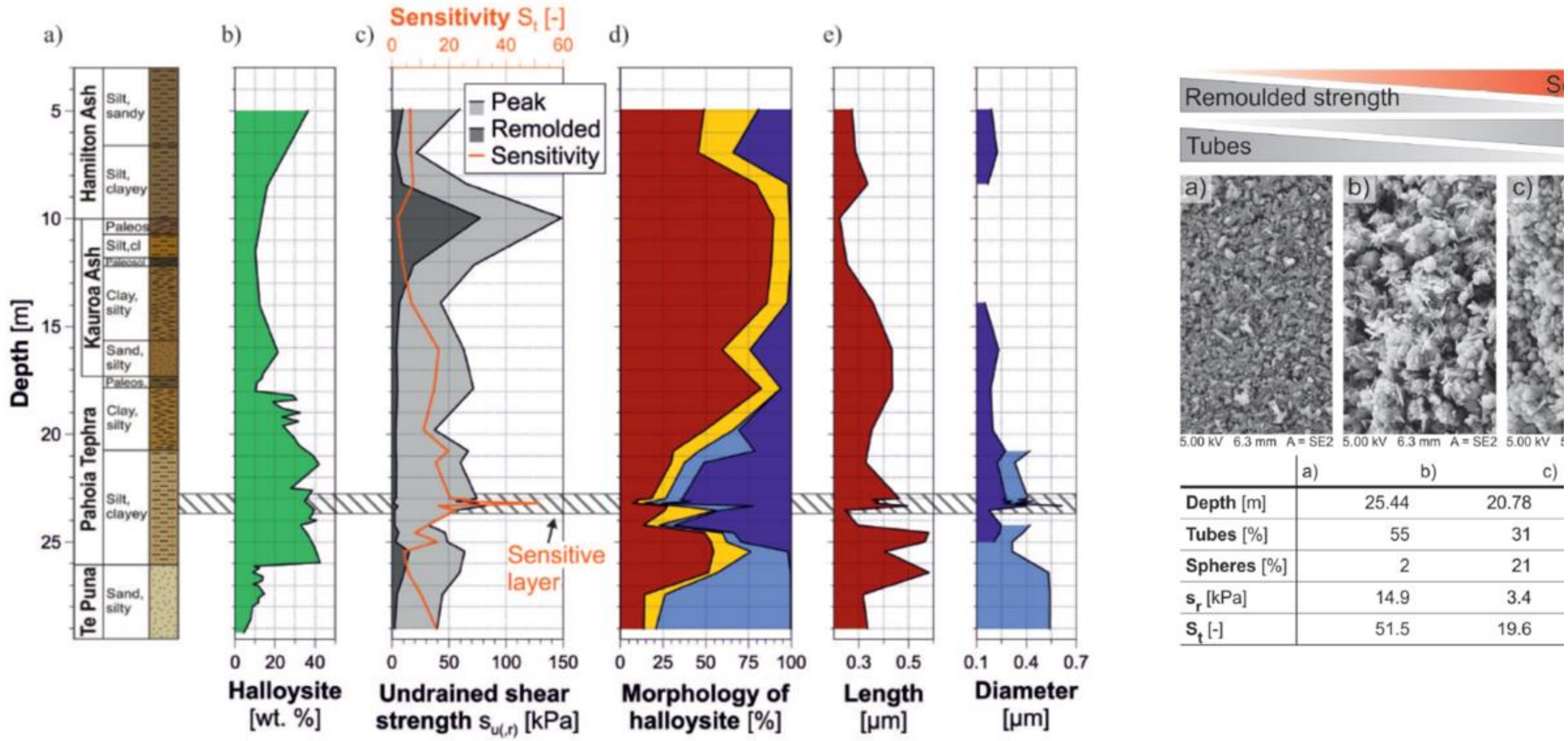

	a)	b)	c)
Depth [m]	25.44	20.78	
Tubes [%]	55	31	
Spheres [%]	2	21	
s_r [kPa]	14.9	3.4	
S_t [-]	51.5	19.6	

Figure 2.4. The borehole log from directly behind the landslide scarp at Bramley Drive, Omokoroa (left). The highly sensitive layer is at approximately 23 m depth within Clayey SILT Pahoia Tephra's, and corresponds to high spherical halloysite concentrations and lower tubular halloysite concentrations observed in SEM images (right). Figure: Kluger *et al.* (2015).

2.3 Tauranga basin geology

2.3.1 Background

The Tauranga basin is a sedimentary basin bound by the Kaimai Ranges (west) and Papamoa Range (South). The Tauranga basin region broadly encompasses a late Pliocene – Pleistocene sequence of internally and externally sourced volcanogenic sediments and volcanic rocks (Briggs, 1996). Following deposition of the local basement c. 2.09 Ma (Waiteariki Ignimbrite) (Briggs *et al.* 2005), a period of rapid subsidence created approximately 570 km^2 of accommodation space. Basin infill consist largely of fine grained pyroclastic material derived from Taupo and Coromandel Volcanic Zones (**Figure 2.6**). Local volcanics have also contributed to sediment infill through minor eruptive events. A marine transgression ~ 6500 B.P resulted in flooding of inland areas, creating the Tauranga Harbour. Bordering the harbour are steeply cut, N – NE trending flat surfaced terraces, comprised mainly of normally consolidated reworked and in *in situ* volcanic material (Briggs *et al.* 1996). Many relict landslide bowls scar the cliff faces. The stratigraphic units comprising the terraces are outlined below. Tauranga stratigraphy and geologic maps are presented in **Figure 2.5** and **Figure 2.6** (Briggs *et al.* 1996).

2.3.2 Stratigraphy of the terraces of the Tauranga Basin

2.3.2.1 The Matua Subgroup

Matua Subgroup sediments consist of highly variable terrestrial and estuarine sedimentary deposits, derived from erosion, transportation, and redeposition of consolidated and unconsolidated volcanic rocks and tephras. Sediments include horizontally and vertically variable deposits of pumiceous and rhyolitic silts, sands and gravels, estuarine and lacustrine muds, peats, lignites, intercalated with local and distal tephra deposits. (Briggs *et al.* 1996). Matua Subgroup sediments form the backbone of a number of up to 60 m high terraces that jut out as peninsulas into the Tauranga Harbour. Drill holes have encountered Matua Subgroup sediments to a depth of up to 150 m. Matua Subgroup deposits include all deposits that post-date the Waiteariki Ignimbrite (2.18 Ma) and pre-date the Hamilton Ash Formation (0.35 Ma) (Briggs *et al.* 1996).

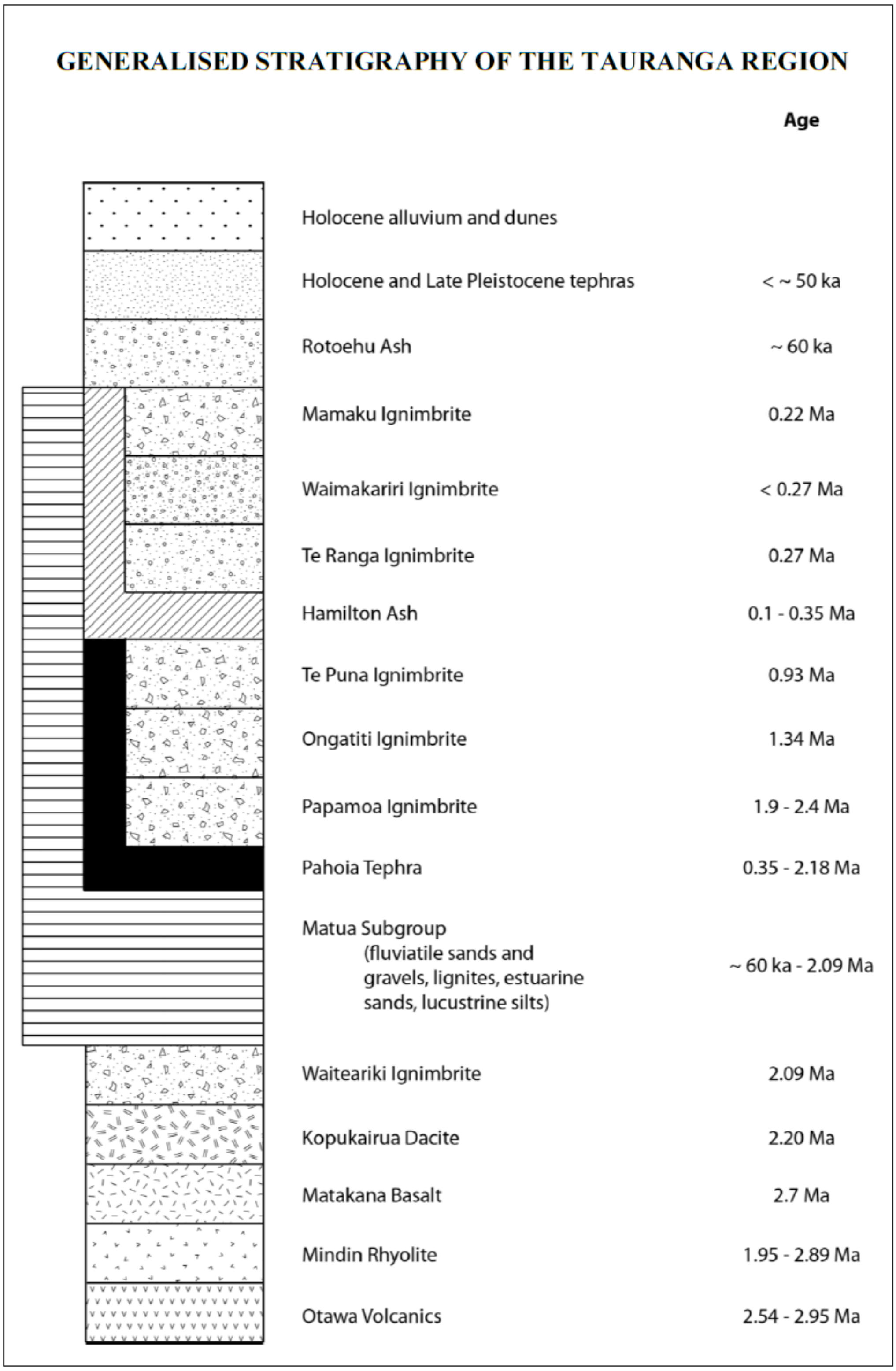

Figure 2.5. Stratigraphy of the Tauranga region compiled from Briggs *et al.* (1996).

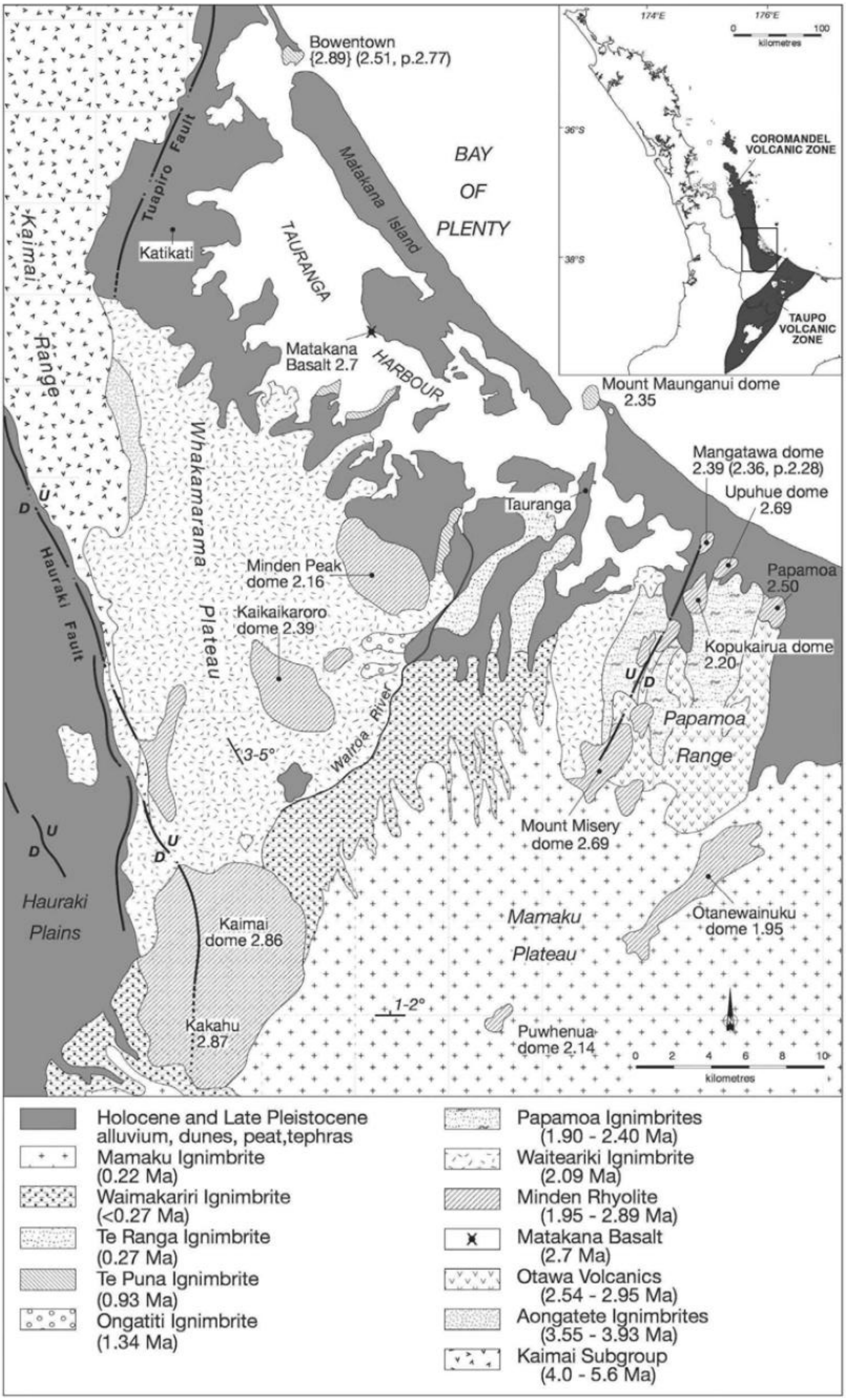

Figure 2.6. Geological map of the Tauranga region from Briggs *et al.* (2005).

2.3.2.2 Pahoia Tephras

The Pahoia Tephras is an umbrella term for all tephra derived deposits older than the Hamilton Ash Formation (0.35 Ma) and younger than the Waiteariki Ignimbrite (2.18 Ma), intercalated within the Matua Subgroup. Pahoia Tephras include local and distal ignimbrites, and paleosols. Briggs *et al.* (2005) suggests that the Pahoia Tephras may be a correlative of the extremely weathered, clay-rich rhyolitic tephra deposits that underlie the Hamilton Ash sequence in the Waikato Region. Pahoia Tephras are exposed at coastal sections at Greerton, Maungatapui, Matapihi, at the base of Mount Maunganui, Matua, alongside the Waikareao expressway, Omokoroa and Pahoia Peninsulas, and on Matakana and Motuhoa Islands. Pahoia Tephra units unpredictably vary, horizontally and laterally (Briggs *et al.* 1996).

2.3.2.3 Te Puna Ignimbrite

The Te Puna Ignimbrite is a non to partially welded brown ignimbrite. It is either a locally erupted, small volume ignimbrite (<5 km^3), or distal deposits from ignimbrites sourced from the TVZ (Taupo Volcanic Zone). A younger plateau age obtained by Briggs *et al.* (2005) for the Te Puna Ignimbrite suggests that the source is likely to be distal, erupted between 1.21 - 0.89 Ma, however the localised occurrence of Te Puna Ignimbrite suggests a local source (Briggs *et al.* 1996). Exposures include coastal cliffs at Omokoroa (3 m), at Pahoia Point (10 m), and adjacent to the Wairoa River (>16 m thickness) on Te Puna Station Road. Arthurs (2010) attempted to correlate the Te Puna Ignimbrite to the extensive, distinctive pinkish marker beds of the Kidnapper Ignimbrite (c. 1.0 Ma) on the basis of (i) deposit mineralogy (primarily quartz and plagioclase feldspar with hydromica visible in pumice fragment hand specimens), (ii) pyroclastic structures especially accretionary lapilli in the air-fall tephra, and (iii) stratigraphic position (age). Conversely, Briggs *et al.* (1996) suggests that the Te Puna Ignimbrite has a reverse magnetic orientation (Matuyama Chron, 2.58 - 0.78 Ma), while the Kidnapper Ignimbrite is normally oriented, within the Jaramillo Subchron (0.99-1.07 Ma). Thus, they cannot be derived from the same eruption.

2.3.2.4 Hamilton Ash Formation:

The Hamilton Ash Formation is an inconsistent sequence of strongly weathered clay beds, derived from both the direct deposition of rhyolitic ash and associated paleosols, as well as occasional loessic beds (Lowe *et al.* 2001). Originally the Hamilton Ash Formation was divided into 9 units (H1-H9) by Ward

(1967), however the uppermost H8-H9 units have been revised as the Rotoehu Ash and Younger Tephras. Six or more ignimbrite generating volcanic centres were active during this time, making it difficult to characterise each bed mineralogically and geochemically in order to define a source (Lowe *et al.* 2001). Hamilton Ashes are widespread throughout the Hamilton and Coromandel regions. The sequence can be up to 6 m thick, and is 2.5 m thick at Omokoroa. Hamilton Ashes are dated between 0.35 – 1 Ma.

2.3.2.5 Rotoehu Ash

Rotoehu Ash is typically a whitish-grey, fine to coarse ash sized tephra which directly overlies the Hamilton Ash as a prominent marker bed (Briggs *et al.* 1996). Rotoehu Ash is widespread, and in the Tauranga region thickness varies between 0.3 to 2.4 m (Briggs *et al.* 1996). Literature suggests an age of around 45 ka (Lowe & Hogg, 1995).

2.3.2.6 Post – Rotoehu Ash

Overlying the Rotoehu Tephra is a sequence of tephras sourced from the Taupo Volcanic Zone which constitute the uppermost soil layer (Briggs *et al.* 1996).

2.4 Landslides in sensitive soils: progressive evolution of shear zones

The theory of progressive failure of landslides in sensitive clays has long been embedded in the literature (Skempton, 1964; Bjerrum, 1967; Bishop, 1971; Palmer & Rice, 1973; Bernander, 2000). Complexities involved with modelling true conditions of soil mechanics during progressive failure are still presently under debate.

“Progressive” refers to the stable growth of a shear band in response to an energy release, whereas “catastrophic” is permitted when a shear band becomes self-propagating (Purzin *et al.* 2010). Skempton (1964) described progressive failure by the following declaration: “if for any reason a clay is forced to pass the peak at some particular point within its mass, the strength at that point will decrease. This action will throw additional stress on to the clay at some other point, causing the peak to be passed at that point also. In this way a progressive failure can be initiated and, in the limit, the strength along the entire length of a slip surface will fall to the residual value” (**Figure 2.7**) (Terzaghi & Peck, 1948; Skempton, 1964; Bjerrum, 1967).

Fig. 7. Progressive failure along a circular failure surface.

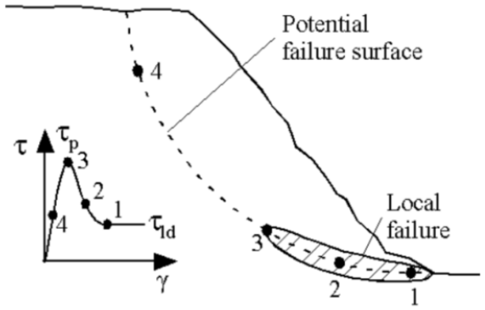

Figure 2.7. Progressive failure along a circular failure surface, related to the shear stress vs shear strain curve. At points 1 and 2, the soil is becoming fully remoulded as a result of local failure, at point 3 there is a sharp strain increase where soil falls from its peak to residual shear strength, and point 4, a zone some distance away from the toe of the slope where soil behaves elastically as it has not reached peak strength (Locat *et al.* 2011).

Progressive failure is used in a spatial sense, where the failure surface begins at some point and propagates toward boundaries (Thakur, 2011). Loss of shear strength within the failure surface is therefore denoted as development of displacements. The term shear band is the connected zone on which the landslide "slides", and is used synonymously with failure surface, shear zone, slip line, or discontinuity (Thakur, 2011). The following section addresses the historical development of theories surrounding progressive failure mechanisms in sensitive soils.

2.4.1 Historical development of progressive failure theory

Progressive failure was first theorised and applied to retrogressive landslides, or landslides where the scarp progresses backward away from a free face, by Terzaghi and Peck (1948). Key developments in progressive failure theory in the 1960's were (1) that stability is controlled by the residual, rather than peak strength of the soil (Skempton, 1964), and (2) propagation of the failure surface is controlled by the release of energy during strain softening (peak shear strength – residual shear strength) (Bjerrum, 1967; Bishop, 1971). Kjellman (1954) first considered that progressive failure could occur in normally consolidated sensitive soils, but most initial research focussed on progressive failures in overconsolidated clay slopes (Bjerrum, 1967; Bishop *et al*., 1965).

2.4.2 Failure modes of sensitive clay landslides

Four main geomorphic expressions of retrogressive landslides were documented by Tavenas (1984) and Karlsrud (1984): single rotational slides, multiple regressive slides (earth flows) (**Figure 2.8**a), translational progressive slides (**Figure 2.8**b), and spreads (**Figure 2.8**c) (Locat *et al.* 2011). Initially, one slide was considered to trigger the next, rather like falling dominoes (Tavenas, 1984, Locat *et al.* 2011). Recent authors (Bernander, 2000; Quinn *et al.* 2011) resolved that rather than this domino effect, where the shear plane develops with failure of each block, progressive landslide failures are controlled by a shear zone that at least partially develops before any sliding of overlying blocks. Progressive shear zone development could occur over a single earthquake event, or over geological time due to cyclic loading. Quinn *et al.* (2011) proposes the slope to be only marginally stable once the failure surface forms; only a small perturbation is required to initiate failure. Geomorphic evidence which supports this theory include (1) smooth failure surfaces (if discrete failures were occurring, the surface should be highly disrupted), (2) pre-existing weak layers, (3) tension cracks near the final scarp and (4) an outline of moisture of the slide in aerial photographs (Quinn *et al.* 2007).

Bernander (2000) concluded that progressive failure can occur by thee modes: (1) upward progressive failure, where the failure surface propagates inward and upward from a perturbation at a river bank, (2) downward progressive failure, where the failure surface propagates downward towards a free face, induced by a load far back, and (3) instantaneous development of a failure surface concurrent with widespread liquefaction of a silt or clay layer under transient seismic loading during an earthquake (**Figure 2.9**).

Downward progressive or translational progressive failure, for example the slide in 1950 at Surte, Sweden (Locat *et al.* 2011), is where a local instability generated by a small disturbance such as pile driving propagates down the slope, inducing an increase in lateral earth pressure downhill. If total pressure surpasses passive resistance, global failure occurs. Downward progressive failures are generally translational, and primarily occur in long, gently inclined slopes, along a normally or slightly overconsolidated sedimentation plane parallel to the ground surface. (Bernander, 2000; Locat *et al.* 2011).

Upwards progressive failure (**Figure 2.9**) generally takes place in sediments where river erosion has engraved steep slopes. Erosion at the river bank initiates progressive failure along a sensitive sedimentation plane almost horizontally (Bernander, 2000). Material overlying the shear zone breaks into several blocks, creating a thumbprint morphology of horsts and grabens (Quinn *et al.* 2007).

Locat *et al.* (2011) developed Quinn's and Bernander's ideas by modelling progressive failure in Eastern Canadian and Scandinavian sensitive clays. A key idea central to the theory is that failure is initiated by a critical disturbance force, which is smaller than the force which passively propagates the failure surface. This could explain why failures in slopes comprised of sensitive soils can fail after thousands of years of stability (Locat *et al.* 2011). If the active or passive resistance of the failure surface is not reached, an “unfinished landslide” results with only cracking and minor slope movement (Bernander, 2000).

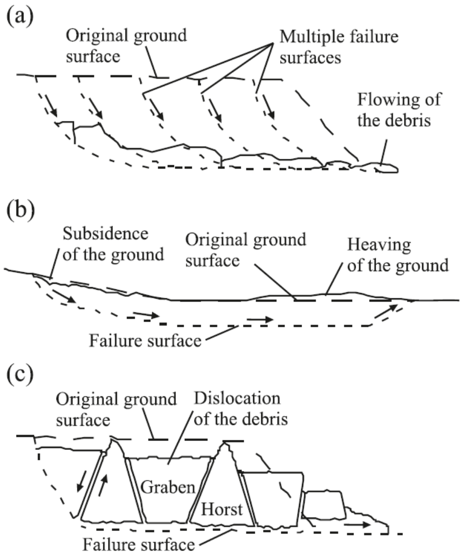

Figure 2.8. Three of the four main types of failures that occur in sensitive clay; (a) multiple regressive slide/flows, (b) translational progressive slides, and (c) spreads (Locat *et al.* 2011).

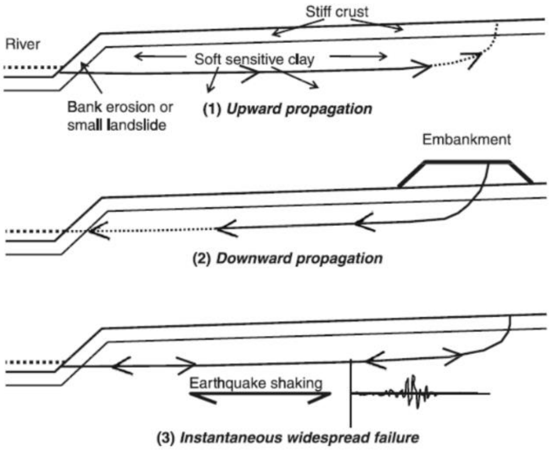

Figure 2.9. Continuous failure surface development under different mechanisms (Bernander, 2000).

2.4.3 Application of fracture mechanics to progressive failure

Skempton (1964) and Bishop (1968) suggested that fracture mechanics principles had potential to be applied to progressive failures. This is because sensitive soils are known to be brittle materials (Bjerrum, 1967, Quinn *et al.* 2011); only minor stresses are required to induce fracturing or overcoming of peak strength. Recently, Quinn *et al.* (2011) published a paper applying fracture mechanics theory to progressive failure in sensitive materials in Eastern Canada. Quinn considers a developing shear band in an idealised infinite slope comprising sensitive clay with a step cut at the toe. Three regions exist within this shear band; (1) a zone of soil which has already been softened to residual strength (τ_R), (2) a relatively small “end region” where brittle deformation governed by fracture mechanics is transitioning soil from peak to residual strength upslope of the residual region, and (3) a region of soil at peak strength (τ_P) which is located upslope of the end region. The length of the end region is proposed as critical in propagation of the shear band. Overall, greater soil brittleness or sensitivity results in greater energy release for driving fracture through strain softening (Quinn *et al.* 2011).

2.5 Strain softening, strain localisation and shear band formation

2.5.1 The stress-strain response and strain softening

Under triaxial compression, the stress-strain response of the soil depends on several factors, including the soil stress history, current stresses, and the soil structure, among others (Briaud, 2013). Normally consolidated, soft and loose soils do not exhibit peaks, and strain increases gradually to a plateau before reaching the critical state, which is where the soil volume does not change during shearing (**Figure 2.10**). Overconsolidated, hard and dense soils exhibit stress-strain curves with peaks followed by a drop in stress, known as strain softening, before reaching the residual stress (**Figure 2.10**) (Briaud, 2013).

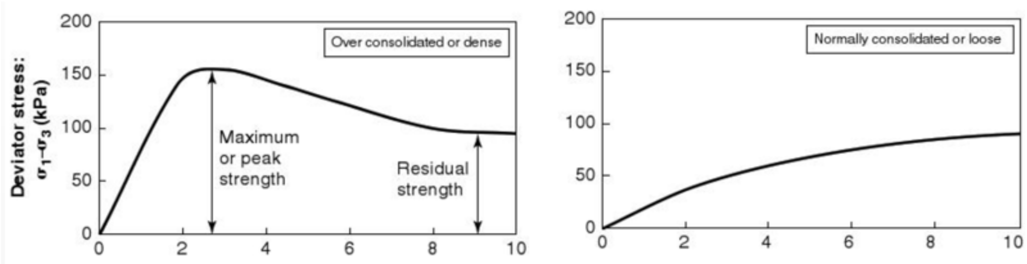

Figure 2.10. Idealistic stress-strain response curves for overconsolidated soils (left) and normally consolidated soils (right). Overconsolidated soils exhibit peaks followed by a region of strain softening, while normally consolidated soils strain gradually with stress until they plateau. Stress-strain curves of both soils will eventually meet at the critical state, where soil volume doesn't change upon further shearing (Briaud, 2013).

Mohr-Coulomb criteria define cohesion and friction between soil particles as the two components that contribute to soil strength (Bjerrum, 1961; Skempton, 1964). Friction forces exist between interparticle contacts or asperities, causing resistance to sliding (Skempton, 1964). Cohesion exists as true cohesion in the form of cementation, or as apparent in the form of electrostatic bonding of particle surfaces to water (Skempton, 1964). Friction and cohesion softening, or the reduction of friction and cohesion between the peak an residual state, was first proposed as the reason behind strain softening by Skempton in 1964, for the case of *long term stability* of overconsolidated clays under drained conditions. In the range of 10-20 % strain, or *short term stability*, cohesion and friction in sensitive soils has been shown to remain unchanged between the peak and residual states (Gylland, *et al.* 2013c, Gylland, *et al.* 2014, Thakur *et al.* 2014).

2.5.2 Excess pore water pressure induced strain localisation and strain softening

There is multiline evidence from several studies (Bernander, 2000; Andreson & Jostad, 2002; Jostad *et al.* 2006; Thakur, 2007; Thakur, 2011; Gylland *et al.* 2014; Thakur *et al.* 2014) that strain softening in sensitive soils at the fully softened state (10 – 20% strain) is actually controlled by the shear induced pore pressure rather than a reduction in effective friction and cohesion (Skempton, 1964). Evidence of these findings is outlined henceforth.

Prior to strain softening, strain localisation occurs, which is where strain is localised into one or more shear bands in an initially homogenously deforming sample, during undrained, static loading (Thakur *et al.* 2014, Gylland *et al.* 2014 after Mandel, 1966). Once fully developed, all further deformation tends to concentrate in these zones (Gylland *et al.* 2013c; 2014). Vardoulakis & Sulem (2004) found that excess pore pressure gradients are essential for strain localisation to occur. Initially, during compression, strain localisation has been found to occur in the pre-peak region, or at the peak stress (Mandel, 1966).

Thakur (2011) modelled initiation and growth of shear bands in undrained compression, with complementary experimental results from undrained plane strain biaxial tests on the quick Tiller Clay (St = 300) to validate his model. Plane strain devices are less commonly used, but are useful in that they replicate conditions where the soil is only free to deform in two directions. He found that (a) following strain localisation, contractant behaviour in shear bands induces excess pore pressures, resulting in a loss of resistance within the shear band and strain softening observed (**Figure 2.11**), and (b) at higher rates of compression, shear band thickness decreases, and strain softening increased (**Figure 2.12**).

The evolution of strains in the samples during compression (Thakur, 2011) in the plane strain biaxial tests was captured using Digital image correlation (DIC) technique, where velocity fields are measured by taking two consecutive photos and calculating the distance two particles have travelled in this time. Thakur (2011) was able to show that strain localisation occurred in the pre-peak regime, and that failure was progressive (**Figure 2.13**). Light zones in P1 - P2 (**Figure 2.13**) show that prior to peak stress deformation is concentrated

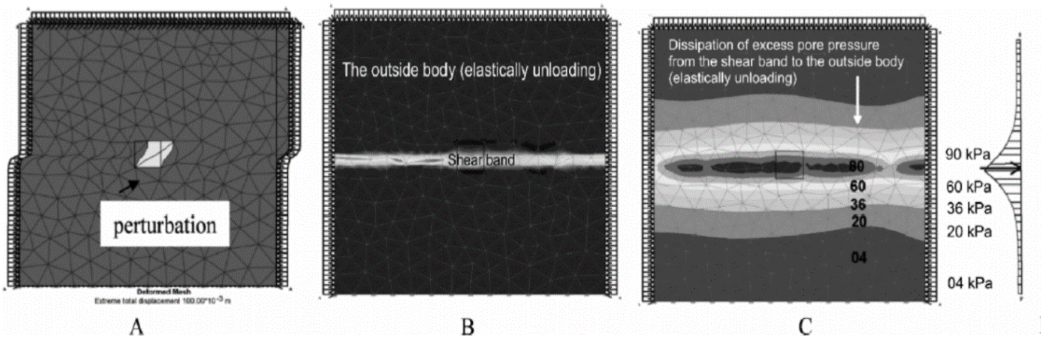

Figure 2.11. Mesh results modelling the initiation and growth of a shear band under strain from a direct shear test. The shear band was initiated at an embedded perturbation (A). At point B the shear band is forming, and at point C, the shear band dissipates excess pore water elastically (Thakur, 2011).

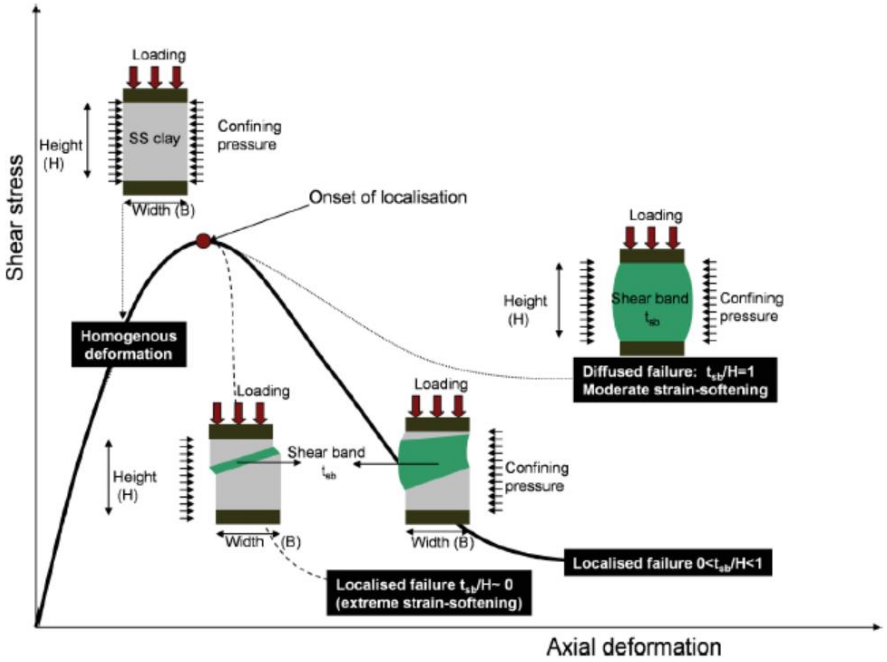

Figure 2.12. An idealised result of Thakur's model, showing that shear band width decreases with increasing deformation rate. The shear band thickness is dependent on the post – peak strain softening of sensitive clays (Thakur, 2011).

in the upper region i.e. localisation is occurring during the hardening region. During P3 - P4, a shear band from the upper right corner began to develop. It is completely formed during P5 - P6. Deformation from the outside of the specimen was also captured by the DIC technique. Deformation during P3 - P4 was smooth, whereas during P5 - P6 and P7 - P8, deformation was non-smooth, indicating multiple shear bands forming in different directions (**Figure 2.13**) (Thakur, 2011).

In 2012, Gylland presented a PhD thesis including studies on material and slope failure in sensitive marine clays in Scandinavia, and subsequently published several papers (Gylland *et al.* 2012, Gylland *et al.* 2013a, Gylland *et al.* 2013b, Gylland *et al.* 2013c; Gylland *et al.* 2014). Samples of sensitive marine clay derived

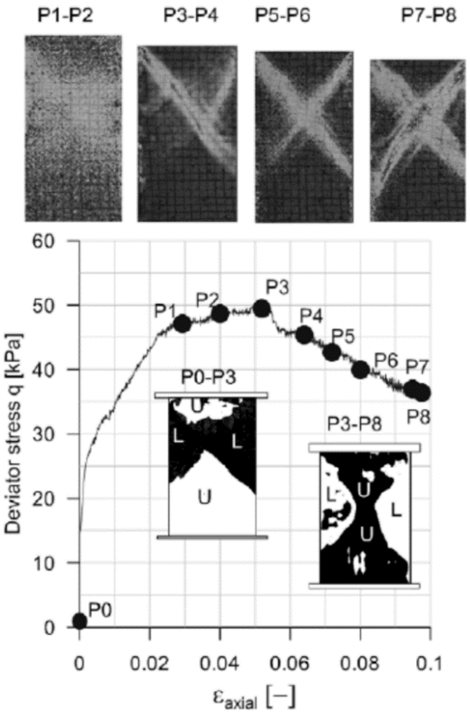

Figure 2.13. Shear zone development from digital image correlation (DIC) images at various times throughout shearing by the plane strain biaxial. L and U correspond to localised and non-localised zones respectively. The development of shear zones between P1-P2 and P7-P8 images is progressive and non-uniform. Strain was also captured from DIC, as shown by the images below. Strain at P1-P3 was smooth, whereas strain at P7-P8 was non-smooth, signifying development of multiple shear bands (Thakur *et al.* 2014).

from glacially eroded sediments were collected 10 km south of Trondheim, Norway. The clay is fairly homogeneous with thin silt layers, and has the typical “cardhouse” structure and associated moisture content above the liquid limit. The clay fraction consists of illite, chlorite and feldspars, and the coarser fraction is comprised of quartz and feldspars.

Gylland *et al.* (2014) studied the global response of shear band initiation in sensitive clay during undrained shear, in a triaxial device modified so that shear band formation was favourable. The modification consisted of roller bearings on which the bottom plate could slide. This modification also allowed horizontal shear band displacement to be measured. Consolidated undrained triaxial tests were performed on samples retrieved from depths of approximately 8.6 m, 9.6 m 10 m and 12 m. Samples were tested at four displacement rates: 0.005 mm/min (very slow, VS), 0.05 mm/min (slow, S), 0.5 mm/min (fast, F), and 5.0 mm/min was (very fast, VF). All samples exhibited planar shear band failure modes, with the exception of VS, where barrel failure occurred. Gylland’s (2013) results aligned with Thakur’s (2011) findings, in that excess pore pressure governs both initial strain localisation and strain softening processes in shear band within sensitive material. Higher test rates resulted in thinner shear bands and a greater softening response (**Figure 2.14**). Gylland attributed post-peak increases in pore pressure

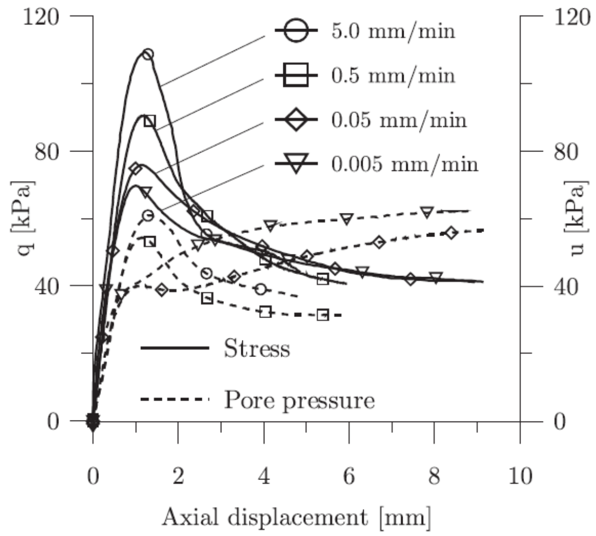

Figure 2.14. Results from the base-sled testing show that for increased displacement rate, the peak shear strength is higher and the softening response is greater (Gylland *et al.* 2014).

(**Figure 2.14**) to delayed dissipation of excess pore pressures along the shear band registering with the pore pressure sensor at the base of the sample.

Microstructural analysis using thin section and micro-CT (Gylland *et al*. 2013b, c) techniques gave strong evidence that strain softening and progressive shear band formation is governed by excess pore pressure. Micro-CT scans showed that material contracted locally within shear bands (shown by densified clay regions in **Figure 2.15**b), meaning pore pressure must have been released from densified pores (**Figure 2.15**b) and (**Figure 2.15**a) grains were reoriented along the shear bands, providing a preferential pathway for excess pore pressure to drain along.

Figure 2.15. (a) (left) shows reoriented materials locally in the shear zone and (b) (middle & right) shows densification of material locally in a shear zone (Gylland *et al.* 2013a, b).

2.6 Cyclic soil failure in sensitive soils

2.6.1 Background

Concerning sensitive soils, most studies have concentrated on static failure mechanisms, rather than cyclic failure mechanisms (Park & Kutter, 2015). In Tauranga and the wider geographical context of New Zealand, cyclic failure mechanisms are especially important to understand due to the high occurrence of earthquakes. It is also unknown whether other cyclic forces, such as oceanic tides, and solar radiation induced temperature change contribute to sensitive soil failure.

2.6.2 Historical earthquake activity in Tauranga

Earthquake activity in the Tauranga Region has historically been low, however New Zealand historical earthquake record only extends back 170 years (Wilkinson, 2013). The devastating earthquakes in Christchurch in 2011 (182 casualties) have proven that old faults, lying hidden beneath layers of sediment, have the potential to activate after long periods of inactivity, with devastating effects (Wilkinson, 2013). Little is known about the deeper basement structure and significant earthquake events over Tauranga's geological history (Briggs *et al.* 1996). Old faults with significant offsets within the Tauranga vicinity include the Hauraki Fault (max throw 4 km), the Papamoa Range faults, and the surmised Tuapiro Fault adjacent to Katikati (Briggs *et al.* 2005). Briggs *et al.* (1996) envisaged a series of NNE trending faults that control the structure of Omokoroa Peninsula. Ota *et al.* (1992) reports that subduction related earthquakes occurred off the east of New Zealand between approximately 900-1,200 BP and 600-2,000 BP.

2.6.3 Behaviour of soil subjected to cyclic loading

Cyclic loading is where the soil is subjected to a cyclic shear stress (T_{cyc}), which is a wave form that fluctuates (loads and unloads). Examples of cyclic shear stresses include earthquakes or pile driving vibrations. If any average shear stress, or overburden shear stress (T_{av}) is applied to the soil (for example a house, or heavy rainfall event), T_{cyc} will fluctuate around this value (**Figure 2.16**a). Depending on the value of the average and T_{cyc} applied, the sample may be in a constant overall state of positive stress, or it may be fluctuating between positive (compression) and negative (extension) stresses during testing (Anderson, 2007).

When a soil or any material is loaded and unloaded at a very low level of τ_{cyc}, the loading and unloading curves repeatedly follow the same path, producing only elastic strains. This is known as rate dependant hysteresis, where the output (strain) reduces back to its original value if the input (stress) is removed (**Figure 2.17**) (Visintin, 1994). For soil, plastic deformations begin to occur after a very miniscule amount of volumetric strain (est.10^{-5}) (Nova, 2012). In most cases of soil loading therefore, rate independent hysteresis occurs, where even after the input (stress) is removed, the output (strain) has a permanently changed value i.e. plastic strains that accumulate within the sample are irreversible (**Figure 2.16**) (Nova, 2012).

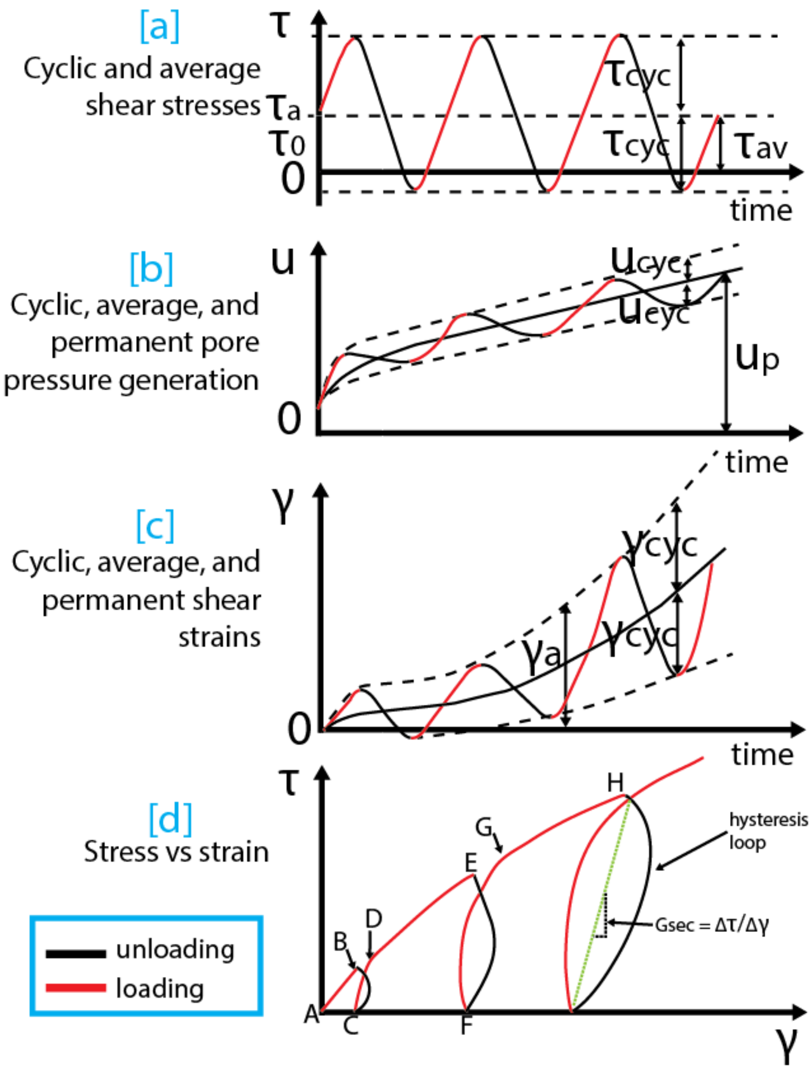

Figure 2.16 a-d. τ_{cyc} fluctuates around the applied τ_{av} (a). With each loading cycle (red) strain increases with stress (c, d). With each unloading cycle (black) strain curves back towards the origin, but is inhibited by development of a permanent plastic strain (d). The loading curve bounces back to the same gradient it was at previously, as seen by the similar trend of AB, DE, GH (d). With each cycle, pore pressure does not have enough time to dissipate, hence a permanent pore pressure develops incrementally (b). The top three figures are adapted from Anderson (2015), while the bottom figure is adapted from Nova (2012).

During the loading portion of the stress-strain curve in **Figure 2.16d** (A-B), the curve reaches a maximum stress before unloading sends the curve back towards the origin (B-C). A portion of strain (permanent strain) remains, causing the curve to loop back on itself when loading starts again (C-D). During unloading, the strain trends back towards 0, but a portion remains (**Figure 2.16c, d**) called the permanent shear strain (γ_p) (Nova, 2012; Anderson, 2015). The loading portion of the curve trends along a related gradient, e.g. AB, CE loading portions trend along the same gradient, but the hysteresis loops increase in area, and decrease in inclination. The increase in area is interpreted as greater energy dissipation, whereas a reduction in inclination (Gsec, **Figure 2.16d**) is related to a loss in stiffness. This change in hysteresis loops is brought about by the unloading portion of the curve.

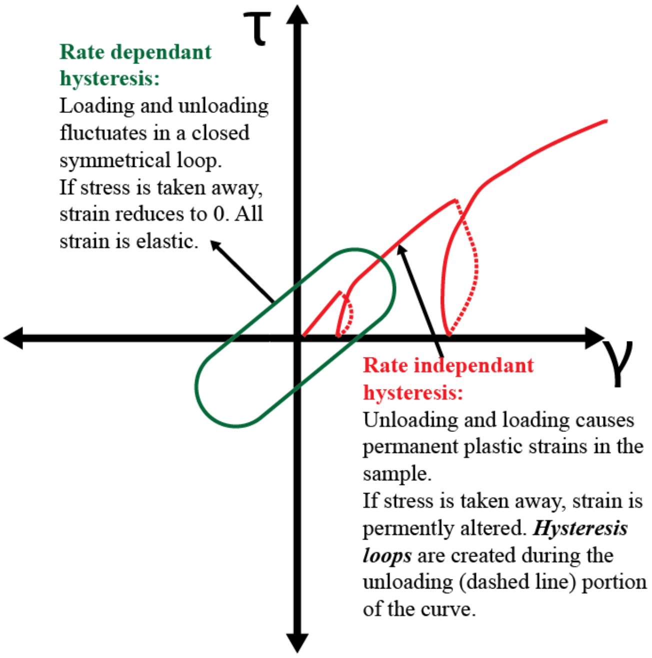

Figure 2.17. Explanation of the different types of hysteresis. Unless the soil is subjected to very low stresses, soil usually experiences rate independent hysteresis, where a permanent plastic strain occurs as a result of stress (Visintin, 1994; Nova, 2012).

Figure 2.18 displays the different stress paths for monotonic and cyclic loading during an undrained test. τ is the shear stress (y axis), and σ' is the effective normal stress (x axis). Initially, the sample is consolidated to the estimated *in situ* effective normal stress (green line on x axis). τ_{av} may then be applied. With each cycle, permanent pore pressure (u_p) and permanent strain (γ_p) develop, as the soil skeleton compresses and stress is transferred to the water (**Figure 2.16**b). u_p and γ_p are the values at the end of a cycle when the shear stress returns to the original shear stress at the start of the cycle. The cyclic pore pressure (u_{cy}) and the cyclic shear strain (γ_{cy}) are the single amplitude values i.e. half the peak to peak values within a cycle. The average shear strain (γ_a) is the average of the high and low peak values in a cycle. Eventually, the effective stress is reduced so that the effective stress path (**Figure 2.18**) aligns with the critical state line failure envelope (Anderson, 2007). Direct shear (DSS) tests and cyclic triaxial tests show different strain responses. In DSS tests, strain develops symmetrically. Because of anisotropic loading conditions in triaxial testing (extension stress that is smaller than the compressive stress) the shear strain is non-symmetrical (Anderson, 2007).

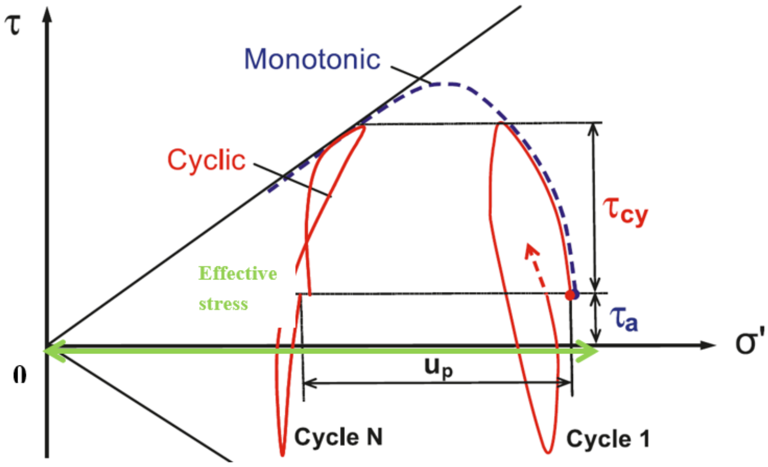

Figure 2.18. Effective stress paths for undrained tests for monotonic and cyclic loading. τ is the shear stress, and σ' is the effective normal stress. τ_{av} is average shear stress, τ_{cy} is cyclic shear stress, u_p is permanent pore pressure (Figure adapted from Anderson, 2007).

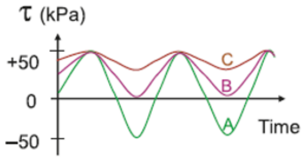

Test	τ_{max}	τ_a	τ_{cy}	Result
A	50	0	50	Failure (γ = 15%) 10 cycles
B	50	25	25	γ_p = 0,8%, γ_{cy} = 0,3% 2500 cycles
C	50	42.5	7.5	γ_p = 0.03%, γ_{cy} = 0.02% 2500 cycles

Figure 2.19. The number of cycles to failure and amount of permanent shear strain (γ_p) and cyclic shear strain depend on the values for τ_{av} and cyclic shear stress τ_{cyc} determined before the test is carried out (Figure: Anderson, 2007).

The maximum shear stress (τ_{max}) is the summation of τ_{av} and τ_{cy}. Anderson (2007) demonstrated this by testing material at the same level of τ_{max}, while changing τ_{av} and τ_{cyc}. Results showed that at different combinations of τ_{cy} and τ_{av}, the samples failed at remarkably different numbers of cycles and different ratios of permanent and cyclic shear strain (**Figure 2.19**).

Anderson (2007) plotted the number of cycles to failure, and the average cyclic and average shear strains at failure as a function of the T_{av} and T_{cyc} for triaxial and DSS tests in Drammen Clay. Failure in this case was defined as 15 % strain. An example of a plot is outlined in **Figure 2.20**. T_{cyc} and the T_{av} are the y and x axes respectively, and are both normalised by the static shear strength (S_u). 9 different tests, each at a different combination of T_{av} and T_{cyc} were plotted. The number of cycles to failure and the average and permanent cyclic strains at failure were presented next to each of the plots. Relationships between the plots showed that it was feasible to draw contours between the data. The contours generally showed that failure occurs at large γ_{cyc} when T_{av} is small and T_{cyc} is large, and large γ_{av} when T_{av} is closer low and T_{cyc} is high (Anderson, 2007). The number of cycles to failure is also plotted, so that contours of expected cycles to failure can be added to the contour plot. With more data plots, an idea about the general failure behaviour of the soil is established. The contour plots are useful in that they display a wide range of information on one graph (Anderson, 2015).

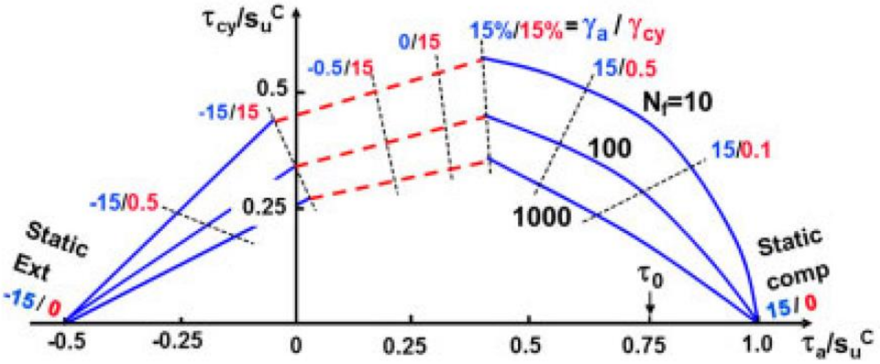

Figure 2.20. The cyclic contour plot developed by Anderson (2015) for Drammen Clay. The x-axis is normalised average shear stress (T_a/S_u) and the y-axis is normalised cyclic shear stress (T_{cyc}/S_U). Solid lines depict the contours for cycles to failure, while dashed lines depict contours for average shear strain (blue) and cyclic shear strain (red) at failure.

CHAPTER 3

METHODOLOGY

3.1 Introduction

This chapter outlines field and laboratory methods used. All testing followed referenced standards, and any deviations are explained in comprehensive detail. Following a desk top study, a criterion was developed to find study sites. After site identification, field and lab testing was carried out sequentially on both sites. The methods section is split into field and lab methods.

3.2 Site selection

The ideal site for this study would have the following aspects:

1. Sensitive soil layers exposed in the failure scarp of a landslide or in the presumed failure surface of a landslide in the Tauranga Basin. The exposures must be reasonably thick and consistent enough for extensive sampling i.e. thick enough to take triaxial samples of reasonably homogeneous sensitive cohesive material. Wetness of sample was also important as dry material fractures upon hammering in sample tubes;
2. Accessible and safe enough to obtain samples;
3. Compliance of the property owners in order to have access and perform testing on the site.

After these criteria were developed, geotechnical consultancies and authorities were approached to see if any sites were accessible as well as to get general advice on localities. Consultancies approached included Coffey Geotechnics, Opus, Terrane Consultants, and Tonkin and Taylor, and authorities included Tauranga City Council and Western BOP District Council. See Chapter 4 for the full list of sites investigated and how study sites for this thesis were chosen.

3.3 Field methods

3.3.1 Geomorphic mapping

Aerial photographs were obtained from both Google Earth as well as Tauranga City Council and Western Bay of Plenty Regional Council websites. Printed aerial photographs were used as base-maps to trace on geomorphic features while walking around each site. The aerial photographs were loaded into ArcMAP and geomorphic features were drawn using ArcMAP in GIS.

3.3.2 Field shear vane

A Pilcon Geotechnics field shear vane was used to measure the *in situ* shear strength of the soil outcrops and boreholes, following standard methodology set out by the New Zealand Geotechnical Society (NZGS) (2001), with the slight modification that Cunningham (2012) used, where the blade was turned 10 times instead of 5 times to obtain the remoulded strength.

3.3.2.1 Limitations of the in situ shear vane for shear strength testing

The major limiting factor introduced when using the standard method set out by NZGS (2001), is that the remoulded shear strength measurement is obtained from a shear surface which has been pre-defined by the initial peak strength measurement. Wyatt (2009) tried to correct this limitation by remoulding the soil by hand, replacing it into the borehole and obtaining the remoulded strength with the shear vane. Hand remoulding instead of vane remoulding was shown to introduce much more variability in remoulded shear vane shear readings. This variability was probably due to differences in time and pressure placed on the soil, compaction of the soil, and changes in boundary conditions and friction of the failure surface (Wyatt, 2009).

3.3.3 Stratigraphy and soil description

Soil descriptions followed guidelines issued by the New Zealand Geotechnical Society (2005). Published information was used to document stratigraphy of the site. Local stratigraphy of the sample sites was logged.

3.3.4 Field sampling

Field sampling was conducted following site selection criteria for sensitivity based on shear vane tests and stratigraphic observation. Bulk samples were extracted for particle size analysis, Atterberg limits, natural moisture content, bulk density, particle density and SEM analysis. At each site, stainless steel push tubes 50 by 60 mm cores were extracted for bulk density, and 97 by 48 mm stainless steel push tubes were used for triaxial testing. Firstly, a flat bench was dug into the sensitive layer. The push tubes were then hammered in (**Figure 3.1**). Approximately 15 cm space between each push tube was measured to avoid disturbance. For the Omokoroa push tube samples, water was poured around the outside of the tube to lubricate the sample so that fracturing was less likely. A flat slab of wood was held carefully on the end of the push tube while hammering it in to prevent the tube deviating from vertical.

Figure 3.1. An example of a bench dug into a sensitive layer. Triaxial and bulk density push tubes were gently hammered into the profile from a vertical direction.

3.4 Lab methods

Moisture content, bulk density and Atterberg Limits followed methods outlined in NZS 4402 (1986), porosity was determined by methods presented in McClaren & Cameron (1996), and particle density followed Head (2014). Particle size was determined using the University of Waikato SOP (Standard Operating Procedure) method was used to find particle size. This method is based on Konert & Vandenberghe (1997). These methods are presented in detail in **Appendix 3.4**.

3.4.1 Triaxial testing at the University of Waikato

The stress-strain-pore water pressure relationships from triaxial testing, and subsequent testing on the failed sample give crucial insight into failure mechanisms in sensitive soils. Previous studies concerning shear band analysis in sensitive soils have utilised equipment where shear band formation is forced or favourable, such as the bi-axial device used by Thakur (2007) and the modified triaxial used by Gylland *et al.* (2014).

The triaxial was chosen over other shearing devices (for example the ring-shear), because of opportunity to compare results with recent literature investigating sensitive soil failure (Gylland *et al.* 2013c; Gylland *et al.* 2014). Gylland *et al*. (2014) used a modified triaxial, where the base sled could roll horizontally during compression, allowing the sample to fail preferentially by shear deformation.

In this study, resource constraints meant that the triaxial could not be modified in any way to favour shear band formation. Previous studies (Wyatt, 2009; Cunningham, 2012) have used consolidated undrained (CU) tests on similar sensitive material in the Tauranga Region. The most common failure types were single and double shear bands, therefore the CU test was considered feasible for the study of shear bands. I concluded that it was logical to study the effect of changing effective stresses on shear band formation, as the effective stress was something we could control without modifying the triaxial. Authors have also recommended using the consolidated, undrained test to best replicate conditions under rapid landsliding (Selby, 1993; Gylland *et al.* 2014). Testing at three different effective confining pressures also allowed us to deduce Mohr-Coloumb shear strength values. The British Standard 1377 (1990) Part 8: Shear strength tests (effective stress) was followed, with several exceptions which are outlined. The full method is outlined in **Appendix 3.4.1**.

3.4.1.1 The triaxial apparatus

The triaxial apparatus used in this study was a VJ Technology Triplex Multitester triaxial, of which a simplified view can be seen in **Figure 3.2**. The triaxial system was fully automated so that stress/strain/pore water pressure measurements were obtained electronically. Cell and back pressure was manually controlled by increasing air pressure inside two butyl rubber bladders, one each for cell and back pressure, inside de-aired water chambers. Physical volume change of de-aired water moving in and out of the sample was measured via a volume change transducer connected to the rubber bladders and cell and back pressure lines. Vertical strain was measured by a linear displacement sensor attached to the top of the triaxial cell. Pore water pressure was measured from the bottom of the cell by a transducer.

3.4.1.2 Test procedure

Each sample took between 2-3 days to complete, with saturation taking approximately 5-8 hours, consolidation 16-24 hours, and testing 1-2 hours. Data from the triaxial was recorded via a 16 channel VJ Technology MPX3000 data logger. WINCLISP software was utilised to display and control data from the data logger. The data was downloaded in raw format to calculate geomechanical properties.

Firstly, water was distilled using a Merrit Water Still 4000, after which it was transferred a Nold Deaerator where it was de-aired until no bubbles were observed

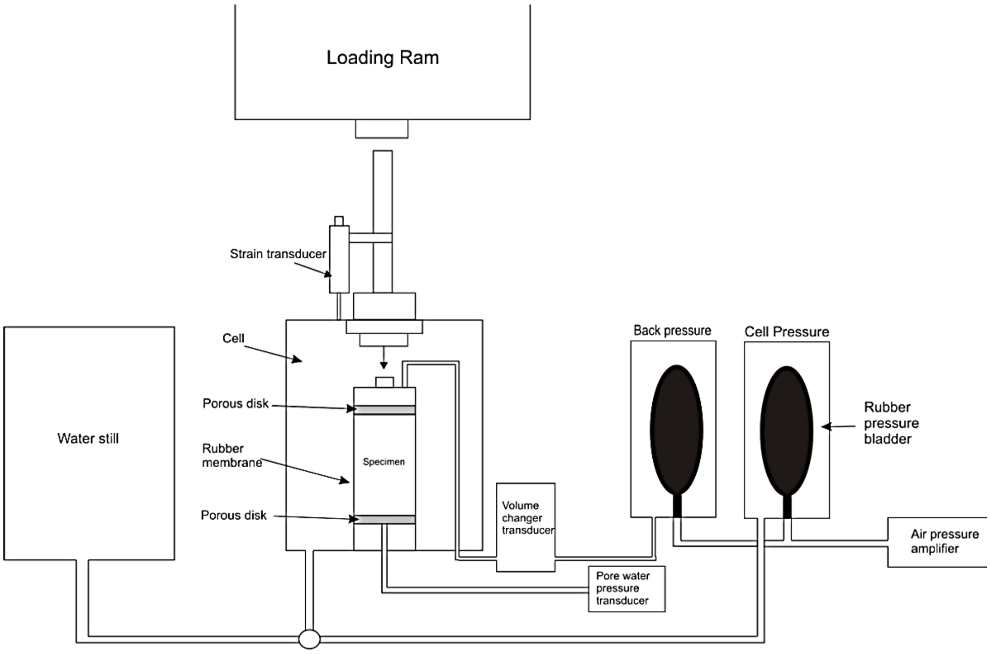

Figure 3.2. A simplified view of the triaxial set-up. Figure: Cunningham, 2012.

to be collecting on the surface of the water. The entire triaxial system was flushed with freshly de-aired water prior to each test to minimise air bubbles in the system.

3.4.1.2.1 Saturation

The purpose of saturation is to ensure that all voids in the specimen are filled with water. This is achieved by raising the pore water pressure to greater than 300 kPa, which is the pressure at which air goes into solution. During saturation, as stated by the BS 1377 (1990), cell pressure was increased incrementally by 50 kPa, and back pressure was increased to no more than 10 kPa below the cell pressure, in order to maintain a slight positive effective stress. After raising the cell pressure, pore water pressure was left to settle to a constant reading to equilibrate with back pressure between increments. The change in pore pressure at each increment is recorded and used to calculate the B value (**Equation 3.1**):

$$B = \frac{\delta u}{50}\ (\%)$$

Equation 3.1

Increments were increased until a B value of ≥ 0.95 was achieved, which is when the sample is considered saturated. For the Matua samples, it was found that the samples were already saturated, therefore a B value of 1 was achieved after the first increment (BS 1377, 1990). Cell and back pressure were still raised incrementally to greater than 300 kPa to ensure all air diffused into water so that there would be no random air pockets introducing heterogeneities in pressure during testing.

3.4.1.2.2 Consolidation

Several factors must be known to estimate the consolidation stress in the field, so that the same stress can be applied to the sample in the triaxial. Factors that must be known include the sampling depth, the approximate bulk density and thickness of overlying stratigraphy, and the water table depth. Firstly the *in situ* effective stress was calculated by **Equation 3.2**:

$$\sigma' = \sigma - u$$

$$(bulk\ density\ of\ soil * depth\ of\ soil) - (depth\ of\ water\ table * unit\ weight\ of\ water)\ (kPa)$$

Equation 3.2

Following saturation, back pressure was closed and effective stress was applied by increasing the cell pressure to the value determined by **Equation 3.2**. The back pressure was then opened and readings of volume change and pore water pressure was taken at suitable intervals until the pore water pressure equilibrated with the back pressure i.e. pore water pressure dissipation was > 95 %. The volume change was plotted against square-root of time to determine the testing time for the compression stage.

3.4.1.2.3 Compression

Compression was run immediately following consolidation. The test rate as per the British Standard 1377 (1990) recommends that specimens should not fail before 2 hours. The test rate is generally calculated as per consolidation characteristics for each different confining pressure, so that pore pressure could equalise through the specimen during compression. However, during rapid loading in actual landsliding, pore pressure does not have time to dissipate. Hence we chose a higher loading rate than recommended (0.5 mm/min) for all tests on Matua and Omokoroa material. Gylland *et al.* (2014) also did triaxial tests on sensitive materials at higher and lower rates. We chose to leave the rate equal for all samples so that cohesion and friction parameters could also be obtained. During compression, the specimen was compressed at constant cell pressure and constant rate. Back pressure remained closed so that drainage was not permitted, so the moisture content remained the same throughout the test. Measurements were recorded every 15 seconds by the data logger to increase the accuracy of the plots. The test was run until 20% axial strain was reached.

3.4.2 Triaxial testing at the University of Bremen

Cyclic and static triaxial testing was carried out at the MARUM (Centre for Marine and Environmental Sciences) Centre at the University of Bremen, Germany. The testing was under the INTERCOAST project IC28 with PhD student Max Kluger. Static triaxial testing was carried out in accordance with the German Standard (DIN 18137, 2011).

The cyclic triaxial (**Figure 3.3**) was constructed on site at the MARUM centre. (Kreiter *et al.* 2010a; 2010b). The Cyclic triaxial, also known as a Dynamic Triaxial Testing Device (DTTD) comprises a servo driven hydraulic cylinder, which can be controlled and configured in real time, a hydraulic power unit, load and pore water pressure transducers, a pneumatically controlled confining and back pressure unit, and a control station with a user interface to initiate testing.

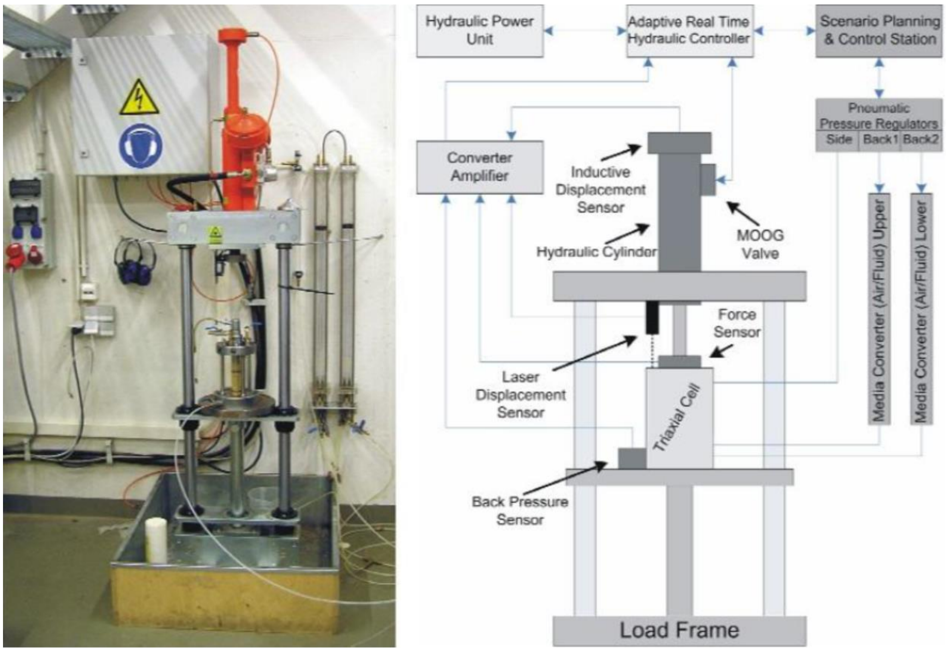

Figure 3.3. The dynamic triaxial testing device constructed by Kreiter *et al.* (2010a).

Two static triaxial tests were carried out at the University of Bremen. These tests followed the German Standard (DIN 18137, 2011). The two methods achieve sample preparations, saturation, consolidation and compression by different methods, of which the main points are outlined in **Table 3.1**.

3.4.2.1 Cyclic triaxial testing

Cyclic tests followed static testing methodology up to consolidation. The full methodology for cyclic triaxial testing can be viewed in **Appendix 3.4.2**, and a brief comparison between British and German standards for triaxial testing is outlined in **Table 3.1**. Thereafter, the methodology was adopted from Anderson (2015) so that contour plots could be produced from the cyclic triaxial results. This involved applying different combinations of average shear stress and cyclic shear stress to the sample. The method in brief was:

1. **Consolidation**

   Firstly, the sample was anisotropically consolidated to 240 kPa as per static triaxial testing methods (consolidation represented by the green arrow on the x axis in **Figure 3.4**).

2. **Static triaxial testing**

   Secondly, two static shear tests were completed so that (1) the static shear strength could be used to normalise the cyclic shear stress and average shear stress on the contour plot, and (2) the failure envelope for the cyclic tests could be defined (**Figure 3.4**).

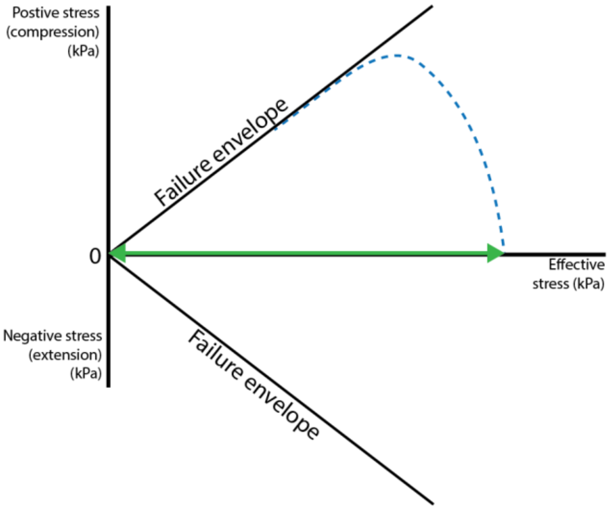

Figure 3.4. A schematic of a deviator stress vs effective stress (p-q) plot for a static triaxial test. The blue dashed line is the stress path of the sample as it is compressed. Figure adapted from Anderson, 2015.

   The slope of the stress path following peak stress (failure) represents the critical state, or when the sample is shearing at a constant rate (Kramer, 1996). After large strains all samples reach this state, therefore this line can be used as the failure envelope for future cyclic triaxial tests.

3. **Choose cyclic and average shear stress combinations**

   Because the contour plots are such a novel concept and there were no other standards but the original to compare to, it was logical to replicate average (τ_a) and cyclic shear stresses (τ_{cy}) that Anderson (2015) employed in his testing regime. Average shear stress is applied in the triaxial as twice the deviator stress (**Equation 3.3**).

$$\tau_a = 2q$$

Equation 3.3

Where τ_a is the average shear stress and q is the deviator stress. A schematic in **Figure 3.5** exemplifies a deviator vs effective stress plot (p'-q'), showing the application of firstly effective stress (green arrow on x-axis), secondly average shear stress, and finally cyclic shear stress.

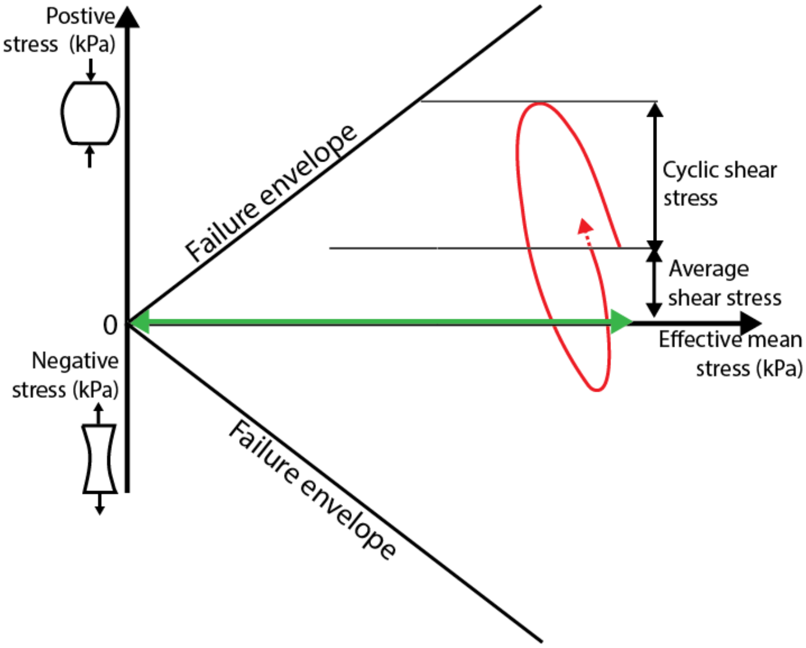

Figure 3.5. A schematic of the stress path plot of deviator stress vs effective stress (p'-q') for a cyclic triaxial test with small average shear stress application and slightly larger cyclic shear stress application. Eventually the cycles move to the left as effective stress is lost and the failure envelope is reached. Figure adapted from Anderson, 2015.

4. **Apply average shear stress**

   Following saturation and consolidation to an effective *in situ* stress of 240 kPa, an average shear stress (**Figure 3.5**) was imposed by increasing the normal stress to the desired value at a rate of 0.05 kPa/s. The sample was left for several hours until a stable axial strain and pore water pressure was reached, as described in Anderson (2015).

5. **Apply cyclic shear stress**

   The cyclic stress is applied by setting the dynamic frequency and dynamic stress and testing begins. A value of 1 was used for dynamic frequency as this value replicated the natural frequency of the structure. Anderson (2015) completed cyclic triaxial tests where the dynamic frequency was altered, however this was out of the scope of this study.

The dynamic stress is twice the cyclic shear stress i.e. the full amplitude of the cycle.

6. **Failure characterisation**

   The point at which the sample has failed is subjective to the failure criterion chosen. Anderson (2015) defined failure as when cyclic strain (γ_{cyc}) or average strain (γ_{av}) reached 15%. For our results, a consistent failure criterion was required so that tests could be compared on the cyclic contour plot. We noticed that for all samples rapid strain had begun to develop by 5% average or cyclic shear strain rather than 15% (**Figure 3.6**). Therefore this value of 5% was uniformly used as a failure criterion for all tests.

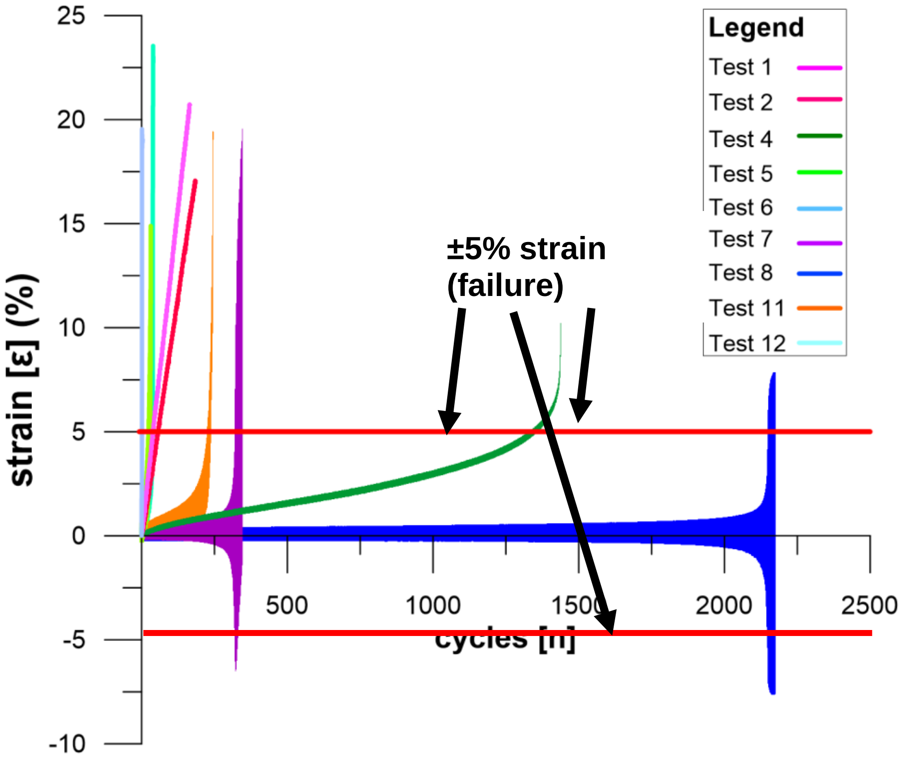

Figure 3.6. Strain vs cycles for all valid tests in this thesis. Failure is defined as 5% for all tests.

   The exact value defining failure was the first occurrence of 5% strain obtained from the raw data, and the cycle at failure was the correlating peak and trough of deviator stress of this 5% value.

7. **Calculate relevant parameters**

   Parameters obtained from raw data from triaxial testing included average and cyclic shear strain at failure, average and cyclic pore pressure at failure, cycles to failure, and G_{sec}, a parameter indicative of stiffness (Kramer, 1996) at both cycle 1 and failure.

A) The cycle at which failure occurred was found by first locating the first occurrence of 5% cyclic strain or average strain failure in the raw data.

B) The peak and trough of the deviator stress correlating with the 5% strain value was used to determine the exact data values of the cycle. The pore water pressure and average shear strain (γ_{av}) and cyclic shear strain (γ_{cyc}) values could then be determined by the following equations:

$$Average\ shear\ strain\ \epsilon_{av} = \left(\frac{(\varepsilon_{max} + \varepsilon_{min})}{2}\right) \times 100\ (\%)$$

Equation 3.4

$$Cyclic\ shear\ strain\ \epsilon_{cyc} = \left(\frac{(\varepsilon_{max} - \varepsilon_{min})}{2}\right) \times 100\ (\%)$$

Equation 3.5

$$Average\ pore\ pressure\ u_{av} = \left(\frac{(u_{max} + u_{min})}{2}\right) \times 100$$

Equation 3.6

$$Cyclic\ shear\ strain\ u_{cyc} = \left(\frac{(u_{max} - u_{min})}{2}\right) \times 100$$

Equation 3.7

C) G_{sec} or the stiffness parameter (**Figure 3.7**) was calculated from the gradient of the cycle concerned by **Equation 3.8**. This is demonstrated by

$$G_{sec} = \frac{\Delta stress}{\Delta strain}$$

Equation 3.8

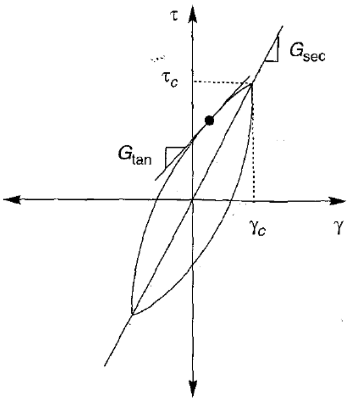

Figure 3.7. How to calculate G_{sec} for a particular cycle (Kramer, 1996).

Table 3.1. Differences between the German and British static triaxial testing standards.

Step	**British Standard 1377, 1990**	**DIN 18137 (2011)**
Sample preparation	Sample height must be ≥ 2 x sample diameter	Sample diameter must be a minimum 36 mm (10 cm ^{2}) for fine grained materials
Saturation	• Cell and back pressure is incrementally increased by 50 kPa, each time forcing de-aired water into the sample. After increasing pressure, PWP settles to a constant value. The B value (δu/50) is then calculated. • Cell and back pressure are incrementally increased until a B value of greater than 0.95 is achieved. Cell and back pressure must be greater than 300 kPa, as this is when air goes into solution.	• Air removal: Vacuum pressure of -95 kPa is applied to the sample. The sample is then immediately filled with water to ensure air voids are emoved. • A back pressure of 300 kPa is applied with an increment of 10 k/N n^2 per minute. • The saturation test for B value is then carried out by increasing cell pressure by 30 kPa, and waiting for PWP to naturally rise to a B value greater than 0.95 (95% of voids are considered saturated). • Back pressure is increased to 400 kPa if a B value of >0.95 is not eached, then 500 kPa etc.
Consolidation	• Consolidation is done after saturation. • With the drainage closed, cell pressure is increased so that the difference between cell pressure and back pressure is the effective stress. • PWP is left to settle to a constant value. • The drainage is opened concomitant with the start of a stopwatch. Change in PWP over time is recorded. Consolidation is considered complete when PWP reaches a stable value.	• Consolidation can be done before or after saturation. In our case, we consolidated before the saturation test. • Consolidation is done with open drainage as it is measured by change in axial strain over time rather than PWP change over time. Once axial strain settles to a constant value the sample is considered consolidated.
Testing rate	Testing rate is calculated from a number of variables, including the significant strain interval (E_f), the significant testing time (t_f), and the length of the consolidated specimen (L_c), as **Equation 3..** $A = \frac{E_f \times L_c}{t_f}$ **Equation 3.9**	Plasticity Index (PI) indicates the testing rate under drained conditions. For undrained conditions, the drained value is divided by 2.

Pore pressure measurement	PWP transducer connected to the base of the sample	PWP is measured by a single transducer which is connected by tubes to both the base of the sample and the top of the sample.
Axial strain measurement	Strain transducer attached to the top of the sample	Strain is measured by lasers at the top of the sample
Isotropic conditions	De-aired water fills the cell, creating side stress and axial stress so that isotropic pressures act on the sample.	Glycerine is added to the cell to just above the sample, creating the side stress. The axial stress is applied through a stamp. Both are applied together to create isotropic conditions.
Force sensor	The force sensor is located above the sample.	The force sensor is at the base of the sample inside the cell. For cyclic testing, if the force sensor is above the sample, frictional forces and inertial forces introduce significant error.

3.4.3 Thin section creation

3.4.3.1 Background

The idea to create thin sections of failed triaxial specimens was inspired by Gylland *et al.* (2013c), who was inspired by the works of Pusch (1970), who observed particle reorientation and particle breakage within shear bands in quick clay using Transmission Electron Microscopy (TEM). Gylland identified important features of shear zones with optical microscopy techniques, such as thickness, spacing, mineralogy, particle reorientation, and overall shear structure to name a few. It was unknown whether this method would be successful in sensitive volcanic clays. It was thought that the small particle size of the clays might inhibit the resin from impregnating properly. However, several trials using different combinations of resin and drying procedures were undertaken, and results showed that in thin sections of soil could be captured. Acetone drying of material following Camuti & McGuire (1999) was trialled, however air-drying, which Gylland *et al.* (2013c) also used, was found to be sufficient.

3.4.3.2 Method

1. **Photographing the intact specimen**
   The intact failed specimen was photographed from all angles to capture the failure mode. Single plane (shear), double plane (wedge), intermediate and barrel failures were used as a reference.
2. **Trimming the failed sample**
   The specimen was trimmed into vertical rather than horizontal blocks so that samples would be comparable with Gylland *et al.* (2013c). Blocks were cut so that they would roughly fit the dimensions of the glass slide (44 mm by 22 mm). Blocks were cut with a sharp knife immediately after the triaxial test was completed (**Figure 3.8**). Care was taken when cutting to reduce smearing of the failure surface as much as possible.
3. **Drying thin section blocks**
   The trimmed bocks were left to air-dry at room temperature for two weeks. Complete drying is important as the epoxy resin is hydrophobic. Although air drying mechanically alters the clay fabric, the method induces the least disturbance in comparison with other methods such as acetone drying (Camuti & McGuire, 1999). Based on Gylland's observations (Gylland *et al.* 2013c), the location, distribution and thickness of zones of shear and particle re-orientation are not significantly affected by air drying.

Figure 3.8. Omokoroa (240 kPa) post-failure, showing the cut failure surface exposing the shear zone.

1. **Replacement of pore fluid by resin impregnation**
    a) Dried blocks were very carefully placed on aluminium foil on a hot plate at 60 - 70º so that the soil could heat up to allow the resin to easily impregnate (**Figure 3.9**).
    b) Nuplex KI36 hardener and resin was used as it was low enough viscosity to impregnate the sample surface. 2 parts resin by 1 part hardener was slowly mixed on a hot plate to avoid entrapping air (**Figure 3.10**). Once a homogeneous colour was achieved, the mixture was deemed ready to begin applying.
    c) The resin was applied to the failure surface evenly with a wooden spatula. It was also applied to the sides of the specimen in order to preserve the quality of the dried specimen. Care was taken to ensure the surface was topped up with resin. Once the resin stopped absorbing into the sample, excess resin was wiped off the surface.
    d) The resin was then left to cure overnight at 60º on the hot plate;

Figure 3.9. The dried block heating up on the hot plate prior to impregnation of resin. Heat allows the resin to permeate deeper into the sample.

Figure 3.10. The hardener and resin mixture was applied to the failure surface.

e) Another coating of the K136 resin was added and left to cure overnight. This was to increase the sample stability during grinding and excess sample removal.

2. **Grinding off excess resin**

a) The surface coating of resin on the failure surface was removed by grinding it face down in a slurry of grinding powder and water on a glass plate (**Figure 3.11**). The sample was checked every 30 seconds to a minute by running the sample under water, drying it, and checking under light to see if resin still remained. Grinding continued until a matte surface was achieved and no resin was on the sample surface;

Figure 3.11. Excess resin is ground off using a slurry of grinding powder and water, so that an even coating of resin is visible on the surface.

b) The sample was then thoroughly washed and returned to the hot plate at approximately 60˚. The sample was completely dried prior to gluing on frosted slides.

3. **Frosting slides**

a) Ward's slides were used to make thin sections on;

b) The slide was washed in clean water and then placed on the suction pad. The slide was moved around to remove air and the suction was turned on;

c) The grinder was turned on and the slide was manually moved back and forth across the grinder while being lubricated. Approximately 0.03-0.04 mm was removed by the grinder to ensure the slide was frosted;

d) The frosted slide was rinsed under water and then left the cool overnight with the frosted side facing up.

4. **Block mounting**

a) A mixture of 7:3 Hillquist resin and hardener was used to mount the blocks;
b) Resin and hardener were weighed, heated on the hot plate to 60º, then mixed uniformly using a wooden spatula;
c) A thin layer was applied to the surface of the block sample, using a wooden spatula, and left for 3-5 minutes;
d) Once small bubbles were visible, the frosted side of the thin section was placed on the surface. Using even pressure, the slide was moved in a circular motion to extrude and air bubbles under the glass (**Figure 3.12**);
e) Once all bubbles were removed, the block was put glass side down on a cool plate and left to solidify overnight.

5. **Excess sample removal**
   a) Following solidification of the resin overnight, any resin that had accumulated on the other side and the edges of the slide was carefully scraped off with a razor blade;
   b) The excess block was slowly trimmed of using a blade;
6. **Grinding the thin section**

   The thin section was ground down gradually until a satisfactory thickness was achieved by incrementally checking the sample under the optical microscope.
7. **Cover slip mounting**

   Once dry, a cover slip was added, and the thin section was marked in a corner with a name with a diamond tipped pencil.

Figure 3.12. The frosted slide was out face down and moved in a circular motion to remove air bubbles between the sample and the slide.

3.4.4 Micro-CT

Micro-CT (Micro-computed technology) imaging utilises the same methods as hospital CT scans to X-ray images in 3D, however on a much lesser scale (Bruker, 2015). Inspiration for this method came from Gylland *et al.* (2013c), who analysed "mini-plugs" (9 mm by 9mm) of the shear zone, by micro-CT, at a resolution of 5 μm. X-rays project density differences within the sample by presenting them as a range of grey-scale pixels. The user can then specify a density as a specific value e.g. a black colour is a pore space. Mini-plugs of clay were scanned using a Bruker Skyscan 1272 micro-CT scanner at the University of Auckland. An entire failed sample was scanned by the Skyscan 1172 at the University of Bremen, Germany.

1. **Subsampling of the triaxial sample**
   Small (12.4 mm by 47 mm) hollow plastic tubes were lubricated on the exterior, and pushed carefully from the vertical direction through the shear zone of the triaxial sample. The sample had been previously cut close to the shear zone so that the tube did not need to be pushed in far. The moisture content of the sample was preserved by plugging each end of the tube with melted wax. The samples were packaged to avoid disturbance. For the cyclic sample, the entire principle shear zone was captured, so only the ends of the triaxial sample were trimmed off.
2. **Micro-CT scanning**
   a) All micro-CT systems utilise static acquisition geometry, where X-ray source and detector are separated by a fixed distance, and image magnification is adjusted by the movement between them (**Figure 3.13**). The intensity of the X-ray beam is reduced if the opening angle of the beam is small and the magnification increased. In most micro-CT systems, if the magnification of the sample is increased, the object moves closer to the X-ray source, thus reducing the quality of the detected beams. The Skyscan-1272 overcomes this reduction in quality by widening the opening angle of the beam, and increasing the size of the format detector (**Figure 3.13**).
   b) Specifications for the Skyscan 1172 (OM1 cyclic): Beam energy 110 kV, flux 100 μa, copper aluminium filter, 360° rotation with 0.6° step size.
   Specifications for the Skyscan 1272 (OM1 static): Beam energy 60 kV, flux 130 μa, copper aluminium filter, 180° rotation, 0.4° step size.

c) The sample was placed on a rotatable stage. Each scan took approximately 3 hours. An X-ray beam projects through a slice of the sample. X-ray photons bounce off different densities within the sample and are detected on the opposite side by a detection screen. The stage is rotated incrementally to create a “slice stack”. The sample can be captured after a 180º rotation, or for better quality, 360º rotation. 180 º rotation was chosen over the more thorough 360º rotation because of time and budget constraints. During scanning, several errors or artifacts of the scanning process result in abnormalities in the projection. The range of artifacts is ring, noise, beam hardening and scatter, metal artifacts and out of field artifacts (Boas & Fleischmann, 2012) (**Table 3.2**).

3. **Image reconstruction**

   The image slices were reconstructed into a spatially related 3D image voxels using the software nRecon. Voxels are like pixels but 3D i.e. they have a designated volume. nRecon uses a modified Feld-kamp algorithm (Feldkamp *et al.* 1984). M1 had 939 slices, OM1 (static) had 1572 slices, and OM1 (cyclic) had 2137 slices to reconstruct.

4. **Projection and software analysis**

   CTVox software was employed to create images of the samples. Colours can be applied to different densities within the sample, allowing designation of different materials

Table 3.2. Types of artifacts produced during X-ray scanning (Boas & Fleischmann, 2012).

Artifact type	**Summary**
Ring artifact	Ring artifacts are caused by a miscalibrated or defective detector element, resulting in rings centred on the rotation centre.
Noise	Poisson noise is a consequence of statistical error of low photon counts. It causes random thin bright and dark streaks that appear preferentially in the direction of greatest attenuation.
Beam hardening/scatter	Beam hardening and scatter result in dark streaks between two high attenuation objects (metal or bone) with surrounding bright streaks.
Metal artifact	Metal streak artefacts are due to a combination of beam hardening, Poisson noise, motion, and edge effects.
Out of field artifact	This is due to a non-perfect projection algorithm. A better algorithm should capture the field of view that is smaller than the object scanned, reducing the radiation dose.

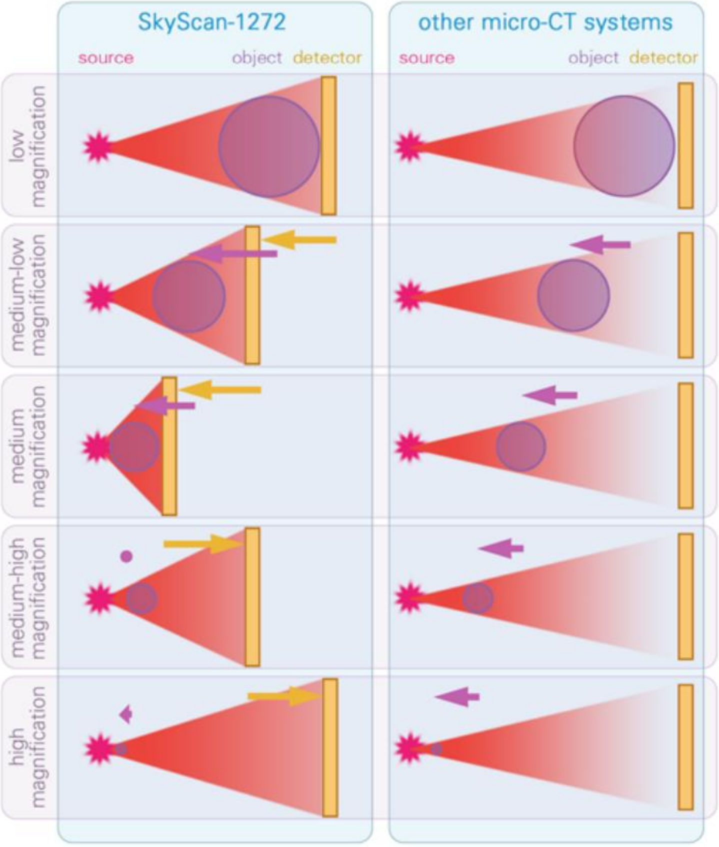

Figure 3.13. The Skyscan 1272 uses a wider beam and larger detector panel to increase the quality of projected slices (Bruker, 2015).

CHAPTER 4

FIELD OBSERVATIONS AND STRATIGRAPHY

4.1 Introduction

This chapter outlines the process of site selection, and observations, geomorphology, and stratigraphy of each site. Site 1 (Bramley Drive, Omokoroa) is a well-studied site (see Chapter 2, Literature review for information on Bramley Drive). It made sense therefore to attempt to locate sites that were of similar origin. Methods for site selection and soil logging are briefly outlined in Chapter 3: Methodology. This chapter provides a more comprehensive description about how sites were initially located and chosen over others.

4.2 Site selection

The first step in the hunt for recent landslides in sensitive material was to talk with geotechnical consultancies, as they would have the best knowledge of historical landslide sites. Coffey Geotechnics offered several options worth investigating. A site in Maungatapu where a landslide occurred in 2012 was investigated, however it was found that geomorphic evidence of failure was largely obscured, and the material was too sandy to be considered sensitive clay. A 40 m exposure at Tauriko was also investigated, however the soil was found to be too dry for sampling. The majority of the profile was composed of Te Ranga Ignimbrite, which is known to be sandy and variably sensitive (Matt Packard, Pers. Comm. 12/12/14). Material at the base of the cliff was tested by shear vane and hand shear, and was found to be non-sensitive. Another locality of Te Ranga Ignimbrite on the same site at Tauriko was investigated, and found to be sensitive, however could not be investigated because of project constraints of the construction site. Highly sensitive Pahoia Tephra material was found while hand auger drilling at the construction site of the school (entrance Pyes Pa Road), however this was non-practicable to investigate as the site was going to be remediated. Lastly, a landslide now fully remediated behind the Apata Coolstore was investigated, however no exposed stratigraphy with sensitive material was found.

Advice given from consultants was to firstly walk around shore platforms of the steep cliffed peninsulas in the Tauranga Basin at low tide to look for landslide exposures. Peninsulas explored are outlined in red in **Figure 4.1**, and included Maungatapu, Matua, Tauranga CBD, Te Puna, Plummers Point, Omokoroa, Pahoia, and exposures at the end of Turner Road, Prestidge Road, Walker Road , Sharp Road, Matahui Road, Park Road, Beach Road, Whakamarama Road, Youngson Road, Waipapa Block Road, Esdaile Road, and Plummer Road.

Three sites were chosen on the criteria suitability of each site. These were Bramley Drive at Omokoroa, (37°37'48.11"S 176° 2'43.99"E) Rewarewa Place at Matua (37°40'20.84"S 176° 6'57.28"E), and the public reserve at the end of Park Road in Katikati (37°32'14.45"S 175°56'2.24"E) (**Figure 4.1**). Field investigations at site three were carried out, but no geomechanical tests were done because it was not a landslide site. Site investigation information is presented in **Appendix 4.2**.

Figure 4.1. Sites explored in the Tauranga Region. Outlined red indicates peninsulas which were walked around. Red dots include face exposures tested with a shear vane. Yellow dots are the three sites chosen: Katikati (3) Omokoroa (1), and Matua (2).

4.3 Site 1: Bramley Drive, Omokoroa

4.3.1 Criteria suitability

The site at Omokoroa is a recently failed landslip at a steep coastal escarpment. The original failure occurred in 1979, and two further events occurred in 2011 and 2012. The site was chosen because (1) soils at the site were previously identified as highly sensitive, (2) the site is easily accessible, (3) the council was compliant in allowing access, and (4) there is an abundance of research involving available. For a comprehensive overview of previous research at Omokoroa, please refer to Chapter 2: Literature review.

4.3.2 Geomorphologic site description and site history

4.3.2.1 Omokoroa Peninsula

Omokoroa has long been recognised as subject to erosion and landslip events. Previous studies which provided insight into geomorphologic features include Gulliver & Houghton (1980), Keam (2008), Arthurs (2010), Cunningham (2012) and Christophers (2015). The NNE aligned peninsula is studded with active and relict landslip scars (**Figure 4.2**). Most of these scars are on the western side of the peninsula where the cliff heights range between 20 – 30 m. Pulses of sediment in cores taken on the eastern side of the peninsula show that large landsliding events have also occurred form the now urbanised eastern coastal cliff, potentially activated during a local earthquake event which also washed tsunami deposits into the area of Omokoroa Domain (Christophers, 2015). Recent (< 20 years) landsliding events at Omokoroa include Bramley Drive, Walnut Grove, Gerard Place, and Ruamoana Place (Keam, 2008) (**Figure 4.2**). The most extensive failures recorded in recent history include the failure at Bramley Drive in 1979, and between lots 30 and 31 at Hamurana Road in October 1962 (**Figure 4.2**). Both failures were large; Bramley Drive was 60 m width and had a run out distance of 150 m, while the failure at Hamurana Place was 60 m wide and 20 m high (Gulliver & Houghton, 1980).

4.3.2.2 Bramley Drive landslip pre-2011-2012

The original landslip was the largest event at the location, where a 34 m high section of cliff failed over 60 m cliff section following a period of heavy rainfall (Gulliver & Houghton, 1980). A largely intact block of material was rafted away, failing on a highly sensitive Pahoia Tephra layer approximately 20 m below

Figure 4.2. An aerial view of Omokoroa (2015, GoogleEarth), and respective landslide scarp locations. Historic landslides, including Bramley Drive (BD), Ruamoana Place (R), Hamurana Place (HP), Walnut Grove (WG), and Gerard Place (GP) are outlined in red. Inferred relict landslip scarps are outlined in yellow, after Christophers (2015).

the headscarp (Tonkin and Taylor, 2011) (**Figure 4.5**). The landslide is classified as a sensitive clay rotational slide (Hungr *et al.* 2014). Features created that indicate slumping include the bowl shaped scar in the cliff, and the largely intact “block” of material overlying the sensitive remoulded debris. Geomorphic indications of sensitivity included the exceedingly long (150 m) runout distance of the sensitive material (Gulliver & Houghton, 1980). Sensitivities of up to 140 were measured during the geotechnical investigation following the slide (Gulliver & Houghton, 1980).

4.3.2.3 Bramley Drive landslip post 2011-2012

Reactivation of the Bramley Drive landslip and initial movement of adjacent failures including Ruamoana Place occurred following a storm on 11 May 2011. Regression at the Bramley Drive failure was at the southern, over steepened end of the headscarp. On the 26th April and 13 August 2012, as shown by aerial photographs (**Figure 4.3**) the headscarp further retrogressed 3 – 5 m to its current position, 30 m back from its original position, based on the cliffs surrounding the scarp (**Figures 4.3, 4.4 & 4.6**). The slope angles of this headscarp range from 50 – 60 ^{o}, with a maximum of 70 ^{o} at the southern extent (Moon *et al*. 2013).

Approximately 3500 m^3 of remoulded material from both events inundated the bowl of the landslip, covering most of the original remoulded material, with the exception of a vegetated area of original 1979 remoulded material on the south side (**Figure 4.5**). The reworked nature and deposition of material at a distance approximately 100 m from the cliff edge shows that sensitive materials have contributed to flowsliding, however to a lesser degree than the 1979 event (Moon *et al.* 2013). The 2011-2012 landslips exposed a bench around 25 m depth which is believed to be the weakly – non welded Te Puna Ignimbrite (**Figure 4.7**).

4.3.2.4 Bramley Drive 2012 - 2015

Moon *et al.* (2015) monitored the erosion of the landslide at Bramley Drive using laser scanning and LIDAR data. Throughout 2012 blocks of weaker paleosol material fell from the scarp to the upper bowl of the landslide. This material was transported away by seepage from a layer at the base of the landslide. In early 2013 horizontal drains were installed in this layer of the Pahoia Tephras to remove water. This has resulted in a build-up of talus debris at the base of the landslide (Moon *et al.* 2014). Several minor mass wasting events that have occurred include increased rill erosion from the headscarp between May and September 2014, and a small planar slide on about June 24 2014 (**Figure 4.7**). This slide was through the tephra layers only and is attributed to an over steepened scarp rather than sensitivity. The geomorphic map of the landslip (**Figure 4.7**) was drawn in January 2015. The landslide bowl coincides with the approximate top of the Te Puna Ignimbrite, which outcrops as a bluff on both sides of the landslide. The remoulded debris from the 2011 and 2012 landslips appear to have broad upper and lower steps. The steps probably follow the approximate topography of the underlying 1979 debris. A portion of the 1979 landslide was preserved as vegetated area shown in hatch (**Figure 4.7**).

Figure 4.3. Bramley Drive landslip before in 2007 (top) and after the landslip (2015), which occurred in 2011-2012 following heavy rainfall. The previous position of the headscarp before the 2011-2012 events is the dashed red line in the bottom figure. (Figure source: WBOPDC Mapi viewer, 2015).

Figure 4.4. The exposed back scarp following the 2011-2012 events. Photo: Vicki Moon.

Figure 4.5. The remoulded debris lobe from the 2011-2012 events. Photo: Vicki Moon.

Figure 4.6. Bramley Drive failure viewed from the Harbour. Photo: Peter Clarke.

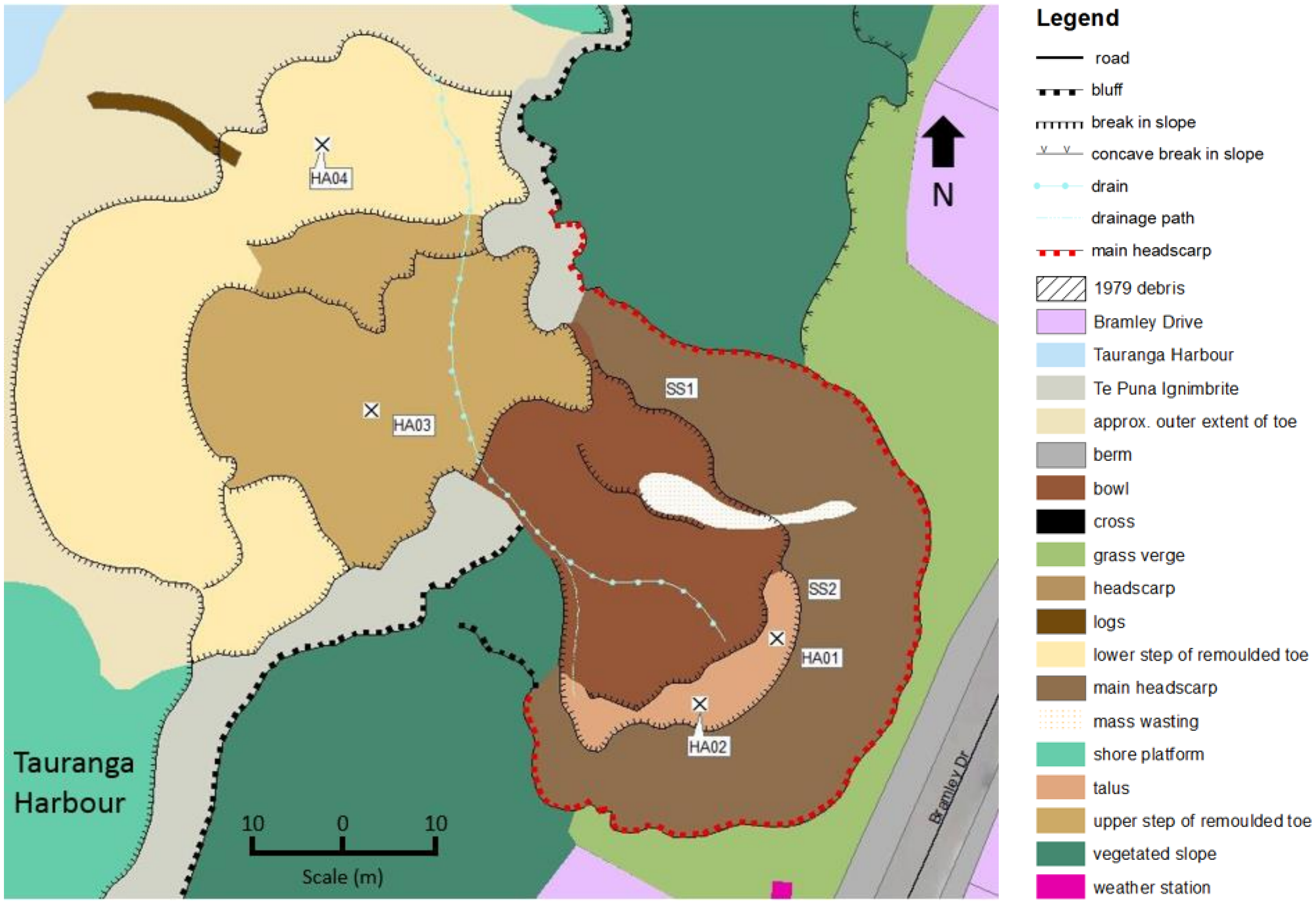

Figure 4.7. The geomorphic map of Bramley Drive landslip, mapped in December 2014.

4.3.3 Stratigraphic observations

Several sites were investigated to locate the most sensitive material at Bramley Drive. A highly sensitive layer is known to exist at around 23 m below the failure scarp (**Figure 2.4**). This layer is located slightly above the Te Puna Ignimbrite, which outcrops on both sides of the landslide (**Figure 4.7**). The ignimbrite - soil contact was traced towards the scarp, in order to try and locate the highly sensitive layer in the borehole.

4.3.3.1 Sample site 1: OM2

At sample site 1 (SS1, **Figure 4.7**), the extra-sensitive layer found in the machine borehole core (machine borehole drilled adjacent to the weather station, **Figure 4.7**) could not be located with shear vane testing; soils were sensitive (OM2, **Table 4.1**) however no extra-sensitive layers were detected (**Table 4.1**).

Table 4.1. Shear vane results for OM1 and OM2

Sample	Peak Vane strength (kPa) ± S. Error	Remoulded vane shear strength (kPa) ± S. Error	Sensitivity (%)
OM1	66 ± 3	5 ± 1	15 ± 3
OM2	60	9 ± 3	6 ± 3

OM2 is defined as a Silty CLAY, with low plasticity, minor manganese inclusions and moderate weathering, as indicated by limonite staining in **Figure 4.8**. Shear vane results confirmed the soil was in the sensitive range (5 - 8) according to NZGS (2005) (**Appendix 4.3.3**). The soil also smeared and hands were left slightly damp upon remoulding between fingers. However, when gently hammering in metal triaxial cores, it was found that the soil fractured. The soil was therefore

Figure 4.8. The Silty CLAY Pahoia Tephra tested at SS1, with a small digital camera bag for scale.

deemed too dry to be tested further; deformations during sampling would significantly affect triaxial results.

4.3.3.2 Sample site 2: OM1

The next sampling site was located in the bowl of the landslide (SS2 in **Figure 4.7**). This site was chosen because extra-sensitive soils were located with the shear vane (**Table 4.1**), as well as the safe location slightly away from the main failure scarp (**Figure 4.9**). The soil was correlated to the borehole drilled behind the face in February 2013 (**Figure 2.4)** (Steinborn, 2015), by matching the stratigraphic similarities in the soil logs. OM1 correlates with the Silty CLAY Pahoia Tephra layer at 19 m depth in the borehole (**Figure 2.4**). The quick clay layer observed in this borehole at approximately 23 m depth would be ideal to sample, however the position of this layer below the outcropping scarp meant that it was impossible to sample without borehole drilling.

The upper layer of Pahoia Tephra (OM1a) (**Figure 4.10**) was a highly plastic, highly weathered, pale orange-brown Silty CLAY with some fine sand (15-25%) and minor manganese (8-15%) (OM1, **Table 4.1**). The unit was extra-sensitive (St = 15) and hands were moist after hand shearing. The basal contact of this unit was a prominent, up to 5 cm thick manganese rich layer.

Below this contact is a soft, extra-sensitive (St = 15), highly weathered, highly plastic Silty CLAY (OM1), with minor manganese (**Figure 4.10**). This unit also appeared to be homogeneous with no cross bedding observed. This unit was chosen for sampling in preference to the overlying sandy unit, because greater heterogeneities are introduced by sand, which is not ideal for triaxial testing.

Figure 4.9. SS2 location on the failure scarp.

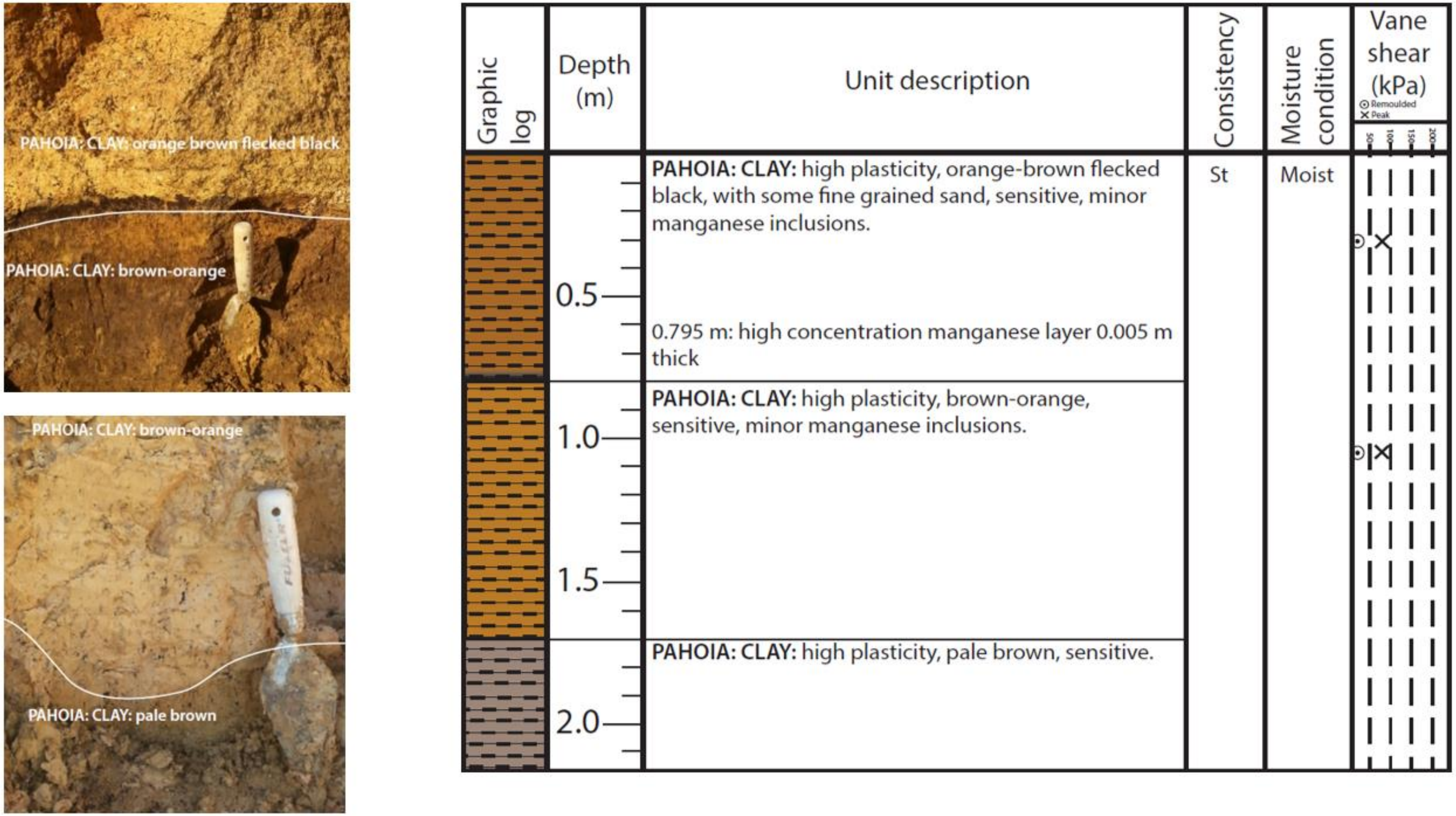

Figure 4.10. Stratigraphic log and photos of SS1, Bramley Drive, Omokoroa.

4.4 Site 2: Matua Peninsula

4.4.1 Criteria suitability

The second site selected for this thesis was located on a coastal escarpment on the south side of Matua Peninsula, Tauranga City. The site was referred by a student from the University of Waikato (Amy Christophers), who completed a small project at the site in 2012.The site complies with all site criteria; it is a recently (2012) failed, accessible landslip with sensitive soil layers exposed in the failure scarp. Landowners were initially compliant, until January 2015, when the property owner decided against further research to be undertaken on the property. This was only found out after initial investigations including mapping, sampling and general observations had been completed. In order to overcome this accessibility issue, neighbouring properties were consulted as to whether soil sampling of the sensitive layers of interest could be continued on their properties, by following the layer along its contour. This approach was successful; and sampling was able to be continued.

4.4.2 Geomorphologic site description

4.4.2.1 Matua Peninsula geomorphological description

Matua Peninsula is a marine terrace within the Tauranga City margins (Briggs *et al*. 1996) (**Figure 4.11**), with a gently undulating surficial gradient, which abruptly transitions into steep coastal cliffs, which wrap around the peninsula. These coastal cliffs range from 10 – 20 m high. The site investigated is on the southern side of Matua peninsula, where the cliff height ranges between 18-20 m (**Figure 4.11**). The site lies to the south of a peak at 23 m (**Figure 4.12**).

Overall, the cliff is heavily vegetated and in the range of 50-60° steep. Following the 2012 events, some properties have since installed retaining walls piled to below the level of the cliff, while others have temporary retaining walls, and some have no retaining wall at all because of the high cost involved ($100,000+). Storm-water is collected in a 710 mm drain at the eastern end of Rewarewa Place (**Figure 4.12**). Local residents of Rewarewa Place were interviewed at the time of investigation. Of main concern was that during storms, the storm-water drain was not sufficient in capturing the water, causing overland flow to occur on the clifftop properties (Don Liechel, personal comment, 13/01/2015).

Figure 4.11. Matua Peninsula aerial 2015. The area investigated is outlined in red and shown below in Figure 4.12 Photo: http://gismob.tauranga.govt.nz

Figure 4.12. Aerial photo taken in 2015 of the south side of Matua Peninsula, with overlain 1 m contours. Several landslides occurred following heavy rainfall in 2012 (red outline), including the largest one studied in this thesis. Storm water drains at the eastern end of Rewarewa Place, as outlined in blue. The yellow circle indicates the peak at 23 m. Photo: http://gismob.tauranga.govt.nz/

4.4.2.2 Matua landslide geomorphology

The site was initially investigated by Coffey Geotechnics in August 2012 following the slip which occurred on 12th August 2012. This report was used in conjunction with site investigations I completed in January 2015. Coffey Geotechnics also completed geotechnical reports and retaining wall design for adjacent properties following the slips in 2012.

The property where the landslide occurred is rectangular in shape and largely flat until approximately 3-4 m from the edge of the cliff face (**Figure 4.13**), where a gentle downslope gradient is observed. A small timber retaining wall stepped down 1 m from the lawn edge separates the lawn from the landslide scarp. Small tension cracks are also present approximately 1m back from the step down in the lawn, indicating that the top of the current failure is over steepened and still at risk of minor landsliding (**Figure 4.13**). A narrow timber staircase supported by timber foundations provides access to Tauranga Harbour via the western edge of the scarp. A coastal escarpment profile (**Figure 4.14**) shows the length of the scarp to be approximately 15 m long, at an angle of 52°, decreasing slightly towards the landslide toe. The scarp does not appear to have obvious curvature, however minor ridges occur on either side of the scarp.

Landslide debris covers a roughly circular area of about 1700 m^2. The debris consists of remoulded clay material as well as significant intact blocks with upright trees. There is a pronounced gap of approximately 2 m between the base of the escarpment and the start of the landslide debris.

4.4.3 Stratigraphic observations

The stratigraphic column of the cliff section was obtained by utilising the hand auger boreholes drilled by Coffey Geotechnics in 2012 (**Appendix 4.3.5**). The escarpment comprises mainly of a thick sequence of Matua sediments (**Figure 4.14**). Aquifers (sandy-gravelly material) occur at 10-12 m and 15-17 m depth. Sensitive soils, including very stiff SILT and very stiff Silty CLAY (sensitive to extra-sensitive) occur at 12-15 m and 17+ m respectively. Overlying the Matua Subgroup from bottom to top are thinner layers of the Hamilton Ash and Rotoehu Ashes. Sensitive material at 12-15m depth from the top was exposed on too steep a slope to obtain samples safely, therefore sensitive layers at 17+ m depth below the top of the cliff were targeted.

4.4.3.1 Engineering geological description of M1

M1 (**Figure 4.15**) was identified as a Silty CLAY with minor (8 – 15%) fine to medium grained sand. *In situ* material was saturated and a creamy-white colour with inconsistent pale-pink bands and pale-orange mottles. Shear vane values returned sensitivities between 10 to 12, with an average of 10 (**Table 4.2**), and hand shear testing also showed the soil to smear upon remoulding between the thumb and the forefinger. The worm test for plasticity of *in situ* material showed that material was of low plasticity. Manganese concretions were present at concentrations of between 10 – 50%, indicating that pore water was basic enough for precipitation of manganese (Vodyanitskii, 2009).

Table 4.2. Shear vane results for M1.

Sample	Peak Vane strength (kPa) ± S. Error	Remoulded vane shear strength (kPa) ± S. Error	Sensitivity (%)
M1	60 ± 0.4	6 ± 0.6	10 ± 1

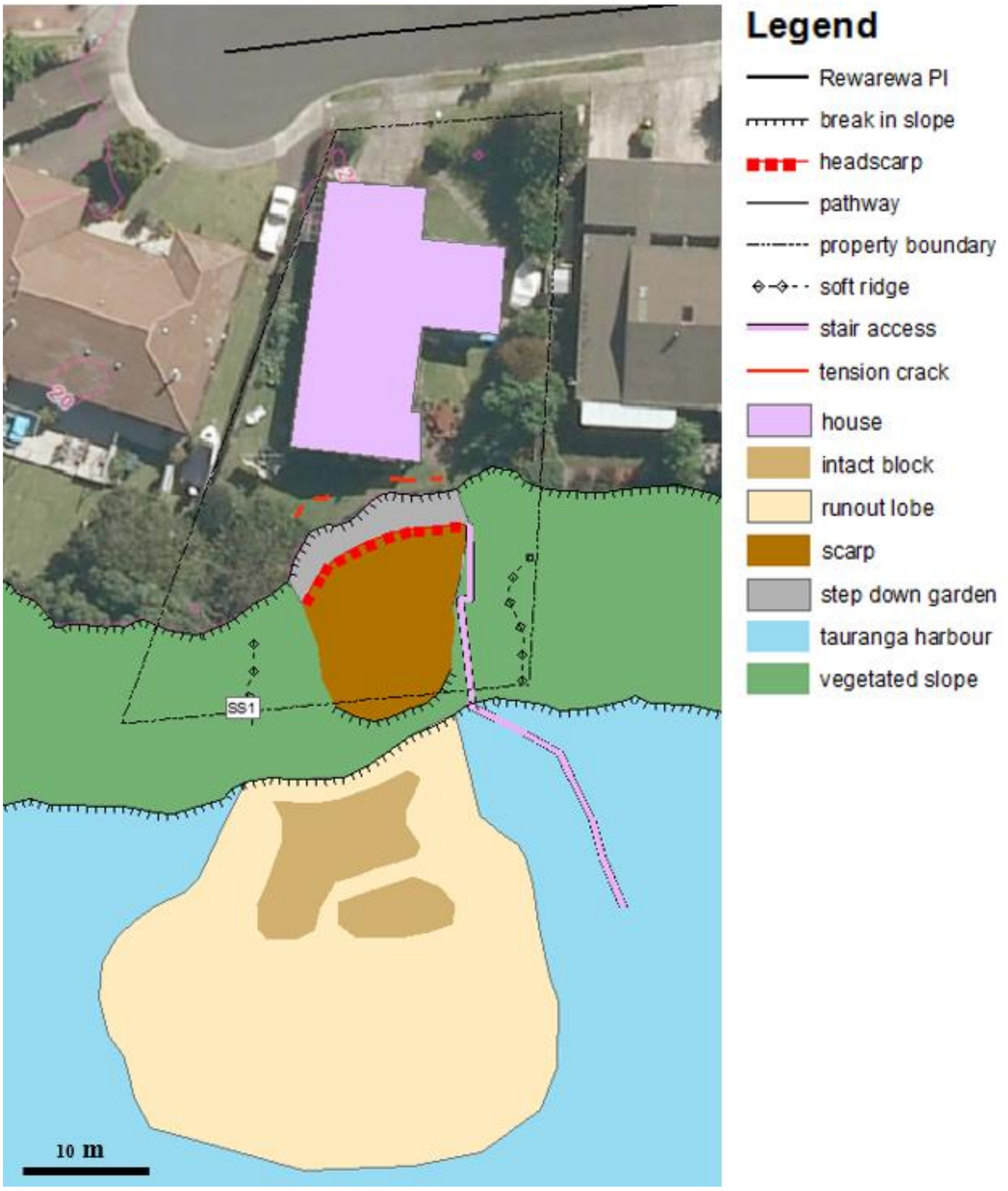

Figure 4.13. Geomorphological map of the Matua failure, drawn in ArcMAP over a Tauranga City Council aerial photo with overlain contours from 2015.

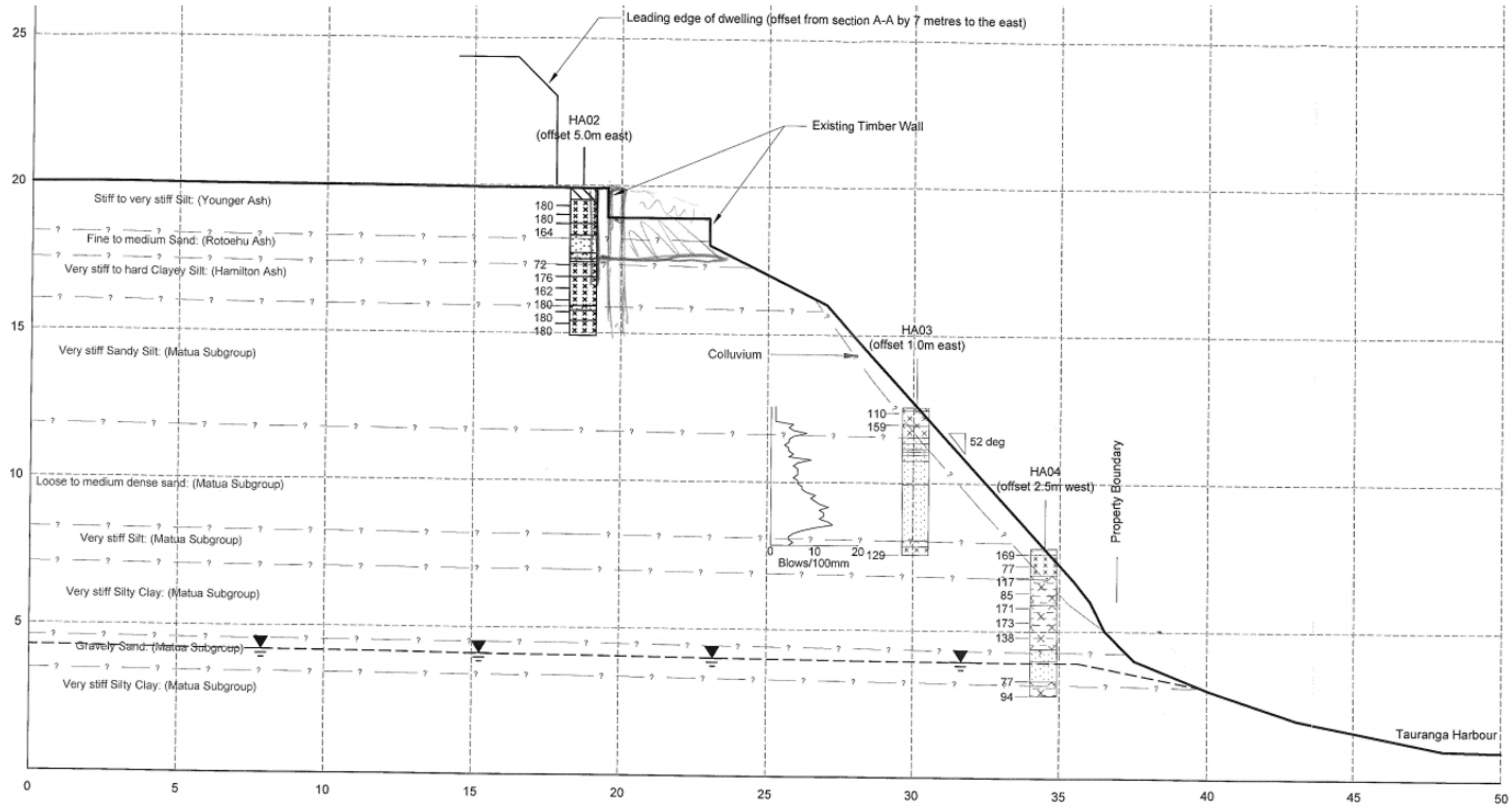

Figure 4.14. A cross section profile of the Matua landslide from the initial investigation following the slip in 2012 (Coffey Geotechnics, 2012).

The soil was saturated at the time of sampling, and seepage was observed from the exposed face (**Figure 4.15**). M1 correlates with the Silty CLAY described at the base of the Coffey Geotechnics hand auger borehole (HA04) (**Appendix 4.3.5**).

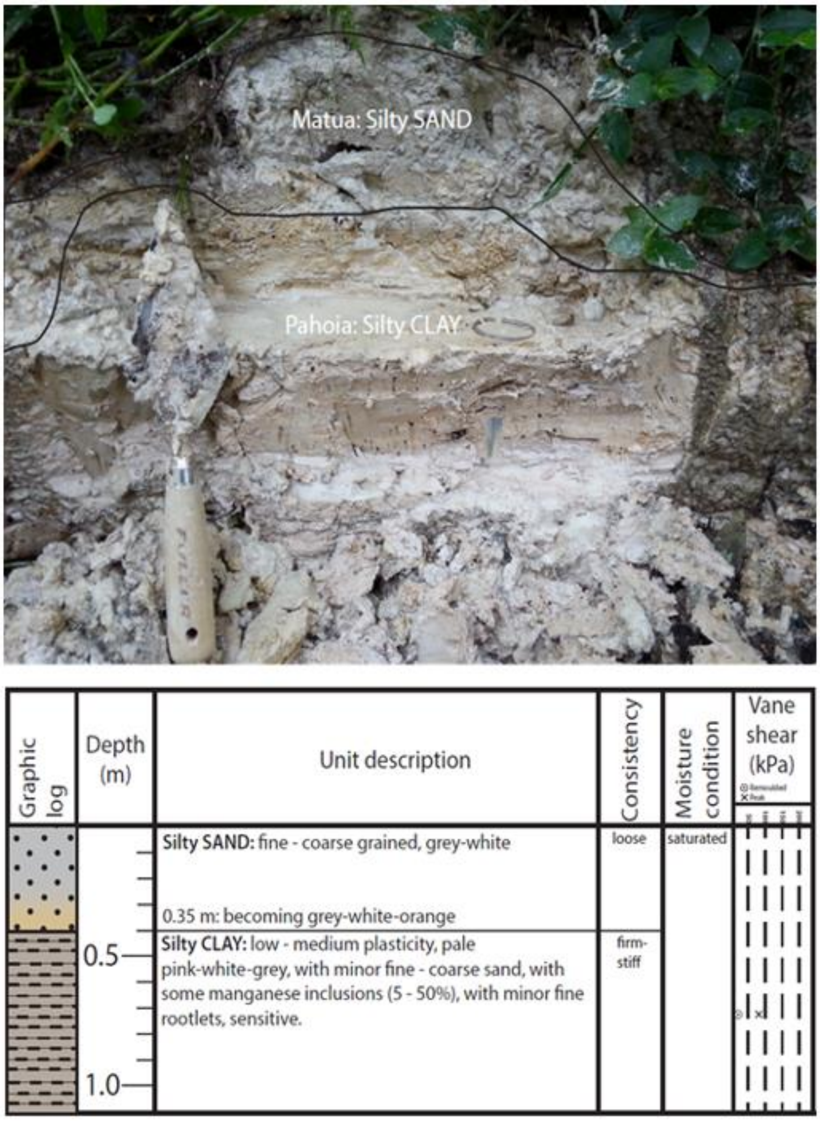

Figure 4.15. Stratigraphy of the sampling site M1. Matua silty SAND overlies extra-sensitive Pahoia silty CLAY (M1).

CHAPTER 5

GEOMECHANICAL PROPERTIES & FAILURE MODES

5.1 Introduction

Standard geomechanical properties including natural moisture content, Atterberg Limits, particle size and density, and bulk density are presented in sections 5.2 – 5.4 for Matua (M1) and Omokoroa (OM1) samples. Consolidated undrained triaxial test results including deviator stress vs axial strain plots ($\sigma_1 - \sigma_3$ vs ε_{axial}), p'-q' plots, and Mohr-Coloumb failure criteria (φ' and c') are presented for M1 and OM1 samples in section 5.5. Shear zone characteristics of the failed triaxial samples are presented in section 5.6. Raw data for geomechanical properties and triaxial results are presented in **Appendices 5.1** and 5.5 respectively.

5.2 Moisture content, bulk density, porosity & void ratio

Mean moisture content, bulk density and porosity results for M1 and OM1 are presented in **Table 5.1**. Overall, M1 and OM1 are both highly porous, low density, saturated materials. OM1 has a slightly higher moisture content in comparison to M1. M1 has a considerably greater wet bulk density (1690 kg m^{-3}) than OM1 (1320 kg m^{-3}). OM1 has a slightly higher porosity of 69.7 % than M1 (64.7 %).

Table 5.1. Mean moisture content (%), wet bulk density (kg m-3), dry bulk density (kg m^{-3}), porosity (%) and void ratio (-), compared with sensitivity for Matua (M1) and Omokoroa (OM1) samples.

Sample & location	Material (classification, probable origin)	Moisture content (%± S. Error)	Wet bulk density (kgm^{-3} ± S. Error)	Dry bulk density (kgm^{-3} ± S. Error)	Porosity (%± S. Error)	Void ratio (-± S. Error)	Sensitivity (%± S. Error)
M1 (slip face, Matua)	Extra-sensitive Silty CLAY with some sand, reworked tephra	64 ± 0.3	1690 ± 100	980 ± 60	66 ± 3.1	1.8 ± 0.3	10 ± 1
OM1 (slip face 19 m below surface, Bramley Drive, Omokoroa)	Extra-sensitive Silty CLAY, reworked tephra fall	72 ± 1	1320 ± 50	760 ± 30	70 ± 0.1	2.3 ± 0.0	15 ± 2.8

5.3 Particle size and density

Particle size and density results for M1 and OM1 are presented in **Table 5.2**. Particle size divisions include clay size (< 2 μm), silt size (2 – 63 μm) and sand size (63 – 2000 μm) (NZS 4402, 1986). Clay is the dominant component of both Matua and Omokoroa samples. M1 has a substantial amount of sand, while OM1 does not. Silt concentrations are moderate in both samples, with OM1 having a higher percentage than M1. Particle density of OM1 is in-keeping with previously published values of extra-sensitive material in Tauranga (2220 – 2663 kg m^3). M1 however has a slightly greater particle density at 2777 kg m^3, although the large standard error could mean that this is an over or under estimate (**Table 5.2**).

Table 5.2. Particle density and percentage of each particle type measured for each sample.

Sample	Particle density (kg m^3)	Clay (%)	Silt (%)	Sand (%)
OM1	2517 ± 9.7	62.6 ± 4	37.3 ± 4	0.1 ± 0
M1	2777 ± 257	40.1 ± 11	22.3 ± 7	37.6 ± 17

5.4 Atterberg Limits

Atterberg Limits for M1 and OM1 are presented in **Table 5.3**. Sensitive materials from NZ typically have medium to high liquid limits, high plastic limits, and low to medium plasticity indices according to ranges outlined by Briaud (2013) (Keam, 2008; Wyatt, 2009; Arthurs, 2010; Cunningham, 2012).

Table 5.3. Atterberg Limits for OM1 and M1.

Sample	Liquid Limit (%)	Plastic Limit (% ± S. Error)	Plasticity Index (%)	Liquidity Index (-)	Activity (%)
OM1	66 $R^2 = 0.99$	41 ± 0.4	25	2.9	0.4
M1	52 $R^2 = 0.87$	37 ± 2	15	1.8	0.4

OM1 has a slightly higher liquid limit than M1 (**Table 5.3**). Both OM1 and M1 have liquid limits which fall into the upper end of the “medium” range outlined by Briaud (2013) in **Table 5.4**. Plastic limits for OM1 and M1 are both high, while plasticity indices for both samples are low or low-medium. Liquidity indices for both M1 and OM1 were greater than 1, with OM1 having a particularly high liquidity index value of 2.9 (**Table 5.3**).

Table 5.4. Atterberg limit indices, adapted from Briaud (2013).

Parameter	Low	Medium	High
Liquid limit	10-40	40-80	>80
Plastic limit	10-20	20-30	>30
Plasticity index	0-20	20-50	>50

Activity is a measure of the plasticity of the clay sized particles, and is regulated by the dominant clay mineral species (Selby, 1993). Selby (1993) broadly defines activity by three classes: inactive, normal or active (**Table 5.5**).

Table 5.5. Activity classification by Selby (1993) after Skempton (1953).

Classification	Activity
Inactive	< 0.75
Normal	0.75 – 1.25
Active	> 1.25

Activity does not take into account ionic and pore fluid concentrations in the soil, and is more a quick measure of chemical reactions, as shown by correlations with the cation exchange capacity (CEC) (Selby, 1993). Both OM1 and M1 have low activities, classed in the inactive range according to Skempton (1953). OM1 and M1 both plotted below the A-line on the plasticity chart (**Figure 5.1**), therefore classed in the silt with high compressibility range (MH).

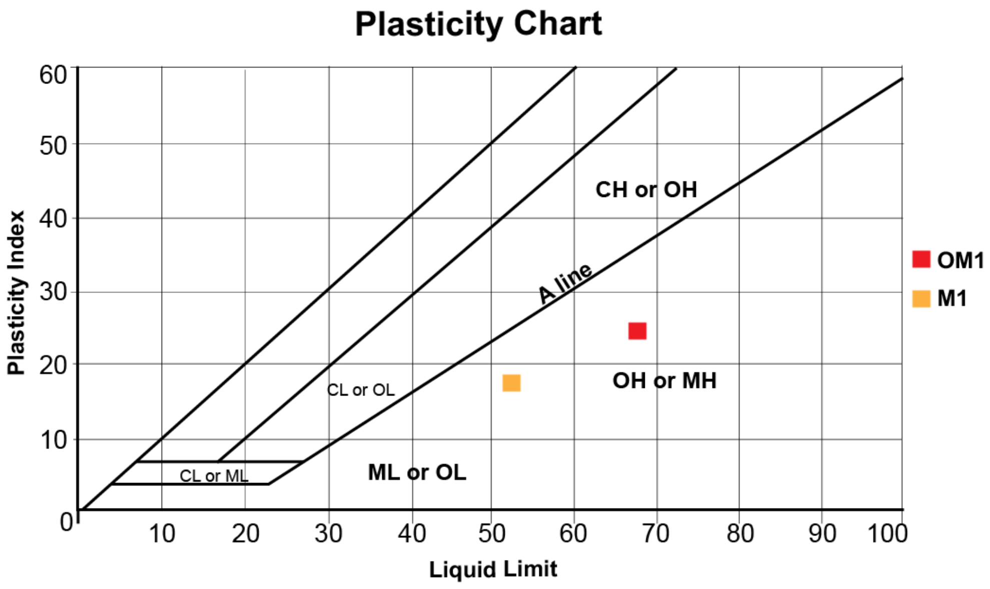

Figure 5.1. A-line plasticity chart with Omokoroa (OM1) and Matua (M1) plotted.

5.5 Triaxial

Consolidated, undrained, (CU) effective stress triaxial tests were performed on both M1 and OM1 samples. The following section presents results for effective stress, stress-strain and pore water pressure characteristics, Mohr-Coloumb failure criteria, effective stress path properties (p’-q’ plots), and post-failure sample characterisation.

Two sets of triaxial tests were completed for OM1, as thin sections developed from the initial tests were unsuccessful. Thin section production was successful following the first set of triaxial tests for M1.

5.5.1 Errors in triaxial test results

The sampling technique, where push tubes were gently hammered into the soil, results in compaction in the centre of the sample, which has the effect of increasing sample strength (Gylland *et al.* 2014). The effect of hammering may result in sample disaggregation, which decreases sample strength. Ideally, block samples of *in situ* material would be trimmed down to give a more accurate stress-strain and pore pressure response, but this sampling equipment was unavailable. To minimise error, samples that were obviously fractured as a result of sampling were discarded. Some fractures on the interior of the sample cannot be observed until cutting the sample open post-testing. These errors introduced by sampling are difficult to quantify, but since all samples were retrieved by the same method, the test results are as uniform as possible.

Ideally, all soil samples would be comprised of similar material so that results are reproducible. Rather, soil is a naturally highly variable material, so while the sample may look relatively homogeneous on the exterior, irregularities may exist in the interior of the sample; for example a minor sand pocket, a root system, a larger particle, or a weathering plane. Irregularities like these must be taken into account when interpreting results. An example of this, is that a soil with say a weathering plane that was not observed before triaxial testing would significantly decrease the strength of the soil. All samples were cut open after testing in an attempt to quantify if natural variations that may have influenced results.

5.5.2 Effective stress calculation

Before triaxial testing was undertaken, estimated *in situ* effective stress parameters were calculated using **Equation 3.11**, and are presented in **Table 5.6**.

Table 5.6. Estimation of *in situ* parameters required to calculate the effective stress for each sampling site.

Sample	Depth in profile (m)	Estimated force of overlying soil (K Nm^{-2})	Water table depth (m)	*In situ* effective stress (kPa)	Effective stress values used (kPa)	Label
OM1a	24 m**	15	8	280	205	**OM1a1**
					280	**OM1a2**
					355	**OM1a3**
OM1b	19	15	8	240	140	**OM1b1**
					240	**OM1b2**
					340	**OM1b3**
M1	16	23	8	150	75	**M1a**
					150	**M1b**
					225	**M1c**
					250	**M1d**

** Upon correlating the depth in profile of OM1 with the borehole core log behind the failure scarp (Kluger *et al.* 2015), the depth was revised to 19 m, which is presented as the correct depth in other chapters.

5.5.3 Consolidated undrained triaxial tests

5.5.3.1 Background

Possibilities for the global response for stress, strain and pore water pressure for soils during undrained consolidated triaxial tests are briefly outlined.

Dense, hard and overconsolidated soils generally show *brittle* type failure, where the stress-strain curve reaches a peak stress at less than 5% strain, followed by a region of *strain softening* (**Figure 5.2b, c**). Strain softening was initially considered by Bishop (1971) to be a reduction in stress after peak stress.

Recent authors (Tavenas, 1984; Quinn *et al.* 2011) consider the horizontal strain or shear band displacement required to reach the residual state equally as important to consider with stress. In this study strain softening was quantified as a percentage of the overall stress lost between the peak deviator stress (q_{max}) and the deviator stress following remoulding at 20% strain ($q_{remoulded}$) (**Equation 5.1**).

$$strain\ softening\ (\%) = \frac{(q_{max} - q_{remoulded})}{q_{max}} * 100$$

Equation 5.1

It was not feasible to include horizontal strain measurement in our experimental setup, therefore the brittleness parameter we used is an estimate of strain softening.

During *brittle* failure, the pore water undergoes compression (positive stress) in the strain hardening region, thereby reducing effective stress. After the peak (failure) is reached, depending on the material, the sample either contracts or dilates (**Figure 5.2d**) (Boulanger & Idriss, 2006). Following failure at peak deviator stress, sandy material expands in volume (*dilation*) causing the pore water pressure to become negative and increasing effective stress (**Figure 5.2c**) (Briaud, 2013). Overconsolidated or sensitive material however *contracts* following failure, and pore pressure slightly increases, further reducing effective stress (**Figure 5.2b**) (Boulanger & Idriss, 2006; Gylland *et al.* 2014). The term contractive is widely used in drained triaxial tests, where it defines a reduction in volume (Lancellotta, 2008). Since our tests are undrained, volume change cannot be directly measured; rather it is inferred by a contractive response, defined by positive pore pressures following failure, rather than negative pore pressures, which define the response as dilative. This evidence has been used to infer contraction by Gylland *et al.* (2014) and Boulanger and Idriss (2006). The transition between dilation and contraction following failure occurs over a narrow range of Atterberg Limits from materials that display more sand-like behaviour (*dilation*) to materials that display more clay-like behaviour (*contraction*) (Boulanger & Idriss, 2006).

Normally consolidated, soft and loose soils exhibit ductile failure, where a peak deviator stress is gradually reached at around 15 – 20 % strain (**Figure 5.2a**, d) (Head, 1998; Briaud; 2013). Here, the pore water pressure gradually increases, simultaneously reducing the effective stress, until failure occurs. In p'-q' diagrams, the curve touches the CSL, but does not contract (trend left) or dilate (trend right) along the CSL.

Whether the same soil type is normally or over consolidated, as long as the void ratio is consistent between both samples, after large strains, both stress- strain curves reach a common strength. This is called the *critical state* (Briaud, 2013) (**Figure 5.2d**). Once the critical state is reached, the soil does not change volume during shearing. Soils that have failed and lost significant strength after failure, but have not yet reached the critical state, are in the *softened state* (Thakur *et al*. 2014).

5.5.3.1.1 Real time and delayed data from sensors

It is important to note that the stress and strain sensors capture real time data, while the pore pressure sensor is at the base of the sample, meaning that the response captured is global, and unable to capture local variations of pore pressure change within the sample.

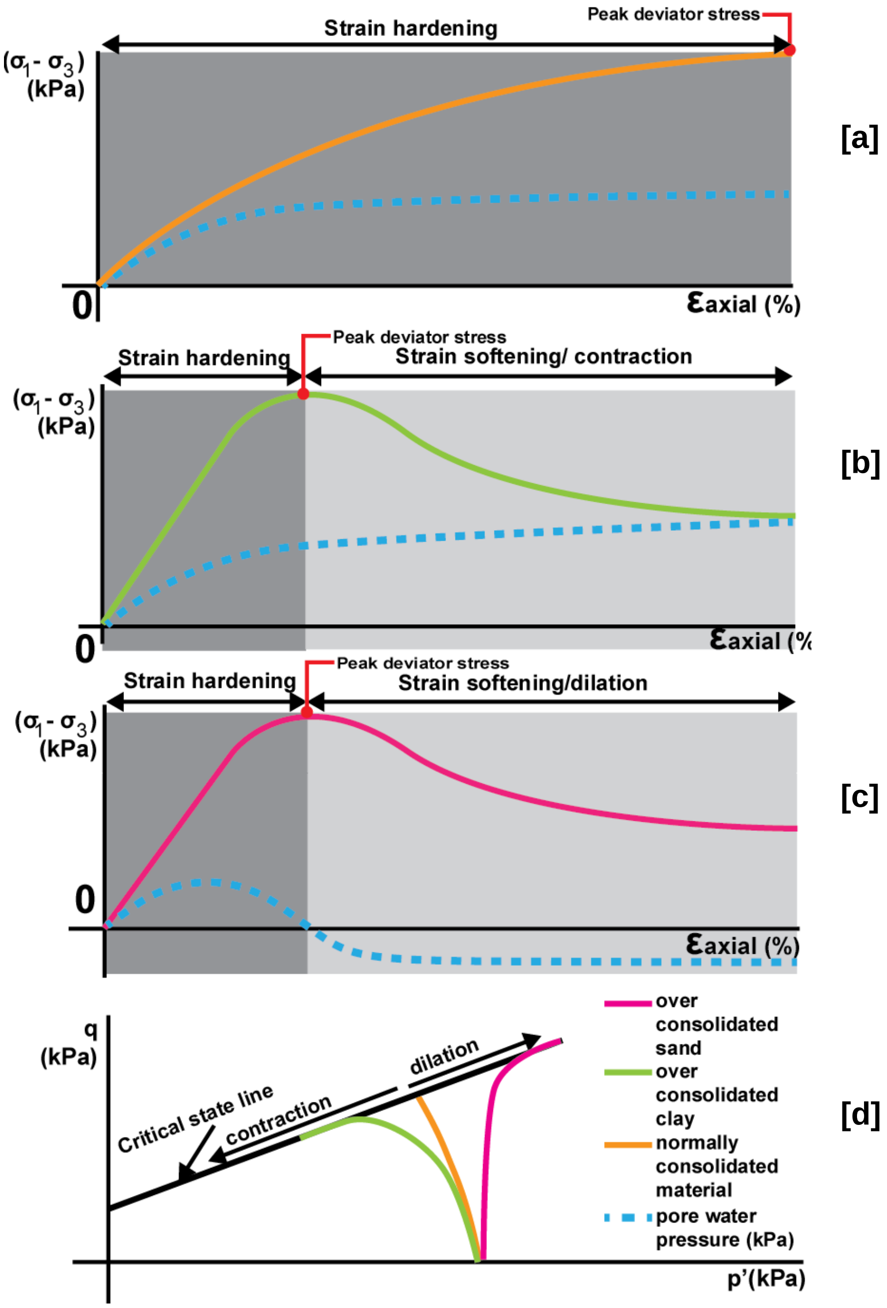

Figure 5.2a-d (top to bottom). Schematics of the different behaviours expected for over consolidated sand (pink), overconsolidated clays (green), and normally consolidated material (orange)for both q (deviator stress) vs ε_{axial}, and q' vs p' (effective stress). Schematics are adapted from Boulanger & Idriss (2006) and Briaud (2013).

5.5.3.2 Omokoroa samples (OM1a & OM1b)

5.5.3.2.1 Pre-peak strain hardening region

All six stress-strain curves exhibit a rapid rise in the strain-hardening region prior to peak stress (**Figures 5.3** &**5.4**). All OM1 samples fail at less than 5% strain (**Table 5.7**, **Figures 5.3** & **5.4**). Peak deviator stress and also the curvature of the peak increases with increasing effective confining pressure for all results.

Table 5.7. Failure characteristics for OM1a, b and M1, including axial strain at failure ($\varepsilon_{failure}$), deviator stress at failure ($q_{failure}$) pore pressure at failure ($u_{failure}$) and strain softening at failure.

Sample	Effective confining pressure [kPa]	$\varepsilon_{failure}$ [%]	$q_{failure}$ [kPa]	$u_{failure}$ [kPa]	Strain softening [%]
OM1a1	205	3.1	265	462	31
OM1a2	280	3.4	324	194	32
OM1a3	355	3.5	383	556	32
OM1b1	140	1.9	179	120	14
OM1b2	240	3.2	246	156	20
OM1b3	340	2.0	299	192	50
M1a	75	2.2	131	27	13
M1b	150	2.3	137	96	29
M1c	225	2.2	207	154	33
M1d	255	4.4	250	168	29

5.5.3.2.2 Post-peak strain softening region

Following peak deviator stress, strain softening, or a reduction in deviator stress with strain occurs for all samples. All samples reach the fully softened state, (15-20% strain) (**Figures 5.3** & **5.4**) but have not yet reached the critical state, where the stress-strain curves converge horizontally on the same line (Thakur *et al.* 2014; Briaud, 2013).

Strain softening in OM1a/b tests increases with increasing effective confining pressure, from 14% at 140 kPa effective confining pressure to 50% at 340 kPa effective confining pressure (**Table 5.7**, **Figure 5.6**).

5.5.3.2.3 Pore-water pressure

OM1a1 & 2 (**Figure 5.3**) have pore water pressure (PWP) curves that rise sharply, mirroring the stress-strain curves for most of the pre-peak region, until they both deviate and peak slightly prior to peak deviator stress. Both PWP curves drop in the region immediately after peak deviator stress, then rise before finally reaching a steady rate of increase towards 20% strain (**Figure 5.3**). For OM1a3, PWP also mirrors the stress-strain curve before peak deviator stress, rising sharply, however the fall in PWP prior to peak deviator stress is not observed. Following failure the curve steadily increases towards 20% strain.

PWP increases rapidly in the strain hardening region for all three tests on OM1b (**Figure 5.4**). Unlike OM1a1-3, the PWP peak does not clearly precede the $\sigma1 - \sigma3$ peak, although the PWP peaks are still very close or slightly after peak $\sigma1 - \sigma3$ is reached. The fall in PWP seen in OM1a1-2 is not observed on any of the OM1b tests. Following peak σ1 – σ3, the PWP curve for OM1b1 dissipates slightly, while for OMb2 the PWP it flattens off, while for OM1b3 it significantly increases at a steady rate before slightly flattening near 20% strain (**Figure 5.4**).

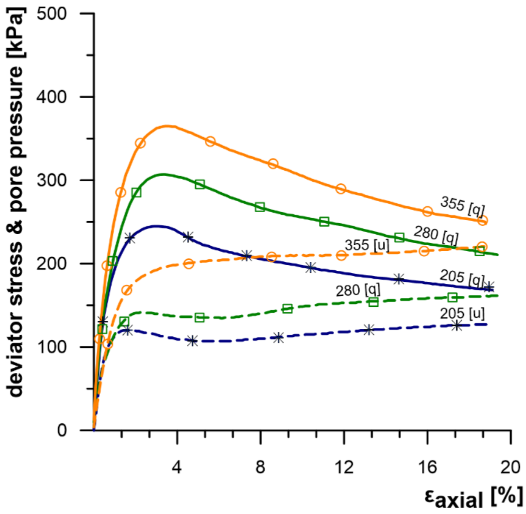

Figure 5.3. Deviator stress (σ1 – σ3) and pore water pressure (u) (both kPa) vs axial strain (ε_{axial}) for OM1a1, 2, 3.

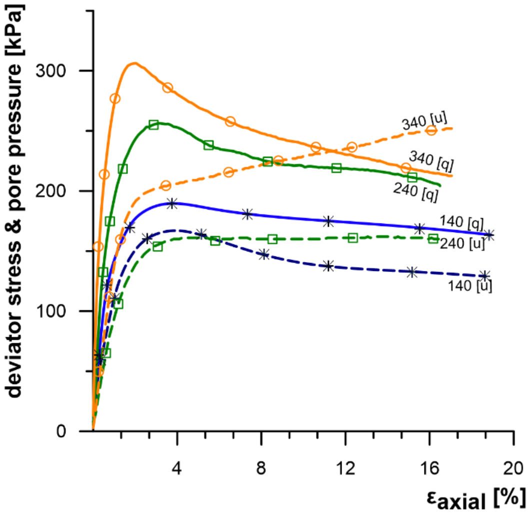

Figure 5.4. Deviator stress (σ1 – σ3) and pore water pressure (u) (both kPa) vs axial strain (εaxial) for OM1b1, 2, 3.

5.5.3.3 Matua stress-strain curves (M1)

5.5.3.3.1 Pre-peak strain hardening region

Stress-strain curves for Matua samples have peaks followed by a strain softening region (**Figure 5.5**). In the pre-peak strain hardening region, stress-strain curves rise sharply before reaching a peak. Samples M1b,c have more abrupt transitions from hardening to softening, with highly curved peaks, whereas samples M1a & M1d transition more gradually from strain hardening to strain softening (less curved peaks). All M1 samples fail at less than 5% strain (**Table 5.7**). Like OM1a/b samples, peak deviator stress increases with greater confining pressures (**Table 5.7**).

5.5.3.3.2 Post-peak strain softening region

The amount of stress lost during strain softening is close to 30% for samples tested at 150, 225 and 255 kPa, while the sample tested 75 kPa displays less strain softening at 12% (**Figures 5.5** & **5.6**).

5.5.3.3.3 Pore-water pressure characteristics

During the strain hardening region of the stress-strain curve (**Figure 5.5**), PWP rises rapidly in response to stress, however the responses are slightly delayed in comparison with OM1a/b, where the PWP near exactly mirrors the stress-strain curves. The minor PWP peak prior to peak deviator stress did also not occur like samples OM1a (1&2). Following peak stress, PWP flattens out and increases only very slightly towards 20% strain for samples M1b-d, while for M1a, pore pressure decreases after failure before slightly rising again towards 20% strain (**Figure 5.5**). Very slight dips in pore pressure occur in samples M1a and M1c (**Figure 5.5**).

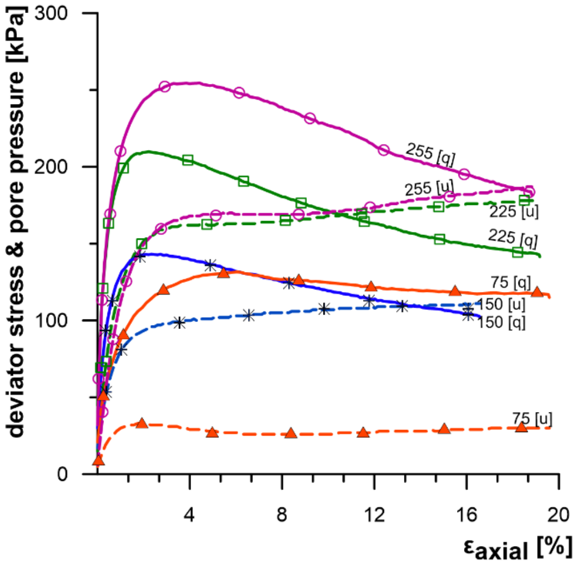

Figure 5.5. Deviator stress (σ1 – σ3) and pore water pressure (u) (both kPa) vs axial strain (ε_{axial}) for M1a, b, c, d.

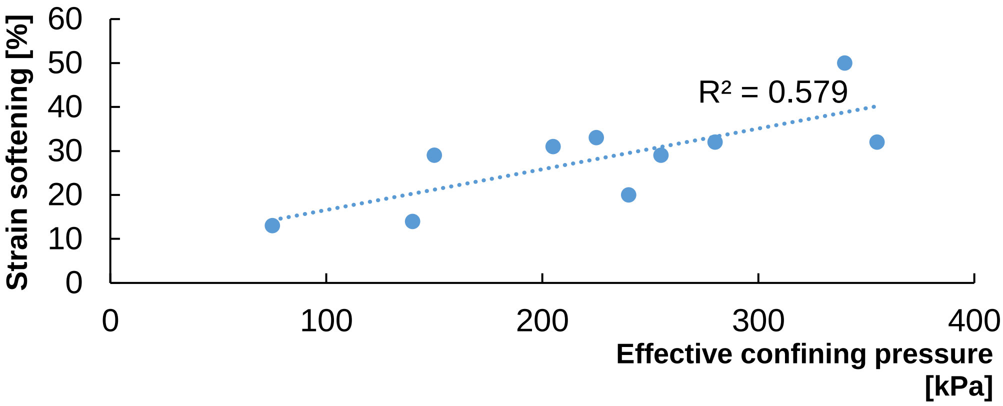

Figure 5.6 The relationship between strain softening and confining pressure for all M1 and OM1 samples.

5.5.4 Stress path characteristics

The stress path in two dimensions describes the evolution of effective p' and q' stresses, which are defined by **Equation 5.2** and **5.3** (Briaud, 2013).

$$p' = \frac{\sigma_1{}' + \sigma_3{}'}{2}$$

Equation 5.2

$$q' = \frac{\sigma_1' - \sigma_3'}{2}$$

Equation 5.3

σ_1 and σ_3 are respectively the effective vertical and horizontal stresses in the triaxial test (Briaud, 2013).

Stress paths for OM1, OM2 and M1 (**Figures 5.7, 5.8** and **5.9**) trend left, with the exception of the OM1b1 and M1a. A sharp trend left indicates sample *contraction* after failure. The p'-q' plot for OM1b1 and M1a deviates slightly to the left, however does not have a pronounced drop in deviator stress along the critical state line like OM1b2, 3, indicating slight contraction. Another general trend is that higher confining pressures correlate with an initial increase in effective stress in the pre-peak strain hardening region, followed by a reduction in effective stress

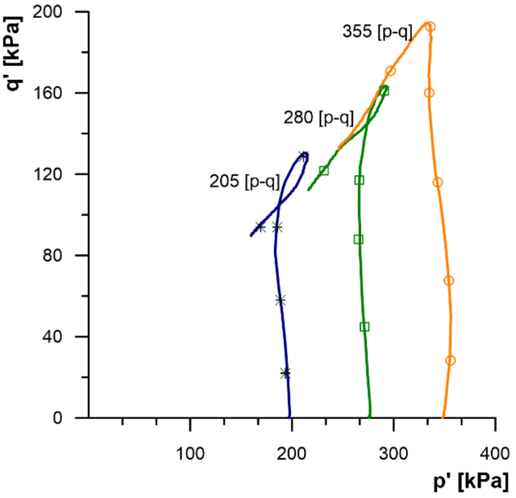

Figure 5.7. Stress paths (p'-q') plots for OM1a1, 2, 3.

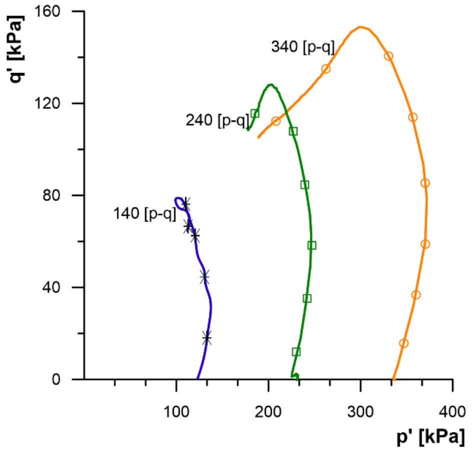

Figure 5.8. Stress paths (p'-q') plots for OM1b1 (140 kPa), 2 (240 kPa) and 3 (340 kPa).

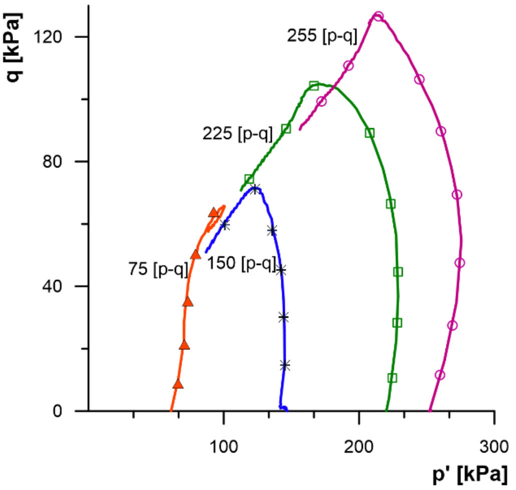

Figure 5.9. Stress paths (p'-q') plots for M1a (75 kPa), b (150 kPa), c (225 kPa), d (255 kPa).

before failure at peak deviator stress. This effect is more pronounced at greater confining pressures, and is seen in OM1a3, OM1b2, 3 and M1b, c and d (**Figures 5.7, 5.8** and **5.9**).

5.5.5 Mohr-Coloumb failure criterion

The Mohr-Coulomb failure criterion (British Standard BS1377 1990) was used to determine the peak effective cohesion (c') and peak effective friction angle (φ') for M1 and OM1. Mohr circles representing different consolidation stresses are presented on the same axes (**Appendix 5.5.5).** A line tangential to the Mohr circles is used to obtain the effective friction angle (φ') or the angle between then tangent and the x-axis, and effective cohesion (c'), which is the y-intercept of the tangent (Briaud, 2013). Mohr circle plots are presented in **Appendix 5.5.5**, and a summary of friction angle and cohesion at failure for M1 and OM1 is presented in **Table 5.8**. OM1 has a higher cohesion and lower friction angle in comparison to M1.

Table 5.8. Effective friction and cohesion of OM1 and M1 samples

Sample	Effective cohesion (c')	Effective friction angle (φ')
OM1a/b (average)	26	31
M1 a-d	17	32

5.6 Post triaxial test sample condition

Photos of the failed sample and sketches of exterior deformation are presented in order of least – highest confining stress (kPa). The post failure sample condition of the sample is suggestive of what kinds of deformation contribute to failure (Selby, 1993). OM1b1 is not presented because the triaxial machine did not automatically stop compression at 20% strain like other tests, leaving the failed sample too compressed to asses failed condition.

Four modes of failure were used to characterise each sample in this study, based on those outlined in Selby (1993). Shear failure (a) (**Figure 5.10**), wedge failure (b), intermediate failure (c) and barrel failure (d). Shear failure, where the specimen has failed at an angle on a single sliding plane, is indicative of brittle deformation. Brittle to ductile deformation can result in wedge failure, where two sliding planes intersect each other at an approximate perpendicular angles (**Figure 5.10**b) (Selby, 1993). Ductile deformation results in either a combination of shear and barrel shape, referred to herein as intermediate (**Figure 5.10**c). Ductile deformation may result in barrel failure, where the sides of the sample bulge evenly outwards (**Figure 5.10**d).

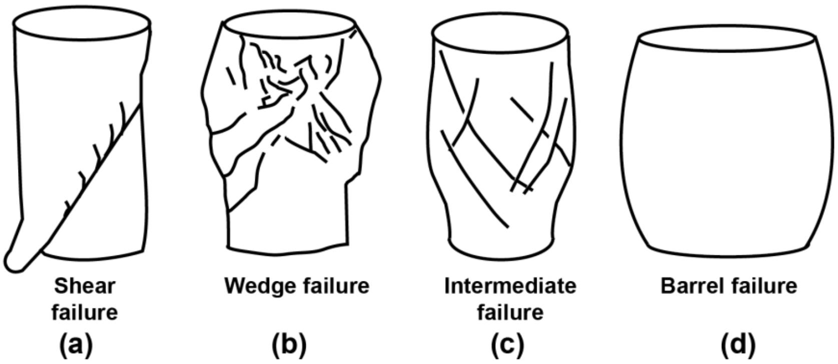

Figure 5.10. Different modes of failure that can occur under triaxial testing (adapted from Selby, 1993).

Brittle and brittle-ductile deformation may result in shear zones which accommodate most of the deformations, called *Principal shear zones*, herein referred to as PSZ’s (Gylland *et al.* 2013c). *Secondary shear zones (SSZ’s)* are shear zones that accommodate less deformation than the PSZ. *Minor shears* are shear structures associated with the PSZ and SSZ but with generally shallower orientations in comparison with the PSZ. Inclination, spacing, and thickness of both the PSZ, SSZ and minor shears are described.

The legend for **Figure 5.12**-**Figure 5.20** is presented in **Figure 5.11**. In the images of failed samples presented the black outline represents the final deformed shape of the sample. The dark grey shaded regions outline the primary shear zones (PSZ), while light grey regions are secondary shear zones (SSZ). Orientation angles shaded black are the average angle of the adjacent PSZ, while yellow orientation angles denote the angle of minor shears adjacent to the label. Labels A, B, C and D show the different sides of the failed specimen.

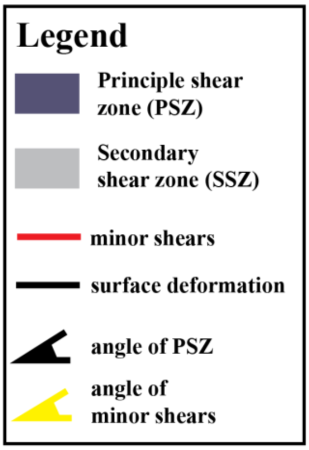

Figure 5.11. The legend for failed pictures of triaxial samples.

5.1.1 OM1

Wedge, shear and intermediate failure modes occurred for OM1a and OM1b. OM1a1 (**Figure 5.12**) appears to have failed along a single PSZ, which starts at 1.5 cm below the top of the sample, and bisects the sample at an angle of 50-70°. Limited deformation of the non-sheared portion indicates deformation was largely confined to the PSZ. The close spacing of minor shears and thinner PSZ in the upper half of the shear zone in comparison to the lower half indicate that the upper half is more highly sheared than the lower half. Within this top portion of the shear zone, minor shears are short (< 10 mm) and decrease clockwise in orientation from 50° to 35°. The shear zone is estimated to be 2 mm thick at the top, widening to 15 mm thickness at the base. Towards the base of the sample, minor shears are not visible and the thickness of the shear zone increases, showing that strain in the PSZ becomes less localised (**Figure 5.12**).

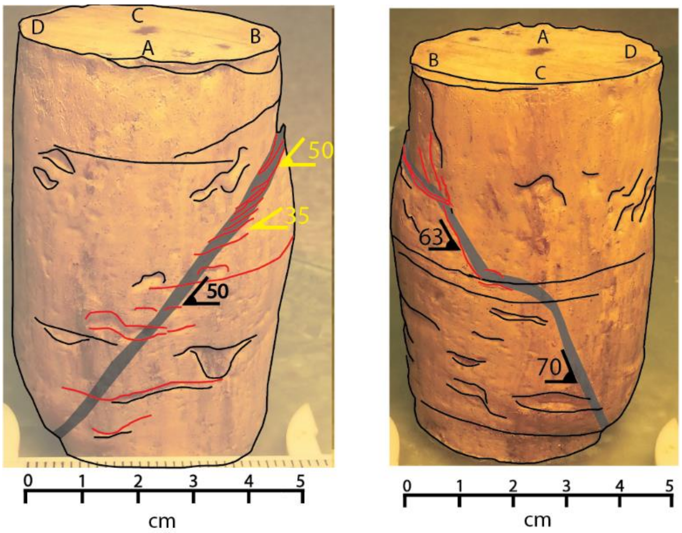

Figure 5.12. The failed triaxial specimen OM1a1, tested at 205 kPa confining pressure.

OM1b2 (**Figure 5.13**) failed primarily on a single PSZ which extends from the top to bottom of the sample. Minor wedge shear development was observed on the sheared block. The orientation of the PSZ decreases from 68° to 45° from top to bottom, while the estimated width of the PSZ is 3 mm at the top, 12 mm in the centre, and 5 mm at the base. Minor shears, like those observed in OM1a1 were present throughout the shear zone length. Some of these shears are long (30 – 40 mm), extending into the matrix of the sample, but the majority of minor shears are short (10 – 20 mm) and confined to the PSZ. Orientation of these minor shears shallowed from 48° at the top of the shear zone to 15° at the bottom (**Figure 5.13**).

OM1a2 (**Figure 5.14**) failed primarily on a PSZ at an estimated angle of 60-68^{o}, shallowing to 45^{o} at the base of the shear zone. Several minor shears were

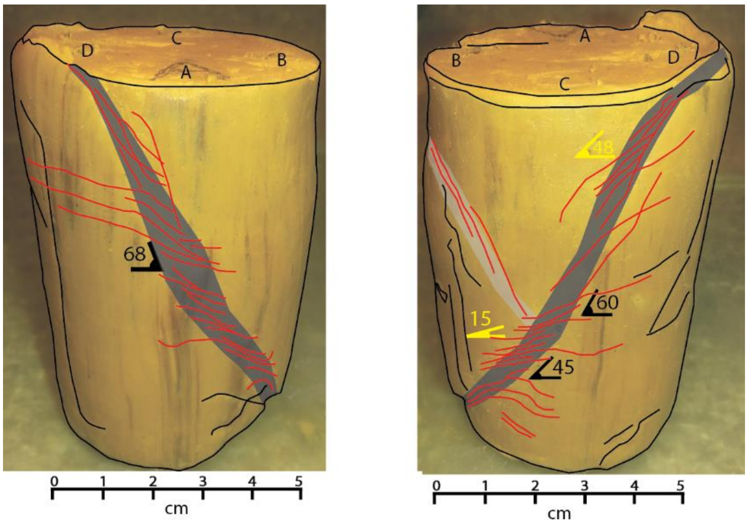

Figure 5.13. The failed triaxial specimen OM1b2, tested at 240 kPa confining pressure.

visible which suggest wedge development outside of the PSZ (red lines in top right of side D, **Figure 5.14**). A SSZ (grey shading, side C-D, **Figure 5.14**) associated with the PSZ is 4-5 mm thick, oriented at 70º and has minor shears oriented at 60º. On side A the PSZ is thicker (8-10 mm), than the PSZ on side C (2 mm). The PSZ on side A starts 19 mm below the top of the sample and cut through the middle of the bottom of the sample. Minor shears observed within the PSZ on side A are long at the top (20-30 mm), short in the middle (10 mm), and and long again at the base (20-30 mm). Minor shears decrease clockwise in orientation from top (67°) to bottom (30°) of the PSZ on side A.

OM1b3 (**Figure 5.15**) does not have distinct PSZ, but rather a more chaotic pattern of deformation. The failure appears to be intermediary between wedge and shear. On side A, a double banded shear feature is prominent, while on the other side the shear zones appear to intersect each other, more similar to a wedge failure. The shear zones on side A are inclined at 58º, and thickness is between 2-5 mm. Some minor shears are observed, but are much less uniformly distributed around the shear zones in comparison with minor shears in OM1a2, OM1b2 and OM1a1. The upper half of the specimen also appears to have accommodated most of the deformation by slightly bulging outwards, while the bottom has remained more or less a cylindrical shape.

A chaotic pattern of shear zones is also evident for OM1a3 (**Figure 5.16**), with shearing tending towards wedge failure, with two PSZ's trending from the top of B to the bottom of D, and one zone trending from the top of A to the bottom of B (**Figure 5.16**).

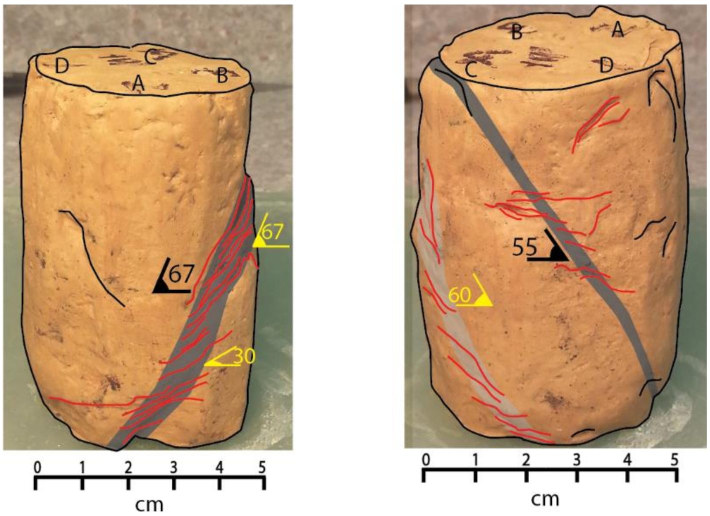

Figure 5.14. The failed triaxial specimen OM1a2, tested at 280 kPa confining pressure.

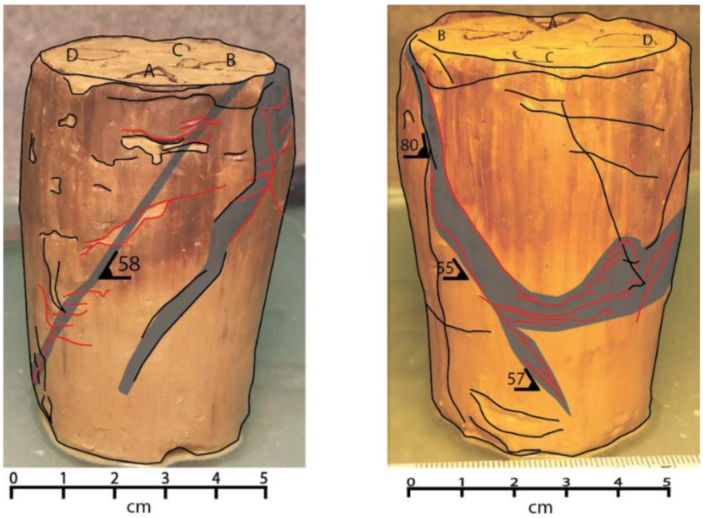

Figure 5.15. The failed triaxial specimen OM1b3, tested at 340 kPa confining pressure.

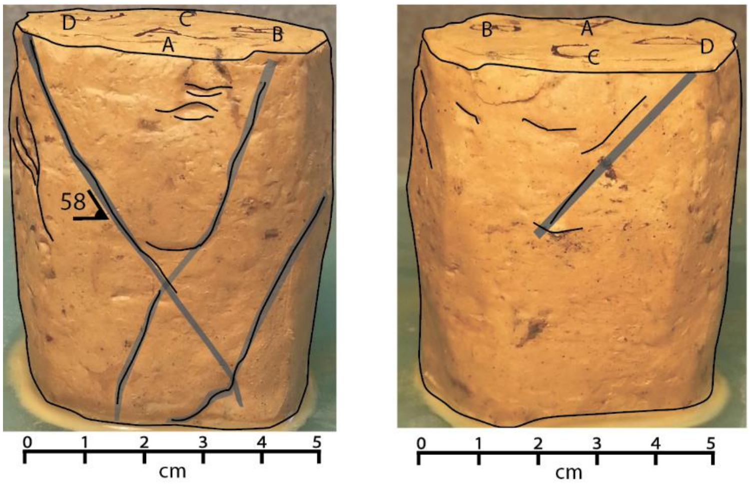

Figure 5.16. The failed triaxial specimen OM1a3, tested at 355 kPa confining pressure.

The angle between these shear zones is approximately 60°. No minor shears within the shear zones were observed. The thickness of these zones is 1-2 mm.

5.6.1 M1

M1a displayed mainly barrel type failure (**Figure 5.17**), and to a lesser degree, shear failure, with two shallow angled zones (35°), approximately 15 – 20 mm thick. Minor shears are evident in these zones, but are longer (15 - 40 mm) than minor shears in other samples. The shear zones are evidence for weakly concentrated zones of deformation, however are not prominent enough to classify the dominant failure as shear rather than barrel.

M1b (**Figure 5.18**) displayed a complex deformation pattern, most like a wedge failure, with two antithetic PSZ's, one from the top of B to the middle of A, and one from the top of D to bottom of B (**Figure 5.18**). D-B shear begins at the top of the sample, is inclined at 70° and is associated with a secondary shear zone (SSZ) (light grey shading). The other shear begins part way down the sample, bisecting the major shear. Minor shears associated with these PSZ's are approximately 10 – 40 mm long. These shear zones do not penetrate right through to the other side of the sample, where a horizontal pattern of minor shears is evident on the surface. Overall, deformation is not entirely concentrated within shear zones; global deformation, or deformation over much of the sample is evident.

Deformation in M1c (**Figure 5.19**) has been expressed as a vague wedge failure, however the sample has clearly been globally affected so that deformation is not confined explicitly to shear zones. Two PSZ's were identified based on minor shear concentration and tracing this zone to offset on the exterior of the sample. One PSZ extends from the top of B to the bottom of D, and the other is antithetic, extending from near the top of D to the bottom of B. D-B shear zone is inclined at 67-68°, while B-D shear zone is inclined at a shallower 50º. The D-B PSZ is a continuous feature on both sides of the sample, whereas the B-D PSZ is not obvious on the other side of the sample (**Figure 5.19**). The surface offset at the top of the steeper shear zone shows that deformation has been most concentrated in this zone. Minor shears within this main shear zone decrease in inclination from 67° to 25°, and range between 20 – 30 mm long.

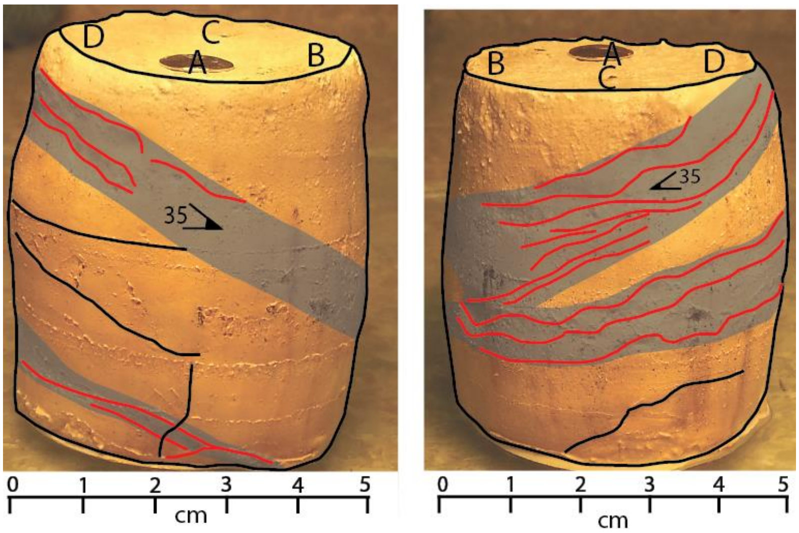

Figure 5.17. The failed triaxial specimen M1a, tested at 275 kPa confining pressure.

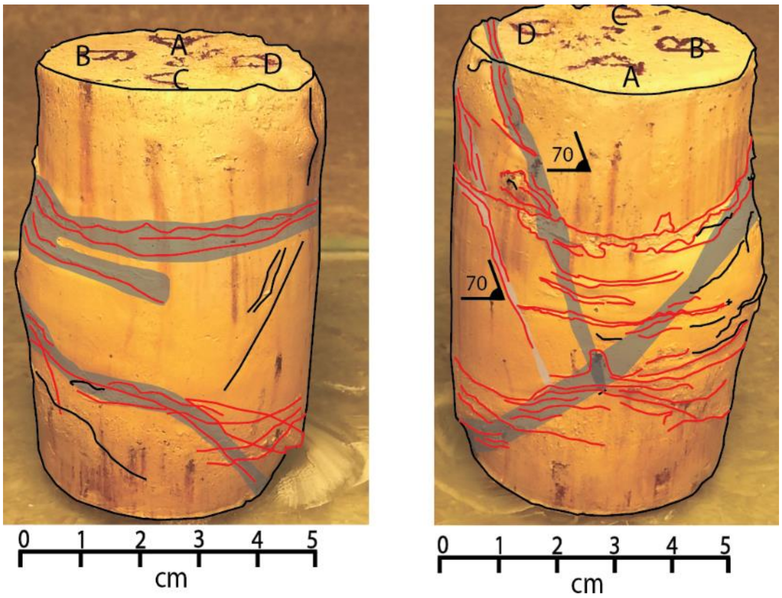

Figure 5.18. The failed triaxial specimen M1b, tested at 150 kPa confining pressure.

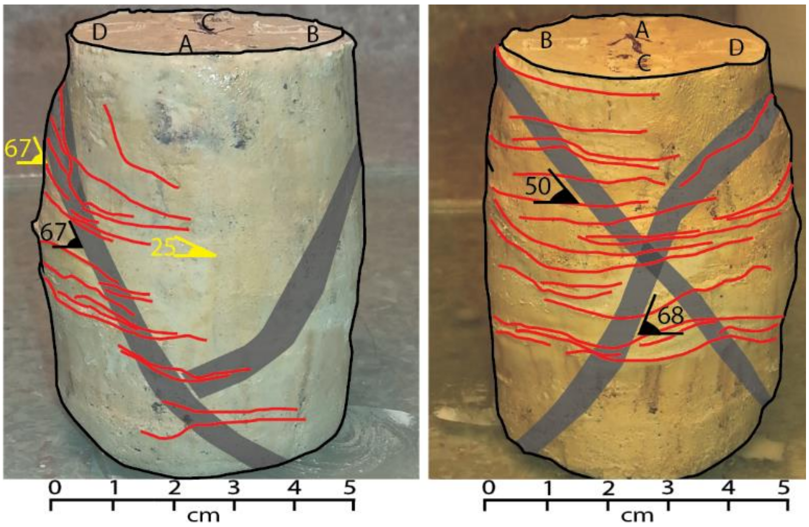

Figure 5.19. The failed triaxial specimen M1c, tested at 225 kPa confining pressure.

M1d (**Figure 5.20**) specimen appears to have failed at the boundary between a sandy clay (top) and silty clay (bottom). Deformation is most concentrated in a PSZ approximately 8 – 12 mm thick and horizontally aligned on the silty clay side of the material boundary. The lower material is a silty clay, and appears to have slightly bulged outwards, while the sandy clay material in the upper half is still largely cylindrical. Minor shears align roughly horizontally with the PSZ, and are between 15 – 50 mm in length.

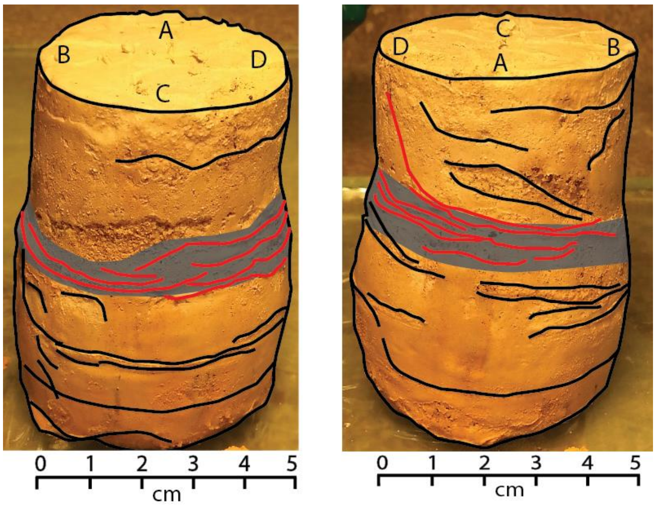

Figure 5.20. The failed triaxial specimen M1d, tested at 255 kPa confining pressure.

5.7 Geomechanical properties summary

This chapter presents the geomechanical properties for two extra-sensitive materials. Standard geomechanical properties presented in sections 5.2 – 5.4 are summarised in **Table 5.9**. Both Omokoroa (OM1) and Matua (M1) samples have high porosities and void ratios, high moisture content, and low wet bulk density. Both samples had clay dominant particle size fractions, with minor fractions comprised of silt (OM1), and sand and silt (M1). Both Omokoroa and Matua samples had high liquid and plastic limits, low activity, and plotted below the A-line on the plasticity chart. The combination of these indices has been widely reported for volcanic ash soils in both New Zealand (Keam, 2008; Wyatt, 2009; Arthurs, 2010, Cunningham, 2012) and Indonesia (Wesley, 1973 & 1977).

Triaxial characteristics and post sample shear characteristics are summarised in **Table 5.10**. All samples failed at less than 5% strain. M1 and OM1a/b deviator stress vs axial strain plots were similar in that they both had initial regions of rapid strain hardening, followed by a peak, then variable strain softening regions. Peak deviator stress, peak curvature and amount of strain softening generally increased with higher effective confining pressures for both materials. At higher effective confining pressures, pore pressure rose after peak deviator stress, and the p'-q' plot trended left, indicating a contractive sample response at failure (OM1a2-3, OM1b1-3, M1b-d). At lower effective confining pressures, while strain softening still occurred, pore pressure dropped slightly after failure, and the p'-q' curves touched the CSL without trending strongly left or right, indicating initial sample contraction, but slight dilation after peak stress.

Matua material has a lower cohesive component (17) while Omokoroa material has a high cohesive component (26). Matua samples have a slightly greater friction angle than Omokoroa samples (32º and 31º respectively).

Failed triaxial samples unveiled information about how the samples deformed as a response to different confining pressures. Some element of shear – wedge development was observed in all samples, indicating brittle, contractive deformation governs deformation to a degree in both materials. Lower confining pressures resulted in less brittle deformation in M1a (OM1b1 was not able to be examined as it was over compressed by the triaxial machine after failure), which had a dominant barrel shape and minor shear development. The higher degree of strain softening did not strongly correlate to development of single shear zones. In samples with single shear zones, the sheared block displayed greater deformation than the non-sheared block (OM1a1/a2, OM1b2). The occurrence of sand lenses in Matua material appeared to control the position of the shear zone, with the silty clay adjacent the sand lense accommodating most of the deformation (M1d).

PSZ thickness did not bear obvious trends to the effective confining pressure, however the weakly developed PSZ's in M1a were much thicker (15 – 20 mm) than M1b, c (3 – 6 mm). Orientations of PSZ also do not bear an obvious relationship to effective confining pressure, however M1a does also have more shallow orientations than M1b, c, while M1d has a horizontal orientation, correlating to the position of the horizontal sand lense. The only SSZ to occur was in M1b. This SSZ had the same orientation to the PSZ but was slightly thinner. PSZ's in OM1 samples were generally thinner at the top and wider at the bottom, and the overall thickness decreased with increasing confining pressure. The angle of the PSZ decreased from top to bottom in OM1b2 and OM1a2, but stayed roughly even for other samples. Secondary shear zones were present in OM1 b2, OM1a2 and OM1a3. SSZ's were of similar orientations to the PSZ, and were thinner than PSZ's.

Minor shears, or shear structure associated with the PSZ are present in all samples except OM1a3. In M1 samples, the length of minor shears generally decreases when shearing is more concentrated in the PSZ. The orientation of minor shears decreases from the top to bottom of the PSZ in M1c, while the other samples (M1a, b, d) had more horizontal minor shears. Minor shear length in OM1 samples bore no correlation to effective confining pressure. Like M1c, orientation of minor shears decreases from top to bottom of the PSZ in OM1a1, OM1a2, and OM1a3.

Table 5.9. Summary of geomechanical properties including sample type and origin, density characteristics (w = wet bulk density, P_d = particle density, n = porosity, e = void ratio, St = sensitivity), particle size and density characteristics (P_s = particle density), Atterberg Limits, and activity (LL = liquid limit, PL = plastic limit, PI = plasticity index, LI = liquidity index).

		Density characteristics					**Particle size + density**				**Atterberg Limits**				
	Soil description, dominant clay mineral species, geological origin	***w*** **(%)**	**P_d (kgm^{-3})**	***n*** **(%)**	**e (%)**	**St (%)**	**P_s (kg m^3)**	**Clay (%)**	**Silt (%)**	**Sand (%)**	**LL %)**	**PL (%)**	**PI (%)**	**LI (%)**	**Activity (%)**
Omokoroa (OM1)	Extra-sensitive Silty CLAY, reworked tephra fall	72	1320 ± 50	70	2.3	15	2517	63	37	0	66	41	25	2.9	0.4
Matua (M1)	Extra-sensitive Silty CLAY with some sand, reworked tephra	64	1690 ± 100	65	1.8	10	2777	40	23	37	52	37	15	1.8	0.4

Table 5.10. Summary of triaxial characteristics (**$\varphi_{failure}$ =** friction angle at failure, **$c_{failure}$ =** cohesion at failure, **$q_{failure}$ =** deviator stress at failure**, $u_{failure}$ =** pore pressure at failure**, SS =** strain softening**)** and post triaxial sample characteristics **(l =** length**, w =** width **a =** angle).

		Triaxial features									Post failure sample shear features							
												PSZ(s)			SSZ		Minor shears	
Site	**Label**	**Effective confining pressure (kPa)**	**$\varphi'_{failure\,(°)}$**	**$c'_{failure}$ (%)**	**ε_{axial} at failure (kPa)**	**$q_{failure}$ (kPa)**	**$u_{failure}$ (kPa)**	**PWP response**	**SS (% $\sigma1 - \sigma3$)**	**Post-peak response**	**Failure mode (shape and deformation)**	**w (mm)**	**a (°)**	**a between PSZ's(°)**	**w (mm)**	**a (°)**	**l (mm)**	**a (°)**
Matua	M1a	75	33	17	2.2	131	27	Peak before failure then flatten out	13	Slight dilation	Barrel with slight shear development (ductile- brittle)	15 - 20	35	-	-	-	15 -40	35
	M1b	150			2.3	137	96	Peak after failure then slowly rise	29	Contraction	Shear – wedge (brittle)	D-B: 3-4 A-B: 4-6	DB: 70 A-B: 45	65	D-B: 1-2	D-B: 70	10 -40	Roughly horizontal (180)
	M1c	225			2.2	207	154	Peak after failure then slowly rise	33	Contraction	Shear – wedge (brittle)	B-D: 5 D-B: 5-6	B-D: 50 D-B: 67-68	62-63	-	-	20 -30	67 at top 25 at base
	M1d	255			4.4	250	168	Peak after failure then slowly rise	29	Contraction	Shear (brittle) at boundary of Silty CLAY and Clayey SAND	8-12	Horizontal (180)	-	-	-	15 -50	Horizontal (180)
Omokoroa	OM1b1	140	26	31	1.9	179	120	Peak after failure then slowly drop	14	Slight contraction	-	-	-	-	-	-	-	-
	OM1a1	205			3.1	265	462	Peak before failure, drop slightly then slowly rise	31	Contraction	Shear (brittle)	2 at top 15 at base	50-70	-	-	-	10	50 (top) decreasing to 35 (middle)
	OM1b2	240			3.2	246	156	Peak after failure then flatten	20	Contraction	Shear (brittle)	3 at top 12 middle 5 at base	68 at top 45 at bottom	-	4	60	10 -40	48 at top 15 at bottom

		Triaxial features									Post failure sample shear features							
												PSZ(s)			SSZ		Minor shears	
Site	Label	Effective confining pressure (kPa)	$\varphi'_{failure}$ (º)	$c'_{failure}$ (%)	ε_{axial} at failure (kPa)	$q_{failure}$ (kPa)	$u_{failure}$ (kPa)	PWP response	SS (% $\sigma1 - \sigma3$)	Post-peak response	Failure mode (shape and deformation)	w (mm)	a (º)	a between PSZ's(º)	w (mm)	a (º)	l (mm)	a (º)
	OM1a2	280			3.4	324	194	Peak before failure, drop slightly then slowly rise	32	Contraction	Shear (brittle)	1-2 varying to 8-10	60-68 at top 45 at bottom	-	4-5	70	20-30 at top, 10 middle, 20-30 at bottom	67 at top 30 at bottom
	OM1b3	340			2.0	299	192	Peak before failure then slowly rise	50	Contraction	Shear – wedge (intermediate)(brittle)	2-5	58	-	-	-	8-35	variable
	OM1a3	355			3.5	383	154	Rapidly peak before failure then slowly rise	32	Contraction	Shear- wedge (brittle)	D-B: 1-2 B-D: 1-2	D-B58 B-D58	66	B-D: 1	B-D: 58	-	-

CHAPTER 6

SHEAR ZONE MICROSTRUCTURE

6.1 Introduction

This chapter describes the microstructure of shear zones from failed triaxial specimens M1 and OM1b. Material characteristics and shear zone microstructures are analysed in thin section and Micro-CT. Thin section analysis of shear zones follows the model of Gylland *et al.* (2013c), who used polarised microscopy to analyse microstructural detail. Thin section techniques were applied to all shear zones, but not all were successful due to errors introduced during thin section methods, such as inadequate impregnation of soil with epoxy resin, or brittleness of material once dry. Seven thin sections captured shear zones from Omokoroa failed samples (240 & 340 kPa confining pressure) and Matua failed samples (150 & 255 kPa confining pressure).

Mini-plugs of shear zones from M1 (225 kPa) and OM1b (340 kPa) were scanned with a Bruker Skyscan 2000 Micro-CT at the University of Auckland. The entire shear zone of an OM1b specimen tested in a cyclic triaxial was captured by a Skyscan 1172 micro-CT at the University of Bremen, Germany. In thin section, shear zones were identified as distinct from surrounding material by particle reorientation within the shear zone and offset of strata and particles. In Micro-CT scans, shear zones were identified based on material density differences.

6.1.1 Shear zone microstructure terminology

Shear zone terminology in this chapter is based on the original work of Skempton (1966) who established terminology specific to rock failure at tectonic scales. Morgenstern & Tchalenko (1967) adapted this terminology when studying the evolution of shear bands in kaolinite under direct shear. Gylland *et al.* (2013c) later adapted Morgenstern & Tchalenko’s (1967) methods and terminology by examining the evolution of shear zones under triaxial compression on sensitive clays from Norway. Both latter studies used thin section techniques to analyse shear zone microstructure. Terminology henceforth is based on these studies.

Morgernstern & Tchalenko (1967) describe shear induced fabrics, or homogeneous fabrics separated by discontinuities by three terminologies: (1) ***kinematic***, (2) ***sequential***, and (3) ***mechanistic***.

Kinematic terminology refers to the structural features in the fabric. Two main types of discontinuities have been described: displacement discontinuities, and strain discontinuities (**Figure 6.1**). During elastic deformation, neither displacement or strain discontinuities exist (Morgenstern & Tchalenko, 1967), but since the elastic threshold is crossed after a very minimal application of stress for most soils (est. 10^{-5} volumetric strain, Nova, 2012), in most situations there is relative slippage between particles, creating some sort of discontinuity (Morgenstern & Tchalenko, 1967). The different types of discontinuities are outlined in **Figure 6.1**.

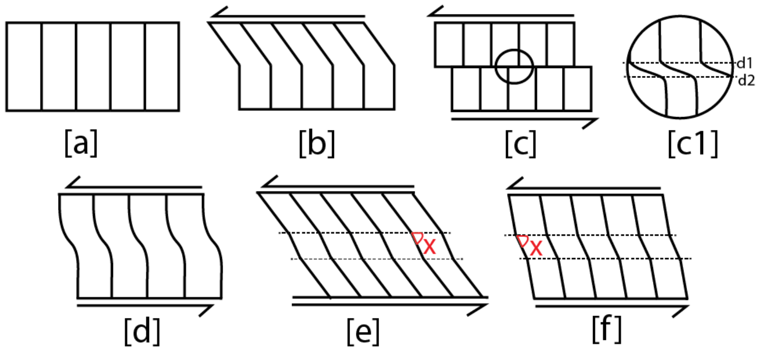

Figure 6.1. The different types of kink bands observed, adapted from Morgenstern & Tchalenko (1967). [a] is unstrained state, [b] is a strain discontinuity, [c] is a displacement continuity, with a zoomed in image revealing a more complex internal structure of the shear zone. [d] is a smooth shear band, where the boundaries of the discontinuities are curved rather than rigid. [e] and [f] are reverse and normal shear bands respectively. For normal shear bands, the internal acute angle (red X) decreases relative to the orientation of the shears, while for reverse shear bands, the internal acute angle increases (red X in e).

Sequential terminology refers to the order of presence of kinematic discontinuities. Notation such as S_1 for the shear zone as a whole, S_2 for the next feature to be observed S_3 for the next and so on (Morgenstern & Tchalenko, 1967). After high levels of strain, for example the sliding plane of a landslide, the first order shear is often referred to as the *principal displacement discontinuity* (PDS) (Morgenstern & Tchalenko, 1967). The main or dominant shear zone, whether or not high levels of strain have been reached, is called the *principal shear zone* (PSZ).

The **mechanistic** terminology relates a specific kinematic discontinuity to its respective orientation and the magnitude of stress acting on it. In undrained material, the Tresca failure criterion predicts that if there is zero volume change in the shear band, the overall angle of the shear is 45º (Briaud, 2013). In drained conditions, the orientation of the shear band is predicted to be at 45º + φ/2 to normal (**Figure 6.2**). Upon shearing in any type of material, several sets or types of shears are well documented to occur in specific patterns, however the sequential evolution of these shears is not well understood. The most accepted model is that antithetic Riedel shears (R and R') evolve early during the shearing process (**Figure 6.3**) (Skempton, 1966; Ahlgren, 2001). The orientation of Riedel shears is related to the friction angle (φ) of the material (**Figure 6.2**) (Skempton, 1966). This condition is only reliable if there is coaxility or equilibrium between stress and strain (Morgenstern & Tchalenko, 1967). Assuming coaxility, in drained conditions, idealised conjugate Riedel shears (R and R') are inclined at 45º ± φ/2, where φ is the friction angle of the material (Skempton, 1966 after Riedel, 1929). Synthetic thrust (P) shears, form later during shearing, and are causal in the development of the PDS shear, which is the final shear which accommodates all further shearing (Morgenstern & Tchalenko 1967; Gylland *et al.* 2013c). P shears are oriented at -45º + φ/2 (Skempton, 1966), and tension (T) shears, which are less reported

Bartlett *et al.* 1981) are oriented at 45º (**Figure 6.2**).

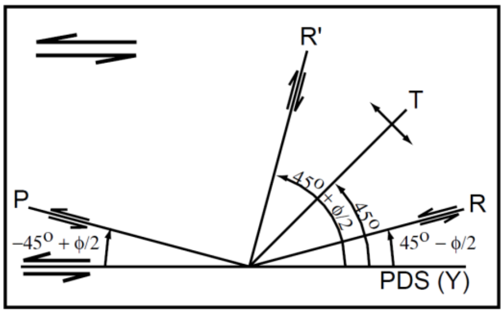

Figure 6.2. The relationship between the orientation of Riedel shears and thrust shears to the friction angle (φ) of the material (Ahlgren, 2001, after Skempton, 1966).

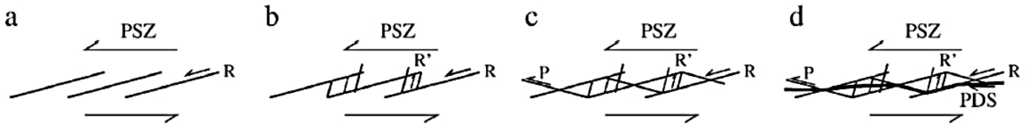

Figure 6.3. The theorised development of Riedel shears throughout the shearing process from [a] only R shears, to [b] R shears and R' shears, then P or thrust shears, which create the causal link for the PDS to develop.

Figure 6.4. Expected Riedel shear orientations for Matua (left).and Omokoroa (right) based on the friction angle of each material.

In reality, and also in the triaxial tests, variability in the angular relationships arise due to the strain rate variation, and changing stress states, which include pore pressure differences. Based on friction angles of 31° (Omokoroa) and 32° (Matua) expected orientations for Riedel shears are outlined in **Figure 6.4**.

6.2 Omokoroa thin sections

6.2.1 Component characteristics and overall structure

Component abundances and characteristics outlined in **Table 6.1** are visual estimates, i.e. no point counting was undertaken. The material is made up of approximately 95% groundmass and 5% coarse fraction. The groundmass is comprised of roughly 75 % clay minerals, and 23% silt sized (0.02 – 0.1 mm) highly weathered minerals. The high degree of weathering is indicated by marked orange colour of the material (Stoops, 2003). The small size and high degree of weathering of the silt sized minerals inhibited determination of mineral type. The only characteristic which proved these particles were minerals was their pleiochroic nature under cross-polarised light (Stoops, 2003).

Only limited classification of clay minerals is possible using optical microscopy techniques. In theory, phyllosilicates should have visible interference colours under cross-polarised light conditions, but their small size allows overlapping to occur so no individual grains are distinguishable (Stoops, 2003).

Table 6.1. Componentry of OS1 thin sections

Component	**Average size (mm)**	**Shape (-)**	**Abundance (%)**
Clay minerals	-	-	75
Silt minerals	< 0.05	-	23
Manganese	0.6	sub-rounded	rare
Ilmenite	0.025	platy-tabular	1
Magnetite	0.025	cubic	1
Lithics	0.4-0.6	sub-rounded	rare
Hypersthene	0.2	tabular	rare
Quartz	< 0.2	angular	rare

The only indication of clay type in thin section is the colour, which in this case a homogenous orange – red stained background indicates a dominance of weathered iron-oxide clay (Stoops, 2003). The fabric or overall structure of the material appears to have a vague horizontal alignment, but no distinct stratification was observed unlike Matua samples, where distinct horizontal stratification was observed.

6.2.2 OM1b2

6.2.2.1 Thin section location

Two thin sections captured the main shear zone observed in sample OM1b2, which was tested at 240 kPa effective confining pressure (**Figure 6.5**).

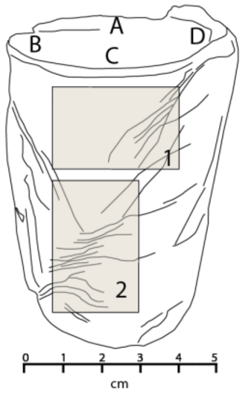

Figure 6.5. Locations of thin sections on the failed OM1b2 sample.

6.2.2.2 Shear zone microstructure

Thin section 1 (**Figure 6.6a**) has three PSZ’s. The overall amount of offset within the thin section is difficult to determine because of the homogeneity of the material, however on the exterior of the sample the offset is in the range of 3 – 4 mm. Shear zones A, B and C have orientations closest to the expected R shears (expected 29.5°, actual 15-20°). Only one R’ shears is observed (orientation 90°). Several shears with orientations similar (expected -29.5°, actual -27° - -30°) to P shears are observed (blue shears in **Figure 6.6a**). Drying cracks were differentiated from shears based on the fact that they did not alter the fabric or displace material. Shear zone A is most prominent, with thicker (0.5 – 1.0 mm) more distinct zones of material reorientation than shear zones B and C. Shear zone A has several branches which converge towards the base of the thin section. Each shear zone is distinct from the surrounding matrix with a well-defined boundary, which varies between straight edged and undulating (**Figure 6.6b**). Within the shear zone small black minerals are aligned in the direction of shear. A weathered mineral domain has caused divergence of a single shear zone at the base of shear zone A (**Figure 6.6a**).

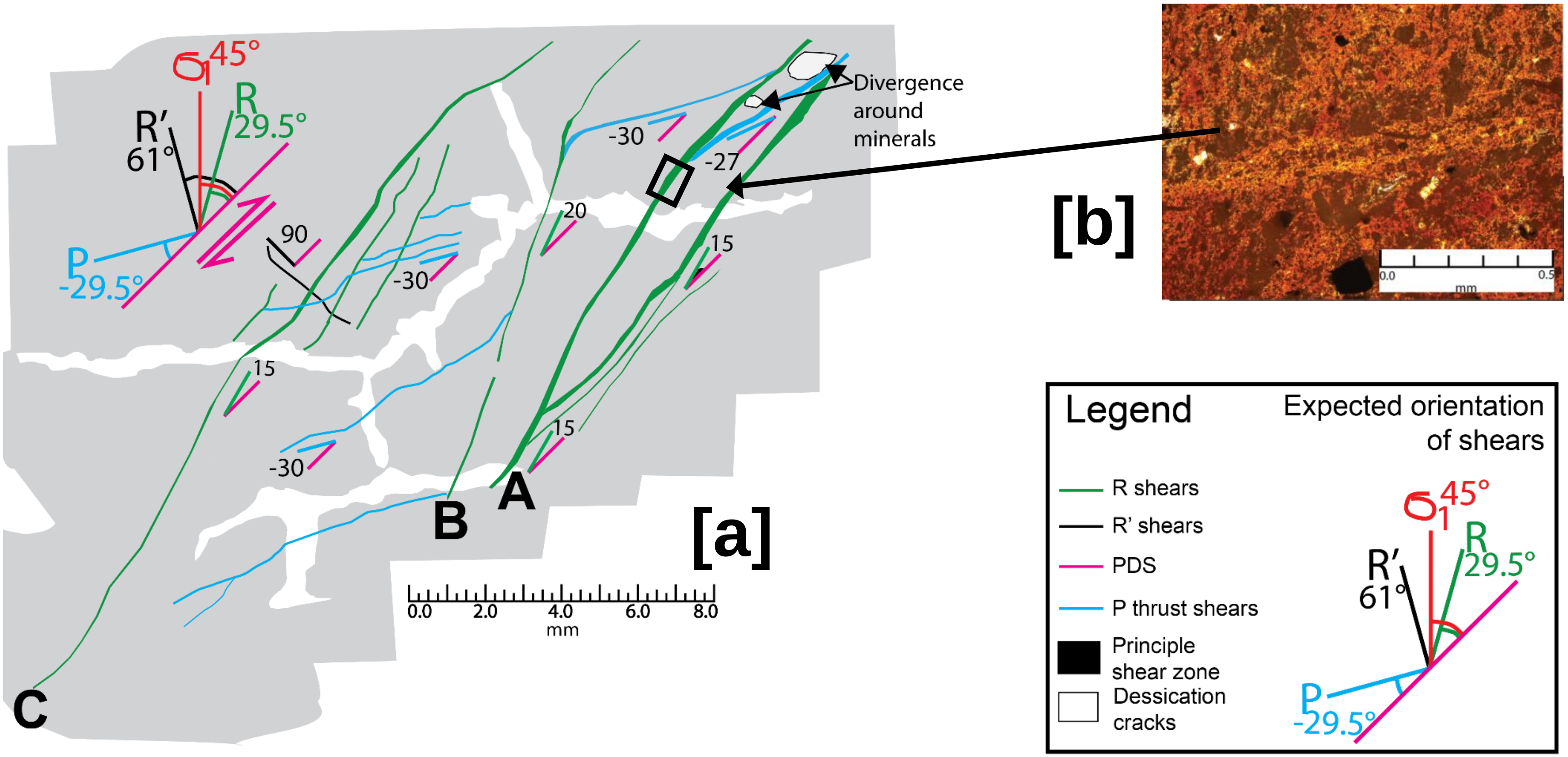

Figure 6.6. [a] Shears observed in thin section 1 at 2.5x magnification. Three PSZ's are observed (A, B, C labels). R shears are shaded green, R' shears are shaded black, P shears are shaded blue. Shear zone orientations with respect to the PDS orientation (pink shading) are included. R shears are spaced intertwine and are spaced closer together, and P shears are more prominent, in comparison to the bottom of the same shear zone (thin section 2), where R shears are spaced further apart, and P shears are less common. [b] is a zoomed in region in the black box, showing an undulating edge of the PSZ.

Shear zone B (middle) and C (left) are thinner (0.25 – 0.5mm) and less distinct, while still continuous features (**Figure 6.6**) in comparison with shear zone A. Shear zone B is thinner at the top (0.05 mm) than the bottom, where it thickens slightly towards the base (0.1 mm). Shear zone C is a continuous feature, however is thinner (0.025 – 0.05) than shear zone B and little mineral realignment is observed. In shear zone B, R shears are roughly 0.1 mm thick, and have orientations around 15° difference to the expected PSZ inclination.

Shears observed in thin section 2 include sets of shears inclined at broadly similar orientations as expected, including R, R’ and P shears (**Figure 6.7**). R shears are the most consistent, with 2 shears spaced at 10 – 15 mm, and inclined at 10 - 15° (A and C) spanning the width of the thin section. R’ shears are less numerous, are oriented 75 - 95° (compared with the expected 61°), and are spaced between 5.5 and 10.0 mm apart. Several possible P shears occur between pronounced R shears, with thicknesses of 0.05 – 0.1 mm, spacing of 2 – 4mm and orientations of -30 - -52° (expected -29.5). Three major PSZ’s where shears are most concentrated were observed, labelled A, B and C. Shear zone A seems to have accommodated most shearing, due to its thickness and high concentration of associated shears. Shearing is less concentrated in the top right section of shear zone A, with several branches diverging, and a wide zone of associated material reorientation. Deformation then concentrates into an intertwining shear zone. Higher light attenuation in some regions within the shear zone show a gradient of deformation within the shear zone i.e. some regions are more highly sheared than others (brighter and less bright regions in shear zone A, **Figure 6.7b & c**). Shear zone A does not appear to offset a weathered mineral domain (outlined in orange). The weathered mineral domain diffuses shear zone A from a clear zone to singular R shears spaced 0.2 – 0.5 mm apart.

Shear zone B is spaced 120 mm above shear zone A. The shear zone is defined by several shears oriented at P thrust shear orientations (-30°) associated with several R’ shears oriented at 75°.

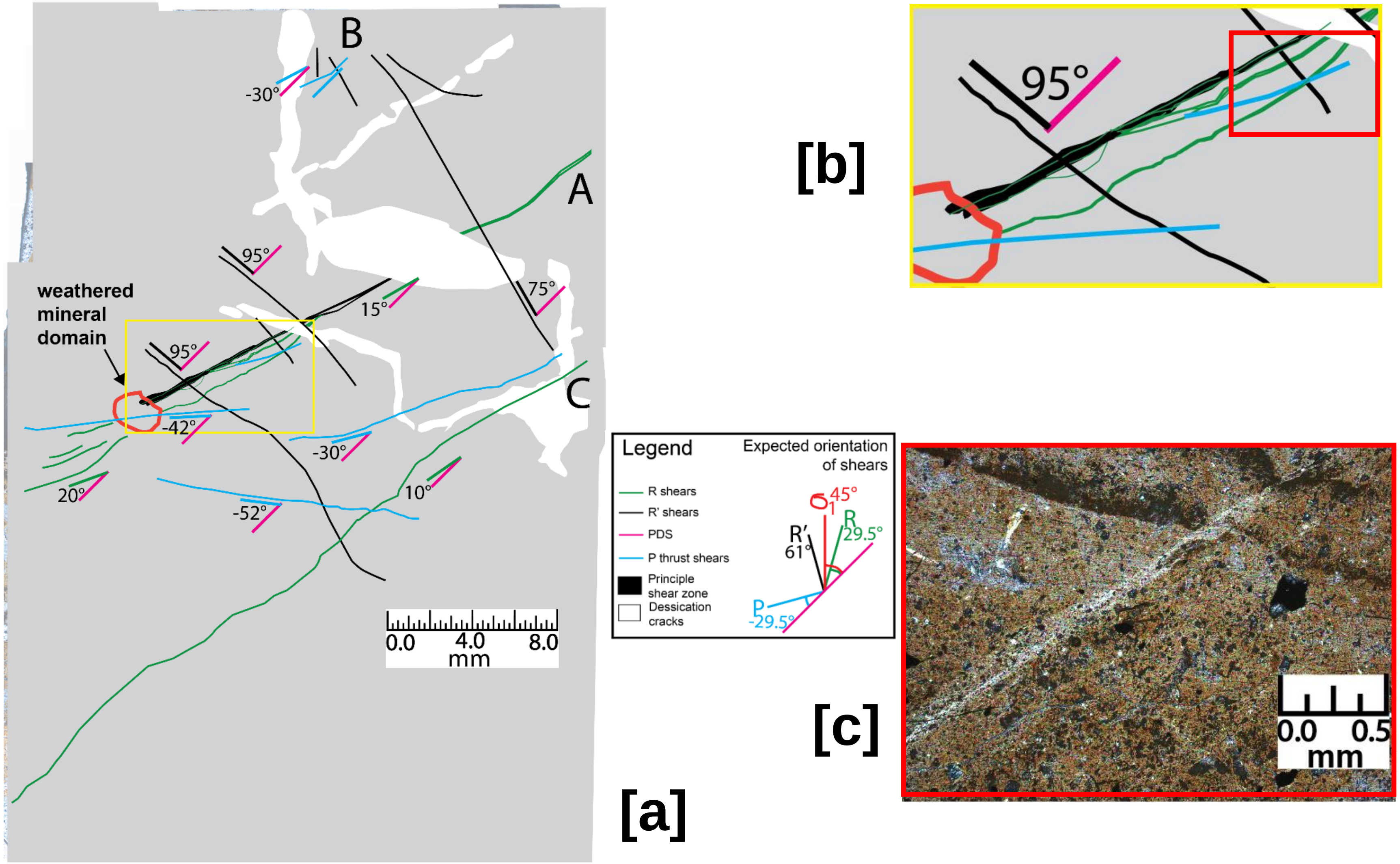
B
-30°
A
weathered
mineral
domain
95°
15°
75°
95°
-42°
C
-30°
20°
-52°
10°
0.0
4.0
8.0
mm
[a]
[b]
95°
Legend
Expected orientation
of shears
R shears
R' shears
PDS
P thrust shears
Principle
shear zone
Dessication
cracks
σ1 45°
R′ 61°
R 29.5°
P -29.5°
[c]
0.0
0.5
mm

Figure 6.7. [a] Shears observed in thin section 2 (OM1b2) and their measured orientations, compared with expected orientations (outlined in the legend) at 2.5x magnification. The three PSZ's are outlined as A, B and C. R shears are spaced further apart, P shears are less prominent, and R' shears are visible, in comparison to thin section 1.The yellow outlined box [b] is the region outlined by the yellow box in Figure 6.7c [c] shows the shear zone at 5x magnification. Variation of light intensity can be seen within the shear zone indicating some zones are more highly sheared than others.

6.2.3 OM2b3

6.2.3.1 Thin section locations

Figure 6.8 shows the locations of three thin sections prepared for sample OM2b3, which was tested at 340 kPa effective confining pressure.

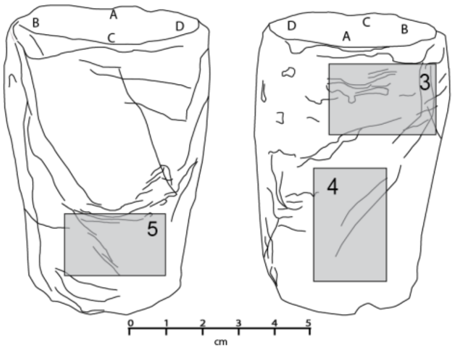

Figure 6.8. The location of thin sections on the failed OM2b3.

6.2.3.2 Shear zone microstructure

Three shear zones are visible in thin section 3 (A, B, C) (**Figure 6.9**). All three zones are inclined at orientations most close to expected orientation of R shears (10 - 20° observed, 29.5° expected). Shear zone A is the most prominent shear zone, inclined at a relatively consistent angle of 10°, and ranging between 0.1-0.25 mm thickness on average, with the exception of a thickened region surrounding a clay coated weathered mineral. Here, the weathered mineral domain has resulted in divergence of the shear zone, with the majority of shearing concentrated on the right side. Shear zone A branches into several minor shears at the top, including short (1 mm) shears oriented at 30° i.e. P shears, and 1 occurrence of an R' oriented shear. Clay coated minerals have been sheared at the base of shear zone A.

Shear zones B and C are 0.1 mm thick, spaced 1.8 mm apart, and are spaced 10 mm from shear zone A. The difference between plane and cross polarised light shows a high concentration of silt to clay-sized weathered minerals (bright coloured specks) reoriented along these shear zones (**Figure 6.9b and c**), and also how R shears diverge around a clay coated mineral.

Thin section 4 (**Figure 6.10**) has three shear zones oriented at 30 - 40°, classifying them as likely R shears. Shear zone A is the most prominent, with thickened (0.5 – 1.0 mm) zones of particle reorientation. Shear zone A branches into several shears near the top of the thin section, where some small (0.75 – 1.0 mm) long R shears cross the shear zone, but other than this shear zone A appears to be unrelated to other shears. A clay coated augite crystal aligned within shear zone A is seen in **Figure 6.10b**. Shear zone B is spaced 8 – 9 mm to the left of shear zone A. Shear zones B and C are spaced 0.75 – 1.75 mm apart, are thin (<0.25 mm), and are connected by a single shear. The inclination of shear zone B increases from 46° to 80°, whereas shear zone C is consistently 80°. Overall, the inclination of shear zones has increased from thin section 3 to thin section 4 i.e. from top to bottom of the sample.

Two major shear zones (A & B), spaced 4 – 4.5 mm apart were observed in thin section 5 (**Figure 6.11a**). Both shears are oriented nearest the expected orientation for R shears. The degree of particle reorientation is thicker in shear zone B is greater than shear zone A. Shear zone A has offset clay minerals, however there is less particle reorientation. Both shear zones are less than 0.25 mm thick. Several other R shears coalesce around the centre of shear zone A (**Figure 6.11b**). One R’ shear, oriented at 90° difference to R shears, links shear zones A and B together.

6.3 Matua thin sections

6.3.1 Component characteristics

Identification of minerals in M1 thin sections was hampered by the fact that sand and silt sized particles were highly weathered, as shown by the highly fractured particles. The top third of the thin section is comprised of sandy clay. Below this is a silt lens (1 – 6 mm thick), and below this, comprising most of the thin section, is a silty clay.

Within the sandy clay, I believe that most of the sand sized particles are made up of highly weathered sub-angular to angular quartz and feldspars as well as rare sub-rounded ilmenite and magnetite (**Figures 6.12 & 6.13**). Rare sub-angular to angular, sand sized plagioclase crystals are identified. Some particles are so weathered that they appear to be hollow (**Figure 6.13**). The sand to silt sized particles are largely suspended in a clay groundmass. Several bands of approximately horizontal orange-red hematite occur in both the sandy clay and silty clay fractions. Hematite, which is evidence of oxidation and weathering, is also

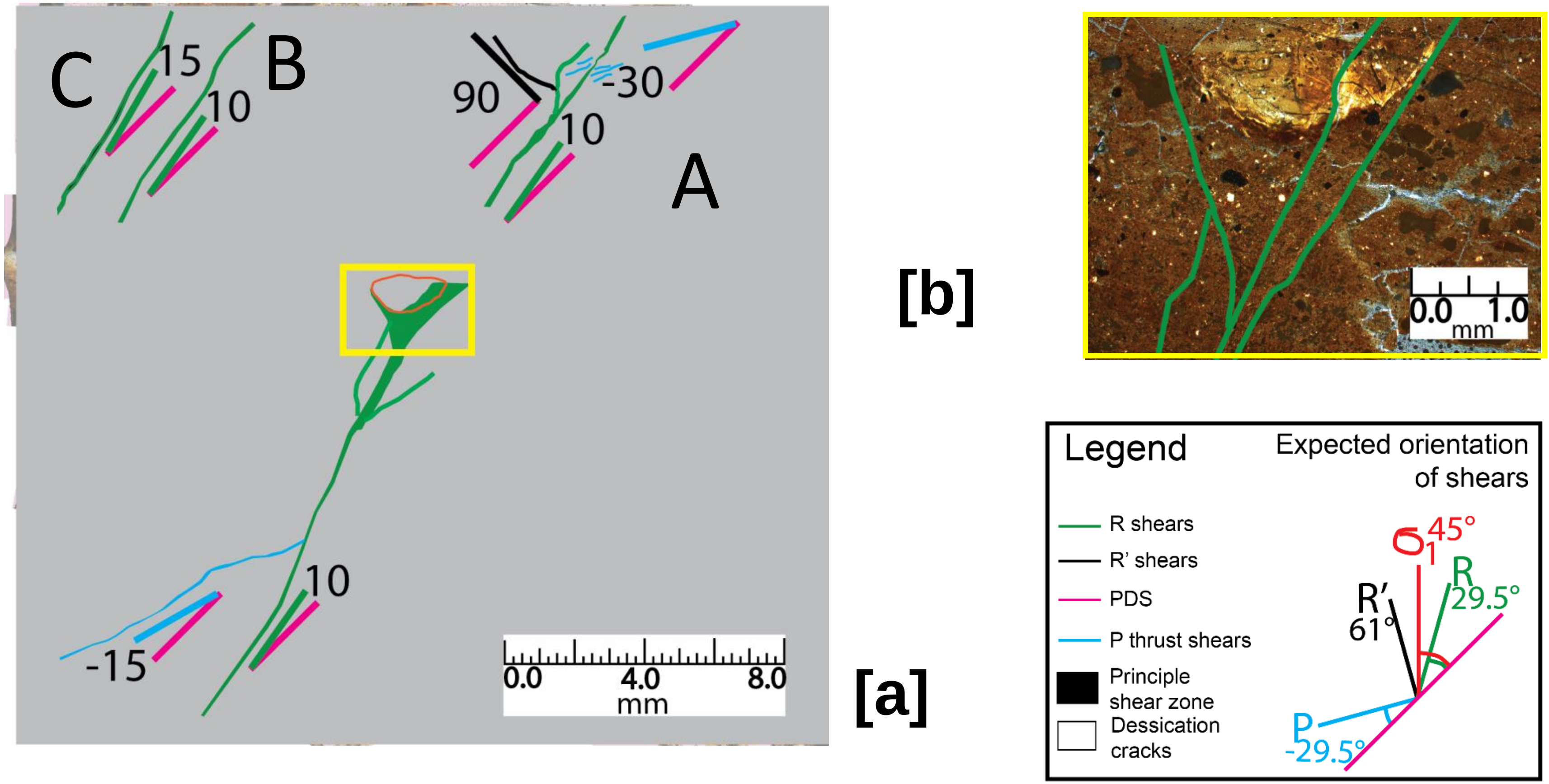

Figure 6.9. Thin section 3: [a] Shears observed in thin section 3 (top OM1b3, side A) and their measured orientations, compared with expected orientations (outlined in the legend) (2.5x magnification). The three PSZ's are outlined as A, B and C. [b] shows where shear zone A diverges and partly bisects a clay coated mineral domain.

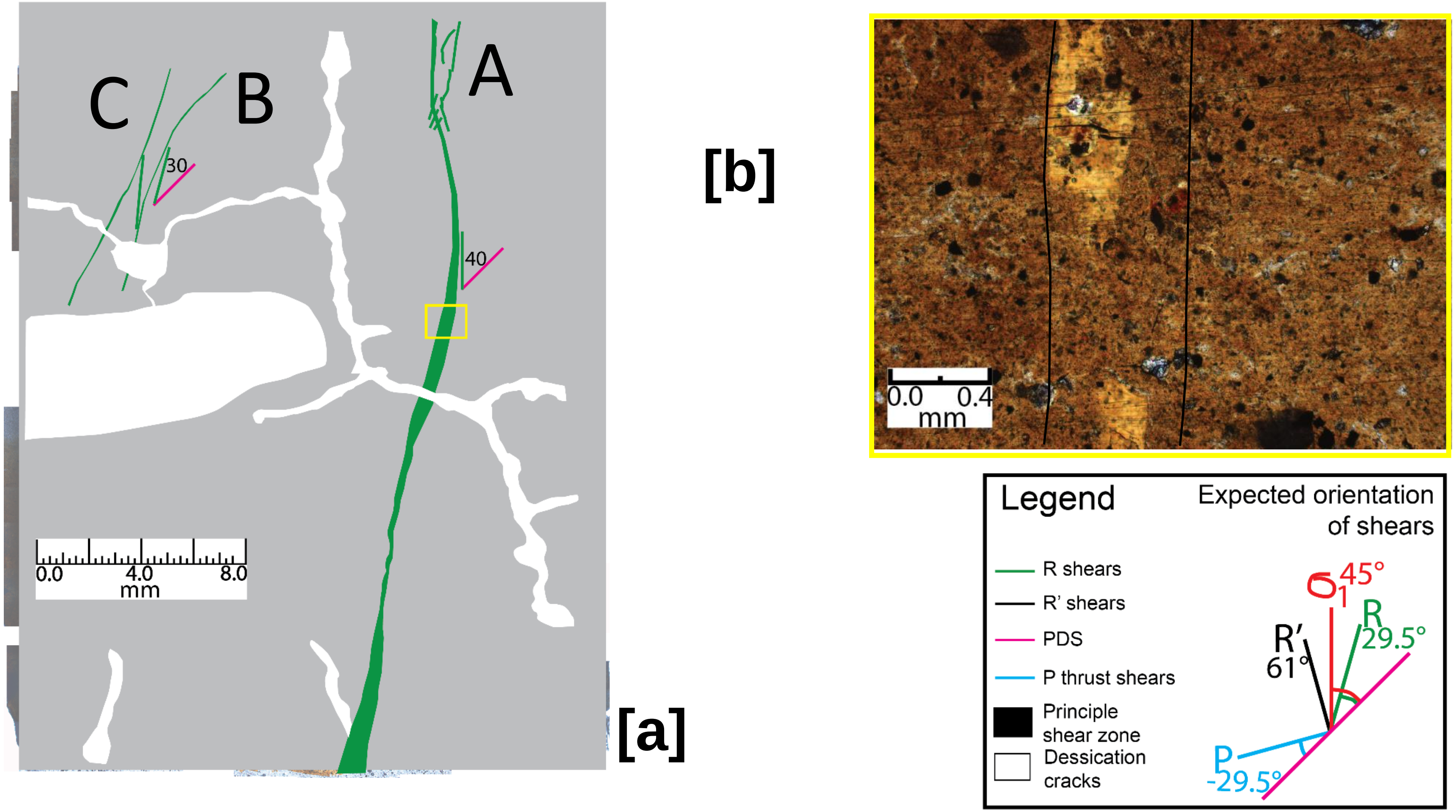

Figure 6.10. [a] Shears observed in thin section 4 (top of OM1b3) and their measured orientations, compared with expected orientations (outlined in the legend). The three PSZ's are outlined as A, B and C. Figure 6.10 [b] shows where shear zone A has sheared a clay coated mineral.

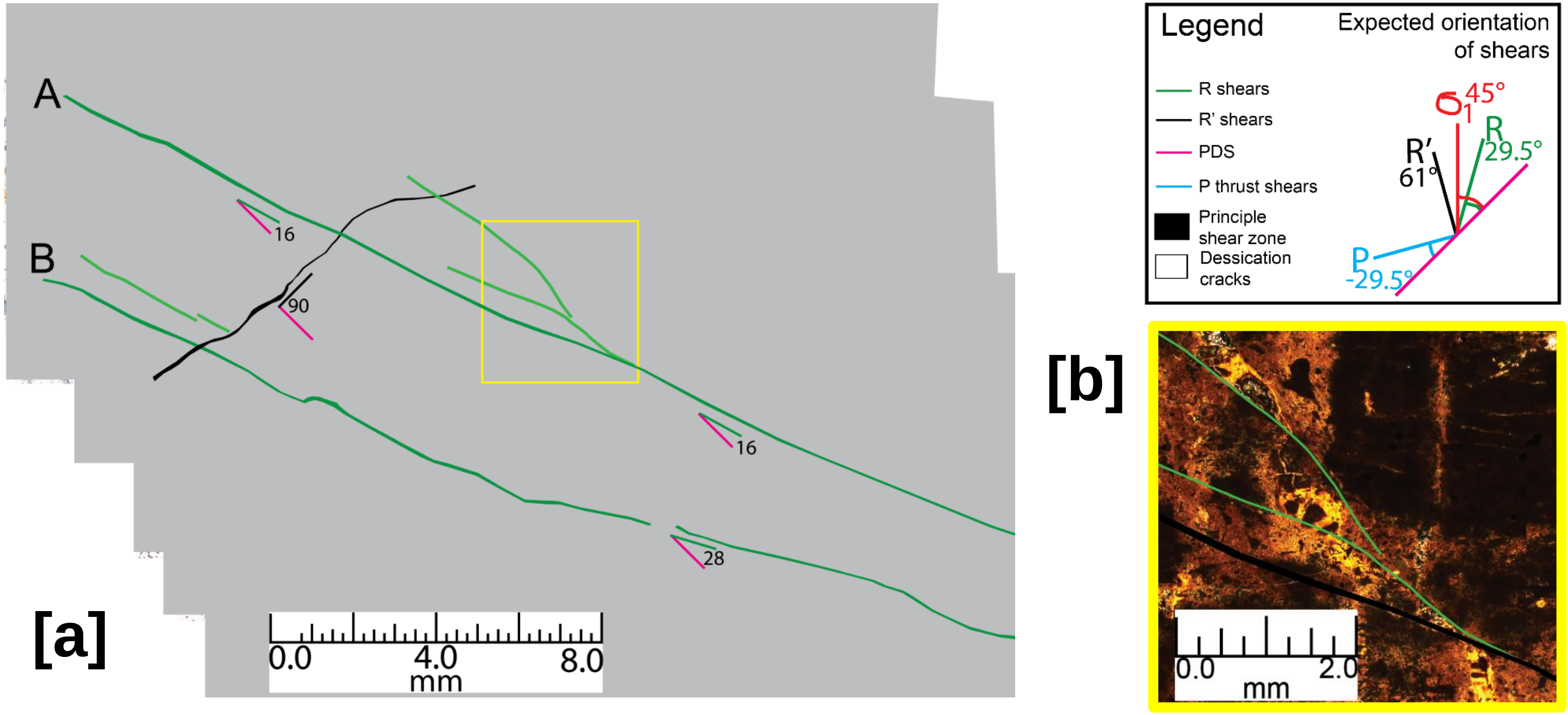

Figure 6.11. [a] Shears observed in thin section 5 (bottom of side D, OM1b3) and their measured orientations, compared with expected orientations (outlined in the legend). The two PSZ are outlined as A and B. A close up region of a sheared clay coated mineral is presented in Figure 6.11b.

present as a faint orange colour in the groundmass, as well as coatings on weathered minerals (**Figure 6.13**).

Colour is said to give an indication of the type of clay mineral (Stoops, 2003). In this instance, the pink – grey – orange colour of groundmass material indicates feldspathic to iron oxide composition. The material is aligned in a rough unistrial fabric (clay minerals are aligned roughly in one direction - horizontal) (Stoops, 2003). Voids, which are shown as spaces occupied by the colour and texture of the glue used to prepare the thin section, are rare, therefore the porosity of the material must be of the clay sized scale. Any aggregation that may have existed was probably destroyed during triaxial compression. Small black amorphous particles that broadly overlay the silty clay are probably isotropic clays (**Figures 6.12 & 6.13**) (Stoops, 2003).

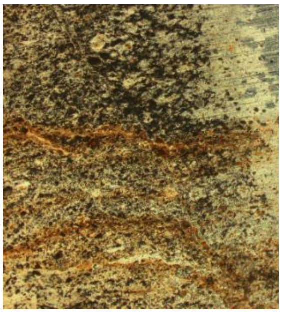

Figure 6.12
Hematite bands in the silty clay matrix of M1 material. Clay minerals appear as black (isotropic), while the light pink –grey –orange groundmass indicates a feldspathic – iron oxide weathered composition (Stoops, 2003).

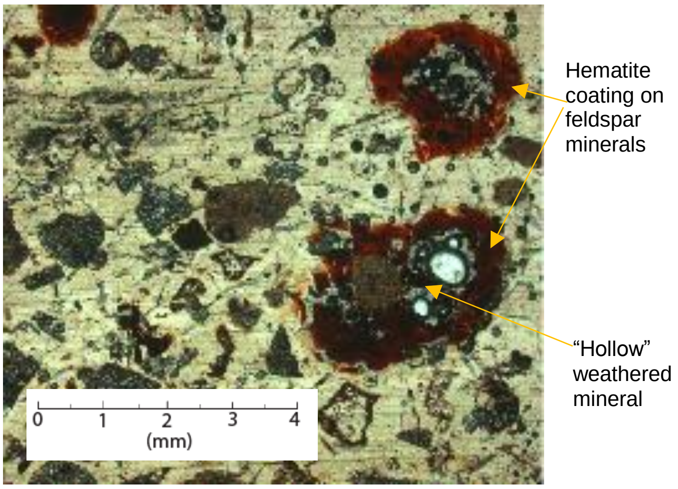

Figure 6.13. Sand particles suspended in a silty clay matrix in M1 material.

6.3.2 M1b thin section

6.3.2.1 Overall structure and thin section location

Thin section 6 exhibits shear zones in samples M1b; these are shaded dark grey in **Figure 6.14**. Three different materials were captured by a single thin section: the top ¼ comprised sandy clay (light brown) followed by a thin lens of silt (darker brown), then approximately 2/3 is comprised of silty clay (light orange brown) (**Figure 6.15**).

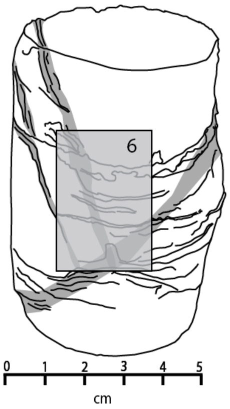

Figure 6.14. Location of the thin section on the failed triaxial specimen for M1b, 150 kPa.

6.3.2.2 Shear zone microstructure

Two PSZ's (A&B, **Figure 6.15**) are observed in thin section 6. Both shear zones are inclined at orientations (10° from the expected PSZ) closest to what is expected for R shears (**Figure 6.15**). Shear zone A (0.25 – 1.0 mm thick) is a continuous feature from the top to bottom of the sample. Shear zone A clearly offsets the sandy clay material at the top of the specimen by 5.5 mm. At the base of shear zone A, the offset seen by displaced limonite layers is reduced to 1 – 2 mm. Within shear zone A there is significant clay mineral realignment in the direction of shear. It is unclear whether realignment increases towards the centre of the shear band as found in Gylland *et al.* (2014). Shear zone A branches out into other minor shears, also oriented at R shear orientations (light grey shaded zones) slightly prior to a manganese nodule (**Figure 6.15**). The branched out shears have similar orientations to shear zone A, are spaced between 0.5 – 0.75 mm and are around 0.1 - 0.2 mm thick. Shear zone B (**Figure 6.15**) is seen in the bottom left of the thin section. This shear is approximately 0.2 mm thick, and is connected to shear zone A via one visible minor shear, which is oriented at 80°,19 degrees greater than expected for R' shears. Other possible R' shears occur at the middle of shear zone A (70 - 75°), and also at the base (80°), coinciding with R shears where shear zone A is branching around the manganese nodule (**Figure 6.15**b, c). Several shears oriented between 18 - 30°, close to the excepted orientation for P shears, connect shear zones A and B.

6.3.3 M1d thin section

6.3.3.1 Overall structure and thin section location

Thin section 7 (**Figure 6.17**) is located across the approximately horizontal shear zone in specimen M1d. The top 1/3 of thin section 7 (**Figure 6.16**) is

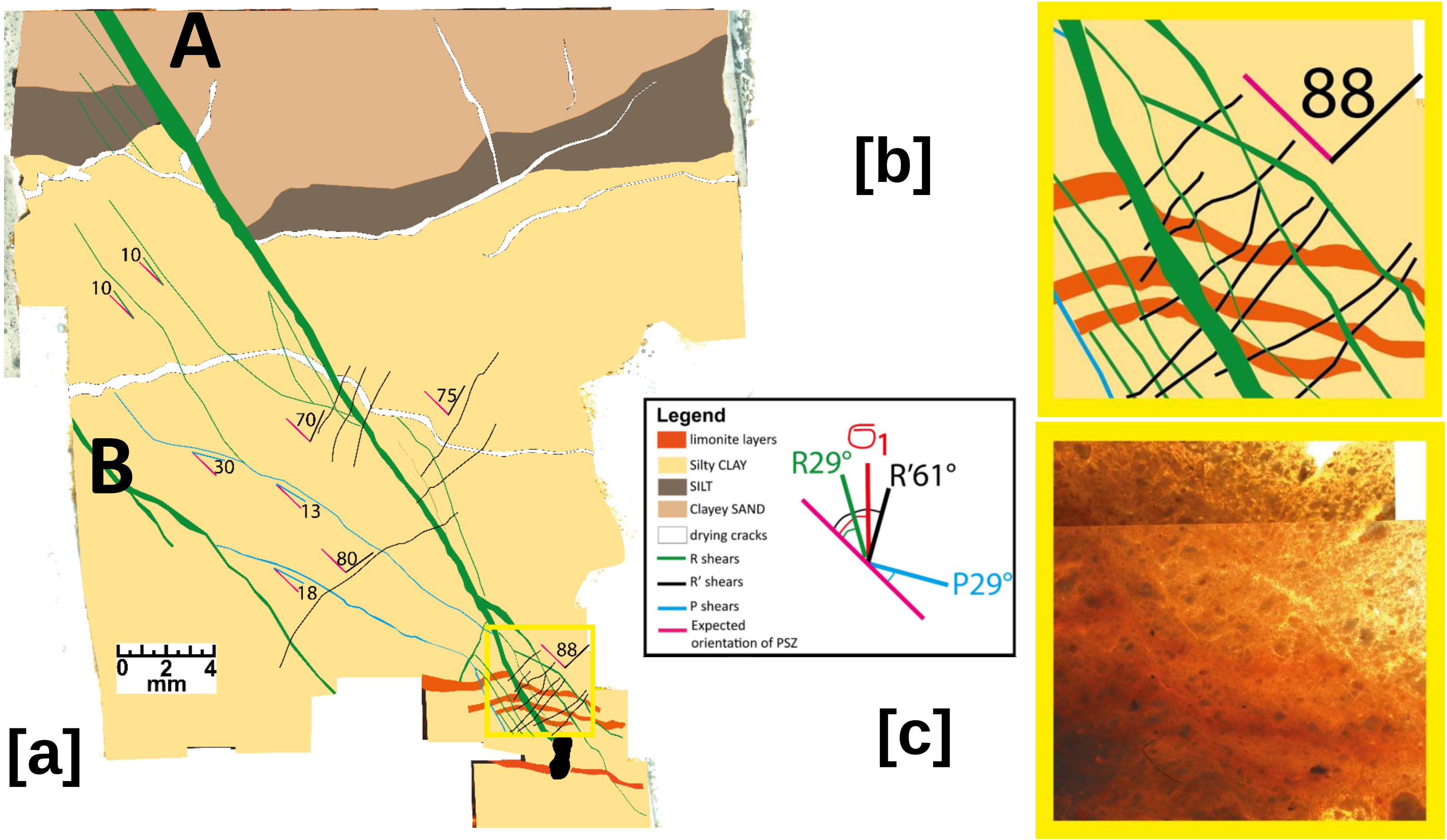

Figure 6.15. (left) Shear zones in failed M1b (150 kPa) material, captured in thin section 6. Figure 6.15b and c (top right) are the zoomed in zone outlined by the yellow box in Figure 6.15a. This zone shows the offset of horizontally bedded limonite layers.

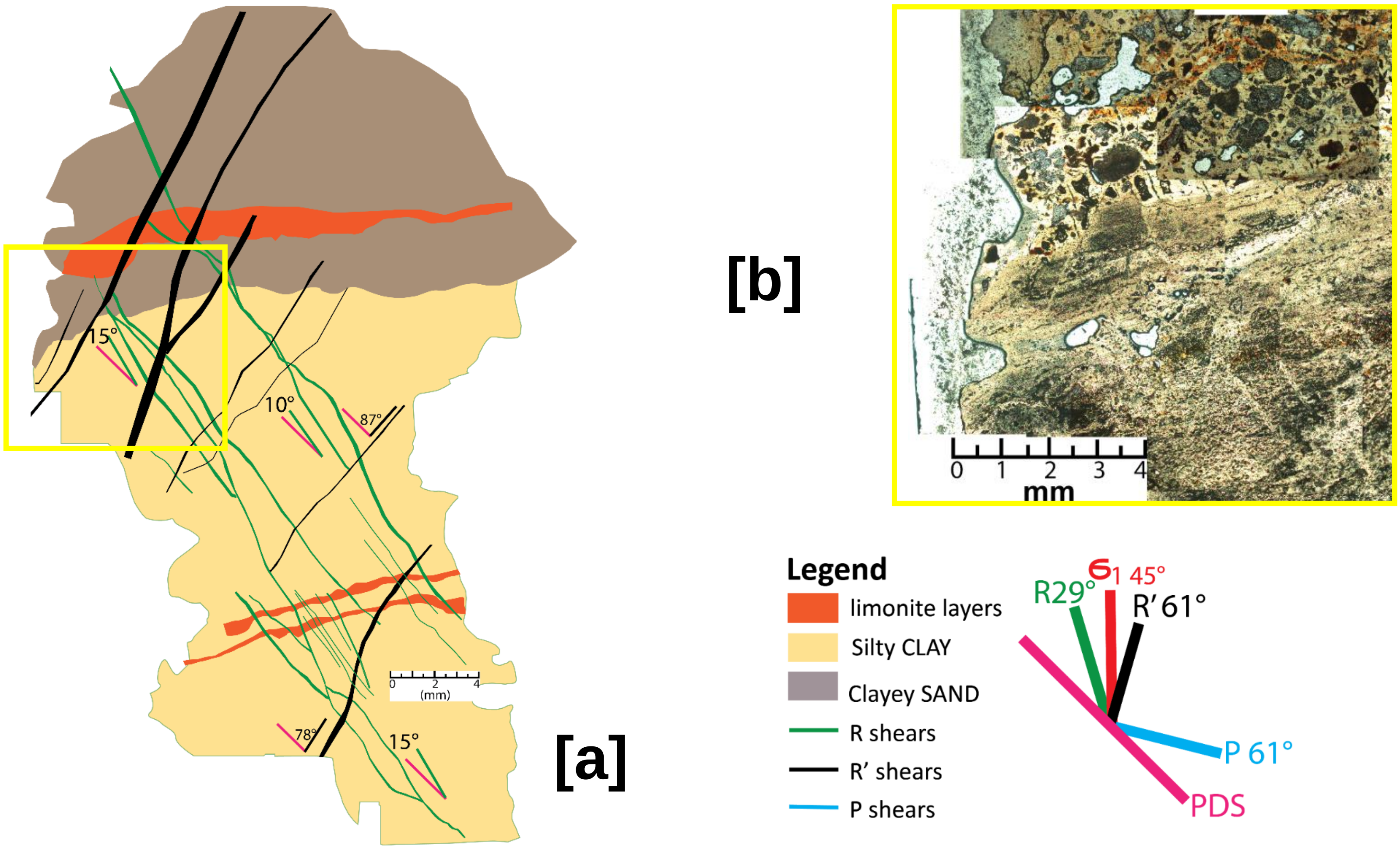

Figure 6.16. [a] Thin section 6 overview, with close-ups of the yellow outlined box of the R and R’ shear zones in Figure 6.16 [b].

other specimens which failed on more distinct shear zones, M1d, (tested at 225 kPa confining pressure) appeared to fail near the boundary between the sandy clay and clayey silt, hence why the boundary was captured during thin section preparation. Upon closer inspection, multiple zones of particle reorientation were identified.

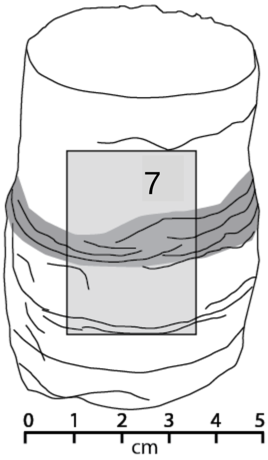

Figure 6.17. Location of the thin section on the failed triaxial specimen for M1d, which was tested at 255 kPa. The dark grey shaded area outlines the shear band location in silty clay material.

6.3.3.2 Shear zone microstructure

No PSZ was identifiable, however a multitude of R and R’ shears were observed criss-crossing the thin section (**Figure 6.16**). R shears are inclined around 10 – 15°, are 0.1 – 0.25 mm thick, and spaced between 0.5 – 5 mm apart. R’ shears are inclined around 78 – 87°, are 0.1 – 0.5 mm thick, and are spaced between 1 – 5 mm apart. Shears that are most easily distinguishable are in the upper left corner, where a distinct offset of the sandy clay is observed (**Figure 6.16**). Here, the abrupt change in material boundary shows that the shear has offset the sandy clay by approximately 1.2 mm. Clay mineral realignment in both R and R’ is observed in the silty clay, however only limited realignment of sand particles is observed. Although sand particles are not reoriented within the shear zone, a high degree of fractionation of sand particles is evident in comparison to regions outside of the shear zone.

6.4 Shear zone microstructure from Micro CT

6.4.1 Introduction

This section presents observations of images produced from the micro-CT scans of shear zones for OM1b3 (355 kPa consolidation stress, static compression), M1 (255 kPa consolidation stress, static compression) and OM1

(240 kPa consolidation stress, cyclic compression, 0 average shear stress, 60 cyclic shear stress). The images are differentiated based on density, allowing the mapping of shear zones and different materials. Static triaxial shear zones were captured with small (10 mm inside diameter, 30 mm long) plastic hollow tubes. These mini-plus were scanned at the University of Auckland with a Skyscan 1272. The micro-CT in Bremen Germany was capable of capturing the entire failed triaxial sample at a greater resolution.

Primary shear zones were clearly visible in both static and cyclic samples of OM1. Principal shear zones in M1 were not observed. This is likely due to a sand lens in the centre of the sample which inhibited shear band formation. Several artifacts were present in the scans. These included ring artifacts (rings centred on the centre of rotation) (**Figure 6.18**), and poisson noise (dark and light streaks orientated in the direction of scanning). Ring artifacts are caused by a miscalibrated or defective detector element, and poisson noise is a consequence of statistical error of low photon counts (Boas & Fleischmann, 2012).

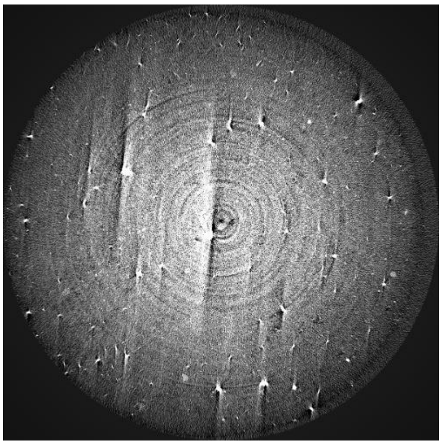

Figure 6.18. Poisson noise (dark and light streaks) seen in OM1b3.

6.4.2 OM1b3

The location of the sub sample of the shear zone in OM1b3 captured by the hollow plastic tube for micro-CT scanning is shown in **Figure 6.19.** The soil was classed into four density zones as outlined in **Figure 6.21**; the densest material are particles suspended in a less dense matrix. Within this matrix are denser regions including the shear zones (dark blue), and less dense clay matrix (dark green and light green).

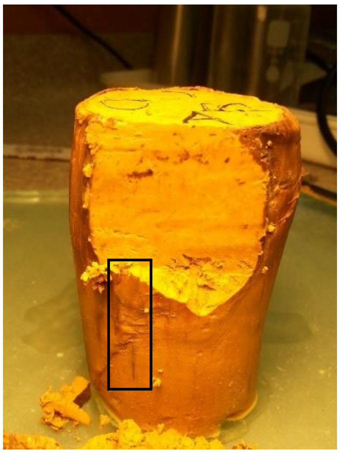

Figure 6.19. The location of the sub-sample of the failure surface for OM1b3.

Particles were analysed by visual assessment. The densest particles (material 1, red, **Figure 6.20**) are sub rounded – sub angular, in the silt size range (2μm - 64 μm), and make up approximately 1 – 5 % of the overall material. These particles graduate from most dense in the centre of the particle to less dense around the particle edges. The particles had a platy appearance upon zooming in, however this was accounted for by error introduced by scanning. It is most likely that these particles are weathered volcanic glass shards, as it is thought the material is an *in situ* pyroclastic air-fall deposit.

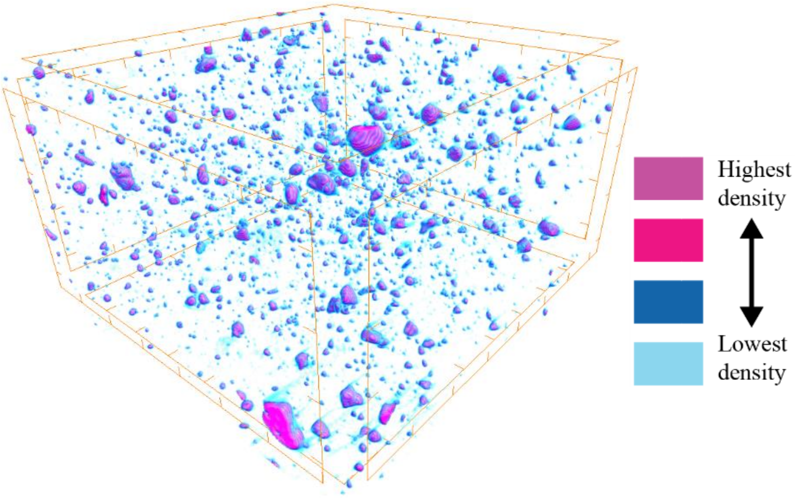

Figure 6.20. The densest particles without the clay matrix. Each unit of the orange bounding box is 500μm.

The matrix material appears as a speckly dark blue (material 2) – dark green (material 3) to light green material (material 4) (**Figure 6.21**). The matrix likely consists of spherical - tubular hydrated halloysite clay minerals (Kluger *et al.* 2015). Two main shear zones were observed in the sample (shear zones A & B, **Figures 6.21** &**6.22**). Shear zones appeared as darker blue fracture zones in

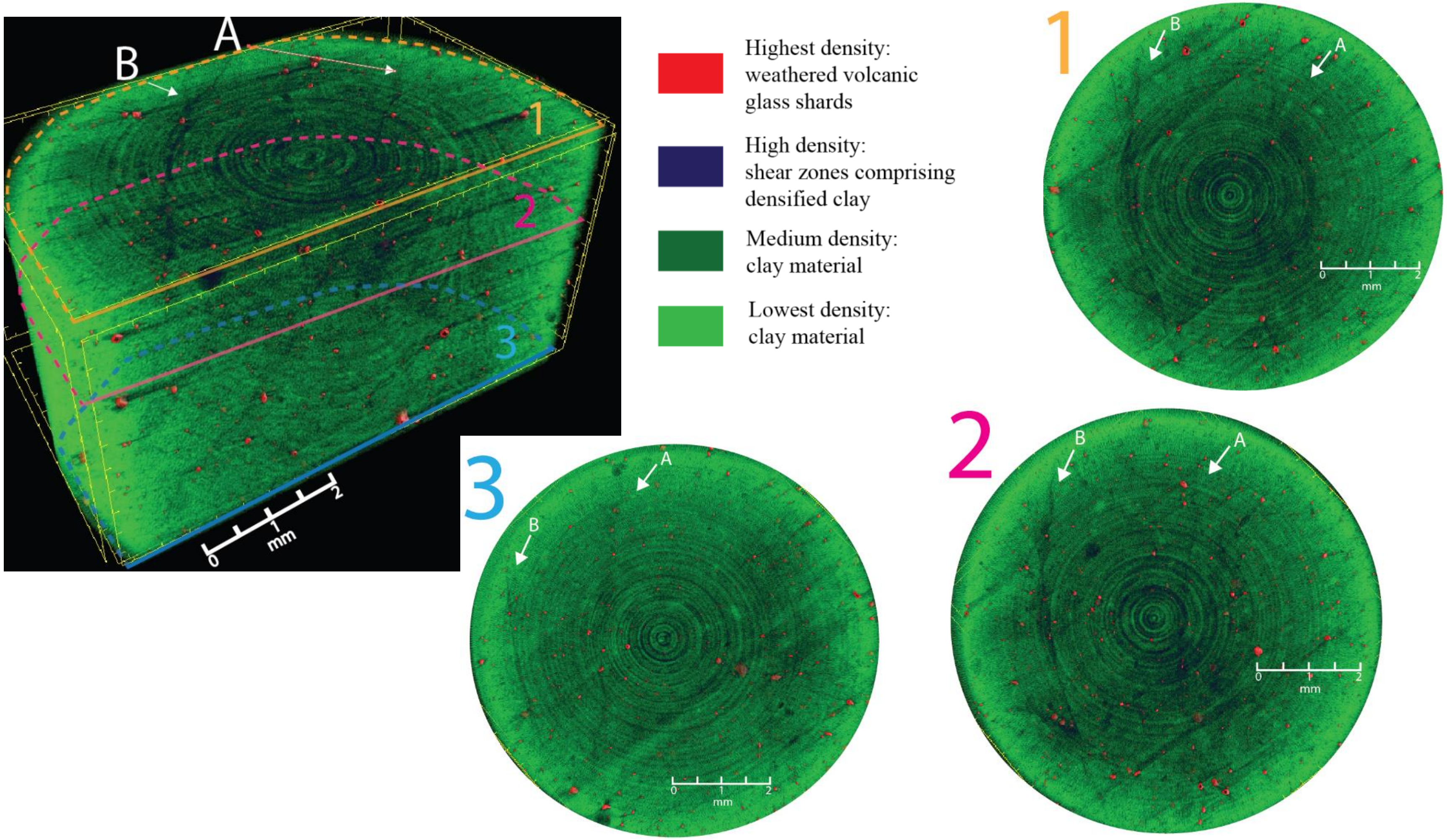

Figure 6.21. Horizontal sections of the shear zones captured by micro-CT scans in OM1b3. Ring artifacts are the concentric rings that radiate from the centre of the sample outwards, as seen in cross sections 1, 2 and 3.

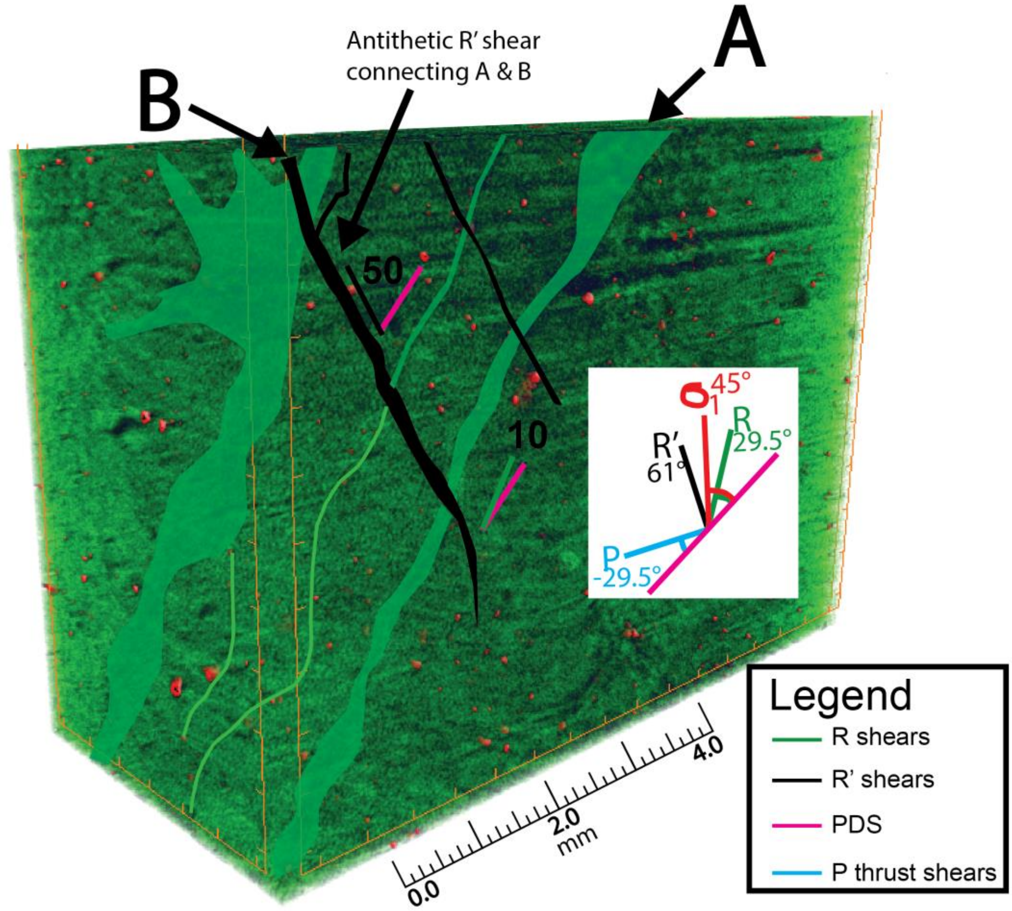

Figure 6.22. The cross section of OM1b3 micro-CT scan showing the R and R' shears

the matrix material i.e. densified regions of clay. The shear zones are around 50 - 100 μm thick, and spaced between 2000 - 3000 μm apart. Both shear zones consist of intertwining fractures or zones of lower and higher densified material, and are oriented at angles near to those expected of R shears (expected 29.5°, observed 10°). R shears are linked by antithetic R' shears, oriented at 50°. One of these R' shears appears to cause slight offset to shear zone A (**Figure 6.22**). The positioning and orientation of the glass shards appears to be unaffected by shearing.

6.4.3 OM1 cyclic compression

Images of the projection captured by the Micro-CT scanner at the University of Bremen, Germany are presented. The whole primary failure surface was captured, as the Skyscan 1172 was able to capture projections at a higher resolution than Skyscan 1272 due to the stage being rotated 360° rather than 180°. Firstly, images of the variants of materials of different densities are presented. Images of the failure surface are secondly presented.

6.4.3.1 Material and shear zone observations

Four different materials of variable densities were apparent from the micro-CT images (**Table 6.3, Figures 6.23 & 6.27**). Material 1 is likely to be manganese nodules, which are recognisable by the naked eye. Material 2 has a smaller and more rounded particle size, and is much more uniformly distributed, and slightly less dense than material 1, indicating that it is probably comprised of weathered volcanic glass shards. Material 3 is concentrated as coatings around materials 1 and 2, but also forms some of the matrix, bridging between dense particles. Material 4 makes up most of the matrix material. Materials 3 and 4 are likely to be clays. The failed sample has a clear principal shear zone (PSZ). The PSZ intersects the sample about 300 mm from the top and follows a roughly straight line towards the bottom of the sample. The PSZ is inclined at approximately 48°, however varies within the sample, as seen by pronounced flattening in the centre of the sample in **Figure 6.27** (XY2-3). The PSZ branches out into several shears near the boundary at both ends. The shear zone comprises of material 2, 3 and 4. Material 4 (dark green-black) forms the dominant outline of the shear zone. The PSZ is comprised of several smaller intertwining shears, which are too small to distinguish properly in the image. Within the shear zone, material 4 is the matrix for what appears to be smaller “crushed” material 2 and 3 (**Figure 6.27** XY1a). Material 3 is clearly realigned, while material 2 is less obviously aligned in the direction of shear. The PSZ connects with a minor shear of similar orientation at the top right of the sample. This minor shear does not offset the exterior of the sample. Between the PSZ and the minor shear are smaller antithetic shears, which vary between 90 - 100° to the orientation of the PSZ. These shears are not continuous and appear inconsistently between the PSZ and minor shear throughout the entire sample.

Errors in within the sample include the bright pink – orange streak visible in **Figure 6.27** (XY5). This appears to be a sample material heterogeneity. The several drying cracks (bright blue cracks) are visible as a result of drying out during sample preparation. The scanning quality of the (Skyscan 1172) micro-CT appears to have much less error associated with the images i.e. no ring artifacts or poisson noise is visible. This is likely because the cyclic sample was scanned over 360° rotation, allowing more images to be interpolated, whereas the static samples were only scanned over 180° rotation.

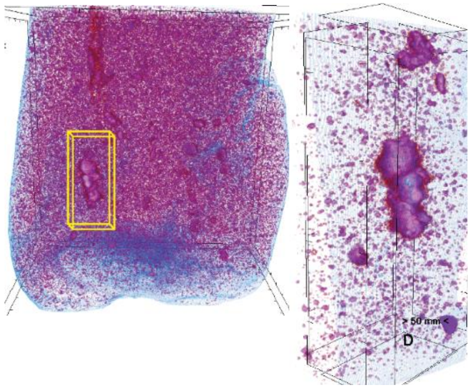

Figure 6.23. The densest particles (type 1 and 2), with a zoomed in image on the right of the area outlined by the yellow box.

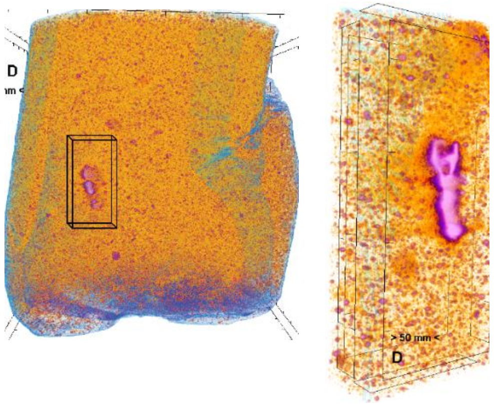

Figure 6.24. Type 3 particles, with a zoomed in image on the right of the area outlined by the black box.

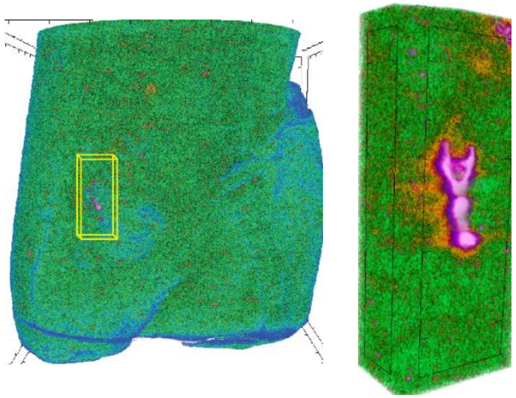

Figure 6.25. Type 4 particles, with a zoomed in image on the right of the area outlined by the yellow box.

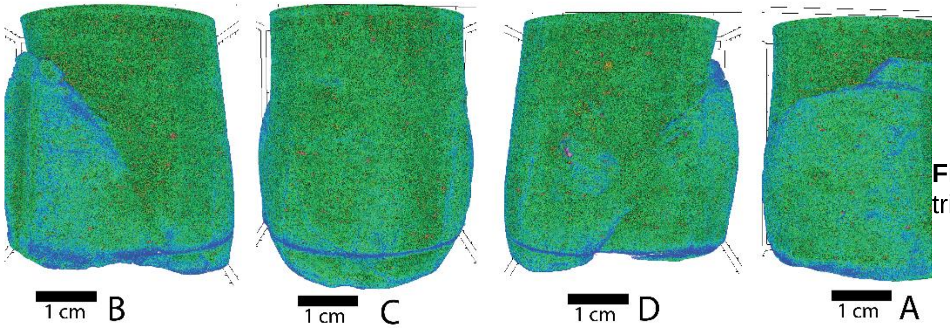

Figure 6.26. Four sides of the failed cyclic triaxial sample (A-D).

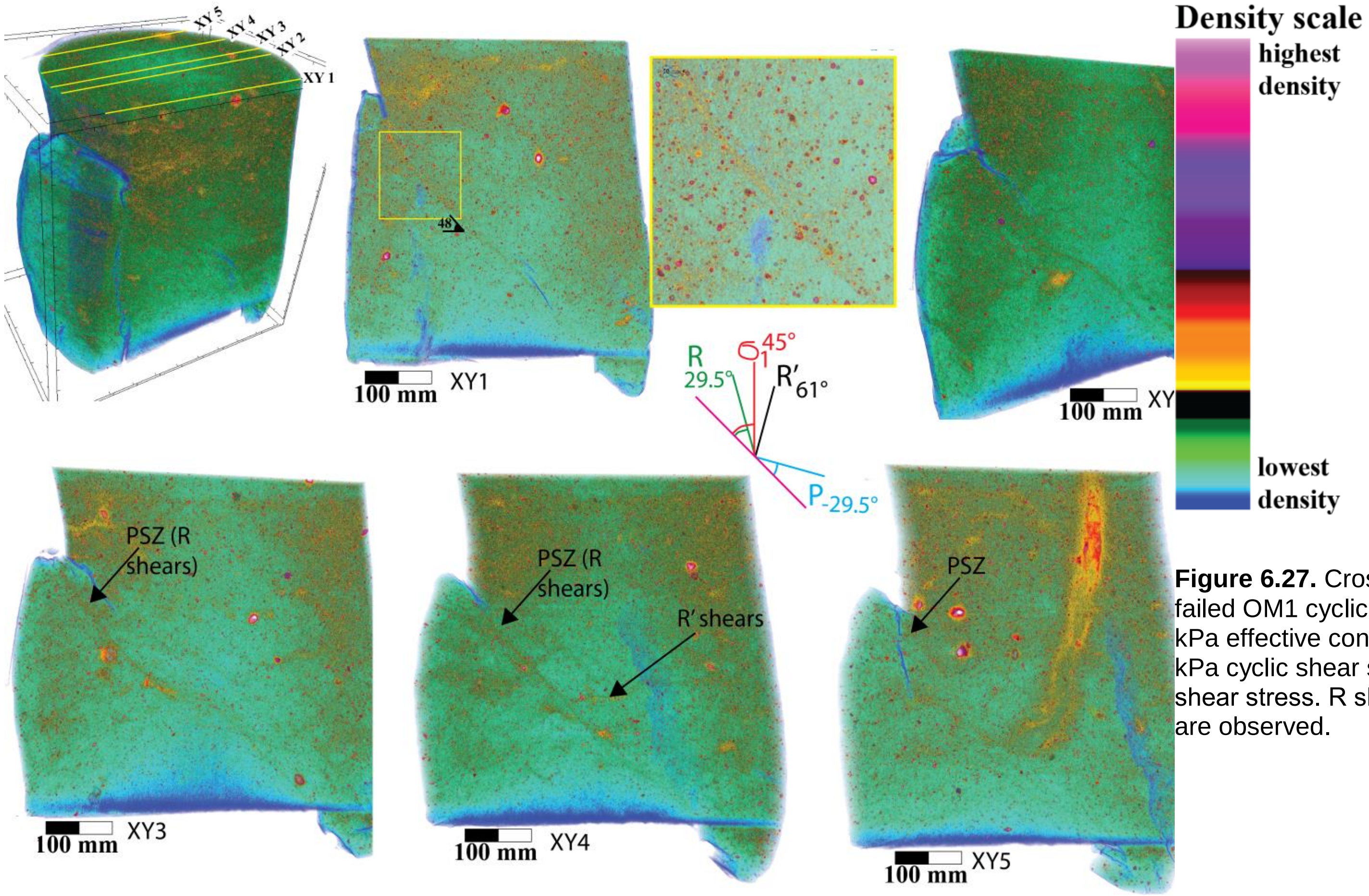

Figure 6.27. Cross sections of the failed OM1 cyclic sample, tested at 240 kPa effective confining pressure, 60 kPa cyclic shear stress, and 0 average shear stress. R shears and R' shears are observed.

6.4.1 M1

The location of the sub-sample taken from the sample is presented in **Figure 6.28**. Ring artifacts and poisson noise were also present in M1 scans. The material was comprised of material of four different densities. The densest particles (Class 1, **Figure 6.29**) were angular to subangular and sometimes platy, 25 – 250 µm, and made up approximately 1% of the material. The distribution of these particles was much less consistent than dense particles in OM1. Evidence of weathering of these particles includes the gradation between more dense in the centre (bright pink) to less dense on the exterior of some particles, and in other particles the lack of dense material in the centre i.e. only the outer shell of the particle has been preserved.

Figure 6.28. Location of the sub sample in M1d, with the PSZ shaded dark blue.

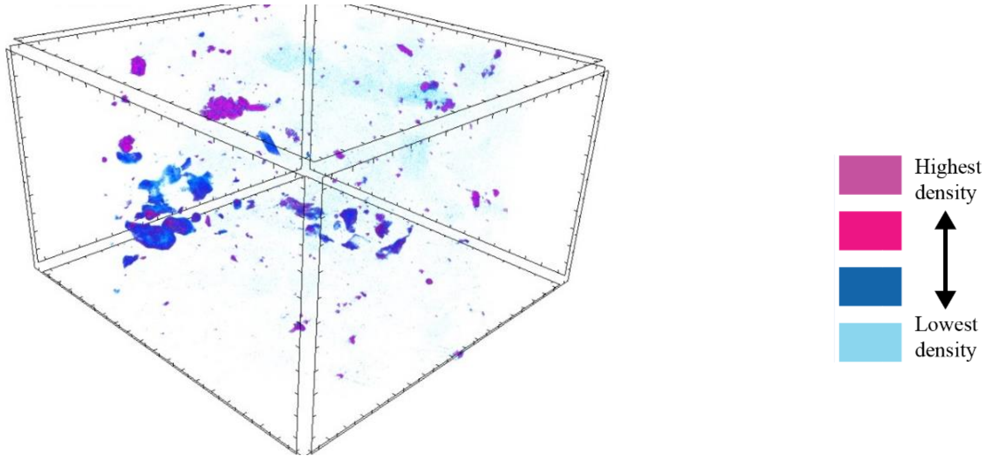

Figure 6.29. The densest particles in M1. The space between each black tick is 250 µm.

The second particle class of lower density (**Figure 6.30**) may be weathered derivatives of the densest particles. These particles were composed of material of the same density of the outer shell of the densest particles, and dense clay material, as seen by the similar colour the particles have to the densest parts of the clay matrix. Within some of the class 2 particles are also regions of material the same density as class 1 particles, further suggesting that they are weathered derivatives. Although vague, the shapes of these particles are platy – oblong – cuboid with sub-angular edges, and are between 100 – 750 µm.

Class 3 and 4 particles are more dense (orange) and less dense (yellow) clay matrix materials (**Figure 6.31**). Clay minerals are horizontally bedded, as expected of Matua Subgroup, which is a fluvial deposit. No obvious principal shear zones were observed. Like the thin section for M1d however, some minor shears were evident, based on their fracturing and offset of larger particles (**Figure 6.32**). Pore spaces and fractures in class 1 and 2 particles are sometimes infilled with class 3 and 4 materials.

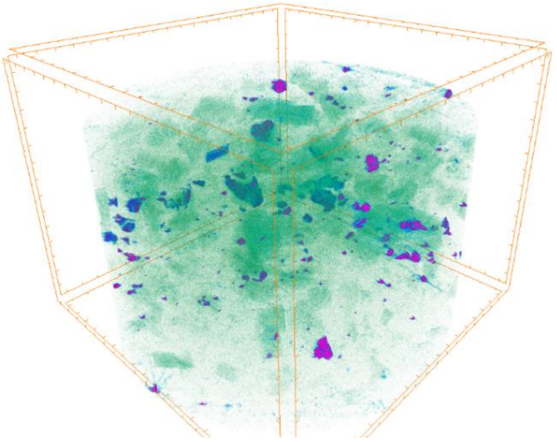

Figure 6.30. Densest particles and less dense particles in M1.

Highest density
🟪
🟥
🟦
🟦
🟩
🟩
🟫
🟧
🟨
Lowest density

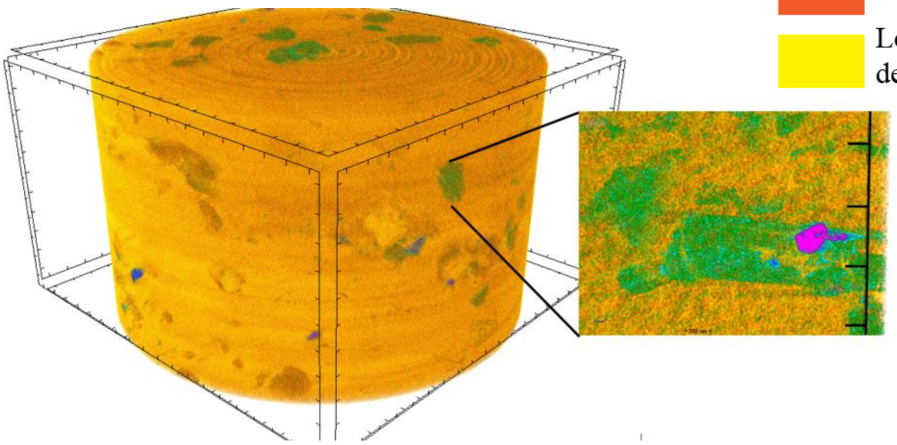

Figure 6.31. Class three (dense clay) and four (less dense clay) with class 1 and 2 materials. A close-up of a class 2 mineral shows that both class 1 remnants and class three and four clay infill.

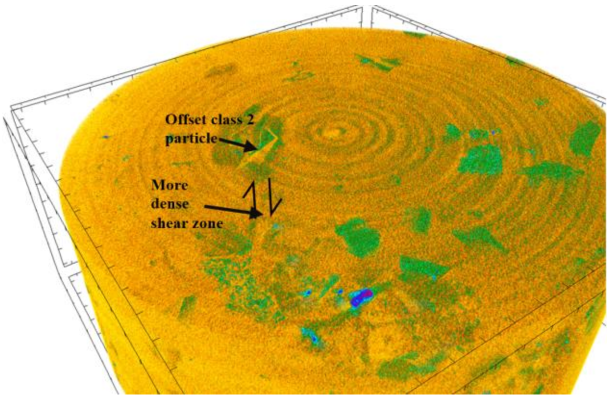

Figure 6.32. A minor shear zone off-setting a class 2 particle in M1.

6.5 Chapter summary

Microstructural characteristics of the 7 thin sections analysed are outlined in **Table 6.2**, while microstructural characteristics of the three micro-CT scans are summarised in **Table 6.3.**

Omokoroa material in thin section comprises weathered clay minerals (estimated 75%) silt (25%) and rare iron-oxide, hypersthene and quartz minerals.

The groundmass material is comprised of small weathered mineral domains, indistinguishable because of their size, but clearly minerals due to their pleiochroism. In micro-CT scans, the material comprises 4 main particle types: (1) randomly distributed, irregular shaped manganese particles, (2) sub-rounded – sub-angular, uniformly distributed weathered volcanic glass shard particles, (3) dense clay, forming bridges and coating materials 1 and 2, and less dense clay (4) which forms the bulk of the matrix. Materials 2 and 4 are distinguishable in the static micro-CT scan; manganese nodules and the dense clay coating (material 3) are not observed. Matua material in thin section was composed of horizontally variable lenses of sandy clay, silt, and silty clay. The sand was composed of weathered feldspars and quartz, while the silt and clay particles are likely also feldspathic in composition. Horizontal bands of hematite were present in both Matua thin sections. Micro-CT scans of Matua material showed (1) angular, randomly distributed particles I classify as either feldspar or quartz sand, (2) highly weathered particles which may have been derived from material 1, and roughly horizontally aligned matrix material, comprised of (1) dense clay material, and (b) less dense clay material.

Thin sections 1 and 2 capture the shear zone on the top and bottom (respectively) one side of the failed OM1b2 sample, which was tested at 240 kPa confining pressure. From the exterior of the sample an estimated 30-40 mm of offset occurred. Both thin sections have 3 PSZ's, where the PSZ is mainly comprised of consistent shears oriented near the expected orientation for R Riedel shears. R' shears are only observed in thin section 2, i.e. towards the base of the thin section. P or thrust shears are present in both thin sections 1 and 2, interlinking PSZ's. The average orientations of R' and P shears observed are greater than the expected orientation calculated based on the friction angle of the material, while R shears are less than the expected orientation. R shears, which form the PSZ's of both thin section 1 and 2, are generally thicker than P and R' shears. No trend between spacing of shears is observed.

Thin sections 3, 4 and 5 captured the shear zones of the failed OM1b3 sample, which was tested at 340 kPa confining pressure. The offset of shears could not be judged because there are no horizontal markers e.g. limonite lenses. Overall, in comparison to thin sections 1 and 2, the PSZ's in thin sections 3, 4 and 5 has less complex deformation, i.e. deformation appeared to be confined more or less to the shear zones identified. Thin sections 3 and 4 capture the top and bottom of side A of the sample, respectively. Three PSZ's oriented closest to the expected orientation for R shears were observed in both thin sections. In thin section 3, R shears lie at less than the expected orientation (observed: 10 - 15º, expected 30º), while in thin section 4, R shears are greater than the expected orientation (30 - 40º). The R shears decrease in overall width from top to bottom of the PSZ. R shears in thin section 5 also comprise the 2 PSZ's, at orientations slightly less than expected (16 - 28º). R' shears occur in thin sections 3 and 5, both inclined at 30º greater than expected. P shears are only observed in thin section 3, with a minor occurrence at the top and base of the PSZ. The micro-CT scan of OM1b3 showed two PSZ's to be comprised of densified clay material. Like the thin sections, both PSZ's are near the orientation expected for R shears, while the R' shears occur randomly, forming shears that link both PSZ's together.

The PSZ of the cyclic sample scanned in Germany consisted of densified material which gradated into less dense material. Some particles, suspected to be weathered volcanic glass shards appeared to be “crushed” as a result of shearing. The PSZ was connected to a minor shear at the same orientation via several smaller, inconsistent shears of antithetic orientations. The principal shear zones had correct orientations for R and R' shears, although R shears were prominent principal shear zones, while R' shears were only minor, less distinct zones that linked both PSZ's together.

Thin section 6 captured the shear zone of the failed M1c sample. Offset was greater at the top of the sample in the sandy clay material (2 PSZ's (A & B) were observed, both at orientations closest to R shears (10º observed, 30º expected). PSZ A clearly accommodated more deformation than PSZ B. Several sets of R' shears are observed, oriented at 10º greater than expected (70-80º observed, 61º expected). Several P shears are observed linking R shears (PSZ's) together, oriented slightly less than expected (13-30º observed, 29º expected). Like PSZ's in Omokoroa thin sections, R shears were generally thicker than P and R' shears. The sand lens at the top of the sample was offset by 5.5 mm, whereas the limonite layers at the base of the sample were only offset by 1 – 2 mm.

Principal shear zone development in thin section 6 was inhibited by an unexpected sand lens in the centre of the sample. Numerous roughly evenly spaced shears at R and R' orientations criss-crossed the thin section, offsetting both sandy clay and silty clay material. Some of these shears were observed in the micro-CT scan of M1d, where they were observed to offset and fracture weathered sand particles.

Table 6.2. Summary of shear zone characteristics for both Matua (M1) and Omokoroa (OM1) materials. **Abund. & dist.** = abundance and distribution, **E (º)** = Expected orientation based on the friction angle, **O (º)** = actual orientation in relation to the expected orientation of the PSZ**, w (mm**) = width, **d (mm**) = spacing.

						R shears					**R' shears**					**P shears**				
Sample	**Material**	**EFC (kPa)**	**TS**	**PSZ(s)**	**Offset (µm)**	**Abund. & dist.**	**E (º)**	**O (º)**	**w (mm)**	**d (mm)**	**Abund. & dist.**	**E (º)**	**O (º)**	**w (mm)**	**d (mm)**	**Abund. & dist.**	**E (º)**	**O (º)**	**w (mm)**	**d (mm)**
OM1	**Bedding:** Massive **Coarse fraction:** highly weathered, rare (≤1 %) quartz, lithics, ferromagnesium minerals & glass shards. **Groundmass:** Clay (inferred hydrated halloysite) (75%) silt (20 – 25%). Silt groundmass pleiochroic indicating weathered mineral groundmass	240	1	3 (A, B, C)	-	3 sets comprising PSZs	29.5	15	0.1-0.25	10 - 30	-	60.5	-	-	-	3 -4 sets connecting PSZ A,B,C,	30	17 - 30	0.1	0.25 - 2.5
			2	3 (A, B, C)	30 - 40	2 sets, comprising PSZ'z	29.5	10 - 15	0.1 - 0.5	10	3 sets offsetting PSZ's	60.5	75 - 95	0.1-0.25	5 - 10	Some interlinking PSZ's A-C, several clustered around PSZ B	30	30 - 52	0.1	1.5 - 4
		355	3	3 (A, B, C)	-	3 sets comprising PSZ's	29.5	10 - 15	0.5 - 1	1 - 10	1 shear intersecting top of PSZ A	60.5	90	0.1	-	Minor occurrence at top and base of PSZ A.	30	15 - 30	0.25	0.25
			4	3 (A, B, C)	-	3 sets comprising PSZ's	29.5	30 - 40	0.1 - 0.5	1.0 - 12.0	-	60.5	-	-	-	-	30	-	-	-
			5	2 (A, B)	-	2 sets comprising PSZ's	29.5	16-28	0.25	4.0	1 shear intercepting PSZ A & B	60.5	90	0.25	-	-	30	-	-	-
M1	**Bedding:** Roughly horizontal, sandy clay, silt, silty clay beds, stained with horizontal beds of hematite	150	6	2 (A, B)	-	2 sets comprising PSZ's	29	10	0.25 -1	0.5-5	2 – 3 sets, one middle of PSZ, one at base	61	70-80	0.1-0.25	0.25 -1	2 P shears, bottom half thin section, connecting PSZ A and B	29	13-30	0.25	2-5

Sandy clay lens: highly weathered quartz, feldspars (70%) in silty clay groundmass (30%) **Silt lens:** grey, horizontally aligned **Silty clay:** pink – grey colour indicates feldspar derived clays	255	7	Numerous minor shears	5 at top thins section, 1 at bottom thin section	Numerous shears. 2 main sets	29	10-15	0.25-0.5	0.5-4	Numerous shears roughly evenly spaced, intersecting R shears	61	78 - 87	0.1–0.5	1 - 6	-	-	-	-	-

Table 6.3. A summary of microstructural characteristics of Micro-CT samples

Component characteristics									Shear zone characteristics			
Sample	**Compression**	**Material**	**Size (mm)**	**Abundance (%)**	**Shape**	**Distribution**	**Notes**	**Figure**	**PSZ's**	**Material description in PSZ's**	**Structure of PSZ(s)**	**R/ R'/P shears**
GM1b	Cyclic	1	5 – 50	< 1	Sub rounded - subangular	Random	Higher density interior, grading rapidly to lower density material coating exterior	Large particle in Figure 6.23	2 (A & B)	1 PSZ, comprised of "crushed" material 2 and 3, in material 4 matrix	1 main PSZ, relatively straight, flattens in middle, branches at both ends. 1 minor PSZ	Yes, PSZ is at R orientation, R' shears randomly appear, connecting both PSZ's
		2	< 1 - 5	1 – 5	Sub rounded - subangular	Uniform	No density variation inside particle	Small particles in 6.21				
		3	< 1	15	Too small to define	Surround materials 1/ and 2 but also form matrix	Coat and form bridges between dense particles	Yellow orange material in Figure 6.24				
		4	< 1	85 - 90	Too small to define	Densified SZ's (dark green/black) to less dense outside shear zones (light green/light blue)	Matrix material	Figure 6.25				
GM1b	Static	1	< 1	1 - 5	Sub rounded - subangular	Uniform	No density variation inside particle	Red particles in Figure 6.21	2 (A & B)	2 PSZ's, both comprised of material 2, gradating to material 3 then 4 on the exterior	50 – 100 µm thick, spaced 2000 – 3000 µm apart	Yes, R and R' shears separated by 60º. No P shears observed
		2	< 1	25	Too small to define	Concentrated in shear zones	-	Dark blue in Figure 6.21				
		3	< 1	45	Too small to define	uniform	-	Dark green				
		4	< 1	25	Too small to define	uniform	-	Lighter green				

Component characteristics									Shear zone characteristics			
Sample	Compression	Material	Size (mm)	Abundance (%)	Shape	Distribution	Notes	Figure	PSZ's	Material description in PSZ's	Structure of PSZ(s)	R/ R'/P shears
M1	Static	1	< 1	1	Subangular – angular	random	Higher density interior, grading rapidly to lower density material coating exterior	Figure 6.29	0	Only minor shears present, offsetting and fracturing material 2, 3 and 4.	Inconsistent shears	-
		2	< 1	20	Platy-oblong-cuboid	uniform	Possible weathered derivatives of material 1	Figure 6.30				
		3	< 1	25	Too small to define	Horizontally aligned with material 4		Figure 6.31				
		4	< 1	54	Too small to define	Horizontally aligned with material 3		Figure 6.32				

CHAPTER 7

CYCLIC TRIAXIAL AND CONTOUR PLOT RESULTS

7.1 Introduction

This chapter outlines the results of cyclic triaxial testing on OM1 material completed at the Centre for Marine Environmental Sciences at the University of Bremen, Germany. The test conditions were based on Anderson (2015), who showed that failure characteristics, resulting from different combinations of (τ_{av}) and cyclic shear stress (τ_{cyc}), could be plotted onto a single graph, giving a broad view of how a specific soil type fails under different conditions. Examples of different conditions *per se* could be a strong earthquake (high frequency, high τ_{cyc}, no τ_{av}), a heavy rainfall event (high τ_{av}, no τ_{cyc}), nearby pile driving (small frequency, low τ_{cyc}, no τ_{av}). The motivation in replicating this technique is to attempt to quantify the failure characteristics of sensitive material at Omokoroa when it is subjected to different amounts of τ_{av} and τ_{cyc}. Presently, known cyclic forces that occur at Omokoroa include small earthquakes, earth and ocean tides, and wind during storm events, while τ_{av} that might influence failure includes heavy rainfall events. The testing framework involves firstly defining the failure envelope and undrained shear strength (S_u) of the material by static triaxial tests. Cyclic triaxial tests at different frequencies, τ_{av} and τ_{cyc} are then completed. My framework included firstly two static consolidated undrained triaxial tests at the same effective stress (240 kPa, the estimated effective stress at the depth the sample was taken from). Since I only had 10 samples, I decided to leave the dynamic frequency, or time for each cycle, at 1 cycle per second, as Anderson recommends. I then did 10 consolidated (240 kPa) undrained cyclic triaxial tests, each at different combinations of τ_{av} and τ_{cyc}. Due to triaxial or sample malfunction, only 7 of these tests were successful (**Table 7.1**). Raw triaxial data is presented in **Appendix 7.**1.

Section 7.2 presents the static triaxial results with the same analysis framework as Chapter 5. In section 7.3, cyclic triaxial results are presented as a sequence of the different responses of deviator stress, effective stress, axial strain and pore water pressure, with two end members and two sub-members of response type identified. Finally, the cyclic contour plot is presented in section 7.4. Chapter 7 is summarised in section 7.5.

Table 7.1. Tav and T_{cyc} applied to each of the cyclic triaxial tests. Tests 3, 9 and 10 (in bold) produced unreliable results so were not included in further analysis.

Test number	**Consolidation stress (kPa)**	**Deviator stress ($\sigma_1 - \sigma_3$)**	**τ_{av} (kPa)**	**τ_{cyc} (kPa)**
1	240	0	0	0
2	240	0	0	0
3	240	60	30	40
4	240	150	75	30
5	240	80	40	60
6	240	150	75	50
7	240	0	0	60
8	240	0	0	40
9	240	-	-	-
10	240	0	0	87.5
11	240	60	30	60
12	240	120	60	50

7.2 Static triaxial test results

Two consolidated undrained triaxial tests were completed in order to gain the static shear strength (S_u) parameter required to generate the normalised axes of the cyclic contour plot, as well as plot an estimate of the expected failure envelope. Both tests were consolidated to 240 kPa consolidation stress. As expected, both tests displayed strain softening, contractive stress-strain curves similar to static triaxial testing presented in Chapter 5 (**Table 7.2**, **Figures 7.1 & 7.2**). During the strain hardening region, the stress - strain curves rise rapidly. Pore-water pressure curves also rise rapidly in the strain hardening region, lagging slightly behind the stress-strain curves. Both tests have sharp transitions from the strain - hardening region to the strain - softening region, indicating a sudden loss of strength. The curves then gradually decrease over the remaining 15 - 20% strain. The shape of the pore water pressure response for both tests is similar to tests in Chapter 5, with a sharp transition from rapidly rising to levelling off following peak deviator stress. Test 2 is notable in that the pore water pressure is greater than the peak deviator stress (**Table 7.2**, **Figure 7.1**). In the strain-softening region, pore water pressure continues to rise for test 2, diverging from the stress-strain curve, while for test 1, the pore-water pressure curve converges with the stress-strain curve towards the fully softened state (**Figure 7.1**).

Table 7.2. Failure characteristics of static triaxial tests 1 and 2.

Test	Consolidation stress (kPa)	Peak deviator stress (failure) (kPa)	Strain at failure (%)	Pore water pressure at failure (kPa)	Strain softening (%)
1	240	223	2.3	152	23
2	240	177	2	192	18

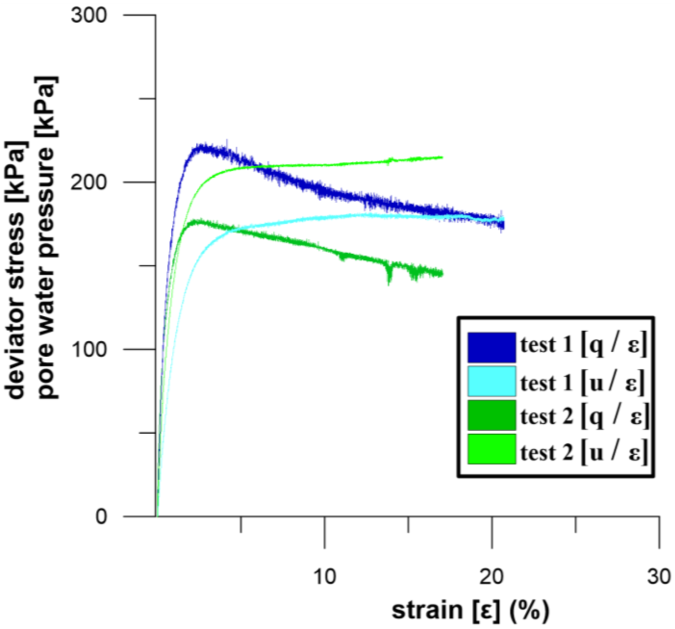

Figure 7.1. Deviator stress vs axial strain (q/ε) and corresponding pore water pressure (u/ε) for tests 1 and 2. Both tests were consolidated to 240 kPa effective stress, then were shear stress was applied in undrained conditions.

Figure 7.2 presents the p'-q' diagrams for test 1 and 2. Effective stress reduces as deviator stress increases for both tests. Test 1 fails at a higher deviator stress and a lower level of strain in comparison to test 2, where effective stress is more gradually lost and failure occurs at a lower peak deviator stress. Curves trend left for both test 1 and test 2, indicating a contractive response following failure. Both curves level off at the peak before sharply trending along their respective critical state lines. These critical state lines were used to draw failure envelopes to gain an estimate of where the cyclic tests are expected to fail. As seen in **Figure 7.2**, there is considerable variability between samples, so the critical state lines drawn are more an estimate than a definite failure envelope. This variability arises from sampling, sample preparation and also natural material variability. We drew both critical state lines on cyclic triaxial p'q' plots, and took an average S_u for normalising results for the contour plot.

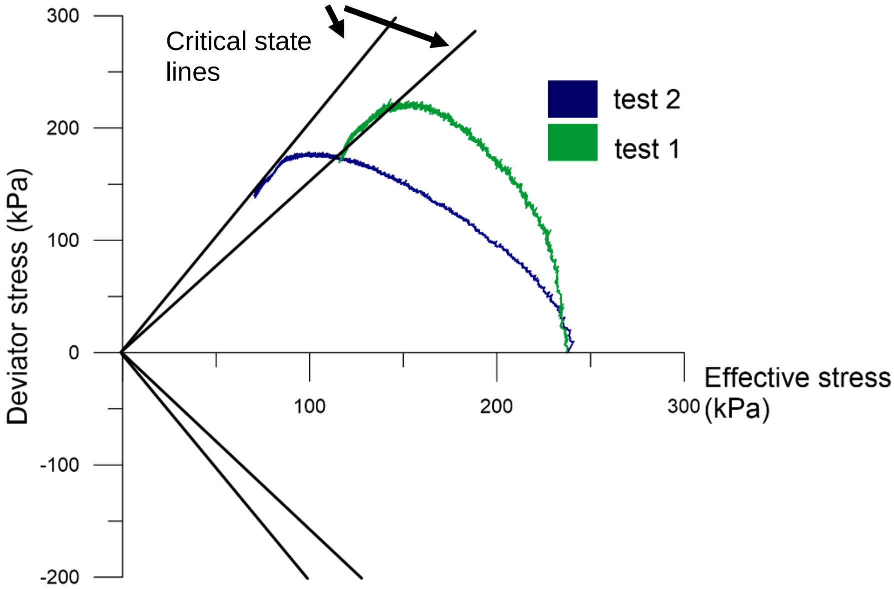

Figure 7.2. The effective stress paths (p'q') for tests 1 and 2. Both stress paths reach a peak, then trend left, indicating contraction following failure (Briaud, 2013).

7.3 Cyclic triaxial test results

7.3.1 Section layout

Of the 10 tests completed, 7 were successful. Four of the seven results are presented herein, to show the different failure characteristics in response to different average shear stress (τ_{av}) and cyclic shear stress (τ_{cyc}) applied. The three other successful tests are presented in Appendix 7.3. On the basis of failure characteristics, I divided the cyclic responses into two end members. Strain accumulation pattern determined the two types, while hysteresis loop characteristics warranted subtype definition.

1. Type 1 is characterised by a failure pattern of positive strain accumulation (tests 4, 5, 6, 11, and 12).
2. Type 2 is characterised by strain which accumulates symmetrically around the origin i.e. in both positive and negative directions.

Four intermediate categories with elements of both type 1 and two (types 1a, b and 2a, b) were also defined. Background information regarding the terminology is presented in Chapter 2: Literature review.

7.3.2 Type 1 response

Type 1 responses have a high application of both τ_{av} and τ_{cyc}, and failure is characterised by positive accumulation of strain. Test 4, 5, 6, 11 and 12 have type 1 response (**Table 7.3**). Tests 4, 6 and 12 are defined as type 1a, while tests 5 and

11 are defined as type 1b.Test 4 is used as an example of type 1a response (**Figures 7.3 & 7.4a-d**), and test 5 is presented as a type 1b response.

7.3.2.1 Type 1a

Tests 4, 6 and 12 have type 1a response. An application of τ_{av} - τ_{cyc} > 0 means that while τ_{cyc} is loading and unloading around τ_{av}, globally, the sample is always in a state of positive stress. Because there is no stress reversal, where the sample is temporarily in a global state of negative stress (τ_{av} - τ_{cyc} < 0), the stress-strain loops do not show flattening within each cycle. A reduction of stiffness (inclination) of stress-strain loops in the clockwise direction occurs between cycle 1 and the cycle at failure. Strain accumulates rapidly following failure for all type 1a responses (except test 6 which could not be measured due to the occurrence of only one cycle).

High applications of both τ_{cyc} and τ_{av} result in rapid failure (test 6). This rapidity of failure (shown by the closeness of the p'q' curve to the failure envelope of test 6) (Test 6, Appendix 7.3) may also be influenced by sample inconsistency, wherein the material may have been inherently weaker in test 6 in comparison to other samples. Initial stiffness appears to be higher for samples with low applications of τ_{cyc} (Test 4). Test 4 is used as an example of type 1a response. During the first 500 cycles, (dark green, **Figure 7.3**), strain accumulates at a steady rate and stiffness (G_{sec}) is high. Towards failure, hysteresis loops become broader and stiffness decreases, shown by the decrease in inclination of the hysteresis loop. The gradual increase of strain shows that significant accumulated within the sample prior to failure. Failure, therefore, is termed progressive. Failure (red hysteresis loops) was characterised by a rapid increase in strain per cycle. In test 4, another dramatic increase in strain occurs around 8% strain, where strain jumps from <0.5 % per cycle to 1% per cycle (**Figure 7.3**). γ_{av} and γ_{cyc} appear to correlate directly to the application of τ_{av} and τ_{cyc}: higher τ_{av} results in higher γ_{av} and vice versa (**Table 7.3**). The number of cycles to failure increases greatly when a small τ_{cyc} is applied, in contrast to a reduction of the τ_{av}, as evidenced by comparing test 4 to test 12 (**Table 7.3**).

Excess pore pressure generation is greatest within the first increment of cycles for tests 12, 4 and 6. In **Figure 7.5d**, during the first increment of cycles (dark green), pore pressure rose most rapidly, resulting in a significant reduction of effective stress. The rate of pore pressure generation slowed and flattened during increments 500-100 and 1000-1330, resulting in smaller reductions of effective stress (lighter green colours in **Figure 7.5**) before failure. Pore pressure peaked prior to failure, before slowing, then flattening off and slightly dropping (**Figure 7.5**). The u_{av} and u_{cy} also roughly correlate to the applied τ_{av} and τ_{cyc} for type 1 responses (**Table 7.3**).

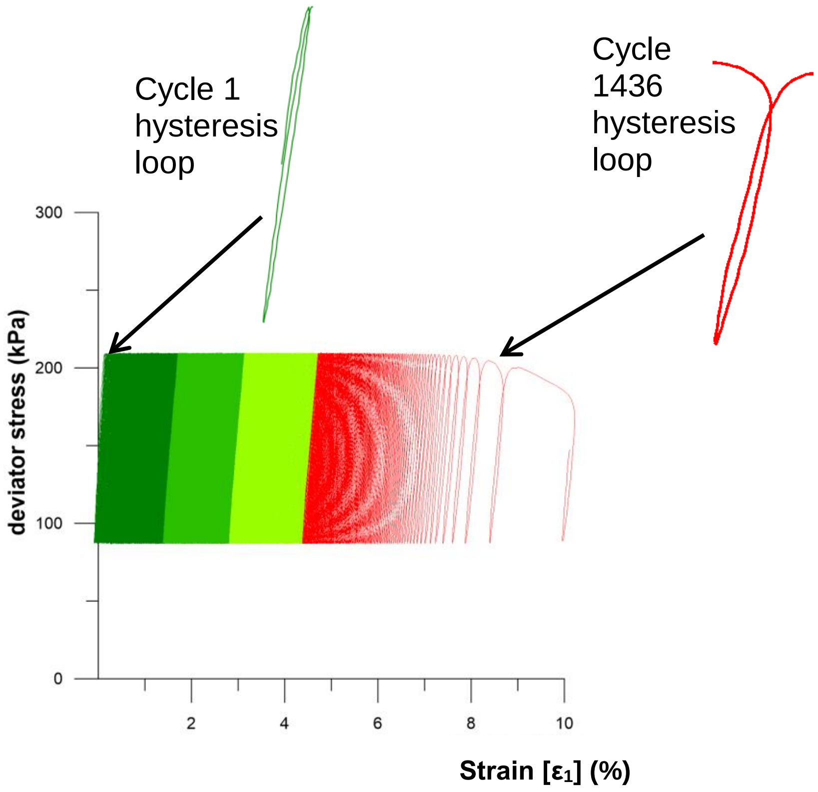

Figure 7.3. Deviator stress (kPa) vs strain (%) for test 4, which showed a type 1 response (75 kPa **T**av and 30 kPa **T**cyc)

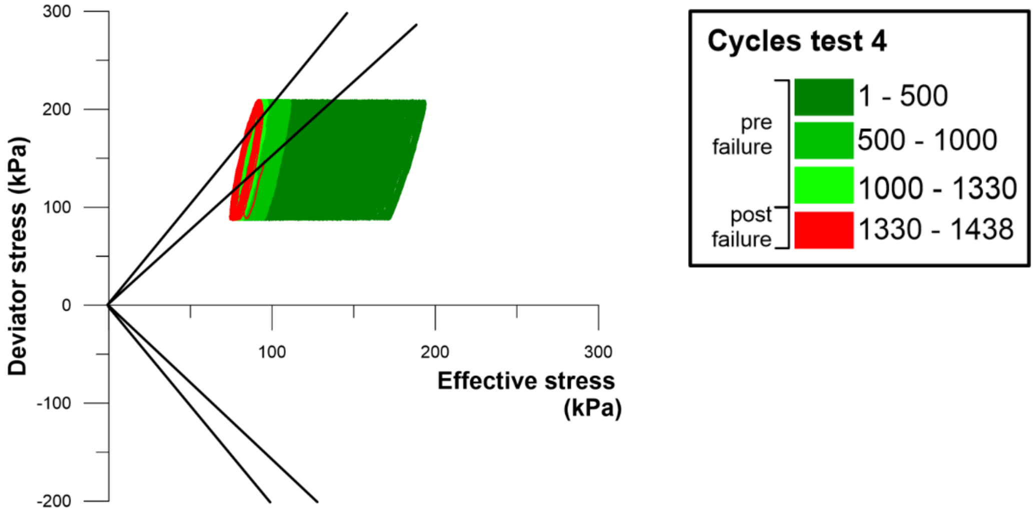

Figure 7.4. Deviator stress vs effective stress for test 4 (type 1 response) (75 kPa **T**av and 30 kPa **T**cyc). The legend is outlined in the black box.

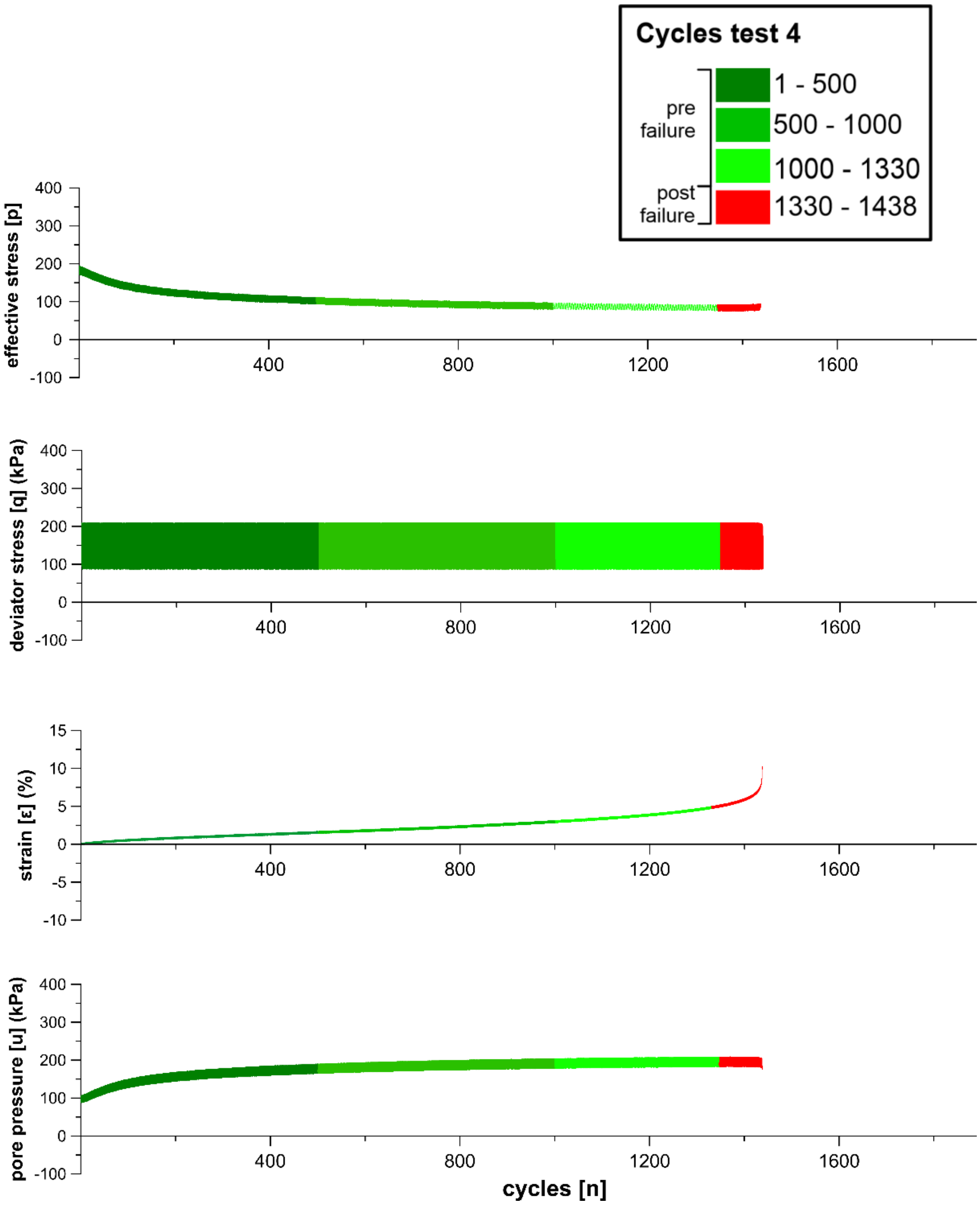

Figure 7.5a-d. From top to bottom: Effective stress (a), deviator stress (b), strain (c), and pore water pressure (d) vs cycles for test 4. The legend is outlined in the black box.

Table 7.3. Cyclic parameters obtained for tests 1-7, in order of the sequence of strain characteristics. **T_{av} (kPa) =** average shear stress**, T_{cyc} (kPa) =** cyclic shear stress, different hysteresis loops shapes are SL = symmetrical loop, AS= asymmetrical S-shaped, SS= symmetrical S-shaped**, n_f =** number of cycles to failure**, γ_{av} (%) =** average shear strain at failure**, γ_{cyc} (%) =** average cyclic strain at failure**, u_{av} =** average pore pressur at failure**, u_{cyc} =** u_{cy} at failure**, Gsec =** stiffness parameter from Kramer (1996).

Test #	**Type**	**Consolidation stress (kPa)**	**τ_{av} (kPa)**	**τ_{cyc} (kPa)**	**Hysteresis loop shape**	**(n_f)**	**(γ_{av}) (%)**	**(γ_{cyc}) (%)**	**(u_{av}) (kPa)**	**u_{cyc} (kPa)**	**Gsec ($\Delta q/\Delta\varepsilon$) at cycle 1**	**Gsec ($\Delta q/\Delta\varepsilon$) at failure**
4	1	240	75	30	SL	1330	5	0	172	9	1410	31
6	1	240	75	50	SL	1	11	8	115	66	53	53
12	1	240	60	50	SL	37	6	1	203	43	465	15
5	1a	240	40	60	AS	23	4	2	209	60	332	70
11	1a	240	30	60	AS	225	3	2	208	71	511	40
7	2a	240	0	60	AS	320	0	5	168	66	679	4
8	2	240	0	40	SS	2155	-1	4	187	60	4679	13

7.3.2.2 Type 1b response

Tests 5 and 11 have type 1b responses (**Table 7.3**). Both tests have slightly higher applications of τ_{cyc} than τ_{av}, and stress reversal with each cycle, where for a small amount of time the sample is temporarily under extensional stress, i.e. $\tau_{av} - \tau_{cyc} < 0$ (**Figure 7.6**). The stress reversal clearly affects the shape of hysteresis curves, warranting sub classification to type 1b, but because the dominant pattern of strain accumulation is still positive, tests 5 and 11 are classed as type 1 rather than type 2.

Test 5 is used as an example of Type 1a response (**Figures 7.6, 7.7, & 7.8a-d**). Like type 1, axial strain accumulates in the positive direction. At the start of both tests 5 and 11, hysteresis loops are steeply inclined (**Figure 7.6**) and more oval shaped. As pore pressure increases, effective stress is reduced, and strain increases, the shape of the loops transitions toward from a symmetrical loop to an S-shape, with distinct flattening (decrease in stiffness) near the x-axis during extension and compression (**Figure 7.6**). Hysteresis loops gradually decrease in inclination and become broader towards failure, after which inclination decreases and broadness increases more dramatically. After failure at 5% strain, strain increases further in a stepwise fashion, correlating to a step up in pore water pressure (**Figure 7.7**). In **Figure 7.7**, this step in pore pressure is correlated to a change in shape of the effective stress loading-unloading curves. The small reduction of τ_{av} between tests 5 and 11 correlates with a significant jump in cycles to failure form 23 to 225 (**Table 7.3**). Test 5 has a slightly greater τ_{av} than test 11, correlating to a slightly greater γ_{av} and u_{av}. Initial stiffness is slightly greater for test 11, also correlating to the lower τ_{av} (**Table 7.3**).

An interesting observation in both tests 11 and 5 is that the effective stress cycles (**Figure 7.8a**) are flatter during unloading, correlating to a slight flattening of excess pore pressure following positive peak stress (**Figure 7.8d**). This effect is amplified after cycle 15, and a small peak within the trough of effective stress cycles is visible, correlating to a more pronounced flattening of pore pressure post-peak. This pattern increases until the step up in pore pressure following failure (Figure 7.8a, d). This slight peak is also observed in test 11 (**Appendix 7.3**).

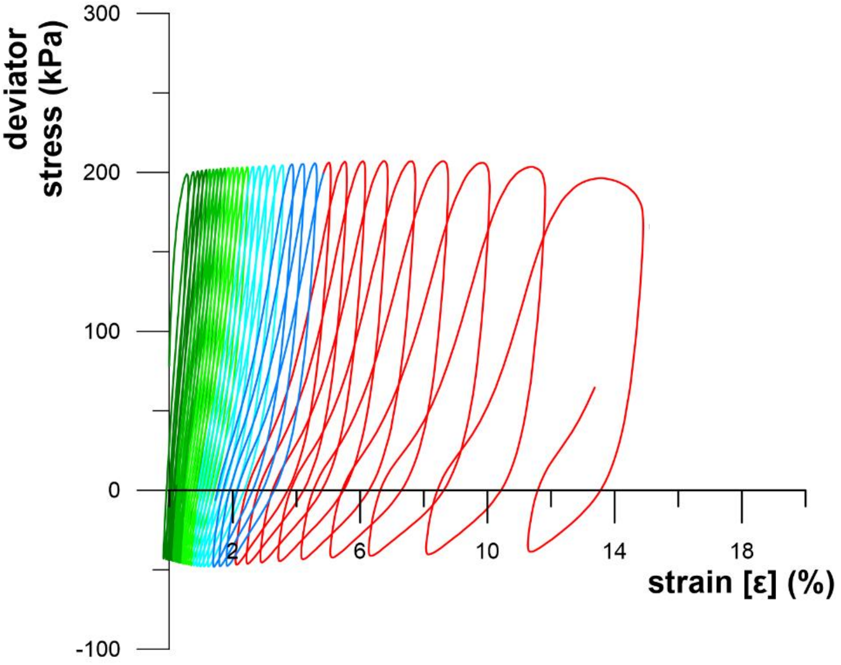

Figure 7.6. Deviator stress (kPa) vs strain (%) for test 5 (40 kPa **T**av and 60 kPa **T**cyc). The legend is outlined in the black box.

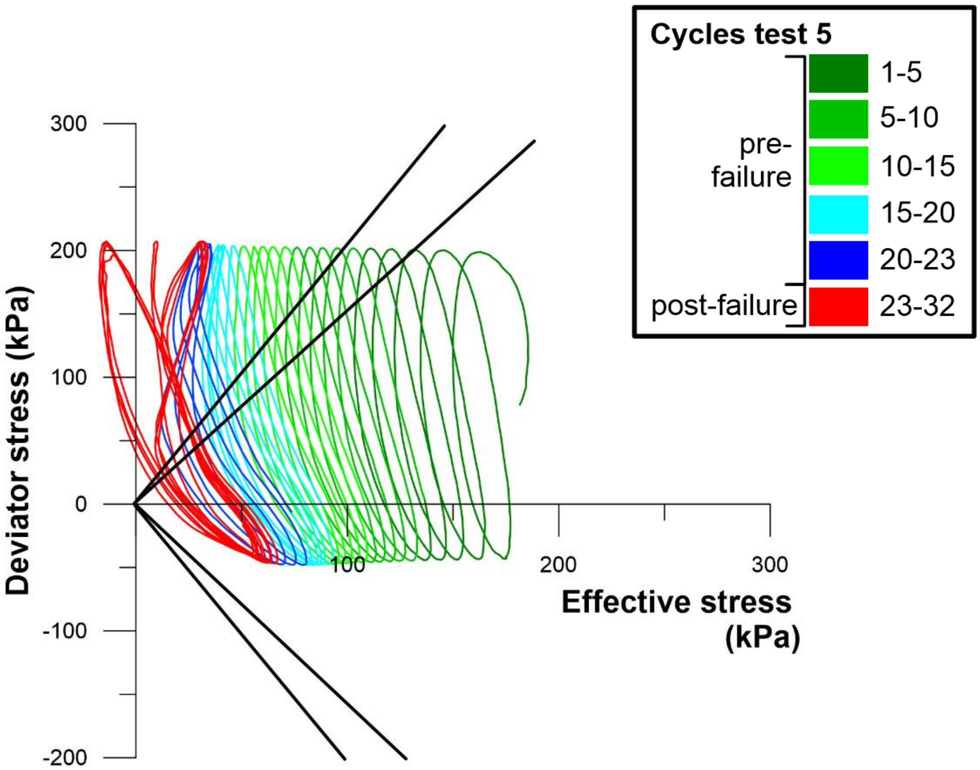

Figure 7.7. Deviator stress vs effective stress for test 5 (40 kPa **T**av and 60 kPa **T**cyc). The legend is outlined in the black box.

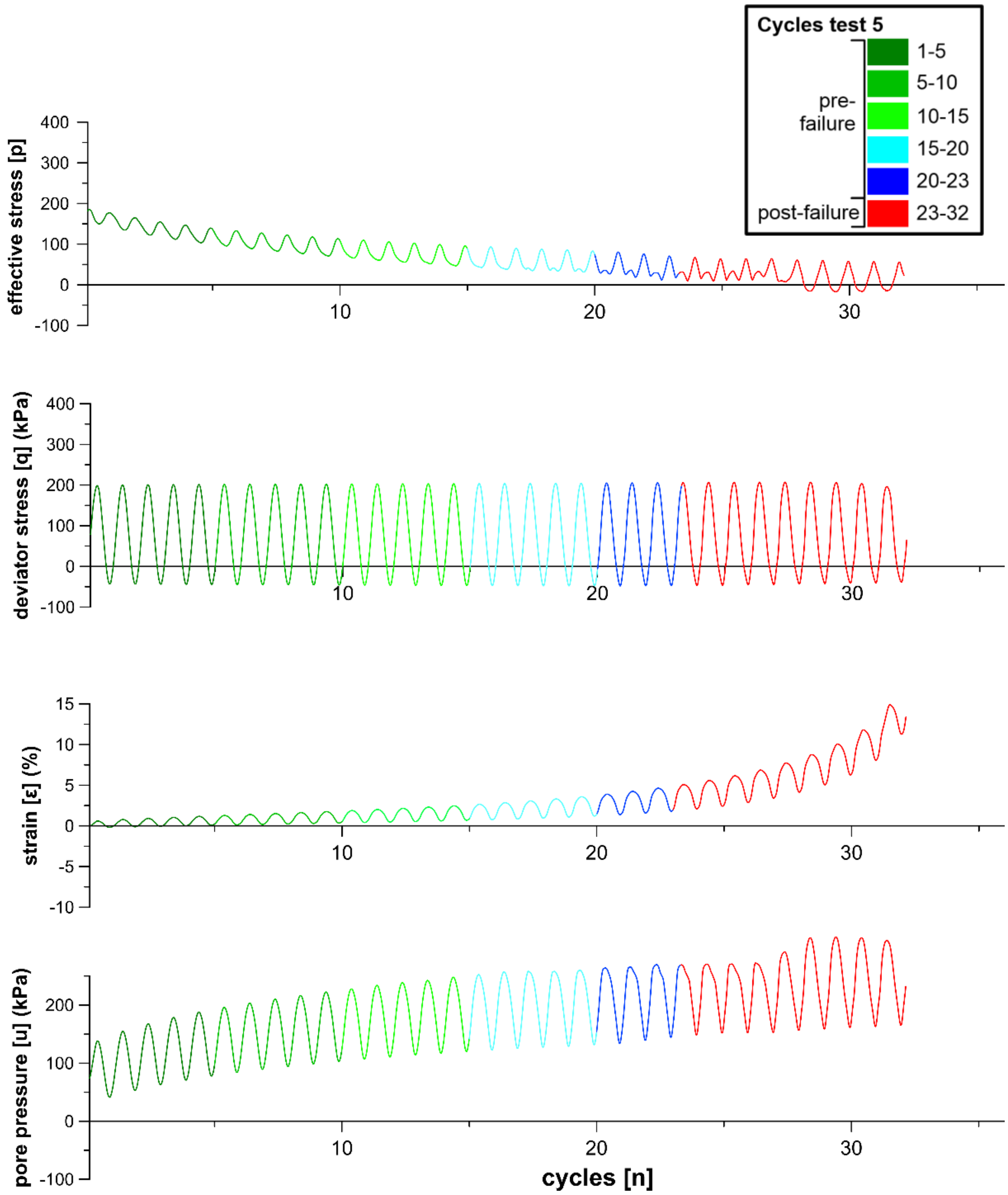

Figure 7.8a-d. From top to bottom: Effective stress (a), deviator stress (b), strain (c), and pore water pressure (d) vs cycles for test 5. The legend is outlined in the black box.

7.3.3 Type 2 response

Type 2 response is characterised by low-high application of T_{cyc} and no application of T_{av}. This resulted in stress-strain loops which accumulated symmetrically around the origin. Type 2b has a high application of T_{cyc} (60 kPa), and failure was characterised by symmetrical stress-strain loops before failure, and asymmetrical loops after failure. Type 2a has a lower application of T_{cyc} (40 kPa) and has symmetrical loops before and after failure. Test 7 displayed type 2b characteristics, while test 8 displayed type 2a characteristics.

7.3.3.1 Type 2a

Refer to **Figures 7.9, 7.10 & 7.11** over the following paragraph. Within the first 500 cycles, pore water pressure generation increases from 0 to 75 kPa, inducing a significant reduction of effective stress (decrease from 240 kPa to 150 kPa). Strain increases very slightly with each cycle in both positive and negative directions. The S-shaped hysteresis loops are steeply inclined and narrow, indicating very little energy dissipation and high stiffness (**Table 7.3**). Between 500-1500 cycles, pore pressure generation is much less than within the first 500 cycles, resulting in a slowing of the rate of reduction of effective stress (**Figure 7.10**). Between 1500-2000 cycles the rate of pore pressure generation increases again and effective stress is further decreased. Deviator stress slightly increases at both positive and negative ends of hysteresis loops. Between 2000-2155 cycles deviator stress and strain increase at a greater rate. Deviator stress and effective stress reach a peak before decreasing drastically, concomitant with a rapid development of positive and negative strains. The trough amplitude of u_{cyc} becomes much higher after failure in comparison with before failure. Hysteresis loops in **Figure 7.10** very roughly follow the failure envelope, however more effective stress is lost before failure occurs than static tests. Unlike test 7, where hysteresis loops become asymmetrical following failure, hysteresis loops remain roughly symmetrical around the origin following failure.

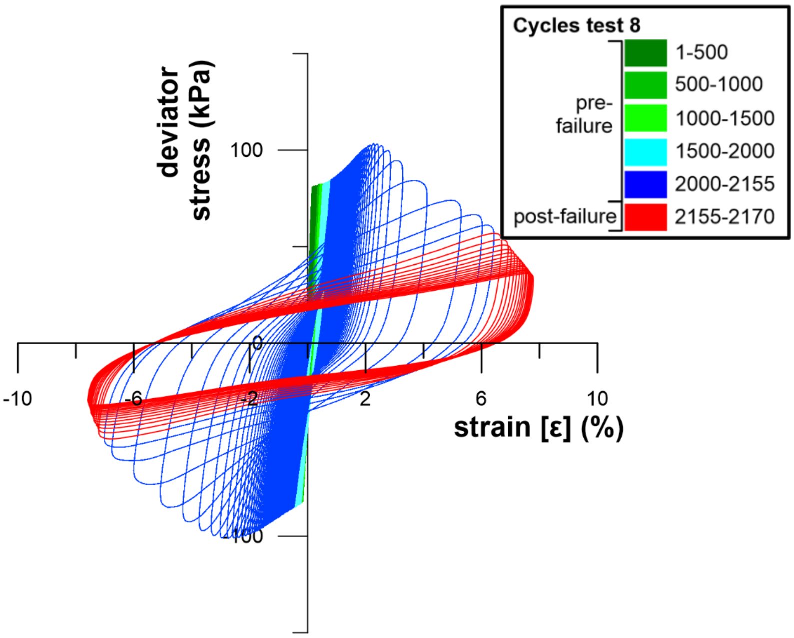

Figure 7.9. Deviator stress (kPa) vs strain (%) for test 8 (type 2a) (0 kPa τav and 40 kPa τcyc). The legend is outlined in the black box.

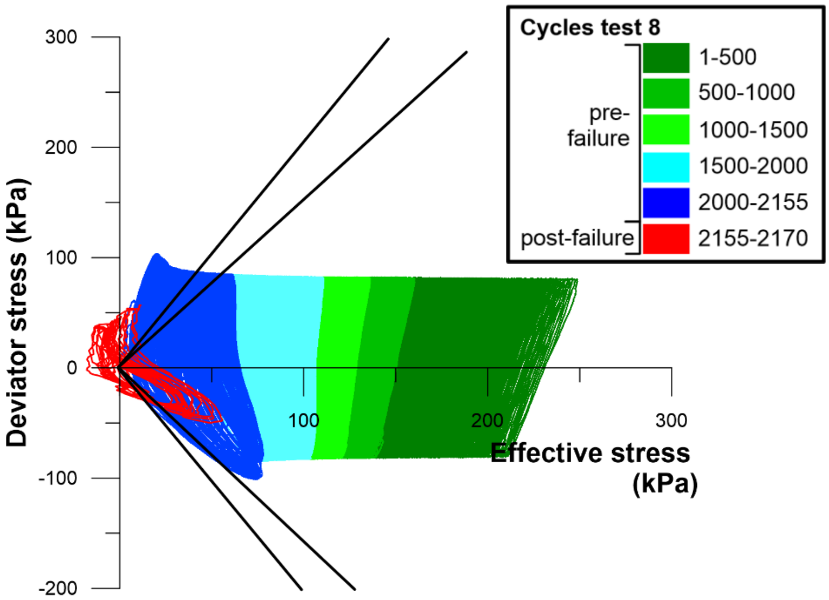

Figure 7.10. Deviator stress vs effective stress for test 8 (type 2a) (0 kPa τav and 4 kPa τcyc). The legend is outlined in the black box.

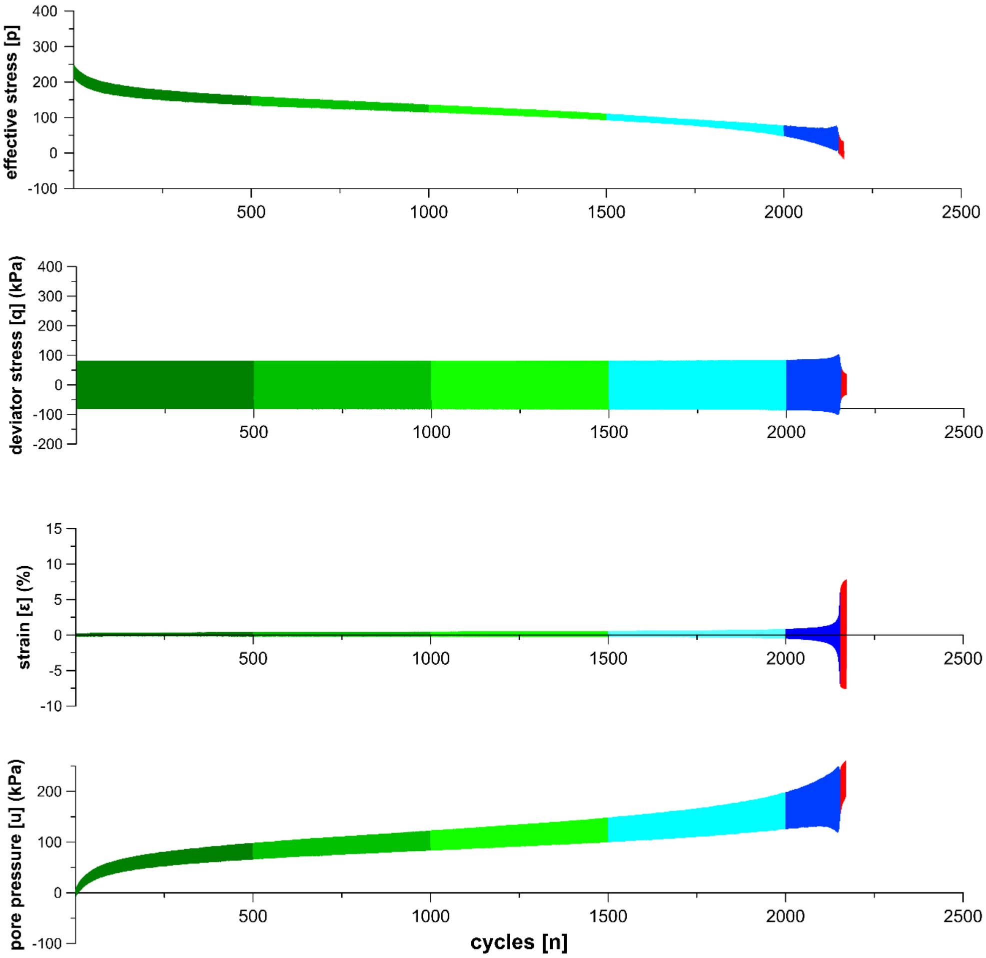

Figure 7.11a-d. From top to bottom: Effective stress (a), deviator stress (b), strain (c), and pore water pressure (d) vs cycles for test 8 (type 2a).

7.3.3.2 Type 2b response

Only test 7 has a type 2b response. The stress-strain curve in test 7 is roughly symmetrical about the origin prior to failure (**Figure 7.12**), in response to the application of 60 kPa τ_{cyc} and 0 τ_{av} (**Table 7.3**). After failure, the stress-strain curve favours positive axial strain preferentially over negative axial strain (**Figure 7.12**). The subtraction of 40 kPa τ_{av} to 0 τ_{av} from tests 11 to 7 correlates with the increase in cycles to failure from 225 to 320 (**Table 7.3**). No application of τ_{av} correlates to $\gamma_{av} = 0$, while the high application of τ_{cy} correlates to $\gamma_{cyc} = 5$ (**Table 7.3**). u_{cyc} is slightly lower for test 7 in comparison to γ_{cyc}.

In cycles 1-100, pore water pressure increases from 0 up to 100 kPa (**Figure 7.14d**), resulting in close to an approximate 75 kPa effective stress reduction. Hysteresis from cycles 1-100 are narrow (low dissipation of energy), S –shaped, meaning stiffness varies throughout the positive and negative stress, and have high inclinations (high stiffness). Hysteresis loops also migrate roughly symmetrically around the origin, meaning that the sample is straining in equal amounts in both the positive and negative directions. Between 100 – 200 cycles, the rate of pore pressure generation slows, resulting in a slowing of effective stress reduction. A slight bump during the rise of each effective stress cycle (highlighted in **Figure 7.14a**) should indicate a similar anomaly in pore pressure (**Figure 7.14d**) however, none is observed, so it remains unclear what causes this bump in effective stress. This bump becomes more pronounced as effective stress is lost, and gradually migrates to the crest of the cycle so that there is a bi-modal peak of effective stress during cycles 200-300. The bump then proceeds to migrate down the other side of the cycle, becoming gradually more pronounced towards failure and after failure (**Figure 7.14a**). Between cycles 200-300 strain slightly increases and pore pressure continues to steadily rise, reducing the effective stress to 75 kPa. Between 300-320 cycles, deviator stress, which has been constant in fluctuating around the applied τ_{av} until this point, suddenly rises and peaks at both negative and positive ends of the hysteresis loops, corresponding to an increase in pore water pressure. The deviator stress peak is curved. After peak deviator stress, positive and negative strains rapidly develop just prior to 5% strain (failure). At the same time as peak deviator stress is reached, effective stress flattens off. During cycles 320-345 (failure) strain rapidly increases and effective stress is suddenly decreased. Hysteresis loops (**Figure 7.12**) rapidly become broader and the inclination of the centre of the loops has a very shallow angle, meaning the stiffness of the soil has been reduced following failure. Hysteresis loops also become asymmetrical, with the majority of strain being positive (**Figure 7.12**).

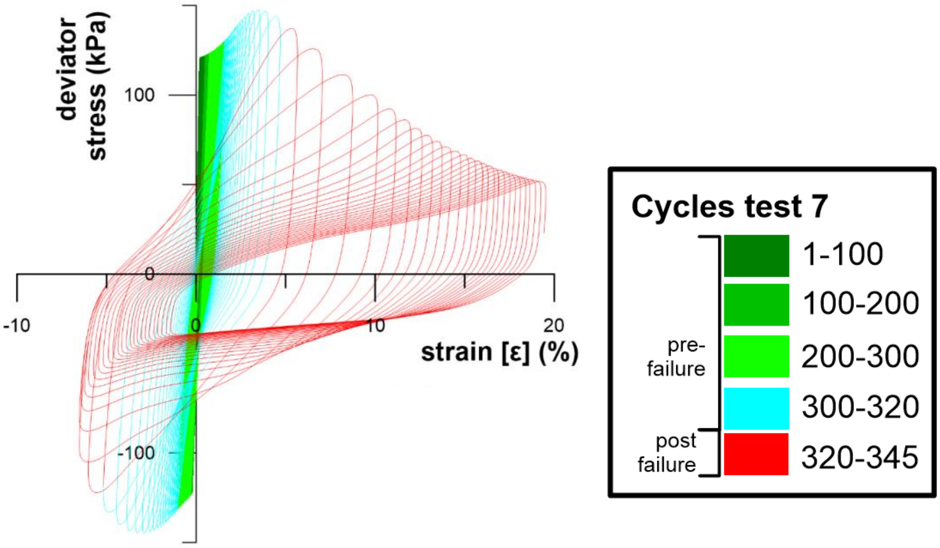

Figure 7.12. Deviator stress (kPa) vs strain (%) for test 7 (type 2b) (0 kPa Tav and 60 kPa Tcyc). The legend is outlined in the black box.

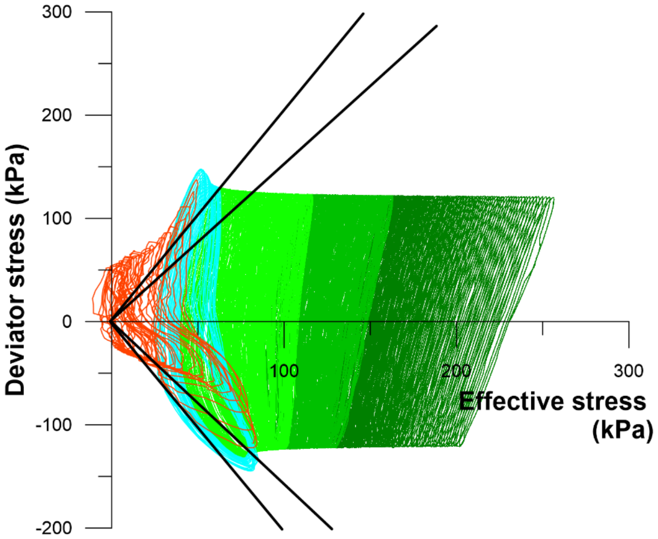

Figure 7.13. Deviator stress vs effective stress for test 7 (type 2b) (0 kPa Tav and 60 kPa Tcyc). The legend is outlined in the black box.

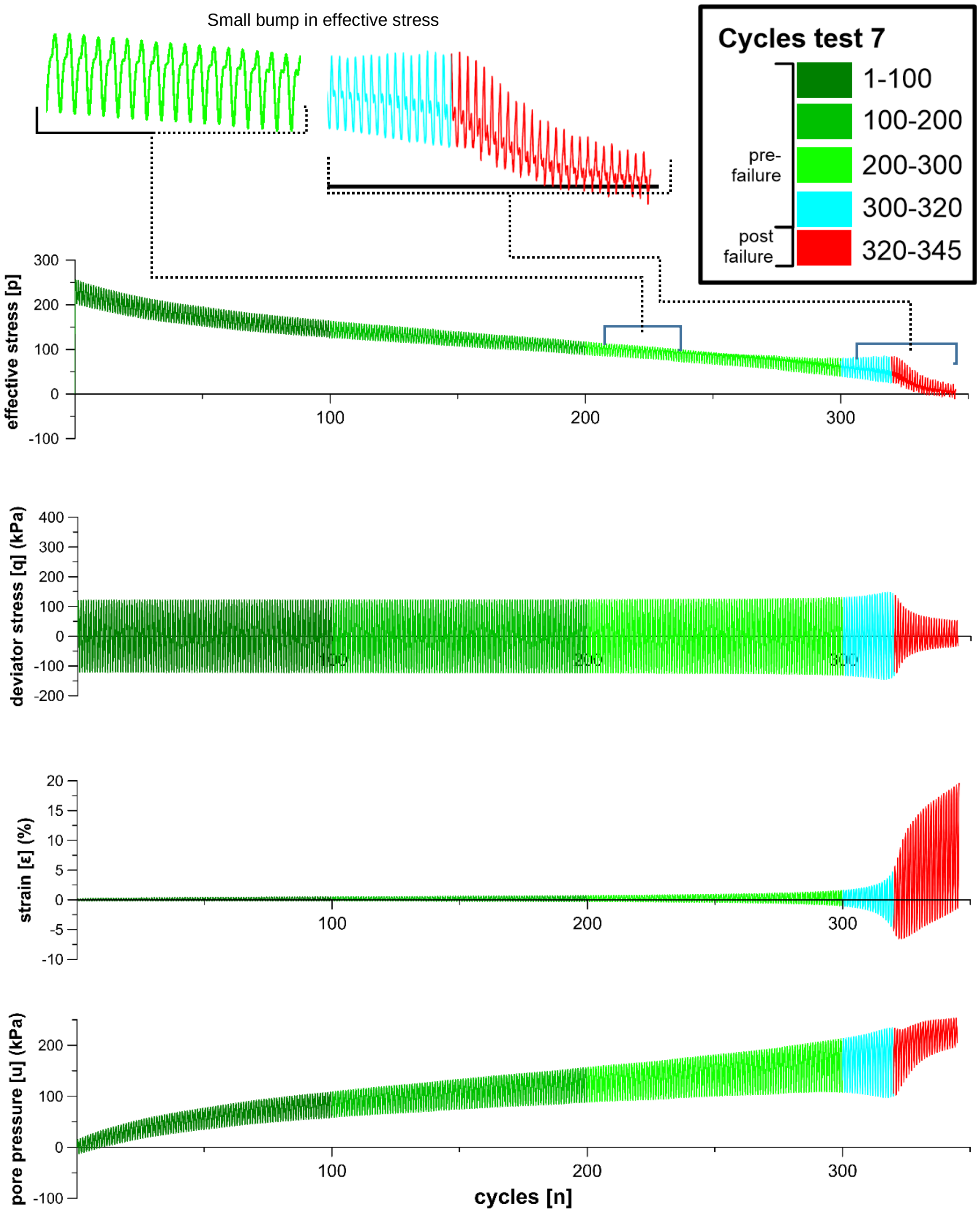

Figure 7.14a-d. From top to bottom: Effective stress (a), deviator stress (b), strain (c), and pore water pressure (d) vs cycles for test 7 (type 2b). The legend is outlined in the black box.

7.4 Contour plots

The cyclic contour plot developed from the cyclic triaxial results is herein presented. τ_{cyc} and τ_{av} were first normalised by the undrained shear strength (S_u = 120 kPa). The normalised values are presented in **Table 7.4**.

Table 7.4. Average and cyclic shears stresses, normalised by the undrained shear strength S_u. The normalised values are used to plot tests on the contour plot.

Test	Undrained shear strength (S_u)	Average shear stress (τ_{av})	Normalized average shear stress τ_{av}/S_u	Cyclic shear stress τ_{cy}	Normalized cyclic shear stress τ_{cy}/S_u
4	120	75	0.63	30	0.25
6	120	75	0.63	75	0.63
12	120	60	0.50	50	0.42
5	120	40	0.33	60	0.50
11	120	30	0.25	60	0.50
7	120	0	0.00	60	0.50
8	120	0	0.00	40	0.33

Using Anderson's (2015) contour plot as a template, contours were drawn on by simply observing the different data point values and drawing lines on where deemed necessary i.e. no algorithm was used to formally define contours. In **Figure 7.15** the original data is plotted, with number of cycles annotated; contours of numbers of cycles to failure are added in **Figure 7.16**. The contours start at the normalised value of 1 (100%) τ_{av}. With a high application of τ_{av}, a very slight application of τ_{cyc} causes the cycles to failure to increase exponentially, as observed by the very closely spaced contours. A general trend observed is that when τ_{cyc} is low, despite a moderate application of τ_{av}, the number of cycles to failure increases dramatically, as seen by the increase in cycles from test 7 (320 cycles) to test 8 (2155 cycles). The <1 cycle to failure contour is defined by the single existence of test 6. The spacing between the 1-100 contour widens as cyclic stress increases and, the contour line decreases in inclination towards the y-axis. The 100-1000 contour follows a similar, but more pronounced pattern with the contour spacing widening, and the contour line reducing in inclination toward the y-axis.

In **Figure 7.17** the average shear strain (γ_{av}) and (γ_{cyc}) at failure for each test is plotted; contours for these annotated points are added in **Figure 7.18**.The γ_{av}/γ_{cyc} at failure contours are also roughly based on Anderson's (2015) contour plot. As τ_{av} increases, γ_{av} increases and γ_{cyc} decreases, and vice versa. The inclination of the contours becomes steeper towards the y axis, and the 0/5% contour becomes slightly inverted towards the opposite direction, due to negative τ_{av} accumulation.

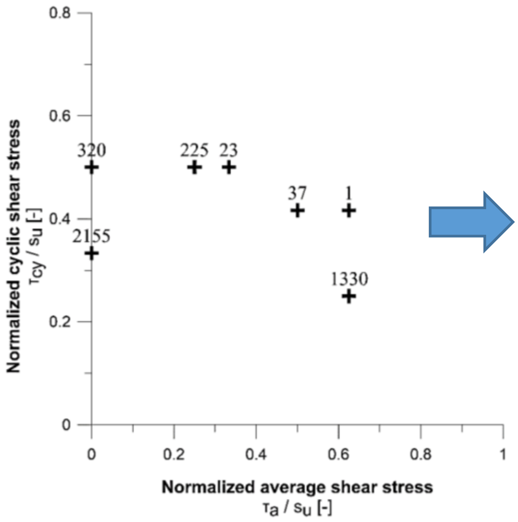

Figure 7.15. The seven plots with cycles to failure (Table 7.2) labelled, before contours are drawn on.

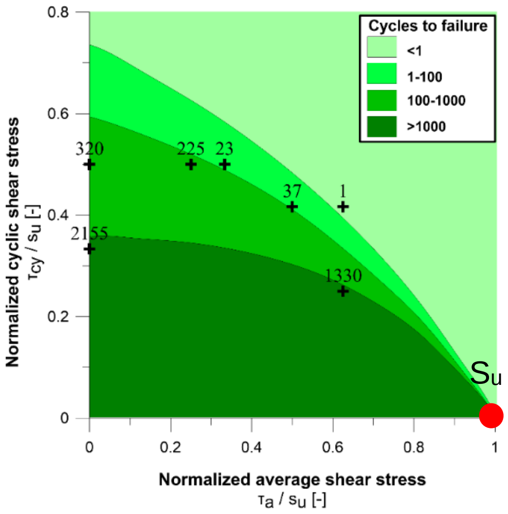

Figure 7.16. Contours drawn on for cycles to failure.

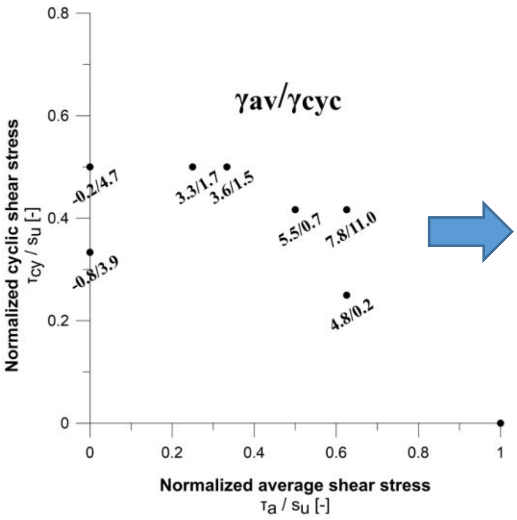

Figure 7.17. The seven plots with average shear strain γ_{av} and γ_{cyc} at failure (Table 7.2) labelled below each plot, before contours are drawn on.

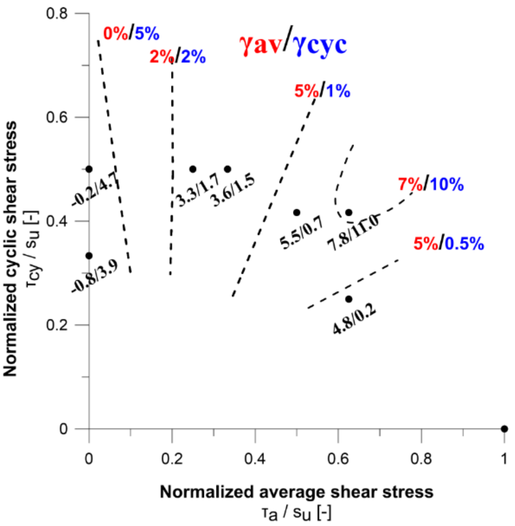

Figure 7.18. Contours drawn on for γ_{av} and γ_{cyc}

The 7%/10% contour, relating to test 6, is opposite to the trend of decreasing / increasing average strain (γ_{av}) with increasing τ_{av}. This may be an anomaly due to sample heterogeneity, or it may also be because test 6 did have the highest application of cyclic and τ_{av} (**Table 7.3**), or a combination of the two. Because only seven results were used to draw contours, the results are not considered robust enough to draw reliable conclusions.

The final contour plot is presented in **Figure 7.19**, and discussed in Chapter 8.

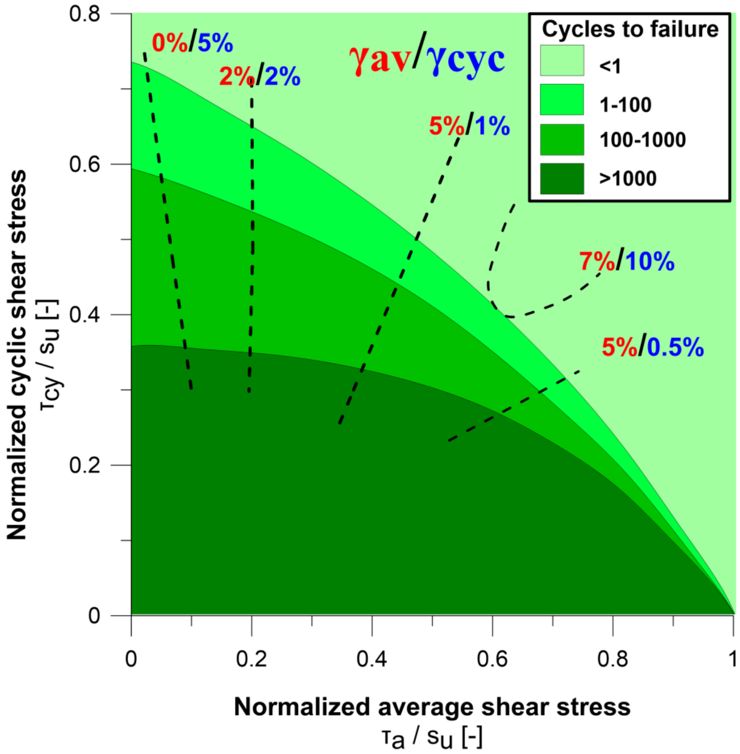

Figure 7.19. The contour plot produced with contours differentiating expected cycles to failure (green shading) and average (γ_{av}) and cyclic (γ_{cyc}) shear strains for different combinations of average and T_{cyc}. An example would be at an average shears stress of 0.4 and T_{cyc} of 0.4, the sample should fail between 1-100 cycles, and have an γ_{av} of close to 5% and γ_{cyc} of close to 1%, as the plot is near that contour.

7.5 Chapter summary

Two static triaxial tests, 7 cyclic triaxial tests and the resultant cyclic contour plot incorporating all tests are presented in Chapter 7. The static triaxial tests provided both (a) the failure envelope/critical state line of the p'-q' plots, which was used as a standard of where cyclic tests should also fail, and (b) the undrained shear strength S_u, which was used as a normalising parameter for both τ_{av} and τ_{cyc} for the x and y axes (respectively) of the cyclic contour plot.

Static triaxial results showed the material to fail at 2-2.3 % strain. The stress-strain curve had a highly curved peak indicating a rapid loss of strength, and pronounced strain softening in the range of 18-23% of total axial strain. Pore pressure curves rise rapidly, and level off and continue to gradually rise following peak deviator stress. P'-q' plots show contractancy at failure rather than dilation.

Cyclic triaxial results appeared to be a sequence with two end members (type 1 and type 2). Type 1 was characterised by an overall positive strain accumulation, while type 2 responses showed symmetrical positive and negative strain around the origin. Subtypes were characterised by changes in the shapes of stress-strain loops.

Subtype 1a had a combination of τ_{av} and low τ_{cyc} applied. Subtype 1a responses (tests 4, 6, 12) had roughly symmetrical loop shaped stress-strain curves. With each loading-unloading cycle, a small positive axial strain accumulated. Hysteresis loops slightly increased in area and decreased in inclination after failure. Following failure, pore pressure slightly decreased, strain increased dramatically, and deviator stress stayed the same. In type 1a tests (excluding test 6 which failed after 1 cycle), effective stress was most rapidly lost within the first increment of cycles, and continued to be lost at a decreasing rate until it reached to near the failure envelope defined by the static triaxial tests.

Subtype 1b has to low τ_{av}/ high τ_{cyc} applied. Type 1b responses (tests 5, 11) are still classed as type 1 because strain still progressively increases in the positive direction. Sub classification is warranted by the change in shape of strain hysteresis loops from a symmetrical loop to an asymmetrical s-shape. Deviator stress decreases following failure while pore pressure increases in a stepwise jump concomitant with decreased effective stress. A reduction of 10 kPa τ_{av} resulted in a jump of 23 to 225 cycles to failure from test 5 to 11.

Subtype 2a has a combination of no τav with low application of τcyc The only type 2a response (test 8) was characterised by roughly symmetrical S-shaped hysteresis loops where, strain incrementally evolved symmetrically in both positive and negative directions about the origin. Effective stress and deviator stress reached peaks before failure, and decreased dramatically following failure, while pore water pressure increased gradually before dipping slightly before failure, after which it increased again. Type 2b (test 7) had roughly symmetrical S-shaped stress-strain curves about the origin until failure, where strain preferentially accumulated in the positive direction, rather more like type 1 stress-strain curves.

All tests decreased in stiffness from cycle 1 to the cycle at failure (**Table 7.3**), with a more pronounced loss of stiffness correlated with high initial stiffness values in tests (4 and 8) with low applications of τ_{cyc}. Overall an application of low τ_{cyc} results in a dramatic increase in initial stiffness and also the number of cycles to failure, as evidenced by tests 4 and 8, which both fail after 1000 cycles. A reduction of τ_{av} has a lesser influence on cycles to failure, for example the reduction of τ_{av} between tests 5 and 11 results in cycles to failure increasing in the range of 100’s rather than 1000’s. γ_{av} and γ_{cyc} and u_{av} /u_{cy} at failure both roughly correlate to applied τ_{av} and τ_{cyc}.

The pattern of increasing γ_{cyc} with increased τ_{cyc} and vice versa with τ_{av} is evident in the cyclic contour plot, with the exception of test 6, which may be a result of (a) error introduced by sample heterogeneity, or (b) the actual correct response of high applications of τ_{av} and τ_{cyc}.

CHAPTER 8

DISCUSSION

8.1 Introduction

This chapter presents the discussion of the geomorphology and stratigraphy, geomechanical properties, and failure mechanisms, for two sensitive soils from Tauranga, one being located at the Bramley Drive landslide (OM1) and the other from a landslide in Matua (M1). Failure mechanisms relate observations in static and cyclic triaxial tests to microstructural properties of shear zones which evolved during triaxial loading, by thin section and micro-CT. In some places, raw data from Wyatt’s (2009) thesis have been utilised to add depth to the data of the two materials I tested. Results are also compared and discussed in light of relevant literature. The localities of samples from previous studies used for comparison in the discussion is outlined in **Figure 8.1**.

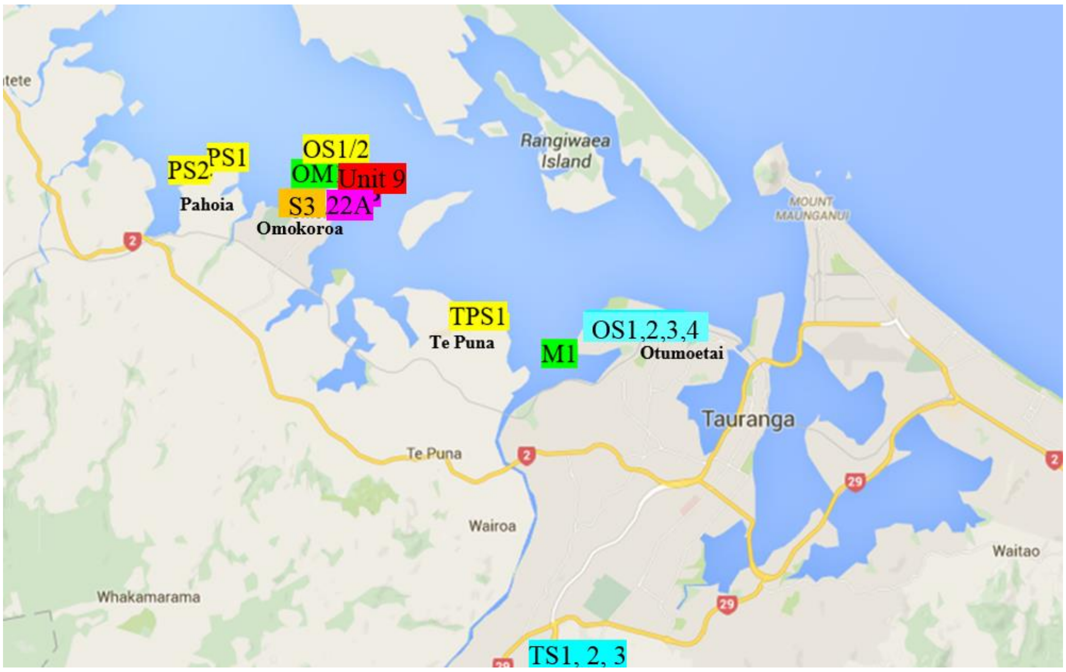

Figure 8.1. Sample sites of sensitive material tested in this study and previous studies. The red label is from Keam (2008), the orange label is from Gulliver & Houghton, 1980, green labels are this study, blue labels are from Wyatt (2009), purple labels are from Arthurs (2010) and yellow labels are from Cunningham (2012).

8.2 Discussion of geomorphology and stratigraphy

8.2.1 Omokoroa

8.2.1.1 Stratigraphy

The geological units at Omokoroa have been well studied (Gulliver & Houghton, 1980; Keam, 2008, Wyatt, 2009; Arthurs, 2010; Tonkin & Taylor, 2011; Cunningham, 2012; Moon *et al.* 2015). The machine borehole core log (drilled adjacent to the weather station in **Figure 4.7**) shows an extra-sensitive layer (S_t > 16, NZGS, 2005) at approximately 23 m depth, within a clayey SILT layer of Pahoia Tephra. Ideally, this material would be tested in this study, owing to its extra-sensitive nature and likely contribution to shear zone development of the Bramley Drive slips. This layer lies above the Te Puna Ignimbrite, which is at a depth of 26 m behind the slide, but outcrops on either side of the landslide bowl (**Figure 4.7**), i.e. the extra-sensitive layer should outcrop just above these exposed ignimbrite outcrops. Shear vane tests at SS1 proved this layer has either (a) pinched out and did not exist at SS1 (**Figure 4.7**), or (b) the site was too dry to allow for sensitivity development. Why this soil has a much higher sensitivity than surrounding material is under investigation by Max Oke Kluger (University of Bremen) and Dr Vicki Moon (University of Waikato).

Moon (2015) postulates that the stratigraphic sequence of the failure scarp on either side of the exposed ignimbrite cliffs to be a thickened sequence of primary and reworked Pahoia Tephras, which accumulated in a paleovalley. A seismic survey carried out adjacent to Bramley Drive by Moon in early 2016 confirms that this paleo valley extends offshore. Whether more paleo valleys like this exist along Omokoroa is yet to be defined by further seismic surveys. The paleo valley and offset of sediments within Omokoroa Peninsula, expressed as a slight tilting of the strata towards the southwest at Bramley Drive, may be controlled by fault movement due to uplift of the central Tauranga Harbour (Christophers, 2015). The paleovalley may have initially been created by a local fault controlled depression. The Te Puna Ignimbrite is known to be a weakly welded to non-welded ignimbrite; at Bramley Drive, a fault controlled depression may have been infilled with a local pocket of non-welded to weakly welded Te Puna Ignimbrite. The extra-sensitive overlying Pahoia Tephras, that further infilled that paleovalley comprise the derived from re-worked or *in situ* volcanic materials, from local (Tauranga Volcanic Zone) or distal (Taupo or Volcanic Zone) sources (Briggs *et al.* 1996). The source of the Te Puna Ignimbrite is also unknown. Evidence for a local caldera source includes negative gravity anomalies in the northern margins of the harbour (Briggs *et al.*

2005), and phenocrysts found by Cook (2016) in an ignimbrite near Waihi suggest a magma chamber underlying north Tauranga Harbour (Cook, 2016). Briggs points out that the orientation and distribution of Te Puna Ignimbrite does not indicate a northern source, but rather a west/southwest source (Briggs *et al.* 2005).

Sensitivity is likely to have developed by the following sequence (Moon *et al.* 2015; Kluger *et al.* unpublished work): (1) Pahoia Tephras were deposited in low energy environments, allowing an open structure of glass shards and porous pyroclastic material to be preserved, (2) small particle size, an open structure allowed capillarity effects to withhold pore water so that (3) weathering of rhyolitic glass shards and plagioclase contributes Si to the pore water, giving preferential conditions favouring halloysite formation. What causes the specific formation of different halloysite morphologies is currently being investigated by Kluger and others at the University of Bremen. So far, it has been found that the highly sensitive layer at 23 m depth is thin, and has a significant increase in the concentration of spherical halloysite, as opposed to overlying Pahoia Tephras, which have higher concentrations of tubular halloysite relative to spherical halloysite (Kluger, unpublished work). The thin, homogeneous nature of this deposit suggests that it was an airfall tephra deposit (Max Oke Kluger, personal comment, 20/03/2016). Therefore, extra-sensitive deposits like this may be correlated to air fall tephras, over reworked tephras.

The Silty CLAY material collected at SS2 (OM2a) is likely to be reworked or *in situ* volcanic material. No cross bedding or distinct stratigraphic features that strongly indicate either situation were found. The unit above OM2b at SS2 (Silty CLAY with some sand) could also be from either a primary or reworked material. The sand could be introduced from either reworking of primary volcanic material with estuarine material, or be a primary eruptive deposit i.e. ash fall or ignimbrite flow. The fairly homogeneous thickness, and no obvious cross bedding, indicate that it could be a primary weathered volcanic deposit, possibly related to the Te Puna Ignimbrite (0.93 Ma; Briggs *et al.* 2005; Arthurs, 2010). This unit also had distinctly higher manganese concentrations, and a thickened layer of manganese at the contact between OM2a and OM2b. Manganese precipitates from soil solution at high pH levels (> 8) (Vodyanitskii, 2009). The concentration of manganese is likely due to high pH pore water pooling at the base of the more permeable (sandy) upper layer, above the less permeable lower (clayey) layer i.e. a higher pH favours precipitation of manganese. The contact was sharp indicating an abrupt change in depositional conditions, or erosion of the underlying clay during deposition of OM2a.

8.2.1.2 Geomorphology

The coastal cliff landslip at Bramley Drive is a significant failure with geomorphological characteristics comparable to sensitive soil landslides of the northern hemisphere. The Bramley Drive landslide has geomorphic features which are most similar to flow failures described by Locat *et al.* (2011) (**Figure 2.10**) rather than spreads or translational progressive slides (Locat *et al.* 2011). These features include a largely scarred, empty landslide crater, a large flowslide runout component, and to a lesser degree, a narrow landslide "neck" (Locat *et al.* 2011). The scarp has a slump-like geomorphology; its failure surface is approximately equidimensional and bowl-shaped (Hungr *et al.* 2014). It is speculated that blocks of Te Puna Ignimbrite underlie the 1979 debris and 2011-2012 debris, giving the "stepped" appearance of the runout lobes. Like landslides in glacial outwash plains, the landslide at Bramley Drive has retrogressed, however in this instance, retrogression has spanned decades, over a relatively short distance, in comparison with the "domino" effect observed in north hemisphere slides, where a series of landslides occurring in rapid succession immediately after one another can result in long retrogression distances (Geertsema *et al.* 2005; Geertsema *et al.* 2006; Hansen *et al.* 2007; Lévy, 2012).

Whether other large landslides of this type around Omokoroa and Tauranga are correlated to paleovalleys and thickened tephra sequences is to be confirmed by further research. Relict landslip scars around Omokoroa (Gulliver & Houghton, 1980; Christophers, 2015) show that the magnitude of the current Bramley Drive slip is not an outlier in terms of size and amount of material eroded at Omokoroa, for example the Hamurana Place slip in 1962 (60 m wide, 20 m high, long runout lobe) (Gulliver & Houghton, 1980). Further seismic mapping of the harbour floor adjacent these relict slips would be beneficial to identify regions that may be at risk of large failures like that of Bramley Drive.

According to a report by Tonkin and Taylor (2011), the 2011-2012 reactivations were due to relaxation of the slope following the 1979 event, triggered by heavy rainfall. They predict that the over steepened central and southern portions will continue to "relax" over the next 10 years until slope equilibrium of between 40 – 50º is reached, as did the slope following the 1979 failure. Currently (May, 2016), no tension cracks are observable.

8.2.2 Matua

8.2.2.1 Stratigraphy

The sensitive sediments at the Matua landslip site are distinctly fluvially reworked tephras; a high degree of channelization is observed in the Matua Subgroup at the site investigated, with silty sand layers cross bedded with silty clay layers. The rapid transition between these two deposits indicates an environment of deposition of higher energy than Omokoroa sediments, with channels constantly changing direction.

8.2.2.2 Geomorphology

From the morphological evidence available, landslide classification was classed as complex. Several lines of evidence indicate that that a relatively thin slice of soil has been transported off the cliff in a sensitive clay slide with both planar and rotational components (Hungr *et al.* 2014). Geomorphic features that fit with the classic planar slide include the long axis of the slip surface, the shallow nature of the slip surface, and the disrupted remoulded material. Geomorphic features that fit with the rotational slide classification include a slightly rotational slip surface and intact blocks of debris. Sensitivity is attributed to having a significant role in failure, as extra-sensitive Pahoia Tephras are present in the stratigraphic profile near the base of the scarp, and sensitive material, identified by shear vane and hand shear tests, constitutes a significant portion of the remoulded debris at the base of the cliff. Because of the long runout component and remoulded nature of the debris, the landslide has the most similarity with flow slides documented in the northern hemisphere (Locat *et al.* 2011), as opposed to other landslide geomorphologies related to sensitivity (Locat *et al.* 2011).

8.3 Geomechanical properties

Sensitive materials from this study are compared to values from previous testing on sensitive soils from Tauranga, (Gulliver & Houghton, 1980; Keam, 2008; Wyatt, 2009; Arthurs, 2010; Cunningham, 2012), Taranaki and Huntly (Jacquet, 1990), the northern hemisphere (Gylland *et al.* 2013a,b,c; 2014), and non-sensitive reference material (Bishop *et al.* 1965). Locations of the samples in the Tauranga Region and which study they are from is presented in **Figure 8.1**. A summary of geotechnical information from these publications is presented in Appendix 8.1, and will be referred to throughout this chapter.

8.3.1 Moisture content, bulk density and void ratio

Typically, sensitive soils have high moisture contents above their respective liquid limits (Gylland *et al.* 2014) in contrast to non-sensitive soils, for example London Clay, which has a moisture content of 22% and a liquid limit of 60 (Bishop *et al*. 1965). In comparison to Keam (2008), Wyatt (2009), Arthurs (2010) and Cunningham (2012), the moisture contents for both OM1 and M1 (72% and 64% respectively) are both within range of extra-sensitive clays in Tauranga (64 – 108%) (Appendix 8.1).

Porosity of OM1 (70%) and M1 (65%) is within a similar range of other extra-sensitive samples from Tauranga (58 – 77%). OM1 is in the upper range, while M1 sits about average. These values lie above the normal range of porosity for soft to stiff clays (37 – 55 %) (Lancellotta, 2009) and above the expected range for unconsolidated clays (40 – 60 %) (Selby, 1993). Moon *et al.* (2015) found sensitive materials from Tauranga, have high porosities due to loosely packed clay minerals and point to point contacts. In their SEM images of Pahoia Tephras from Bramley Drive, Moon *et al.* (2015) found that pore spaces are dominated by ultrapores (0.1 μm) and micropores (0.5 μm), meaning that small pores are omnipresent, but are unlikely to be able to rapidly transmit water. The open, point to point contacts may be correlated to (a) low settling rates of pyroclastic airfall tephras, (b) low settling rates of reworked sediment in a fluvial/ estuarine environment (Cunningham, 2012) and also (c) the evolution of clay minerals, especially halloysite microstructures, which is out of the scope of this thesis (Moon *et al.* 2015). Although the sensitivity is also related to the chemistry and microstructural interactions of clay minerals, high sensitivity is definitely related to collapsing of abundant pore spaces, and consequent release of pore water, causing fluidisation upon remoulding. High porosity can hence be utilised as a broad indicator of sensitivity for volcanic materials in NZ. Cunningham (2012) noted that sensitive materials consistently had void ratios greater than 1.48, however Keam's (2008) estimate of void ratio of an extra-sensitive Omokoroa sample is 0.4 (Appendix 8.1), therefore this indicator may not be reliable. The quick clay from Norway has a lower porosity and higher particle density than Tauranga sensitive materials, albeit a much greater sensitivity. Sensitivity related to glacial till soils is well known to be highly influenced by soil chemistry, and to a lesser degree, porosity (Gylland, 2012).

Wet bulk density has been shown to decrease with increasing moisture content (Selby, 1993). Soils with low wet bulk densities have greater pore spaces available for water to accommodate. Water has a lower bulk density than soil, therefore reducing the wet bulk density of the material (Selby, 1993). **Figure 8.2** shows that Tauranga extra-sensitive material has lower wet bulk densities and higher moisture contents than a non-sensitive material (London Clay) and also a Norwegian quick clay (Bishop *et al.* 1965; Gylland *et al.* 2013a). This is likely due to the high porosity of these soils; the high pore space reduces wet bulk density of the sample. M1 has a high wet bulk density in comparison with other extra-sensitive volcanic material in NZ (**Figure 8.2**, **Appendix 8.1**). M1 and OM1 have a slightly lower porosity than others i.e. slightly more of the sample mass is comprised of soil particles rather than pore spaces. The lower wet bulk density yet relatively high moisture content of OM1 also correlates with a high porosity (70%).

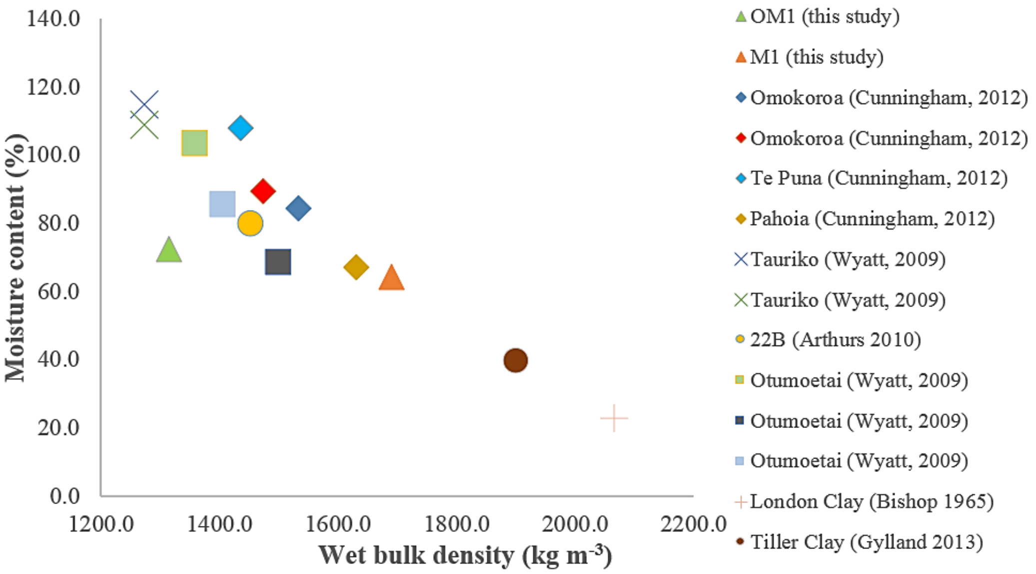

Figure 8.2. The inverse relationship between wet bulk density and moisture content.

8.3.2 Atterberg Limits and particle componentry

OM1 has the highest clay content of all extra-sensitive samples in Tauranga (62.6 %) as well as having the least sand at 0.1 %, whereas M1 is distinctly sandier (42% clay, 23% silt, 37% sand). Interestingly, both M1 and OM1 both have relatively higher clay fractions than other extra-sensitive Pahoia Tephras, which tend to have larger silt fractions (Wyatt, 2009; Cunningham, 2012) (**Appendix 8.1**).

Particle componentry is related to the geological evolution of the soil (Selby, 1993). The high clay and low sand content in OM1 could be evidence for a highly weathered *in situ* pyroclastic or air fall tephra layer with very little to no reworking. Sensitivity in volcanic ash soils has been shown to be related to hydrated and dehydrated halloysite (Moon *et al.* 2015) as well as halloysite morphology (Kluger *et al.* 2015). Moon attributed that sensitivity was definitely related to (a) small halloysite clays with high porosities and low permeabilities, and to an unknown extent related to (b) variation of pore water chemistry changes over time, which influences the cohesion of halloysite minerals. Kluger *et al.* (2015) found that halloysite morphology varies with sensitivity, as evidenced by SEM profiles of the borehole log drilled behind the slip surface. Kluger found that an increase in halloysite spheres and a reduction in tubes correlated with higher sensitivities, and vice versa.

M1 has a relatively high particle density (2777kg m^{-3}) in comparison to other sensitive materials in Tauranga, while OM1 has a mid-range particle density (2517 kg m^{-3}). The reason for M1 having a greater particle density may be due to a higher proportion of heavy minerals in the sand fraction. Jacquet (1990) relates the upper range of particle densities (>2700 kg m^{-3}) for sensitive materials he studied to a greater concentration of heavy iron minerals in the sand fraction. The mineralogy of the sand fraction was not tested so this is only an indication.

OM1 and M1 display a combination of properties typical of volcanic ash derived soils, including high liquid and plastic limits, low activity, high natural moisture content and plotting below the A line on the plasticity chart. Wesley (1973), found the same combination of properties for volcanic ash derived soils in Indonesia, which he correlated to a dominant mineral fraction of hydrated halloysite mineralogy. Although the clay fraction particle size technically defines many of these sensitive soils as clays, they all share the unusual characteristic of plotting below the A-line on the plasticity chart (**Figure 8.3**) in the range of low to high compressibility silts. Although unusual, this characteristic has been widely reported (**Figure 8.3**) for sensitive materials derived from volcanic ash. Soils with halloysite dominant clay fractions are known to exhibit relatively high plastic and liquid limits, and low activity (Smalley *et al.* 1980; Jacquet 1990).

Typical of sensitive soils derived from both volcanic ash and glacial till, M1 and OM1 have moisture contents greater than their respective liquid limits, indicating that upon remoulding, the soil will flow as a fluid without further addition of water (**Appendix 8.1**).

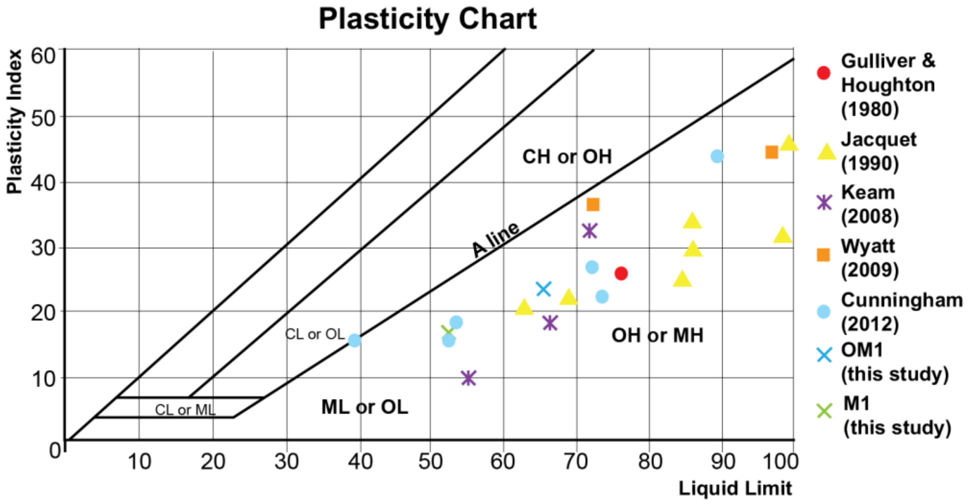

Figure 8.3. The A-line chart, adapted from Cunningham (2012) with additional data from Wyatt (2009), this study, and Gulliver & Houghton (1980).

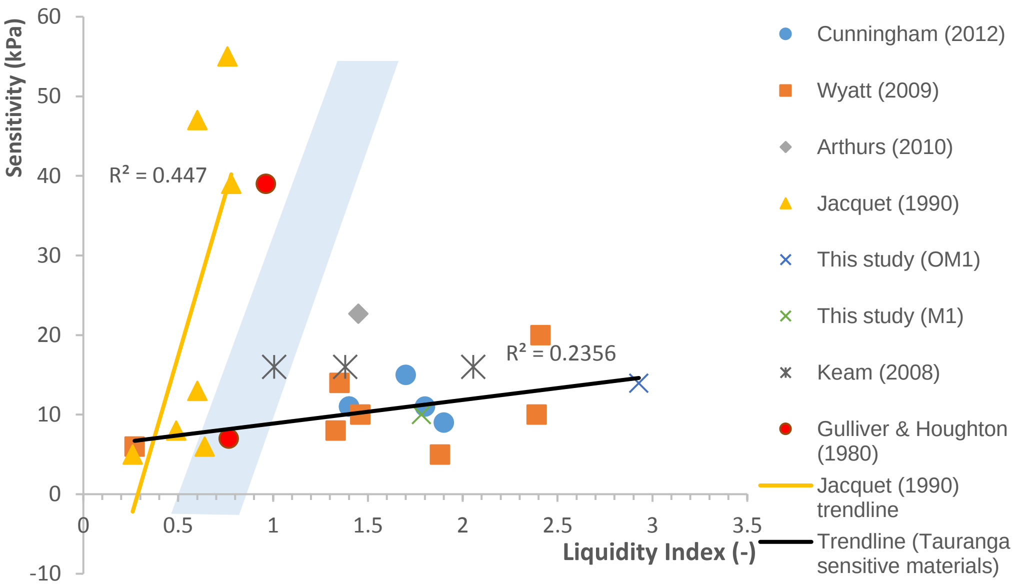

Figure 8.4. The relationship between sensitivity and liquidity index for both sensitive volcanic soils from NZ and Norwegian sensitive soils (shaded blue area) adapted from Rankka *et al.* (2004). A much sharper increase in liquidity indices with sensitivity occurs in Norwegian soils in comparison to most NZ sensitive soils. Four outliers of the trend from NZ are soils from Huntly and Taranaki, from Jacquet (1990), and one sample from Omokoroa (Gulliver & Houghton, 1980).

Liquidity index weakly correlates with sensitivity ($R^2 = 0.24$) for the majority of Tauranga sensitive materials, as shown by sensitivity vs liquidity index in **Figure 8.4**. One exception to this is a sample from Omokoroa (Gulliver & Houghton, 1980) which plots closer to the trend of Norwegian sensitive soils, and andesitic tephra sensitive soils from Taranaki (Jacquet, 1990). The higher sensitivity of soils from Taranaki has been attributed to higher shear strengths (Jacquet, 1990) and lower moisture content. An increase in liquidity index correlates with a much greater increase in sensitivity in Norwegian sensitive soils, in comparison to rhyolitic soils from NZ. Here, an increase in liquidity index with sensitivity is due to leaching ion exchange, or an active dispersing agent i.e. the ionic charge means the clays repel each other when fluidised, resulting in a much greater increase in sensitivity (Rankka *et al.* 2004). A decrease in liquidity is generally caused by drying, weathering, or consolidation (Rankka *et al.* 2004).

8.4 Failure mechanisms in static triaxial tests and their relationship to microstructural observations in thin section and micro-CT

Consolidated, undrained triaxial test results in this study are compared with tests of the same nature from Wyatt (2009) and Cunningham (2012) in **Table 8.1** and Appendix 8.4. Cunningham's (2012) and Wyatt's (2009) data is reanalysed in light of recent literature regarding the formation of shear bands in sensitive material (Gylland *et al.* 2013a,b,c; Gylland *et al.* 2014; Thakur, 2011; Thakur *et al.* 2014). Several further calculations such as the residual effective friction angle and residual effective cohesion, and strain softening parameters were calculated Wyatt's raw data.

Observations of the failed state of the specimen, and correlations between post-peak observations of pore pressure, p'-q' curves, and stress-strain curves, warranted classification into two main failure mechanisms: contractive (Type A) and dilative (Type B) failure. These failure mechanisms are backed up by microstructural and other evidence in sections 8.4.7 and 8.4.8.

Type A or contractive failure mechanisms are characterised by stress-strain curves that have peaks followed by a strain softening region, p'-q' plots that trend left or show contraction at failure, pore pressure curves that flatten or steadily rise following failure, and post failure deformation modes that are mostly shear or wedge. (**Figure 5.2**). Type A is further subdivided into strong contractive behaviour (subtype Aa) and moderate contractive behaviour (subtype Ab).

Type B or dilative failure mechanisms are characterised by stress-strain curves with minor strain softening regions or peaks at 20% axial strain, p'-q' curves that trend right along the CSL at failure (dilation), and pore pressure curves that trended flat or dropped following failure. Type B was also subdivided into subtype Ba (strong dilation) and subtype Bb (moderately dilative).

The classification of each test, and the failure characteristics is presented in **Table 8.1**. Each subtype is discussed in regard to observations, and comparisons are drawn between sensitive soils from Tauranga and sensitive soils from Norway (Gylland *et al.* 2013a,b,c; Gylland *et al.* 2014; Thakur, 2011; Thakur *et al.* 2014).

8.4.1 Important notes on triaxial data interpretation

A crucial difference between triaxial tests in this thesis and in Cunningham's (2012) and Wyatt's (2009) theses is that I chose to use a higher compression test rate of (0.5 mm/min) over all samples. Cunningham (2012) and Wyatt (2009) both used much slower test rates (Wyatt test rate: 0.15 – 0.3 mm/min, Cunningham test rate: 0.014 – 0.019 mm/min) calculated based on each samples' specific consolidation rate (British Standard 1377, 1990). The higher testing rate I chose was because during actual landslide conditions, it is unlikely that pore pressure has a chance to dissipate, so a higher compression rate therefore more closely replicates this situation.

A key point in the observation and interpretation of our triaxial data is that the low permeability of clays inhibits the ability of the pore water pressure sensor, located at the base of the sample, to capture real time changes of pore pressure evolution within the sample (Gylland, 2012). The pore water pressure response for the sample interior is therefore delayed, while the stress and strain responses are real time data.

8.4.2 Subtype Aa: Strain softening, contractive failure

Subtype Aa failure mechanisms are characterised by stress-strain curves that have peaks followed by a strain softening region, p'-q' plots that show contraction at failure, pore pressure curves that steadily rise following failure, and post failure deformation modes that are mostly shear or wedge. (**Figure 5.2**).

Strain softening materials are classically defined as instable, wherein there is the possibility that strain localisation results in the formation of a shear band (Gylland *et al.* 2014, after Mandel, 1966).

During the straight line region of the stress-strain curve pre-peak deviator stress, deformation is mostly elastic, with a minor element of plastic deformation. Because sensitive soils are brittle materials (Quinn *et al.* 2011) during the elastic range, potential energy is increasing as the soil is compressed. Small plastic deformations are likely to be occurring during this range, because in soil, irrecoverable plastic slippage between particles occurs after very small increments

Table 8.1. The failure properties and classification of consolidated undrained triaxial tests from this study, and Wyatt's (2009) and Cunningham's (2012) theses. Classification is based on whether the sample showed contractive or dilative behaviour, the degree of softening, and the pore pressure response. Dark green shading shows strongly contractive behaviour (Aa), light green shows moderately contractive behaviour (Ab), dark blue shows strongly dilative behaviour (Ba), light blue shading shows moderately dilative behaviour (Bb). ECP = effective confining pressure, PWP curve shapes after peak: F = flatten, SR = slowly rise, SD = slowly drop, SS = strain softening, Stress-strain curve shapes: CP = curved peak, SP = sharp peak, P at 20% = peak at 20%, Contraction/dilation at failure: C = contraction, C (M) = moderate contraction, D (M) = moderate dilation, D = dilation, Failure mode: B = barrel, S = shear, W = wedge.

Study	Site	Label	Test rate (mm/min)	ECP (kPa)	PWP curve shape after peak	SS (%)	Stress-strain curve shape	Contraction/ dilation at failure	Failure mode	Classification
This study (2016)	Matua	M1a	0.5	75	F	13	CP	D (M)	B with slight shear development	Bb
		M1b	0.5	150	SR	29	SP	C	S-W	Aa
		M1c	0.5	225	SR	33	SP	C	S-W	Aa
		M1d	0.5	255	SR	29	SP	C	S	Aa
	Omokoroa	OM1b1	0.5	140	SD	14	CP	C (M)	-	Ab
		OM1a1	0.5	205	SR	31	SP	C	S	Aa
		OM1b2	0.5	240	SR	20	SP	C	S	Aa
		OM1a2	0.5	280	SR	32	SP	C	S	Aa
		OM1b3	0.5	340	SR	50	SP	C	S-W	Aa
		OM1a3	0.5	355	SR	32	SP	C	S-W	Aa
Wyatt (2009)	Tauriko	TS1a	0.15 – 0.3	50	SR	2	CP	C (M)	B	Ab
		TS1b	0.15 - 0.3	200	SR	1	CP	C (M)	B	Ab
		TS1c	0.15 – 0.3	300	SR	1	CP	C (M)	I	Ab
		TS3a	0.15 – 0.3	100	F	17	CP	D	I	Ba
		TS3b	0.15 – 0.3	200	F	14	CP	D (M)	B	Bb
		TS3c	0.15 – 0.3	300	SR	17	CP	C (M)	S	Ab
	Otumoetaii	OS1a	0.15 – 0.3	20	SD	22	SP	D	I	Ba
		OS1b	0.15 – 0.3	80	F	23	SP	D (M)	I	Bb
		OS1c	0.15 – 0.3	100	F	28	SP	D (M)	B	Bb
		OS1d	0.15 – 0.3	150	SR	24	SP	C	I	Aa
		OS2a	0.15 – 0.3	20	SD	7	P at 20%	D	S	Ba
		OS2b	0.15 – 0.3	50	SD	6	P at 20%	D	I	Ba
		OS2c	0.15 – 0.3	100	F	11	SP	C (M)	W	Aa
		OS2d	0.15 – 0.3	150	F	18	SP	C	S	Aa

Study	Site	Label	Test rate (mm/min)	ECP (kPa)	PWP curve shape after peak	SS (%)	Stress-strain curve shape	Contraction/ dilation at failure	Failure mode	Classification
		OS3a	0.15 – 0.3	20	P at 20%	0	P at 20%	D	I	Ba
		OS3b	0.15 – 0.3	50	SD	2	P at 20%	D	I	Ba
		OS3c	0.15 – 0.3	80	SD	0	P at 20%	D	B	Ba
		OS3d	0.15 – 0.3	150	SD	1	P at 20%	D	B/S	Ba
		OS4a	0.15 – 0.3	20	F	19	SP	D	B-S	Ba
		OS4b	0.15 – 0.3	50	F	17	SP	D (M)	B-S	Bb
		OS4c	0.15 – 0.3	100	SR	25	SP	C	S	Aa
		OS4d	0.15 – 0.3	150	SR	20	SP	C	W	Aa
Cunningham (2012)	Omokoroa	OS1a	0.014 – 0.019	100	F	8	CP	C (M)	S	Ab
		OS1b	0.014 – 0.019	200	F	5	CP	C (M)	I	Ab
		OS1c	0.014 – 0.019	300	F	9	CP	C (M)	I	Ab
		OS2a	0.014 – 0.019	100	F	16	CP	C (M)	I	Ab
		OS2b	0.014 – 0.019	200	F	26	SP	C	B	Aa
		OS2c	0.014 – 0.019	300	F	24	SP	C	B	Aa
	Te Puna	TPS1a	0.014 – 0.019	50	SD	56	CP	C	W	Aa
		TPS1b	0.014 – 0.019	100	SD	9	CP	C	S	Aa
		TPS1c	0.014 – 0.019	150	SD	12	CP	C	S	Aa
	Pahoia	PS1a	0.014 – 0.019	50	SD	15	CP	C (M)	B	Ab
		PS1b	0.014 – 0.019	100	SR	25	SP	C (M)	I	Ab
		PS1c	0.014 – 0.019	150	SR	24	SP	C	B	Aa
		PS2a	0.014 – 0.019	50	SR	33	SP	C (M)	S	Ab

Study	Site	Label	Test rate (mm/min)	ECP (kPa)	PWP curve shape after peak	SS (%)	Stress-strain curve shape	Contraction/ dilation at failure	Failure mode	Classification
		PS2b	0.014 – 0.019	100	SR	24	SP	C	S	Aa
		PS2c	0.014 – 0.019	150	SR	22	SP	C	B	Aa

of strain (Nova, 2012). Pore pressure rises rapidly during this pre peak region for all tests, independent of changes in confining pressure. Sensitive clays in the Tauranga Region generally have low permeability (10^{-7} – 10^{-9} ms^{-1}, Moon *et al.* 2015). Although there appears to be high connectivity between pore spaces, capillary forces likely inhibit easy movement of water between pores (Moon *et al.* 2015). Despite this low permeability, the pore pressure curve mirrors the stress-strain curve during the pre-peak region.

Strain localisation, or the onset of instability, is where plastic slippage between particles initially concentrates into specific regions (Rudnicki & Rice, 1975; Derues & Viggiani, 2004; Gylland *et al.* 2013c). Vardoulakis (1996) and Vardoulakis & Sulem (2004) found that internal pore pressure gradients are required for the strain localisation to occur under globally undrained conditions. Strain localisation is most likely to occur near an instability, such as denser particles or discontinuities, pore space and water variation, or non-homogeneous boundary conditions, for example end plates (Gylland, 2012). The onset of strain localisation might be slightly inhibited by the thin rubber membrane (Vermeer, 1982). Gylland *et al.* (2014) performed undrained consolidated triaxial tests at different rates with a modified apparatus, which had a base sled on roller bearings, promoting the likelihood of shear failure. With this modification, the onset of strain localisation could be estimated by initial horizontal movement of the base sled. Strain localisation occurred just prior to or at peak deviator stress (Gylland *et al.* 2014). Following strain localisation and shear band formation, contraction of soil microstructure induces further excess pore pressure, some of which drains along the reoriented material in the shear band, and some of which dissipates into the surrounding material. Gylland interpreted the post-peak rise in pore pressure to the drained excess pore pressure registering with the pore pressure base sensor. Gylland *et al.* 2014 also observed that the modified triaxial stress-strain curves generally had lower peaks than normal triaxial tests. He attributed this to progressive failure, where some regions of the shear band were in the strain softening regime while some were still in the strain hardening regime. Thakur (2007) also observed progressive shear band development in sensitive material derived from glacial till.

The triaxial base in our tests was fixed, therefore the onset of strain localisation could not be determined in this way. However, the immediacy of rapid sample contraction at peak deviator stress in p’-q’ plots, correlated with an immediate increase in pore pressure at peak deviator stress, and observed shear banding in failed triaxial samples, suggests that similar processes are occurring in my samples in comparison to Gylland *et al*. (2014). In regard to whether progressive failure occurred, our triaxial tests are not modified, and singular shear bands do not occur in every sample. Rather, shear bands, whether it be one single band or two bands failing by wedge style, are observed in samples with contractive responses. I infer that because shear bands are still present, similar mechanisms of progressive failure, where strain hardening and strain softening are occurring simultaneously at different points within the sample must have occurred in our samples. The progressive failure mechanism, and strain localisation and contraction in localised zones, is further discussed in relation to microstructural evidence in sections 8.4.7 and 8.4.8.

Higher confining pressures generally correlated with sharper peaks for both stress-strain and p'-q' curves, higher peak deviator stresses, and higher pore water pressures, independent of compression rate. This implies that greater confining pressures induce a more rapid accumulation of pore pressure in a localised zone, resulting in a more sudden loss of strength due to plastic straining in the shear zone.

The higher test rates I used correlate with dominantly subtype Aa failure, implying that a higher test rate induces a more contractive response and strain softening. Cunningham's (2012) and Wyatt's (2009) test results show that material clearly influences the type of response, as subtype Aa failure are observed at lower rates. Further tests at different rates on the same material are required to confirm the influence of rate on failure mechanism.

Strain at failure did not correlate with effective confining pressure (**Table 8.1**). Rather, higher strain at failure did correlate with lower sensitivities, and generally lower void ratios. For example, TS3 (Tauriko) and OS3 (Otumoetai) both failed at higher levels of ε_{axial}, and both had lower sensitivities (5 and 6 respectively), and lower void ratios (1.6 and 1.9 respectively) in comparison to other sensitive Tauranga material (**Table 8.1**). A higher percentage of saturated pore spaces means that during failure there is more potential for densification, and higher resultant pore pressures following densification within the localised shear zone.

The post failure specimen or contraction/dilation response did not bear any correlation to whether the pore pressure peaked before or after peak deviator stress (**Appendix 8.4**). Contractive responses did however strongly correlate to pore pressure responses post peak deviator stress, where pore pressure continued to gradually rise, rather than drop as it does in dilative responses. I infer that this increase in pore pressure is the delayed response of the expulsion of pore pressure from the shear zone. This pore pressure response was also observed by Thakur (2007) and Gylland *et al*. (2014) in undrained, consolidated triaxial tests.

The percentage of stress lost after failure showed weak positive correlations (R^2 = 0.01 – 0.33) (OS1, OM1 (both Omokoroa)) to strong positive (R^2 = 0.33 - 0.85) correlations with effective confining pressure for some materials (M1, PS1, OS2 (Omokoroa), OS2, OS4 (Otumoetai)), while for other materials, strain softening showed no correlation (OM1, TS3) or even negative correlation (TS1, PS2, OS3 (Otumoetai) OS1 (Omokoroa) with increasing confining pressures. These contrasting results may show that in some materials, strain softening is related to the effective confining pressure applied, while for others, effective confining pressure does not appear to affect strain softening. More replicates are needed to confirm results.

The rapidity of the stress lost, (steepness of the stress-strain curve during strain softening) correlates strongly with samples tested at higher confining pressures.

The post failure sample condition for Type A responses are typically shear to wedge failure, although some barrel failures did occur for example OS2 (Omokoroa) and PS1/PS2 (Pahoia) (Cunningham, 2012). Contraction therefore does not necessarily result in the formation of shear bands. Post peak strain softening and rises in pore pressure occurred in these samples, but no shear banding was observed, as expected. This could be due to two reasons: (1) several inconsistencies, for example weaker regions, within the samples resulted strain localising in these regions over one region (a shear band) to give a barrel shape, or (2) the original interpretation of failure mode was not accurate or comparable to interpretation of failure mode in this study. Unfortunately, no pictures of failed samples were available to make comparisons for these samples (Cunningham, 2012).

8.4.3 Subtype Ab: moderate strain softening, contractive failure

Subtype Ab shows moderate contraction and strain softening responses, with pore pressure peaks that either flatten or slightly rise after failure (**Table 8.1**). Stress-strain curves have more highly curved peaks, and while there is reduction in strength after the peak has been reached, there is no pronounced drop in resistance i.e. strain softening does occur, but at a lower rate than subtype Aa.

Pore pressure mirrors the stress-strain curve in the pre peak region. Stress-strain peaks were much more highly curved than subtype Aa indicating that strain was accumulating more uniformly in the sample, rather than suddenly in shear zones. P'-q' curves however, show slight contraction at failure, showing that pore pressure had time to slightly dissipate so that contraction was not localised to a shear zone, but not to the extent where pore pressure became negative and prevented the sample from contracting. Post failure samples for type Ab showed barrel, shear and intermediate deformation, likely due to the same reasons outlined for subtype Aa.

8.4.4 Subtype Ba: Dilation

Subtype Ba samples are characterised by p'-q' curves that trended strongly right along the CSL after failure, stress-strain curves that have curved peaks, pore pressure curves that drop after failure, and post failure sample shapes that were either barrel or intermediate (**Table 8.1**).

During compression, pore pressure rises, but since the confining pressure and testing rates are low, I infer that pore pressure uniformly accumulates within the sample, i.e. pore pressure gradients do not form or form to a much lesser degree than subtypes Aa and Ab. With rising pore pressure, the sample uniformly contracts until the critical state is reached, upon which soil grains interlock, causing pore pressure to drop and the sample to dilate (Poulous, 1971; Gylland *et al.* 2014).

No subtype Ba responses were observed in the faster rate triaxial tests in this study. Subtype Ba failure was however observed at low confining pressures for OS1, OS2 and OS4 (Otumoetai, Wyatt, 2009) and at low to high confining pressures in samples OS3 (**Table 8.1**).

Subtype Bb samples (**Table 8.1**) displayed moderate dilation following peak deviator stress, characterised by stress-strain curves that have sharp peaks but with no immediate pronounced drop, pore pressure responses that flattened after failure, p'-q' curves which trended slightly to the right, and post failure sample shapes of both barrel and slight shear development.

Moderate dilation was observed at low to medium confining pressures at low test rates (OS1 and OS4 samples, Wyatt 2009) as an intermediary between contractive responses observed at higher confining pressures and strongly dilative responses observed at lower confining pressures. For the higher test rate used on M1 and OM1 materials, only one dilative response was observed, at the low confining pressure of 75 kPa.

Subtype Bb failed sample shapes are barrel to shear. During compression, pore pressure has mostly increased uniformly throughout the sample, resulting in global dilation (trending right) of the sample once the CSL line is reached in p'-q' plots. Unlike subtype Ba, where pore pressure decreases significantly upon dilation, pore pressure in this instance typically flattens out, which may be as a result of excess pore water drainage from the weak shear zones observed in some samples. While the p'-q' diagram shows subtype Bb samples to have globally dilated, some weak shear zone development shows strain localisation has evidently still occurred in some samples.

8.4.5 Discussion of material brittleness

Brittle materials are often referred to as materials that fail at less than 5% strain (Selby, 1993). Brittle materials have also been defined as materials that release greater amount of energy during failure (Bishop, 1971). If the first definition for brittleness was applied to all sensitive materials (Appendix 8.1) most materials would be classed as brittle. If the second definition of brittleness is applied to the triaxial tests results however, despite failing at low amounts of strain, the amount of stress lost after failure is minimal i.e. the material is not that brittle.

The strain softening parameter used to define the energy loss after failure is from Bishop (1971). This equation only takes the stress into account, and does not consider the strain energy required to reach the residual strength. Tavenas *et al.* (1983) showed that strain, or displacement along the shear band is just as important to consider as stress. Quinn *et al.* (2011) defined a new brittleness parameter incorporating both the stress and strain (**Equation 8.1**)

$$B_{st} = \frac{(S_{t-}1)}{125 S_t \bar{\delta}}$$

Equation 8.1

Where B_{st} is the brittleness, S_t is the sensitivity, and $\bar{\delta}$ is the nominal displacement, or the displacement of the shear band between peak and residual states (Quinn *et al.* 2011). In this study I didn't have any way to accurately measure the shear band displacement, therefore the equation from Bishop (1971) was chosen over Quinn *et al.* (2011). The strain softening parameter therefore is only a rough estimate of the amount of energy released during strain softening.

8.4.6 Discussion of variables affecting failure mechanism

It is clear that the type of material, the test rate, and the amount of confining pressure influence the type of failure mechanism.

Most materials tended toward contractive failure at higher confining pressures, showing the influence of confining pressure on failure mechanism. Not all materials followed this trend, for example OS3, which displayed strongly dilative behaviour at all confining pressures, or OS2, TPS1, PS1 and PS2, (Cunningham 2012) (**Table 8.1**) which tended towards contractive behaviour over all applied confining pressures. This demonstrates that the type of failure is influenced by the type of material.

Higher compression rates correlate with a dominance of Subtype Aa and Ab contractive failure and also shear band formation for both Matua and Omokoroa materials in this study. Tests at lower compression rates (Wyatt, 2009; Cunningham, 2012) resulted in contractive behaviour at low to high confining pressures, but the observation of shear bands was less common. Shear band formation for strain softening materials has been shown to be dependent on testing rate, from both finite element modelling (Thakur, 2011) and experimental observations (Gylland *et al.* 2013c, Gylland *et al.* 2014) on shear zone evolution in quick clay derived from glacial till. A trend of decreasing shear zone thickness with increasing rate was found. At low testing rates, barrel failure was observed in Gylland's experimental data and predicted by Thakur's model.

8.4.7 Evidence of contractive shear zones from thin sections and micro-CT

Three lines of evidence which indicate that strain localisation and pore pressure induced progressive, contractive failure occurred in shear zones of Matua and Omokoroa materials are discussed. Thin section and micro-CT evidence are firstly discussed together, and compared to contractive failure in glacial till sensitive soils (Thakur, 2007; Gylland *et al.* 2013c). Following this, the difference of friction angle and cohesion between peak and residual states of Omokoroa and Matua materials will be discussed in regard to Thakur *et al.* (2014) hypothesis that if there is no change of cohesion and friction angle between peak and residual states (called friction and cohesion softening), then another mechanism (pore water pressure) must be initiating strain softening.

Thin sections captured Type A failure i.e. contractive failure, where pore pressure rises after peak deviator stress, and significant strain softening occurs.

All thin sections in both Matua and Omokoroa material displayed characteristics of shear patterns commonly observed in shear zones in a wide range of materials and at different scales, for example in large scale brittle deformation of rock in the San Andreas fault (Byerlee, 1992) and in micro-scale deformation of kaolin clay (Morgensten & Tchalenko, 1967). The reason that these shears bear similarity is because they are related to the friction angles and principal stresses of the material (Skempton, 1966). The most commonly observed shears in these shear zones, and the shears that I observe in my thin sections, are the conjugate R and R' (Riedel) shears, and P (thrust) shears (Fossen, 2010). While these shears have been observed in many shear zones (Morgensten & Tchalenko 1967; Byerlee, 1992; Ahlgren, 2001; Gylland *et al.* 2013), the order of their development is less well understood, although it is proposed that R shears form first, followed by the less observed R' shears, then P shears, which link the shear zone together to form a final principal displacement shear (PDS).

R shears, which are observed in all thin sections, and also on the failed sample exterior, appear to accommodate most of the shear deformation. This is inferred because R shears have thicker zones of reoriented material, and are in general longer than P and R' shears. The failed samples which have one primary shear zone, for example OM1b2, and M1b, have one R shear which accommodates more shearing than other R shears in the same thin section. R shears also accommodated most of the shearing in thin sections of Tiller Clay (Gylland *et al.* 2013c).

The variability between failed triaxial specimens is too high to justify interpreting whether or not if confining pressure has had an effect on the different characteristics of shears. A study with more replicates and greater variation of confining pressures is required to make these comparisons. Gylland *et al.* (2013c) found that material between R shears was also slightly reoriented. The clay minerals in my thin sections may be reoriented, but the small particle size makes it difficult to tell. The material in Gylland's thin sections was coarser (mostly silt sized grains) so reoriented particles were more easily distinguishable.

Evidence for material contraction in R shears is observed in micro-CT scans of OM1b3. The matrix material in micro-CT, which is likely composed of hydrated and dehydrated halloysite (Max Oke Kluger, Personal Comment, 30/03/2016), is denser in R shears than the surrounding matrix. This increase in density implies reduced porosity, showing that the material has contracted. The denser grains, which I infer to be weathered volcanic glass shards based on their uniform distribution and similar particle shape and size, appear to be unaffected by the R shears. Gylland *et al.* (2013c) also observed contraction in R shears in micro-CT scans of shear zones in Tiller Clay. Denser grains in our thin sections appear to cause shear zones to thicken and spread around the denser particle. This effect is observed in thin section 2 where a weathered mineral domain interrupts the R shear which accommodates most of the deformation. On the other side of the weathered mineral domain, several R shears are observed rather than one R shear. Both P and R’ shears accommodate much less material reorientation than R shears. R’ shears are less ubiquitous than R shears. P shears are more commonly observed, and interlink R shears. No final principal displacement shears are observed.

Evidence for progressive development of shear zones is shown by thin sections 1 and 2, which capture the top and bottom (respectively) of the principal shear zone in OM1b2. In thin section 1, R shears are spaced closer together, are thinner, and the shear zone boundary between reoriented material and material outside the shear zone is sharp (normal kink band) rather than smooth (smooth shear band). P shears are also well developed, interlinking R shears together. In thin section 2, R shears are spaced further apart, the shear band shows elements of graduating from more highly sheared in the centre to lesser around the edges, and P shears are much less developed. These differences show that deformation is more concentrated and well developed in the top of the shear zone, and less well developed in lower part of the shear zone, indicating that deformation is progressive. Similar observations are seen in the M1b thin section, which also failed primarily along a single shear zone. One R shear (PSZ) which is consistent from the top to bottom of the thin section appears to have accommodated most of the shearing. At the top of the thin section, there is greater offset (5.5 mm) and fewer R’ shears in this main PSZ. In the middle of the shear zone R’ shears occur to a minor degree, and at the bottom of the thin section, R’ shears are more prevalent, and there is considerably less offset (1-2 mm). The top of this R shear is more “evolved” in shear zone development than the bottom of the R shear, indicating progressive failure.

In Matua thin sections, shears appear to propagate through sandy clay lenses, depending on their location in the sample. In M1b, R shears offset the sandy clay layer at the top of the sample. In M1d, the principal shear zone is horizontal, and concentrated in the silty clay material just below the boundary with the sandy clay, which occurs as a horizontal lens in the centre of the sample. In thin section, roughly evenly horizontally distributed R and R’ shears offset sandy clay and silty clay material. In micro-CT and thin section, sand grains in shear zones appear fractured, although it is difficult if fracturing is due to shearing or if grains were previously fractured as a consequence of weathering. Triaxial stress, strain and pore water pressure curves show that contraction occurred following failure. I propose that the material boundary acted as the weak zone where strain localisation occurred. Excess pore pressure likely accumulated in the sand lense, resulting in excess pore pressure initiating downward propagating R shear then R' shear development in the silty clay. Failure of the silty clay is shown by the multitude of R and R' shears in thin section, and by deformation concentrated in the silty clay material in the post failure triaxial specimen.

Thin sections 4, 5 and 6, which captured shear zones of OM1b3 (340 kPa effective confining pressure) have a much lesser occurrence of P shears, and minimal occurrence of R' shears. The post failure sample shape shows that deformation was concentrated over several shears in a chaotic fashion, rather than just one principal shear zone like that of OM1b2. The predominance of R shears in thin sections therefore shows that each of these shear zones are less developed, or at an early stage in evolution.

All shears are at higher inclinations than the inclination predicted based on Skempton's equations (**Table 5.10**: Chapter 5, **Table 6.2**: Chapter 6). Thakur *et al.* (2011) and Gylland *et al.* (2014) found shear band inclination to decrease with increasing compression rate. All triaxial tests in this study were done at the same rate, so I am unable to determine if such a relationship exists for my material. The higher inclination of the shear bands however, can be related to the predicted inclination of shear bands by criteria for undrained failure (Tresca Criterion) and drained failure (Coloumb Criterion) (Briaud, 2013). The Tresca Criterion predicts the shear band to be inclined at an angle of $45^{o} + \varphi/2$, where φ is the friction angle of the material. Hence, the angle of the overall the zone is expected to be greater than 45^{o}. The Coloumb criteria predicts the shear band to be 45^{o} in undrained conditions, if no expansion or contraction occurs in the shear zone. I predict that some contraction occurs within the shear zones, implying that some drainage occurs. I infer that the greater inclinations I see are due to primarily undrained contraction in shear zones, with an element of drainage before the shear band formation, explaining the higher shear inclinations.

8.4.8 Evidence of pore pressure induced contraction from cohesion and friction softening

Bernander (2000), Jostad *et al.* (2006), Thakur *et al.* (2014) and Gylland *et al.* (2013c) provided strong evidence that strain softening is controlled by excess pore pressure in shear zones, as opposed to the conventional reduction in friction angle and cohesion of the material between peak and residual states. Thakur *et al.* (2014) performed undrained consolidated triaxial tests at different compression rates on quick clay from Rissa, Norway. He compared the friction angle and cohesion values between the peak and residual states, and found that the values did not change. From this he inferred that pore pressure was the mechanism behind observed strain softening rather than friction and cohesion softening.

A comparison of effective friction angles and effective cohesion between peak and residual states for sites in this study and also for Wyatt's (2009) sites is presented in **Table 8.2**. Sensitive soils form Tauranga have previously been reported to have high friction angles and low cohesion from lab tests (Moon *et al.* 2015). CPTu tests of sensitive soil from Omokoroa however indicate that the shear resistance of these soils are low, hence the high effective friction observed may be related to the confining pressure applied (Moon *et al.* 2015).

Table 8.2. Effective cohesion (c'f) and effective friction angle (φ'f) at failure, and residual states (φ'r) and c'r), for materials tested in this study and also in Wyatt's 2009 samples.

Study	**Compression rate (mm/min)**	**Location & sample**	**c'_f**	**c'_r**	**φ'_f (°)**	**φ'_r (°)**
This study	0.5	Omokoroa (OM1)	26	24	31	26
		Matua (M1)	17	17	32	29
Wyatt (2009)	0.15 – 0.3	Tauriko (TS1)	13	13	28	28
		Tauriko (TS3)	28	24	31	29
		Otumoetai (OS1)	37	22	25	25
		Otumoetai (OS2)	18	18	28	26
		Otumoetai (OS3)	17	17	32	31
		Otumoetai (OS4)	15	12	28	28

Minor to no reductions in effective friction angle and cohesion values are observed for all samples, with the exception of a significant reduction of effective cohesion in OS1 of Wyatt (2009). Slight decrease of cohesion suggests that a small amount of cohesive "glue" bonding particles together is lost in the shear zone, while the slight decrease in friction angle suggests that particles have altered so that the degree of asperity interaction is slightly reduced. Overall, these reduction are minor, indicating that excess pore pressure is the dominant mechanism reducing material strength.

8.4.9 Overall model of contractive shear zone formation

Linking the observations from all of triaxial, thin sections and micro-CT, I infer that the onset of strain localisation occurs between the end of the elastic region (straight line of stress-strain curve) and peak deviator stress of the stress-strain curve. I infer that like the Tiller Clay tested by Gylland *et al.* (2013c) regions of excess pore pressure overcome the material strength, causing elastic stored energy to be released to initiate brittle fracturing (strain localisation). Fracture mechanics principals have been used by Quinn *et al.* (2011) to explain the progressive failure of shear zones in sensitive clay at the landslide scale. After recommendations by Skempton (1964) and Bishop (1968), Quinn *et al.* (2011) shows that energy released during strain softening in the shear zone provides energy for further fracture propagation.

Localisation is most likely to occur within weaker regions or discontinuities. Contraction of the microstructure within the localised shear band into firstly R shears, then R’ and P shears, results in further excess pore pressure generation, most of which preferentially dissipates along the reoriented material in the shear band, and some of which dissipates into the surrounding material. The reasoning behind strain localisation occurring before peak deviator stress is that pore pressure immediately increases following failure, meaning that R shears must have developed to the extent that excess pore water could drain along the shear zone to register with the pore pressure sensor at the base of the sample before peak deviator stress. For samples that had delayed rises in pore pressure in the post peak region I infer that the rise in pore pressure correlates to the complete formation of the shear band i.e. in these cases complete formation was in the post-peak region. In the samples that failed along one principal shear zone, although we have very limited replicates, we observed that deformation was more concentrated in the upper region of the shear zone in comparison with the lower, as shown by greater offset, lower spacing of R shears, and well developed P shears (which are theorised to occur later in the shearing process) in the upper region compared with the lower region. These differences show that shear zone development was likely progressive from top to bottom.

I infer that the rapid loss of stress during strain softening is caused by excess pore pressure lubricating the shear band. This is also observed for large scale sensitive soil landslides, where fluidised sensitive material flows once remoulded (Quinn *et al.* 2011).

8.5 Comparison of static and cyclic failure with research

8.5.1 Discussion of results with current definitions of liquefaction and cyclic softening

The definition of liquefaction historically varies widely to describe soil deformation initiated by monotonic, transient, and cyclic loading (Kramer, 1996). One characteristic that is omnipresent over all definitions is that during rapid loading of undrained soils, excess pore pressure accumulates, causing a reduction of effective stress and densification (Kramer, 1996). While the excess build-up of pore pressure and consequent loss of effective stress is clearly a denominating factor in liquefaction, the processes regarding soil deformation vary in response to the type of material (Boulanger & Idriss, 2006, 2007).

Classically, liquefaction has referred to granular soils, where either flow liquefaction or cyclic mobility result in ground deformations. Flow liquefaction occurs when the static shear stress is greater than the shear stress of the soil in its liquefied state (Kramer, 1996). Cyclic stresses bring the soil to an unstable state, whereafter flow liquefaction is driven only by the static shear stresses (Kramer, 1996). Flow failures occur suddenly, and can travel large distances, for example the Sheffield Dam failure following an earthquake in 1864 (Seed *et al.* 1969). Cyclic mobility occurs when the static shear stress is less than the shear strength of the liquefied soil. Cyclic mobility is driven by both cyclic and static shear stresses, resulting in either lateral spreading on flat ground adjacent to bodies of water, or level ground liquefaction, where excess pore pressures dissipate above the ground, resulting in sand boils and flooding of low lying land (Kramer, 1996).

Robertson & Wride (1998) considered liquefaction in sandy materials to be caused by either cyclic loading, where soil stiffness is lost once the effective overburden stress reaches 0, or strain softening, where significant shear strength is lost after the peak strength is reached.

Recently, case studies have shown that low plasticity silts and clays can lose significant strength during cyclic loading (Chu *et al.* 2004; Martin *et al.* 2004). Stemming from these observations, Boulanger & Idriss (2006) analysed the behaviour of a wide variety of silts and clays under triaxial compression, and found that for monotonic and cyclic loading, the soil behavioural response varied from “clay like” behaviour to “sand like” behaviour over a narrow range of Atterberg Limits (**Figure 8.5**). NZGS (2010) state that “if sufficient shear strain accumulates, sensitive soils may lose significant shear strength leading to slope failures, foundation failures, and settlement of loaded areas". NZGS (2010) then refer clarification of issues of liquefaction and cyclic softening to Boulanger and Idriss papers (2006, 2007). Boulanger & Idriss (2006) differentiate between clay and sand like behaviour based on (1) the Atterberg Limits, (2) the stress, strain and pore water pressure characteristics of the soil, and (3) whether the soil shows stress history normalised characteristics (**Figure 8.5**). When a material showed both sand and clay like responses, they placed emphasis on whether the material showed stress history normalised characteristics i.e. the undrained shear strength is related to the consolidation stress history. Boulanger and Idriss (2006, 2007) do not, however, make any specific reference to how a sensitive clay deforms and whether cyclic softening or liquefaction occurs.

Under Boulanger and Idriss's (2006) classification, strength loss due to cyclic loading for sand like material is referred to as liquefaction, while strength loss for clay like soils is referred to as cyclic softening. From their results, for "clay like" behaviour static and cyclic shear strengths are related, therefore cyclic strength can be determined based on static undrained shear strength. For "sand like" behaviour, cyclic strengths are better estimated by CPT and SPT correlations. Boulanger & Idriss (2007) went on to develop procedures to evaluate the potential for cyclic softening for soils that displayed "clay like" behaviour.

Atterberg limits and static triaxial stress, strain and pore pressure responses for this study, Wyatt's (2009) and Cunningham's (2012) studies are compared to the expected responses for clay, intermediate and sand type materials from Boulanger and Idriss (2006) in **Table 8.3**. All sensitive soils from Tauranga have high plasticity indices and have soil types which vary between silty clays, clayey silts and sandy clays. Based on the Atterberg limits, all sensitive soil responses from Tauranga would classify as "clay like" materials according to Boulanger & Idriss (2006).

For the cyclic triaxial results from my study, the sensitive soil response is comparable to the "clay like" response outlined by Boulanger & Idriss (2006) (**Figure 8.5f**). This observation comes from comparing the clay like response outlined in **Figure 8.5** with cyclic stress-strain curves in Chapter 5. Boulanger & Idriss (2006) classify clay like cyclic behaviour by a loss in stiffness after failure (decrease in curve inclination) and a broadening of hysteretic loops, known as cyclic softening. Sand like behaviour (**Figure 8.5e**) shows these two properties, but also distinctly shows

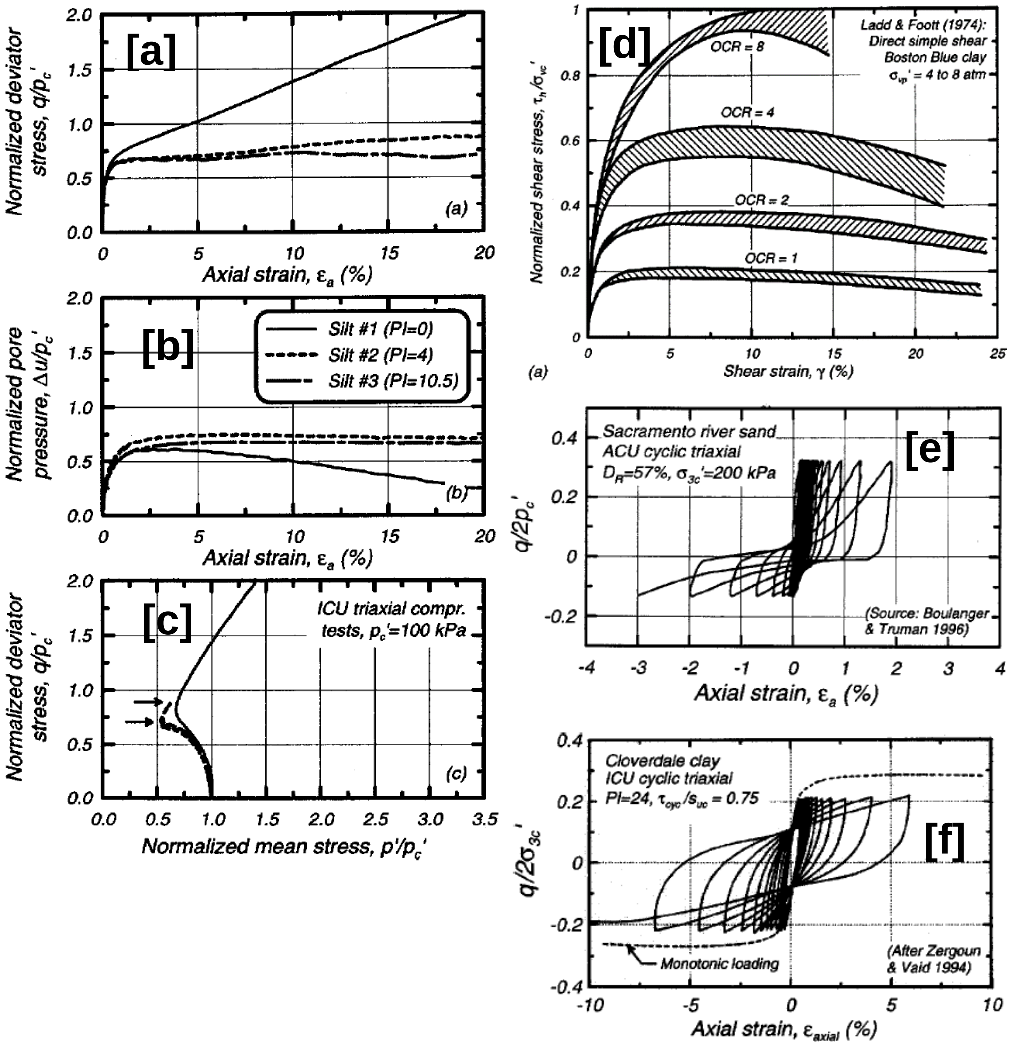

Figure 8.5. The behavioural variation of three fine grained materials from sand like behaviour to clay like behaviour, showing both static and cyclic responses (Boulanger & Idriss, 2006). Material properties are outlined in table 8.2. [a] and [b] shows the normalised shear stress and pore pressure vs axial strain respectively. [c] Shows the p'-q' plots. [d] Shows the consolidation dependant behaviour of clays, while [e] and [f] show the sand and clay like cyclic stress-strain responses respectively. All figures are directly from Boulanger & Idriss (2006). For a, b, and c Silt 1 typifies sand like behaviour, silt 2 intermediate behaviour, and silt 3 shows clay-like behaviour. Atterberg limits for each type are outlined in **Table 8.3**.

a pronounced flattening of the stress-strain loops at the x-axis after failure. My cyclic triaxial results bear the most similarity to clay-like stress-strain loops, where a decrease in stress-strain loop inclination and broadening of loop occurred after failure, but no flattening around the x-axis was observed. (Boulanger & Idriss, 2006).

Section 8.4.6 discusses the variables affecting the type of response observed for static triaxial responses in Tauranga sensitive materials. To recap, I observed that these materials showed both stress history dependant behaviour, rate dependant behaviour, and material dependant behaviour. All Tauranga sensitive materials show at least some degree of stress history related behaviour, shown by the change of response with greater confining pressures. Despite stress-strain characteristics, Boulanger & Idriss (2006) regard soils to be clay-like if they display dependency on stress history. This would classify all sensitive materials (**Table 8.3**) as clay-like according to Boulanger & Idriss (2006). In regard to the stress-strain curves though, only subtype Ba, or strongly dilative responses bear resemblance to clay like stress-strain curves (Boulanger & Idriss, 2006). Contrastingly, the stress-strain curves for subtypes Bb, Aa and Aa show strain softening, where the clay like response described by Boulanger & Idriss does not. Rather, the stress-strain response of sensitive materials bear more resemblance to flow liquefaction curves in sands (Robertson *et al*., 1998), in that they both have peaks followed by significant strain softening. Boulanger & Idriss (2006, 2007) however regard a soil with a plasticity index ≥7 as clay like, with cyclic softening behaviour, despite this similarity between flow liquefaction characteristics.

Flow liquefaction is considered by Robertson (Robertson & Wride, 1998; Robertson, 2010) to be when the soils show strain softening with a loss of shear strength. In landslides, flow liquefaction is likely to occur once the peak strength is reached, because the gravitational stresses are greater than the strength of the soil in the ultimate state (Kramer, 1996; Robertson, 2010). Boulanger and Idriss (2007) highlight that defining the transition from peak to residual strength in sensitive clay is limited by predicting the distribution of strain. I have given evidence from static triaxial data coupled with microstructural shear zone characteristics that excess pore pressure in localised shear bands results in the strain softening observed. I think that this excess pore pressure can be likened to flow liquefaction, in that the soil confined to the shear plane is capable of flowing. Tauranga sensitive

Table 8.3. Atterberg limits and static and triaxial stress, strain and pore pressure responses for this study, Wyatt's (2009) and Cunningham's (2012) studies, compared to the expected responses for clay, intermediate and sand type materials from Boulanger and Idriss (2006).

Study	Sample + location	PI (%)	LL (%)	Silt (2 – 74 µm) (%)	Clay content (<2 µm)	Static stress -strain, pore pressure, & p'-q' plot response after failure (q_{max})	Cyclic stress- strain response after failure
Boulanger & Idriss (2006)	Silt 1	0	26	81	3	q increases, u decreases, p'-q' trends right along CSL (dilation)	Less broad hysteretic loops, flat middle portions of stress-strain curve (0 stiffness)
	Silt 2	4	30	84	11	q slightly increases, u constant p'-q' trends slight right (slight dilation)	Intermediate of silt 1 and silt 3
	Silt 3	10.5	36.5	87	19	q and u constant after peak p'-q' plot trends left but no "contractancy" along CSL. "plastic" behaviour	Broader hysteretic loops, slightly flatter middle portions of curve (slight decrease in stiffness)
This study (2016)	Omokoroa landslide scarp (OM1)	25	66	37	63	q markedly drops, u gradually rises p'-q' plot trends left (contraction)	Broad hysteretic loops, slightly flatter middle portions of curve after failure
	Matua (M1)	15	52	23	40	q markedly drops, u gradually rises, p'-q' plots trend left (contraction)	
Wyatt (2009)	Tauriko road cutting (TS1)	24	81	81	6	<200 kPa : q constant, u flattens, p'-q' trend intermediate (very slight dilation) >200 kPa: q gradually drops, u gradually rises, p'-q' trends left (contraction)	
	Otumoetai (OS1)	43	90	65	10	<100 kPa confining pressure: q gradually rises, u gradually drops, p'-q' trends right (dilation) >100 kPa confining pressure: q drops markedly, u slowly rises, p'-q' trend left (contraction)	
Cunningham (2012)	Omokoroa cutting (OS1)	26	72	49	10	< 200 kPa: q flattens, u flattens, p'-q' trend intermediate (very slight dilation) > 200 kPa: q slightly drops, u gradually rises, p'-q' plots trend left (contraction)	

Study	Sample + location	PI (%)	LL (%)	Silt (2 – 74 µm) (%)	Clay content (<2 µm)	Static stress -strain, pore pressure, & p’-q’ plot response after failure (q_{max})	Cyclic stress- strain response after failure
	Te Puna roadside cutting (TPS1)	44	89	76	3	q gradually drops, u suddenly drops, p’-q’ trends right before reaching the CSL (dilation) then left after the CSL (contraction)	
	Pahoia coastal reserve (PS1)	19	53	85	5	<100 kPa: q markedly drops, u gradually drops, p’-q’ trends right (dilation) >100 kPa: q markedly drops, u gradually rises, p’-q’ trends left (contraction)	
	Pahoia coastal reserve (PS2)	18	54	70	7	< 100 kPa: q markedly drops, u drops then rises, p’-q’ plot trends right before CSL (dilation) then left at CSL (contraction) >100 kPa: q markedly drops, u gradually rises, p’-q’ trends left (contraction)	

materials are more likely to liquefy at higher confining pressures and higher tests rates (**Table 8.3**).

8.6 Connecting the dots: Laboratory observations to macroscopic failure mechanism

Landslide events at both sites occurred following intense, prolonged rainfall (Gulliver & Houghton, 1980; Moon *et al.* 2015). I postulate that failure initiated within a thin, extra-sensitive layer (St = 130) at 23 m depth at the Bramley Drive slip. I suggest that the high rainfall prior to the main sliding events resulted in excess pore pressure accumulation within the already saturated extra-sensitive layer at 23 m, initiating strain localisation and downwards progressive failure. Once a critical end length of the shear band reached the residual strength, the shear band propagated through stiffer overlying tephra layers. Whether the one preceding heavy rainfall event resulted in complete shear zone formation, or that shear zone formation had been progressive over many years, and the final rainfall event resulted in the critical end region becoming long enough for catastrophic failure, is unknown. Progressive failure in the shear band could have had elements of upward and downward propagation; upwards propagation could be influenced by storm waves or tidal forces at the cliff base, and heavy rainfall events could trigger downwards progressive failure. The failure mechanism that initiated the Matua slide is suggested to be similar to Omokoroa, in that heavy rainfall infiltrated through relatively permeable layers, until it reached the sensitive layer, triggering strain localisation and progressive failure.

8.7 Cyclic test results and contour plots

In their conclusions, Boulanger and Idriss (2007) note that the magnitudes of strain or ground displacement that will reduce the shear strength to the remoulded strength of soil that shows clay like responses is difficult to determine. The technique presented by Anderson (2015) is able to show both the average and cyclic shear strains at failure, and the number of cycles to failure for a number of cyclic triaxial tests, each tested at different levels of average shear stress and cyclic shear stress, for one particular soil type. After many samples have been collected, there is enough data regarding these failure characteristics to draw on contours for (1) cycles to failure, and (2) average shear strain and cyclic shear strain at failure. This technique is called a cyclic contour plot, and allows a lot of information regarding a particular soils failure characteristics to be gained from one diagram.

I replicated Anderson's method using 10 tests, each at different levels of average shear stress and cyclic shear stress, of which 7 tests were successful. From these seven tests I constructed a contour plot, which did show relationships between the different stresses applied, and the failure characteristics observed, but the meaningfulness of these results is limited because of the low number of tests used to construct the plot. Further testing needs to be completed to understand the full spectrum of failure criteria for sensitive material from Omokoroa. Further tests could include extension tests, which were not included in this study, and also modification of the dynamic frequency, which in this study was kept at 1 as recommended by Anderson (2015).

Pore pressure incrementally accumulated cycle by cycle for all tests, correlating with a decrease in effective stress, until the CSL line was reached (failure), at which strain began to rapidly develop, further effective stress was lost, and pore pressure continued to rise. A rise in pore pressure following failure suggests similar failure mechanisms to static triaxial results, where the rise is caused by excess pore pressure draining along a shear band. Microstructural evidence is limited in determining failure mechanisms because only one sample was tested for microstructural characteristics by one micro-CT scan (test 8, 40 kPa cyclic shear stress, 0 average shear stress). Observations of this scan were similar to static micro-CT scans in that the shear zone comprised R and P shears, consisting of locally densified clay material. For this test excess pore pressure continued to accumulate in the post peak region, concurrent with loss in stiffness. The correlation between excess pore pressure and contraction of clay microstructure suggests similar flow liquefaction processes are occurring locally in shear bands. One important distinction between the static and cyclic micro-CT scans is that dense particles, inferred to be weathered volcanic glass shards, appear to be crushed within the shear zone in the cyclic sample, whereas in the static micro-CT scan, the glass shards did not appear to be affected by shearing. Whether this is a consequence of the cyclic micro-CT scan being of much greater resolution than the static scan, or if it is actually an effect of cyclic stresses, is yet to be determined by further research.

Two end members of deformation behaviour in regard to stress, strain and pore pressure accumulation were observed over different applications of average shear stress and cyclic shear stress for my 7 tests. Type 1 end members showed a failure pattern that accumulated in the positive strain (compression) direction. Subtype 1b still progressively accumulated positive strain, however the effect of the stress reversal (slight negative stress component) has resulted in the hysteretic loops becoming broader at failure, indicating a greater energy dissipation (Boulanger & Idriss, 2006). Type 2 end members both had only τ_{cy} with no τ_{av}. The result of this was a strain accumulation in both positive and negative directions (compression and extension), and hysteretic loops which became much broader and reduced dramatically in inclination at failure, indicating a significant loss in stiffness, and dissipation of energy respectively.

One interesting observation is that the effect of applying a minor amount of cyclic shear stress, even when combined with high average shear stress, results in (1) a higher initial soil stiffness and (2) failure after many more cycles (tests 4 and 8, **Table 7.3**).

On the contour plot, at moderate applications of normalised average shear stress and cyclic shear stress, failure occurs after one cycle, and significant average and cyclic shear strains accumulate. At high average/low cyclic applied normalised shear stress, failure occurs between 1-100 cycles, and low average/high cyclic strain accumulates. For high applied average/low cyclic normalised shears stresses, failure occurs around 1 – 100 cycles, and high average/low cyclic shear strains accumulate.

8.7.1 What are the cyclic and average shear stresses felt at Bramley Drive during estimated earthquake events?

The Western Bay of Plenty District Council (2004) outlined the expected peak ground accelerations expected for different earthquake scenarios, for different site responses. The material at Omokoroa is classed as type D-E as outlined by NZS 1170.5:2004, i.e. it is a deep, soft soil. Seed & Idriss (1971) calculate the peak average shear stress and peak cyclic shear stress in a material at depth by **Equations 8.2 & 8.3**. τ_{max} is the peak maximum shear stress, a_{max} is the peak ground surface acceleration, g is the acceleration of gravity, σ_v is the overburden stress and r_d is a reduction factor, which estimates the cyclic stress with depth (**Figure 8.6**) (Kramer, 1996 after Seed & Idriss, 1971).

$$\tau_{max} = \frac{a_{max}}{g}\sigma_v r_d$$

Equation 8.2

$$\tau_{cy} = 0.65\tau_{max}$$

Equation 8.3

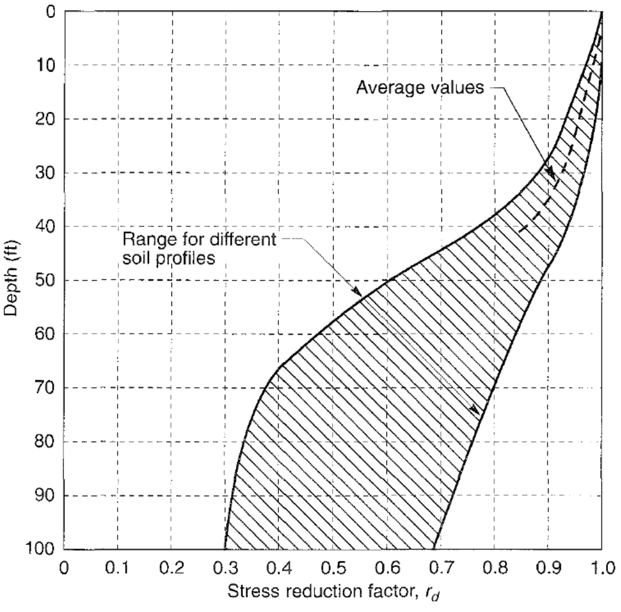

Figure 8.6. The reduction factor profile used to estimate the change in cyclic stress with depth (Kramer, 1996 after Seed & Idriss, 1971).

Table 8.4 presents the peak ground accelerations expected at Omokoroa for four different major earthquake scenarios, based on the findings outlined in WBOPDC (2004). **Equations 8.2 & 8.3** were then used to calculate the expected shear stress and cyclic shear stress at the 24 m depth soil layer I sampled from. The results were then normalised and plotted on the cyclic contour plot (**Figure 8.7**). Because our contour plot is only an estimate, this is more of an example of how the plot could be utilised. The Tauranga event plots just within the margin of the 100-1000 cycles to failure contour, meaning that between 100-1000 cycles at the PGA of this earthquake would produce failure, resulting in average shear strains near 5% and cyclic shear strains between 0.5 – 1%.

8.8 Comparison OM1 cyclic contour plot with other contour plots

The contour plot concept is a relatively new technique that was introduced by Anderson (2007, 2015), and only one other study has replicated the methodology so far. This study was done on BDK Clay, an overconsolidated marine clay in the North Sea (Hue Le & Eiksund, 2014). Four extension cyclic

Table 8.4. Different earthquake scenarios that could affect the Tauranga Region, their expected magnitudes, and peak ground acceleration expected at Omokoroa (WBOPDC, 2003).

Earthquake event	Magnitude	Peak Ground Acceleration	Max Shear	Cyclic shear	Normalized shear stress [τ/su]	Normalized cyclic shear stress [τcy/su]

		(PGA) at Omokoroa	stress at 24 m	stress at 24 m		
Tauranga	5.7	0.33	68.4	44.5	0.6	0.37
Mayor Island	7	0.225	51.3	33.3	0.43	0.28
Kerepehi south	6.7	0.225	51.3	33.3	0.43	0.28
Matata	6.5	0.05	11.4	7.4	0.01	0.06

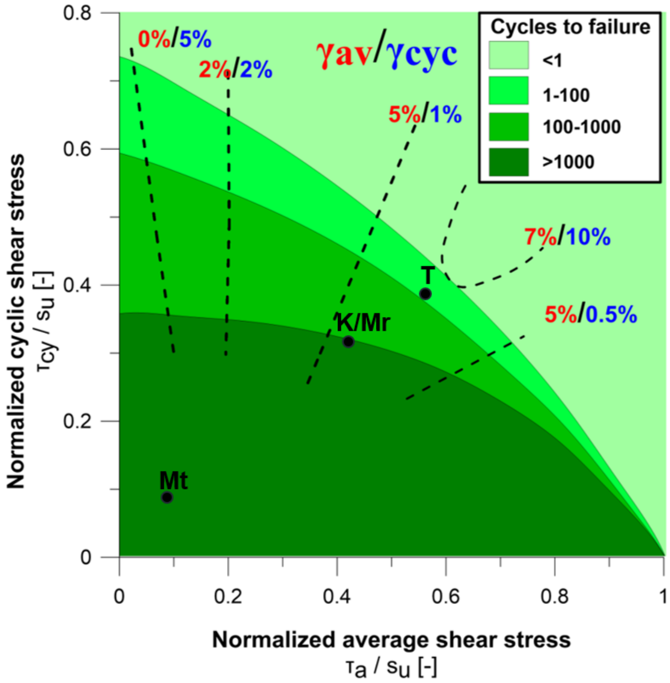

Figure 8.7. The cyclic contour plot presented in Figure 7.19, Chapter 7, with different shear stresses and cyclic stresses affecting the soil I sampled (OM1) at 24 m depth at Omokoroa, based on four different earthquake events outlined in table 8.2. T = Tauranga event, K/ Mr = Kerepehi and Mayor Island events, and Mt = Matata event.

triaxial tests were done in this study. Four was not considered enough to construct a contour plot, so results were plotted onto Anderson's contour plot of cyclic triaxial results on overconsolidated (OCR = 4) Drammen Clay, also a marine clay. A comparison of the contours constructed in this study and Anderson's original contour plot (2015) is presented in **Figure 8.8**.

The Drammen Clay has an overconsolidation ratio of 4, whereas OM1 has been consolidated to estimated effective normal stress (OCR = 1). In comparing the contour line "1 cycle to failure" for the Drammen Clay and OM1, I observe that for Drammen Clay, it takes considerably higher normalised cyclic and average shear stresses for failure to occur at one cycle. Towards the origin, the "100 and 1000 cycles to failure contours" for OM1 in comparison to Drammen Clay contours show that for the same normalised application of cyclic shear stress, OM1 typically requires a greater number of cycles to reach failure in comparison to Drammen Clay. The cyclic and average shear strain at failure contours are significantly

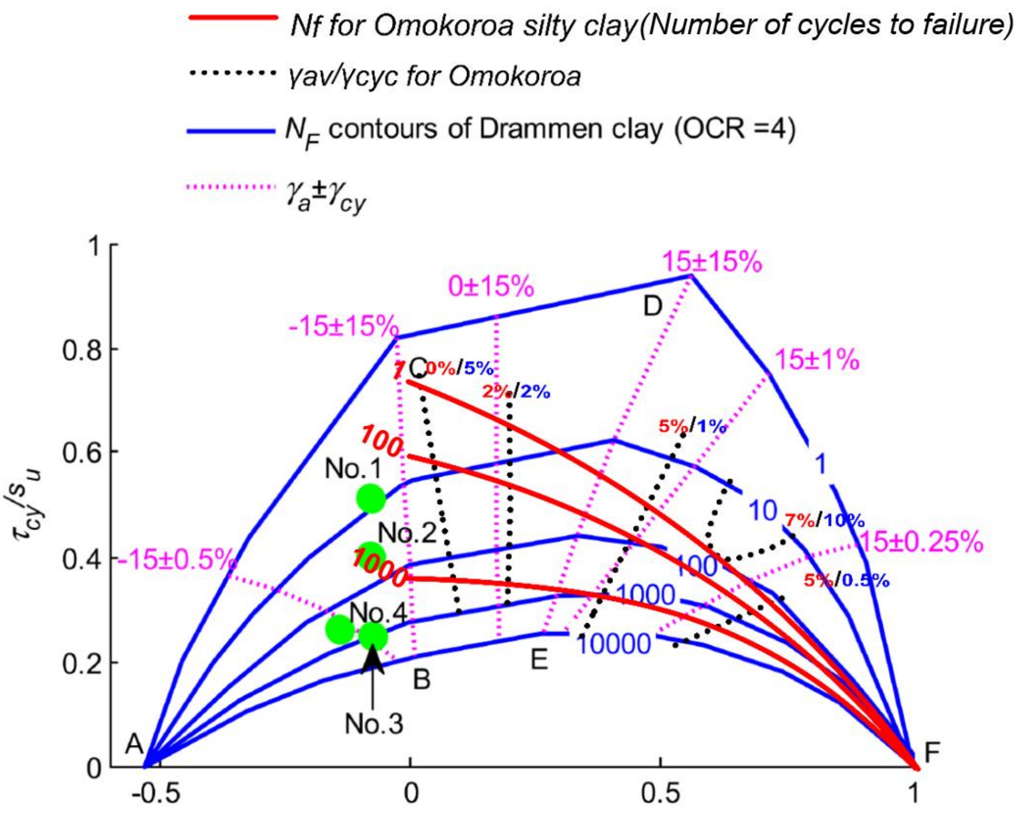

Figure 8.8. The failure contours for Omokoroa in comparison to the original cyclic contour plot for Drammen Clay (Anderson, 2015), and also to several plots (green dots) of Bolders Bank Formation, a marine clay studied by Hue Le & Eiksund (2014).

different to Drammen Clay contours. Overall, OM1 tends to fail at lower levels of average shear strain and cyclic shear strain in comparison to Drammen Clay. The 0/15% strain contour in comparison with the 0/5% strain contour shows that Drammen Clay reaches 0 average strain at higher levels of applied normalised average shear stress than OM1 i.e. the Drammen Clay can withstand high levels of applied normalised average shear stress before average shear strain starts to accumulate. As our contour plot was based on only 7 tests, these interpretations are crude estimates, and the comparison is more of an example of how two different soils types could be compared with more robust data.

8.9 Chapter 8 summary

This chapter links geomechanical properties, static and cyclic triaxial test observations, shear zone microstructure and geomorphological observations for two sensitive soils from Tauranga (M1 and OM1) in an attempt to determine failure mechanisms for each soil type. Failure mechanisms were compared to recent advances in failure mechanism theories for sensitive material from Norway.

The geological units studied are both derived from weathered pyroclastic material. Like previously studied sensitive materials from Tauranga (Moon *et al.* 2015), moisture content, Atterberg Limits, porosity and void ratios are high, and wet bulk densities are low. Unlike sensitive soils previously studied in Tauranga, clay content for both M1 and OM1 are higher than other sites around Tauranga (Moon *et al.* 2015). These characteristics are mainly due to (1) low initial settling rates, which allowed preservation of an open structure of many small, saturated pore spaces, and (2) development of the mineral halloysite, which has been correlated to sensitivity (Moon *et al.* 2015).

Material type, effective confining pressure and test rate each have an effect on the failure mechanism observed for the materials I studied, and also for triaxial tests on sensitive material completed by Wyatt (2009) and Cunningham (2012); high compression rates, and confining pressures more likely result in contractive failure, while for lower rates and confining pressures, dilative failure were more commonly observed. When comparing my static triaxial results with Cunningham's (2012) and Wyatt's (2009) triaxial results, I observed that in general, the high test rate I used (0.5mm/min) correlated to contractive response at failure, and shear band formation, whereas for lower test rates, contractive responses were observed, but shear band formation was less common.

When correlating microstructural observations from thin sections and micro-CT with triaxial results, I observed that like sensitive soils studied by Thakur 2011, Thakur *et al.* (2014) and Gylland *et al.* (2013c, 2014), that for contractive responses in M1 and OM1, initial strain localisation during compression is initiated by excess pore pressure gradients within the sample. The local exceedance of peak strength of the material causes micro fractures, known as Riedel shears and thrust shears, to form progressively in a shear band. Collapse of micro structure in these shear bands results in further excess pore pressure generation, some of which dissipates into the surrounding material, and some of which dissipates along the shear band. This excess pore pressure essentially liquefies the material in the shear band, causing the drop in resistance or strain softening behaviour observed.

Contractive responses observed for M1 and OM1 for static and cyclic triaxial and microstructural properties align more with flow liquefaction phenomena than cyclic softening or cyclic mobility when compared to the literature. While Atterberg limits classify M1 and OM1 as "clay-like" materials according to Boulanger & Idriss (2006), both materials have stress-strain curves that are more similar to typical flow liquefaction stress-strain curves (Robertson, 1998).

Microstructural observations, such as densified clay material within the shear zone (Micro-CT) realigned clay material in shear zones in thin section, and rising pore pressure correlated to a drop in stress in the post-peak stress-strain curve, support evidence that flow liquefaction is occurring locally within the shear band of both materials.

The contour plot technique (Anderson, 2015) shows promise as a geotechnical tool which could be used to analyse the cyclic failure characteristics of soils. Even with very limited 7 samples, contours for both the number of cycles to failure, and average and cyclic shear strains could be drawn.

Landslide events at both sites occurred following intense, prolonged rainfall (Gulliver & Houghton, 1980; Moon *et al.* 2015). I postulate that failure initiated within a thin, extra-sensitive layer (St = 130) at 23 m depth. I suggest that the high rainfall prior to the main sliding events resulted in excess pore pressure accumulation within the already saturated extra-sensitive layer at 23 m, initiating strain localisation and downwards progressive failure. Once a critical end length of the shear band reached the residual strength, the shear band propagated through stiffer overlying tephra layers. The failure mechanism that initiated the Matua slide is suggested to be similar to Omokoroa, with a tentative conclusion that the different geomorphologies are explained by the lack of a paleovalley at Matua.

CHAPTER 9

CONCLUSIONS

9.1 Chapter outline

This chapter presents a summary of the findings in regard to static and cyclic failure mechanisms for two extra-sensitive soils derived from weathered pyroclastic material in Tauranga. Sensitive material was sampled near the failure surface for two coastal cliff landslides that border Tauranga Harbour: (1) a well-studied University of Waikato-University of Bremen landslide site at Bramley Drive, Omokoroa, and (2) a landslide at the south end of Matua Peninsula within Tauranga City. Geomechanical properties, including undrained consolidated static and cyclic triaxial test results are linked to microstructural observations in shear zones created during triaxial compression, in an attempt to determine failure mechanisms. Comparisons are made between sensitive soil failure in weathered pyroclastic material and sensitive soil failure in glacial till material from Norway, described by Gylland *et al.* (2013a,b,c), Thakur (2011), and Thakur *et al.* (2014). Finally, failure mechanisms are related to geomorphological site characteristics, and hypotheses of how global failure might have been initiated at the two sites are made.

9.2 Geomorphology and stratigraphy

Soil sampled at Bramley Drive (OM1) was a highly plastic, extra-sensitive silty CLAY. OM1 was correlated to the borehole log drilled behind the failure surface to be at 19 m depth, within the Pahoia Tephra silty clay layer. Peak vane strength was 60 kPa, while remoulded vane strengths returned values of 9-12 kPa, giving a sensitivity of 15 ± 3. The material is suspected to be either reworked or *in situ* volcanic material, possibly related to the Te Puna Ignimbrite (Briggs *et al.* 1996). Geomorphological characteristics of the Bramley Drive site include a roughly equidimensional, empty landslide crater, a large, long runout component of intact material overlying remoulded sensitive material, and a minor landslide “neck”. These characteristics are most consistent with flow slide geomorphologies described by Locat *et al.* (2011) for sensitive soil landslides in glacial till derived materials. The bowl shaped, slump-like features are most likely related to a paleovalley in which materials at Bramley Drive originally accumulated in.

At the Matua (M1) landslide, material was sampled at a small distance away from the failure because of accessibility issues. Peak vane strengths returned an average value of 60 kPa, while remoulded strengths are 6 kPa, giving a sensitivity of 10. Material was classed as a low to medium plasticity, extra-sensitive silty CLAY. Sandy clay lenses occurred in the material, indicating a high degree of reworking, hence classifying the M1 as Matua Subgroup. The failure surface of the Matua slip has a long axis, is shallow, and slightly curved, indicating that failure was dominantly planar sliding, with a minor rotational element. Landslide debris occurs approximately 2 m from the base of the cliff, and constitutes intact blocks underlain by remoulded sensitive material. These features point to a sensitive layer failing at depth, resulting in a planar- rotational slide, rafting overlying material away from the cliff face.

9.3 Geomechanical properties

In keeping with previously published research on halloysite rich clays derived from pyroclastic material (Wesley 1977; Wesley 2009; Wyatt 2009; Cunningham 2012; Moon *et al.* 2015), porosity, void ratio, liquidity indices and moisture content are high for Matua and Omokoroa materials. High porosity and moisture content account for low wet bulk densities observed in both samples. Unlike sensitive material previously studied in Tauranga (Keam, 2008; Wyatt, 2009, Arthurs, 2010; Cunningham, 2012), samples from both sites have dominant clay fractions, rather than dominant silt fractions. M1 is distinctly sandier (42% clay, 22% silt, 36% sand) than OM1 (63% clay, 37% silt, 0% sand). SEM scans suggest material from both sites to be halloysite dominated, with an open structure of point-point contacts, small, ubiquitous pore spaces, and clay mineral coatings on larger silt and sand sized grains (Moon *et al.* 2015). Both M1 and OM1 have high Atterberg limits, plotting below the A-line as high compressibility silts, and low activities in line with halloysite dominated sensitive material (Wesley 2009; Moon *et al.* 2015).

The high proportion of tiny pore spaces in an open point to point structure is due to initially low settling rates (either ash cloud airfall tephra or fluvial processes) of predominantly ash sized pyroclastic material. Capillary effects have allowed effective cohesion to uphold soil structure since deposition. Saturated pore spaces and weathering of silica and iron oxide material has resulted in formation of various morphologies of halloysite, which has been correlated to high sensitivity at Bramley Drive and other locations around Tauranga (Keam, 2008; Wyatt, 2009, Arthurs, 2010; Cunningham, 2012).

9.4 Static failure mechanisms

Consolidated undrained effective triaxial tests were completed at different confining pressures for both M1 and OM1. A higher test rate (0.5 mm/min) than recommended by the British Standard 1377 (1990) was used to replicate rapid compression that occurs during landsliding. Triaxial results from this study are compared with undrained consolidated triaxial results on other sensitive materials from Tauranga (Wyatt, 2009; Cunningham, 2012).

Two dominant failure mechanisms are defined: Type A is contractive, strain softening failure, while Type B is dilative failure. Each type was further split into two subtypes: Aa showed a strong contractive response, while Ab showed a minor contractive response, Ba is strongly dilative, and Bb is moderately dilative. Idealised failure mechanism schematics for each type are summarised in **Figure 9.1**.

Material type, effective confining pressure and test rate each have an effect on the failure mechanism observed for the materials I studied, and also for undrained consolidated triaxial tests on sensitive material completed by Wyatt (2009) and Cunningham (2012). High compression rates, and/or confining pressures more likely result in contractive failure, while for lower rates and/or confining pressures, dilative failure was more commonly observed. When comparing my static triaxial results with Cunningham’s (2012) and Wyatt’s (2009) triaxial results, I observed that in general, the high test rate I used (0.5mm/min) correlated to contractive response at failure, and shear band formation, whereas for lower test rates used by Cunningham (2012) and Wyatt (2009), contractive responses were observed, but shear band formation was less common. Importantly, this shows that during rapid compression, sensitive materials are more likely to form shear bands, due to excess pore pressure gradients. These observations align with what has been observed in sensitive soils derived from glacial till in Norway (Gylland *et al.* 2013c; Thakur, 2011; Thakur *et al.* 2014). More samples at different test rates are required to determine the effect of rate on shear band formation.

Strain softening was quantified using Bishop’s (1971) method, where strain softening is the percentage of stress lost between the peak and residual stresses. This parameter is limited in quantifying the true strain softening, due to the inability

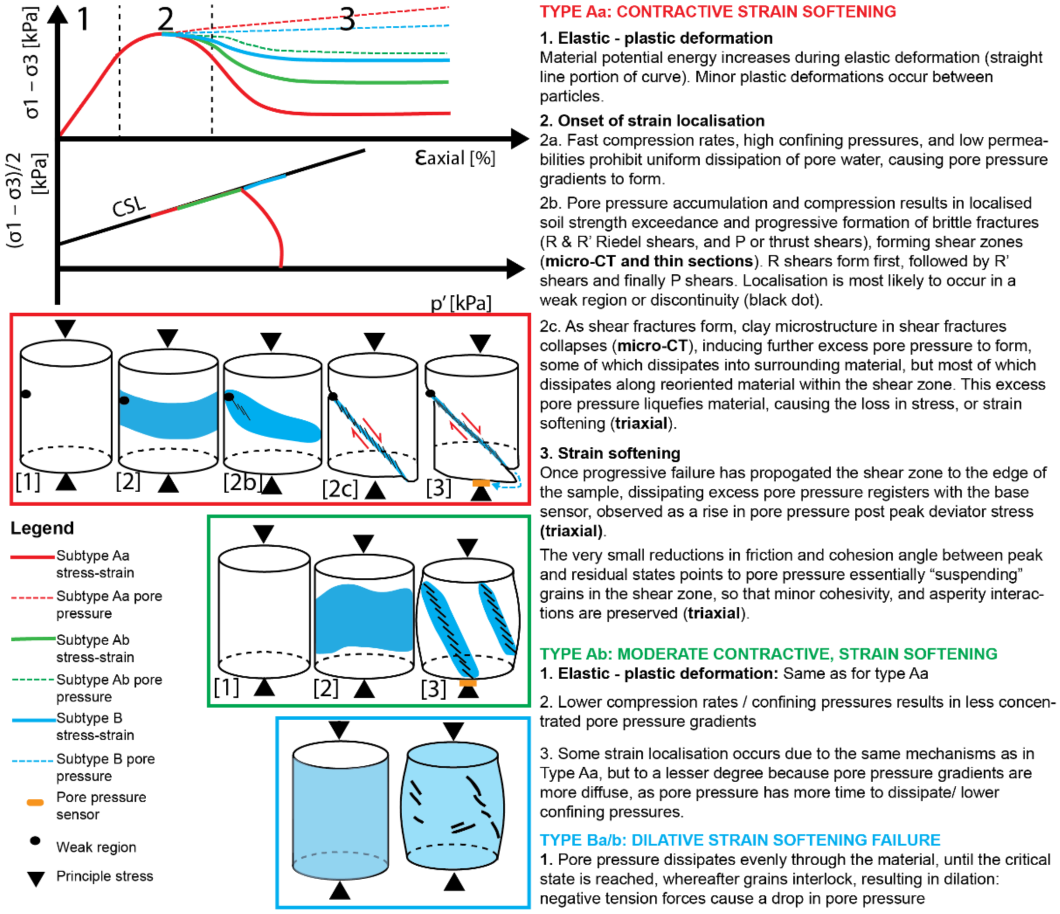

TYPE Aa: CONTRACTIVE STRAIN SOFTENING

1. Elastic - plastic deformation
Material potential energy increases during elastic deformation (straight line portion of curve). Minor plastic deformations occur between particles.

2. Onset of strain localisation
2a. Fast compression rates, high confining pressures, and low permeabilities prohibit uniform dissipation of pore water, causing pore pressure gradients to form.

2b. Pore pressure accumulation and compression results in localised soil strength exceedance and progressive formation of brittle fractures (R & R' Riedel shears, and P or thrust shears), forming shear zones (**micro-CT and thin sections**). R shears form first, followed by R' shears and finally P shears. Localisation is most likely to occur in a weak region or discontinuity (black dot).

2c. As shear fractures form, clay microstructure in shear fractures collapses (**micro-CT**), inducing further excess pore pressure to form, some of which dissipates into surrounding material, but most of which dissipates along reoriented material within the shear zone. This excess pore pressure liquefies material, causing the loss in stress, or strain softening (**triaxial**).

3. Strain softening
Once progressive failure has propogated the shear zone to the edge of the sample, dissipating excess pore pressure registers with the base sensor, observed as a rise in pore pressure post peak deviator stress **(triaxial)**.

The very small reductions in friction and cohesion angle between peak and residual states points to pore pressure essentially "suspending" grains in the shear zone, so that minor cohesivity, and asperity interactions are preserved (**triaxial**).

TYPE Ab: MODERATE CONTRACTIVE, STRAIN SOFTENING

1. Elastic - plastic deformation: Same as for type Aa

2. Lower compression rates / confining pressures results in less concentrated pore pressure gradients

3. Some strain localisation occurs due to the same mechanisms as in Type Aa, but to a lesser degree because pore pressure gradients are more diffuse, as pore pressure has more time to dissipate/ lower confining pressures.

TYPE Ba/b: DILATIVE STRAIN SOFTENING FAILURE

1. Pore pressure dissipates evenly through the material, until the critical state is reached, whereafter grains interlock, resulting in dilation: negative tension forces cause a drop in pore pressure

Figure 9.1. Idealised schematic of the different failure mechanisms observed for my samples and also in Cunningham's (2012) and Wyatt's (2009) samples. Red outline shows contractive failure, green outline shows moderately contractive failure, while blue shows dilative failure.

of the triaxial to capture horizontal strain. This limitation may be why strain softening did not strongly correlate to high confining pressures and test rates as expected. The strain softening parameter I used is therefore an estimate.

Evidence from thin sections for both Matua and Omokoroa showed that shear bands developed progressively. Shear zones at small and large scales, and in a wide range of geomaterials, display similar patterns of shear fracture development. Orientations of these shears are related to the friction angle of the material. R shears are suspected to form first, and accommodate most of the shearing. R' fractures form second, P shears form third and link R shears together and finally one shear, called the principle displacement shear accommodates all further shearing. I observed the commonly seen conjugate Riedel shears (R and R') and P shears (**Figure 9.1**). No PDS shears are observed. I observed differences in shear development over the same shear zone for both M1 and OM1 materials, indicating that failure is progressive. This is in-keeping with the well-established progressive failure mechanisms described for sensitive soils derived from glacial till in the northern hemisphere (Gylland *et al.* 2013c).

Sandy clay lenses that occur within silty clay material in M1 material seem to have an effect of concentrating deformation in the lower silty clay material. I infer that sandy clay lenses create a drainage region for pore water. Pressure from this pore water is translated to the lower silty clay, inducing pore pressure gradients to form and consequential progressive failure to occur.

Both M1 and OM1 are brittle materials, failing rapidly at less than 5% strain, and showing strain softening behaviour. I hypothesise that fracture mechanics principles described by Quinn *et al.* (2011, after Skempton, 1964) apply to M1 and OM1. This means that during compression, potential elastic energy increases until the material overcomes its peak strength. This occurs in regions where excess pore pressure has locally concentrated due to the low permeability and high compression rate preventing pore pressure uniformly dissipating. Elevated pore pressure allows the peak strength of the material to be overcome more easily. Weaker regions in the material also increase the likelihood of strain localisation, due to peak strength being more easily exceeded in these areas.

Contraction of clay microstructure into localised shear fractures was shown by micro-CT scans of shear zones in both OM1 and M1 samples. This proves that localised densification of clay microstructure results in further excess pore pressure generation within shear fractures. This pore pressure liquefies material within the shear zone. The high void ratio and liquid limit of M1 and OM1 mean that very little excess pore pressure is required for the material to liquefy. Liquefied material causes a rapid loss of stress, seen as strain softening in stress-strain curves, and contractive, left-trending curves along the critical state line in p'q' diagrams (**Figure 9.1**). Like sensitive soils derived from glacial till (Gylland *et al.* 2013, Thakur *et al.* 2014), M1, OM1 and materials tested by Wyatt (2009) showed little effective friction and cohesion softening between peak and residual states. This further adds evidence for pore pressure-induced strain softening. Pore pressure provides lubrication to the soil without decreasing asperity interaction or any cohesive forces.

Samples compressed at lower rates and lower confining pressures generally showed a tendency towards dilative failure, or at least less contractive behaviour (**Figure 9.1**). Lower compression rates and confining pressures allow pore pressure to dissipate more evenly within the sample, meaning that strain localisation and strain softening is less likely to occur.

Currently, NZGS (2010) refers to Boulanger & Idriss (2006, 2007) in regard to determining the expected stress-strain behaviour for different materials. Under Boulanger & Idriss's (2006) classification, sensitive materials from Tauranga (this study; Wyatt, 2009; Cunningham, 2012) class as "clay-like" soils, based on their high Atterberg Limits, and stress-history dependant behaviour. Stress-strain curves of sensitive material from Tauranga however, do not resemble the peak-less stress-strain curves that Boulanger & Idriss (2006) propose for clay-like materials; rather, they appear more like liquefaction curves for sand material, with peaks and strain softening regions as outlined by Robertson (1998). As discussed above, I infer that liquefaction is occurring, albeit as a different process to its occurrence in sandy materials. In sandy materials, high permeability allows pore pressure to accumulate evenly within the sample, leading to global liquefaction, i.e. most of the sand material is suspended or liquefied by the excess pore pressure. In sensitive clays, because excess pore pressure cannot dissipate due to low permeability, excess pore pressure induces liquefaction in a localised shear band. Sensitive clays are likely to be more prone to liquefaction in a localised shear band because they have high liquid limits and void ratios, increasing the capability of the soil to liquefy in comparison with non-sensitive materials.

9.5 Cyclic failure mechanisms

Boulanger & Idriss (2007) conclude that for sensitive materials, it is difficult to assess the strain or ground displacement that will reduce the clay from peak to residual strength during cyclic loading. In this study, I utilised a new geotechnical tool, called a cyclic contour plot (Anderson, 2015) that predicts the cycles to failure and also the average shear strain and cyclic shear strain at failure defined as 5% strain, at different combinations of normalised average and cyclic shear stresses. Although only seven samples were used, the contour plot already showed interesting trends for sensitive material. At moderate applications of normalised average shear stress and cyclic shear stress, failure occurs after one cycle, and significant average and cyclic shear strains accumulate. At high average/low cyclic applied normalised shear stress, failure occurs between 1-100 cycles, and low average/high cyclic strain accumulates. For high applied average/low cyclic normalised shears stresses, failure occurs around 1 – 100 cycles, and high average/low cyclic shear strains accumulate. In comparison to Drammen Clay (Anderson, 2015), in general, for the same application of normalised average and cyclic shear stress, failure occurs after a lesser number of cycles, but both average and cyclic strain accumulation is lower.

Boulanger & Idriss (2007) further conclude that it is difficult to predict the strain distribution in sensitive materials. For cyclic triaxial tests at different combinations of cyclic and average and cyclic stress, I saw a similar pattern to failure observed in static tests; in stress-strain curves, excess pore pressure continued to accumulate after failure, and strain softening was observed. The observation of a shear band in test 8 (40 kPa cyclic shear stress, 0 average shear stress) suggests that excess pore pressure and strain localisation may occur by similar processes to static failure. The observation of crushed volcanic glass shards in the failure surface of sample 8 (micro-CT analysis) suggests the effect of cyclic loading induces more intense contraction within the shear zone.

9.6 Hypothesised landslide failure mechanism

Landslide events at both sites occurred following intense, prolonged rainfall (Gulliver & Houghton, 1980; Moon *et al.* 2015). At Bramley Drive, the initial deposition of fine grained pyroclastic material in a paleovalley has allowed an overthickened sensitive soil sequence (Pahoia Tephras) to evolve. I suggest that the high rainfall prior to the main sliding events resulted in excess pore pressure gradients within the already saturated extra-sensitive Pahoia Tephras, especially enhanced by an extra-sensitive layer at 23 m depth, initiating strain localisation and progressive shear fracture propagation through sensitive material. Once a critical end length of the shear band reached the residual strength (Quinn *et al.* 2011), the shear band propagated through stiffer overlying tephra layers. A large portion of the sensitive material in the Pahoia Tephras may have been remoulded, allowing it to liquefy and flow, rafting overlying stiffer layers. Whether the one preceding heavy rainfall event resulted in complete shear zone formation, or that shear zone formation had been progressive over many years, and the final rainfall event resulted in the critical end region becoming long enough for catastrophic failure, is unknown. Progressive failure in the shear band could have had elements of upward and downward propagation; upwards propagation could be influenced by storm waves or tidal forces at the cliff base, and heavy rainfall events could trigger downwards progressive failure. Future research could concentrate on deformation of sensitive material in response to different forces, such as rainfall, solar radiation, and ocean tides to determine progressive failure mechanisms and triggers in the slope. The bowl shaped scarp morphology is likely correlated to the paleovalley margins.

I postulate that sandy layers at Matua created preferential flow paths for infiltrating rainwater, resulting in excess pore pressure accumulation and failure of adjacent sensitive units. Perhaps the lack of both a paleovalley and overthickened sequence at Matua is the reason why the failure mode was largely planar.

9.7 Recommendations for future research

This study highlights some initial findings of failure modes of sensitive material derived from weathered pyroclastic materials in the Tauranga Region. Future research efforts could involve:

1. Undrained, consolidated triaxial tests on sensitive material at different compression rates, with methodology similar to Gylland *et al.* (2013). Ideally, the triaxial base sled could be modified to be able to roll on bearings, with the addition of a displacement sensor. This would allow shear band evolution to be more accurately studied. Thin sections and micro-CT techniques would complement triaxial results in providing shear zone microstructural evidence.
2. SEM (scanning electron microscopy) analysis of thin sections of sensitive material. SEM of thin sections would show the breakdown in clay mineralogy when sheared in relation to non-sheared material.
3. Strain softening behaviour of these sensitive soils could be used as inputs to slope failure models. Modelling should not use finite element techniques, as shear band propagation and strain softening within a shear band are not accurately captured by finite element techniques (Gylland *et al.* 2013c). Fracture mechanics principles defined by Quinn *et al.* (2011) could be used to determine critical shear band length, and other properties outlined by Quinn *et al.* (2011).
4. The contour plot technique shows promise in being a useful geotechnical tool. More replicates are required to make the data and contours more significant. Additionally, variables such as frequency could be changed to determine effects on failure properties. Extension tests would also be useful to include.

9.8 Relevance to local geotechnical practise

Key findings which will benefit Coffey Geotechnics and the wider geotechnical consulting industry are:

1. The static and cyclic strength values of sensitive material are better estimated, allowing greater accuracy for geotechnical design;

2. Improved knowledge of soil behaviour. A general understanding of how sensitive soils from Tauranga behave will allow geotechnical professionals to make better informed decisions on site, and during design phases, reducing the risk of future damage caused by sensitive soils. This will result in more efficiently designed structures, and projects than finish on time and on budget. Successful projects mean that clients are more likely to return, resulting in business growth.
3. This study has shown that sensitive materials are strain softening. Commonly used slope stability software, for example SLIDE software, uses limit equilibrium modelling techniques. This type of modelling does not accurately capture strain softening in shear bands. More complex software, such as Plaxis, may be required for accurate slope stability modelling. Better models will improve knowledge of risks imposed by sensitive soils.

REFERENCES

DIN 18137-2 (2011-04). *Investigation and testing - Determination of shear strength - Part 2: Triaxial test.*

BS 1377-2: 1990. *Methods of test for soils for civil engineering purposes.*

Ahlgren, S. G. (2001). The nucleation and evolution of Riedel shear zones as deformation bands in porous sandstone. *Journal of Structural Geology, 23*, 1203-1214.

Anderson, K. H. (2007). Bearing capacity under cyclic loading — offshore, along the coast, and on land. The 21st Bjerrum Lecture presented in Oslo, 23 November 2007. *Canadian Geotechnical, 46*, 513-535.

Anderson, K. H. (2015). Cyclic soil parameters for offshore foundation design. In V. Meyer (Ed.), Frontiers in Offshore Geotechnics III (pp. 5-84). London: CRC Press.

Andresen, L., & Jostad, H. P. (2002) A constitutive model for anisotropic and strain-softening clay. G. N. Pande, Pietruszczak, S. (Ed.), *Numerical Models in Geomechanics 8th International Symposium* (79-83). Rome Italy: Taylor & Francis.

Arthurs, J. M. (2010). The nature of sensitivity in rhyolitic pyroclastic soils from New Zealand. In Unpublished MSc thesis. University of Auckland.

Bartlett, W. L., Friedman, M., Logan, J.M. M. (1981). Experimental folding and faulting of rocks under confining pressure Part IX. Wrench faults in limestone layers. *Tectonophysics, 79*(3-4), 255-277.

Bernander, S. (2000). *Progressive landslides in long natural slopes, formation, potential extension and configuration of finished slides in strain-softening soils.* Thesis, Lule University of Technology, Sweden.

Bishop, A. W. (1968). Proceedings of the Geotechnical Conference. *Geotechnical Conference* (Vol. 2, pp. 142-150). Oslo: Norwegian Geotechnical Institute.

Bishop, A. W. (1971). The influence of progressive failure on the choice of the method of stability analysis. *Géotechnique, 21,* 168-172.

Bishop, A. W., Webb, D. L., & Lewin, P. I. (1965). Undisturbed Samples of London Clay from the Ashford Common shaft; Strength-effective stress relationships. *Géotechnique, 15*(1), 1-13.

Bjerrum, L. (1961). The effective shear strength parameters of sensitive clays. *In Proceedings of the 5th international conference on soil mechanics and foundation engineering,* Paris, 23-28

Bjerrum, L. (1967). Progressive failure in slopes in overconsolidated plastic clay and clay shales. *Journal of the Soil Mechanics and Foundations, 93*(5), 3-49.

Boas, F. E., Fleischmann, D. (2012). CT artifacts: Causes and reduction techniques. *Imaging Med, 4*(2), 229-240.

Boulanger, R. W., Idriss, I. M. (2006). Liquefaction Susceptibility Criteria for Silts and Clays. *Journal of Geotechnical and Geoenvironmental Engineering, 132*(11), 1413-1426.

Boulanger, R. W., Idriss, I. M. (2007). Evaluation of Cyclic Softening in Silts and Clays. *Journal of Geotechnical and Geoenvironmental Engineering, 133*(6), 641-652.

Briaud, J. L. (2013). *Geotechnical Engineering: Unsaturated and Saturated Soils.* Somerset, NJ, USA: John Wiley & Sons.

Briggs, R.M. Hall, G.J., Harmsworth, G.R., Hollis, A.G., Houghton, B.F., Hughes, G.R., Morgan, M.D., Whitbread-Edwards, A.R. (1996). *Geology of the Tauranga Area – Sheet U14 1:50 000*. Department of Earth Sciences, University of Waikato Occasional Report 22.

Briggs, R. M., & Houghton, B. F., McWilliams, M., Wilson, C.J.N. (2005). 40Ar/39Ar ages of silicic volcanic rocks in the Tauranga-Kaimai area, New Zealand: Dating the transition between volcanism in the Coromandel Arc and the Taupo Volcanic Zone. *New Zealand Journal of Geology and Geophysics, 48*, 459-469.

Bruker (Compiler) (2015). *Skyscan 1272: High resolution X-Ray Microtomograph*. Belgium: Bruker.

Burns, D. A., & Cowbourne, A. J. (2003). *Engineering geological aspects of the Ruahihi Power Scheme, Tauranga.* Presented at the Geotechnics on the Volcanic Edge: New Zealand Geotechnical Society Symposium, Tauranga, March 2003.

Byerlee, J. (1992). The change in orientation of subsidiary shears near faults containing pore fluid under high pressure. *Tectonophysics, 211*(1), 295-303.

Camuti, K., & McGuire, P. (1999). Preparation of polished thin sections from poorly consolidated regolith and sediment materials. *Sedimentary Geology, 128,* 1-2.

Christophers, A., J. (2015). *Paleogeomorphic reconstruction of the Omokoroa Domain, Bay of Plenty, New Zealand.* Thesis, University of Waikato.

Chu, D. B., Stewart, J. P., Lee, S., Tsai, J. S., Lin, P. S., Chu, B. L., Seed, R. B., Hsu, S. C., Yu, M. S., & Wang, M. C. H. (2004). Documentation of soil conditions at liquefaction and non-liquefaction sites from 1999 Chi–Chi (Taiwan) earthquake. *Soil Dynamics and Earthquake Engineering, 24*(9–10), 647-657.

Churchman, G.J., Lowe, D.J. (2012). *Alteration, formation, and occurrence of minerals in soils*. In: Huang, P.M.; Li, Y; Sumner, M.E. (editors) “Handbook of Soil Sciences. 2nd edition. Vol. 1: Properties and Processes”. CRC Press (Taylor & Francis), Boca Raton, FL, 20.1-20.72.

Cook, E. (2016). *Felsic volcansim in the eastern Waihi area; process origins of the Corbett and Ratarua Ignimbrites and the Hikurangi Rhyolite*. In Unpublished MSc thesis: University of Waikato.

Western Bay of Plenty District Council. (2003). *Microzoning for Earthquake Hazards for the Western Bay of Plenty.* ISBN No. 0-9582171-4-9.

Cunningham, M. J. (2012). *Sensitive rhyolitic pyroclastic deposits in the Tauranga region: mineralogy, geomechanics and microstructure of peak and remoulded states.* Thesis, University of Waikato.

Desrues, J. V., G. (2004). Strain localization in sand: an overview of the experimental results obtained in Grenoble using stereophotogrammetry. *Journal of Numerical and Analytical Methods in Geomechanics, 28*, 279-321.

Egashira, K., Ohtsubo, M. (1982). Smectite in marine quick clays of Japan. *Clays and Clay Minerals, 30,* 275-280.

Fossen, H. (2010). *Structural Geology*. Cambridge: Cambridge University Press.

Geertsema, M., Cruden, D. M., & Schwab, J. W. (2006). A large rapid landslide in sensitive glaciomarine sediments at Mink Creek, northwestern British Columbia, Canada. *Engineering Geology, 83*(1–3), 36-63.

Geertsema, M. C., J.J., Schwab, J.W., Evans, S.G. (2006). An overview of recent large catastrophic landslides in northern British Columbia, Canada. *Engineering Geology, 83*, 120-143.

Coffey Geotechnics. (2012). *Hand auger boreholes and cross sections: Matua site.* Coffey Geotechnics, Tauranga.

Goldschmidt, V. M. (1926). Undersokelser over lersedimenter. *Nordisk jordbrugsforskning,* 4-7

Gulliver, C. P., Houghton, B.F. (1980). Omokoroa Point Land Stability Investigation. Tonkin and Taylor Ltd.

Gylland, A. S., Long, M., Emdal, A., Sandven, R. (2013a). Characterisation and engineering properties of Tiller clay. *Engineering Geology, 164*, 86-100.

Gylland, A. S., Jostad, H. P., & Nordal, S. (2014). Experimental study of strain localization in sensitive clays. *Acta Geotechnica, 9* 227-240.

Gylland, A. S., Rueslåtten, H., Jostad, H. P., & Nordal, S. (2013c). Microstructural observations of shear zones in sensitive clay. *Engineering Geology, 163*, 75-88.

Gylland, A. S. S., M.S., Jostad, H.P., Bernander, S. (2012). Soil Property Sensitivity in Progressive Failure of Slopes. *International Review of Civil Engineering, 3*(4), 321-328.

Hansen, L., Eilersen, S., Solberg, I., Svein, H., Rokoengen. (2007). Facies characteristics, morphology and depositional models of clay-slide deposits in terraced fjord valleys, Norway. *Sedimentary Geology, 202*, 710-729.

Hatrick, A. V. (Compiler) (1982). *Report of Committee to Inquire into the Failure of the Ruahihi Canal.*

Head, K. H., Epps, R. J., Scotland, U. K., Hungr, O., Leroueil, S., & Picarelli, L. (2014). *Manual of soil laboratory testing: Soil classification and compaction tests*. (3). London: Pentech Press.

Hue Le, T. M., Eiksund, G.R. (2014). Cyclic Behaviour of an Overconsolidated Marine Clay at Sheringham Shoal Offshore Wind Farm. *Journal of Ocean and Wind Energy, 1*(1), 59-64.

Hungr, O., Leroueil, S., Picarelli, L. (2014). The Varnes classification of landslide types, an update. *Landslides, 11*, 167-194.

Jacquet, D. (1990). Sensitivity to remoulding of some volcanic ash soils in New Zealand. *Engineering Geology, 28* 1-25.

Jostad, H. P., Fornes, P., & Thakur, V. (2006). Calculation of shear band thickness in sensitive clays. *Numerical Models in Geotechnical Engineering, 1,* 27-32.

Karlsrud, K., A., & Gregersen, O. (1984). Can we predict landslide hazards in soft sensitive clays? Summary of Norwegian practice and experiences. *Proceedings of the 4th International Symposium on Landslides* (107-130). Toronto Ontario.

Keam, M. J. (2008). *Engineering geology and mass movement on the Omokoroa Peninsula, Bay of Plenty.* Thesis, University of Auckland, New Zealand.

Kjellman, W. (1954). Mechanisms of Large Swedish Landslides. *European Conference on Stability of Earth Slopes:* Stockholm.

Kluger, M. O., Seibel, D., Moon, V., Kreiter, S., Hepp, D. A., De Lange, W., Jorat, E., Mörz, T. (2015). The role of halloysite morphology on undrained shear strength and sensitivity of volcanic ashes in New Zealand. University of Waikato.

Konert, M., Vandenberghe, J. (1997). Comparison of laser grain size analysis with pipette and sieve analysis: a solution for the underestimation of the clay fraction, *Sedimentology, 44*, 523-535.

Kramer, S. L. (1996). *Geotechnical Earthquake Engineering*. Civil Engineering and Engineering Mechanics. New Jersey, U.S.: Prentice Hall.

Kreiter, S., Hepp, D.A., Ossig, B., Hebig, J., Otto, D., Schlue, B.F., Mörz, T., Kopf, A. (2010b). Cyclic soil parameters of complex offshore soils: a practical engineering perspective. T. Triantafyllidis (Ed.), *Workshop Gründung von Offshore-Windenergieanlagen.* (165-181). Karlsruhe: Karlsruher Institut für Technologie.

Kreiter, S., Moerz, T., Strasser, M., Lange, M., Schunn, W., Schlue, B. F., Otto, D., & Kopf, A. (2010a). Advanced Dynamic Soil Testing — Introducing the New Marum Dynamic Triaxial Testing Device. In D. C. Mosher, R. C. Shipp, L. Moscardelli, J. D. Chaytor, C. D. P. Baxter, H. J. Lee & R. Urgeles (Eds.), *Submarine Mass Movements and Their Consequences* (31-41). Dordrecht: Springer Netherlands.

Lancellotta, R. (1995). *Geotechnical engineering*. A.A. Balkema Publishers, Rotterdam, Netherlands.

Lefebvre, G., Turner, A. K., & Schuster, R. L. (1996). Soft Sensitive Clay. *Landslides investigations and mitigation Special Report Research Board National Research Council, 247,* 607-617.

Leonard, G. S., Begg, J. G., & Wilson, C. J. J. (2010). *Geology of the Rotorua area: scale 250,000.* Institute of Geological Nuclear Sciences (Vol. 1). Lower Hutt: Institute of Geological & Nuclear Sciences Limited.

Lévy, S., Jaboyedoff, M., Demers, D. (2012). Erosion and channel change as factors of landslides and valley formation in Champlain Sea Clays: The Chacoura River, Quebec, Canada. *Geomorphology, 145-146*, 12-18.

Locat, A., Leroueil, S., Bernander, S., Demers, D., Jostad, H. P., & Ouehb, L. (2011). Progressive failures in eastern Canadian and Scandinavian sensitive clays. *Canadian Geotechnical Journal, 48,* 1696-1712.

Lowe, D. J., & Hogg, A. G. (1995). Age of the Rotoehu Ash. *New Zealand Journal of Geology and Geophysics, 38,* 399-402.

Lowe, D. J., Tippett, J. M., Kamp, P. J. J., Liddell, I. J., Briggs, R. M., & Horrocks, J. L. (2001). Ages on weathered Plio-Pleistocene tephra sequences, western North Island, New Zealand. *Tephras: Chronology, Archaeology, 1,* 45-60.

Mandel, J. (1966) Conditions de stabilitie et postulat de Drucker. *Symposiuim Rheology and Soil Mechanics* (58-68). Berlin: Springer.

Martin, J., II, Olgun, C., Mitchell, J., and Durgunoğlu, H. (2004). High-Modulus Columns for Liquefaction Mitigation. *Journal of Geotechnical and Geoenvironmental Engineering, 30*(6), 561-571.

McLaren, R. G., & Cameron, K. C. (1996). *Soil science*. Auckland: Oxford University Press.

Mitchell, J. K., Soga, K., Sons, M., Hoboken, N. J. (2013). *Fundamentals of soil behaviour*. University of Michigan: John Wiley & Sons.

Mojid, M. A. (2011). Diffuse Double Layer (DDL). In J. Gliński, J. Horabik & J. Lipiec (Eds.), *Encyclopedia of Agrophysics* (213-214). Dordrecht: Springer Netherlands.

Moon, V. G., Cunningham, M. J., Wyatt, J. B., Lowe, D. J., Mörz, T., & Jorat, M. E. (2013). Landslides in sensitive soils, Tauranga, New Zealand. C. Y. Chin (Ed.), *Proc. 19th NZGS Geotechnical Symposium*. Queenstown.

Moon, V. G., & de Lange, W. P., Garae, C.P., Mörz, T., Jorat, M.E., Kreiter, S. (2015). *Monitoring the landslide at Bramley Drive, Tauranga, NZ*. Presented at the 12th Australia New Zealand Conference on Geomechanics: ANZ 2015 Changing the Face of the Earth - Geomechanics and Human Influence.

Moon, V. G. L., D.J., Cunningham, M.J., Wyatt, J.B., de Lange, W.P., Churchman, G.J., Mörz, T., Kreiter, S., Kluger, M.O., Jorat, M.J. (2015). Sensitive pyroclastic-derived halloysitic soils in northern New Zealand: interplay of microstructure, minerals, and geomechanics. *International Workshop on Volcanic Rocks and Soils* (3-21). Lacco Ameno, Ischia Island, Italy.

Morgenstern, N. R., Tchalenko, J.S. (1967). Microscopic Structures in Kaolin Subjected to Direct Shear. *Geotechnique, 17*, 309-328.

New Zealand Geotechnical Society (NZGS). (2001). *Guideline for Hand Held Shear Vane Test.* http://www.nzgs.org/Publications/Guidelines/shear_vane_guidelines.pdf.

New Zealand Geotechnical Society (NZGS). (2005). *Guidelines for the field classification and description of soil and rock for engineering purposes.* http://www.nzgs.org/Publications/Guidelines/soil_and_rock.pdf.

Nova, R. (2012). *Soil Mechanics*. London, UK: Wiley.

NZGS. (2010). *Geotechnical earthquake engineering practice.* Module 1 – Guideline for the identification, assessment and mitigation of liquefaction hazards. New Zealand Geotechnical Society. http://www.nzgs.org/publications/guidelines/geoearthquakeengineer.pdf.

NZS 4402.4.1.3:1986, *Methods of testing soil for civil engineering purposes.*

Oliver, R. C. (1997). *A geotechnical characterisation of volcanic soils in relation to coastal landsliding on the Maungatapu Peninsula, Tauranga, New Zealand.* Thesis, University of Canterbury.

Ota, Y., Hull, A.G., Iso, N., Ikeda, Y., Moriya, I., Yoshikawa, T. (1992). Holocene marine terraces on the northeast coast of North Island, New Zealand, and their tectonic significance. *New Zealand Journal of Geology and Geophysics, 35*(3), 273-288.

Palmer, A. C. R., J. R. (1973). The growth of slip surfaces in the progressive failure of over-consolidated clay. *Proceedings of the Royal Society of London Mathematical and Physical Sciences, 332*, 527-548.

Parfitt, R. L. (1990). Allophane in New Zealand-a Review. *Australian Journal of Soil Research, 28*, 343-360.

Park, D. S., Kutter, Bruce L. (2015). Static and seismic stability of sensitive clay slopes. *Soil Dynamics and Earthquake Engineering, 79, Part A*, 118-129.

Poulos, S. J. (1971). The stress-strain curves of soils. Geotechnical Engineers Inc. Winchester, Massachusetts.

Prebble, W.M. (1986). Geotechnical problems in the Taupo Volcanic Zone. Volcanic hazard assessment in New Zealand. *New Zealand Geological Survey Record,* 10, 65-80.

Purzin, A. M., Saurer, E., Germanovich, L.N. (2010). A dynamic solution of the shear band propagation in submerged landslides. *Granular Matter, 12*, 253-265.

Pusch, R. (1970). Microstructural changes in soft quick clay at failure. *Canadian Geotechnical Journal, 7*, 1-7.

Quinn P., D. M. S., Hutchinson D.J., Rowe R.K. (2007). An exploration of the mechanics of retrogressive landslides in sensitive clay. *60th Canadian Geotechnical Conference* (721-727). Ottawa, Ontario.

Quinn P., D. M. S., Hutchinson D.J., Rowe R.K. (2011). A new model for large landslides in sensitive clay using a fracture mechanics approach. *Canadian Geotechnical, 48*, 1151-1162.

Rankka, K., Hulten, C., Larsson, R., Leroux, V., & Dahlin, T. (2004). *Quick clay in Sweden.* Swedish Geotechnical Institute.

Riedel, W. (1929). Zur mechanik geologischer brucherscheinungen. *Zentralblatt für Mineralogie, Geologie und Paläontologie B*, 354-368.

Robertson, P. K., Wride, C. E. (1998). Evaluating cyclic liquefaction potential using the cone penetration test. *Canadian Geotechnical Journal, 35*(3), 442-459.

Robertson, P. K. (2010). Evaluation of Flow Liquefaction and Liquefied Strength Using the Cone Penetration Test. *Journal of Geotechnical and Geoenvironmental Engineering, 136*(6), 842-853.

Rudnicki, J. W., Rice, J.R. (1975). Conditions for the localisation of deformation in pressure-sensitive dilatant materials. *Journal of Mechanics and Physical Solids 23*, 371-394.

Sasaki, S. (1974). Clay mineralogy and genetic environment of Kitami clay. *Nendo Kagaku, 14*, 58-70.

Seed, H. B., Lee, L.L., Idriss, I.M. (1969). Analysis of Sheffield Dam failure. *Journal of the Soil Mechanics and Foundations Division, 95*(6), 1453-1490.

Selby, M. J. (1993). *Hillslope materials and processes*. Oxford, UK: Oxford University Press.

Skempton, A. W. (1953). Soil mechanics in relation to geology. *Yorkshire Geological Society*, 29, 33-62.

Skempton, A. W. (1964). Long-term stability of clay slopes. *Géotechnique, 14*(2), 75-102.

Skempton, A. W. (1966). *Some Observations on Tectonic Shear Zones*. Presented at the 1st ISRM Congress, Imperial College, University of London.

Smalley, I. J. R., Ross, C.W., Whitton, J.S. (1980). Clays from New Zealand support the inactive particle theory of soil sensitivity. *Nature, 288*, 576-577.

Sperazza, M., Moore, J. N., & Hendrix, M. S. (2004). High resolution particle size analysis of naturally occurring very fine grained sediment through laser diffractometry. *Journal of Sedimentary Research, 74*(5), 736-743.

Stoops, G. (2003). *Guidelines for Analysis and Description of Soil and Regolith Thin Sections*. Madison, Wisconsin: Soil Science Society of America.

Tavenas, F., Flon, P., Leroueil, S., and Lebuis, J. (1983). *Remolding energy and risk of slide retrogression in sensitive clays*. Presented at the Symposium on Slopes on Soft Clays (463-478), Linköping, Sweden.

Tavenas, F. (1984). Landslides in Canadian sensitive clays-a state-of-the-art. *Proceedings of the 4th International Symposium on Landslides Toronto Ontario University of Toronto Press Toronto Ontario 1* 141-153.

Tavenas, J., Chagnon, Y., La Rochelle, P. (1971). The Saint-Jean-Vianney Landslide: Observations and Eyewitnesses Accounts. *Canadian Geotechnical, 8*(3), 463-478.

Tonkin & Taylor Ltd. (2011). *Bramley Drive landslip hazard assessment.* Tonkin & Taylor Ltd, Tauranga.

Terzaghi, K., Peck, R. B., & John, Y. (1948). *Soil Mechanics in Engineering Practice*. New York: New Sons Inc.

Thakur, V. (2007). *Strain localisation in sensitive soft clays.* Thesis, Norwegian University of Science and Technology.

Thakur, V. (2011). Numerically observed shear bands in soft sensitive clays. *Geomechanics and Geoengineering: An International Journal, 6*(2), 131-146.

Thakur, V., Jostad, H.P., Kornbrekke, H.A., Degago, S.A. (2014). *Landslides in Sensitive Clays: From Geosciences to Risk Management*. How Well Do We Understand the Undrained Strain Softening Response in Soft Sensitive Clay? (150). Netherlands: Springer.

Torrance, J. K. (2014). *Chemistry, Sensitivity and Quick-Clay Landslide Amelioration*. Landslides in Sensitive Clays: From Geosciences to Risk Management Netherlands: Springer.

Updike, R. G., Carpenter, B.A. (Compiler) (1986). *Engineering Geology of the Government Hill Area, Anchorage, Alaska* Washington: United States Government Printing Office.

Vardoulakis, I., Sulem, J. (2004). *Bifurcation analysis in Geomechanics*. Glasgow: Blackie Academic & Professional: An imprint of Chapman & Hall.

Vardoulakis., I. (1996). Deformation of water-saturated sand: II. Effect of pore water flow and shear banding. *Géotechnique, 46*(3), 457-472.

Vermeer, P. A., Vogler, U., Septanika, E.G. (2004) Modelling strong discontinuities in geotechnical problems. *Proc. 2nd International Symposium on Continuous and Discontinuous Modelling of Cohesive Frictional Materials* (381-394). Stuttgart.

Visintin, A. (1994). *Differential Models of Hysteresis*. Applied Mathematical Sciences (111). Berlin Heidelberg: Springer.

Vodyanitskii, Y. N. (2009). Mineralogy and geochemistry of manganese: A review of publications. *Eurasian Soil Science, 42*(10), 1170-1178.

Ward, W. T. (1967). Volcanic ash beds of the lower Waikato Basin, North Island, New Zealand. *New Zealand Journal of Geology and Geophysics, 10*, 1109-1135.

Wesley, L. D. (1973). Some basic engineering properties of halloysite and allophane clays in Java, Indonesia. *Géotechnique, 23*(4), 471-494.

Wesley, L. D. (1977). Shear strength properties of halloysite and allophane clays in Java, Indonesia. . *Géotechnique, 27*(2), 125-136.

Wesley, L. D. (2007). Slope behaviour in Otumoetai, Tauranga. New Zealand. *Geomechanics News, 74*, 63-75.

Wesley, L. D. (2009). Behaviour and geotechnical properties of residual soils and allophane clays. *Obras y Proyectos, 6* 5-10.

Wieczorek, G. F., Jibson, R.W., Wilson, R.C., Buchanan-Banks, J.M. (1982). *Geotechnical properties of ash deposits near Hilo, Hawaii*. USGS Numbered series: 82-279.

Wilkinson, S., Grant, D., Williams, E., Paganoni, S., Fraser, S., Boon, D., Mason, A., & Free, M. (2013). Observations and implications of damage from the magnitude Mw 6.3 Christchurch, New Zealand earthquake of 22 February 2011. *Bulletin of Earthquake Engineering, 11*(1), 107-140.

Wires, K. C. (1984). The Casagrande method versus the drop-cone penetrometer method for the determination of liquid limit. *Canadian Journal of Soil Science, 64* 297-300.

Wyatt, J. B. (2009). *Sensitivity and clay mineralogy of weathered tephra-derived soil materials in the Tauranga region.* Thesis, University of Waikato.